Chiral Analysis by Chiral Tag Rotational Spectroscopy

Kevin Joseph Mayer

Norfolk, Virginia

B. S., Virginia Tech, 2015

A Dissertation presented to the Graduate Faculty of the University of Virginia in Candidacy for the Degree of Doctor of Philosophy

Department of Chemistry

University of Virginia

May 2022

Abstract

Chiral compounds are of immense importance for medicinal research and pharmaceutical manufacturing. A complete chiral analysis would quantify all stereoisomers of a molecule which scales by 2^N, where N is the number of chiral centers. There are 2^{N-1} diastereomers and for each diastereomer there is an enantiomer. Furthermore, the analysis would allow for quantification of the enantiomeric excess, EE, of each component. This dissertation presents the ability of chiral tag rotational spectroscopy for chiral analysis.

In traditional rotational spectroscopy, enantiomers of a molecule have identical rotational spectra, but diastereomers have unique rotational spectra. Chiral tag rotational spectroscopy works by the addition of a new, known chiral center onto a chiral molecule thereby converting enantiomers into diastereomers. The new stereocenter is added through non-covalent complexation with a small chiral molecule designated a “chiral tag”. Complexation is achieved through the use of seeded molecular beams and are measured using a chirped-pulse Fourier transform microwave (CP-FTMW) spectrometer.

The first component of chiral analysis is the determination of enantiomeric excess in a sample. Since the enantiomers are turned into diastereomeric complexes, the rotational spectra for both are now distinguishable. However, due to the nature of the rotational measurements, the signal levels of the different transitions need to be normalized, which is accomplished through the measurement with a racemic form of the tag. An enantiopure form of the tag is then used, and a ratio of the signal levels, after being normalized, is used to calculate an enantiomeric excess. As many rotational transitions are observed in a rotational spectrum, many enantiomeric excess calculations may be made for improved accuracy and error estimation.

The last component of chiral analysis is the determination of absolute configuration. In chiral tag rotational spectroscopy, the measurement using the racemic tag allows observation of both diastereomeric complexes. In the enantiopure tag spectrum, one of these complexes is reduced in signal intensity, while the other is increased, if the sample is not racemic. This separates the rotational spectra into two distinct groups, which are then assigned by comparison of their rotational constants to rotational constants theoretically calculated using computational quantum chemistry. The accuracy of these methods for absolute configuration assignments is explored, and the ability for high-confidence assignment through comparison of atomic coordinates using Kraitchman's equations.

Table of Contents

Chapter 1

Introduction

I. Chiral Analysis

1) Introduction

Chiral compounds are of immense importance to the pharmaceutical industry.[1] A chiral compound exists as enantiomers, which are a pair of molecules that are non-superimposable mirror images of one another and share the same atoms as well as connectivity. Since enantiomers cannot be superimposed onto one another, this makes them non-identical and allows each enantiomer to have a unique stereochemical structure. The human body is a chiral environment composed of amino acids and sugars which exist exclusively as a single enantiomer.[2] When placed in a chiral environment, such as the human body, chiral compounds can yield different, and sometimes adverse, effects. Enantiomers are stereoisomers that have different configurations at each stereocenter. There are also diastereomers, which are stereoisomers with different configurations at one or more stereocenter, but not all. The number of unique stereoisomers increases exponentially at a 2^N rate, where N is the number of stereocenters. For N stereocenters there will be 2^{N-1} diastereomers and an enantiomer for each diastereomer if there are no meso isomers. A complete chemical analysis of a chiral sample involves the detection and quantification of all stereoisomers within a sample.

The following section is an overview of current chiral analysis techniques and spectroscopic methods. There are two steps for a complete chiral analysis. First is the determination of the enantiomeric excess, the quantification of the amount of one enantiomer over the other. The second step is the determination of the absolute configuration, the identification of

the enantiomer in excess in a sample. Separation methods are the most extensively used chiral analysis method, namely chiral chromatography, which includes gas chromatography (GC), liquid chromatography (LC), and super-critical fluid (SCF) chromatography. Chromatography techniques are only used to measure the enantiomeric excess of a sample. There are many spectroscopic methods such as nuclear magnetic resonance (NMR), circular dichroism (CD), optical rotation, and X-ray diffraction (XRD) that will also be discussed. These techniques are primarily used to measure the absolute configuration of the dominant enantiomer in a sample.

2) Chiral Chromatography

Chiral chromatography uses principles similar to that of the human body where the enantiomers are separated by chiral recognition when placed in a chiral environment. Due to their opposing stereochemistry, each enantiomer will interact differently with a chiral environment, allowing them to elute independently from one another.[3, 4] Separation methods are typically composed of two phases: a mobile phase and a stationary phase. The mobile phase for chiral separations is the inert carrier gas in GC, the solvents or mixtures of solvents in LC, and super-critical fluids (most commonly CO_2) for SCF chromatography. Stationary phases serve as the chiral environments in chromatography and are most commonly cyclodextrins, chiral metal complexes, and amino acids.[5] An achiral column can be used if the analyte is first derivatized by forming a covalent bond between the analyte and an additional chiral molecule of known stereochemistry. The process effectively converts the enantiomers into a mixture of diastereomers by adding an additional stereocenter.[6] Unlike enantiomers, diastereomers can be separated by normal chromatography techniques.

Gas Chromatography

Gas chromatography is best used for volatile compounds.[7] Moreover, the compounds need to be thermally stable to avoid decomposition at operational temperatures. The volatilized sample is carried through the column by an inert gas, where it interacts with the stationary phase and separates based on the polarities of the stationary phase and analyte. Detectors for GC are limited due to the gas-phase nature of the technique, but most often mass spectrometry (MS) is used. Other types of detectors include ionization detectors and various photometric detectors that use emission, absorption, or scattering.[7] As with many techniques, a multidimensional instrument can be used. Multidimension GC (MDGC) makes use of two columns where one is achiral and the other is chiral to further separate and analyze complex chemical mixtures.[8, 9] A major limitation to GC is quantification. Analytes are quantified via a constructed calibration curve or an internal standard of an isotope of the analyte.[6, 10, 11] Caloibration curves may not be viable if standards are not commercially available and isotopically labeled species are more costly.

Liquid Chromatography

Liquid chromatography is used to analyze analytes in the liquid phase or solids that can be dissolved, typically with the solvents used in the mobile phase. LC methods can be used on large biomolecules and pharmaceuticals, making it the most widely used analytical technique. Just like MDGC, LC methods can also be multidimensional, where they employ more than one column to separate analytes.[12, 13] Detection methods used are similar to those of GC; with MS or tandem MS, photometric detectors, and electrochemical detectors. Quantification with MS and some other detectors still require internal standards or calibration curves.[14, 15] If the molecule has a

chromophore, quantification can be achieved using a UV-vis detector where the absorbance peak is obtained and integrated. The peak area of all the components is then compared to yield a relative abundance for each species.

Supercritical Fluid Chromatography

Supercritical fluid chromatography has been increasingly studied over the last decade, due to the decreased analysis time it offers. The mobile phase is a fluid in the supercritical state (both temperature and pressure surpass the species' critical point), which most often are fluorinated carbons, carbon dioxide, and ammonia.[16] The advantages of using fluids such as carbon dioxide is after the collected sample is depressurized, the carbon dioxide can evaporate, and a concentrated sample remains. The detectors and the ability to use two columns in tandem are same as LC.[17] The main advantage of SFC over LC is ability to achieve higher flow rates due to the low viscosity of carbon dioxide. This means the overall analysis time of using SFC is lower than LC.[18] Interestingly enough, recent SCF does not use supercritical fluids, but instead fluids where only the pressure is above the critical point. This method is sometimes referred to as subcritical fluid chromatography.[19]

3) Nuclear Magnetic Resonance

Nuclear magnetic resonance has been an important structure determination tool for over half a century. NMR works by placing nuclei with a magnetic moment, such as ^{1}H, ^{13}C, or ^{19}F, within a strong magnetic field and pulsing a radio wave through the sample. The radio wave perturbs the nuclei, which are then allowed to relax, and a free induction decay is collected. The

free induction decay can then be acquired and Fourier transformed.[20] In normal conditions, enantiomers cannot be discriminated using NMR. However, chiral derivatization methods and chiral resolving agents can be used to distinguish enantiomeric signals. Chiral derivatization in NMR works the same way as in chromatographic methods. The enantiomers are covalently bonded to a chiral molecule of known stereochemistry, forming diastereomers that can be detected using NMR. Chiral derivatizing agent (CDAs) are specific to molecular functional groups, where the most commonly used CDA is Mosher's reagent that interacts with secondary alcohols and amines.[21, 22] Chiral solvating agents work by the same principal as derivatizing agents do, but instead form long-lived noncovalent complexes.[23-25] Chiral solvating agents have advantages over chiral derivation agents because of the minimal sample preparation and the lack of purification needed. Relative abundances can be calculated by integrating the area under the peaks for the now resolved enantiomers quantifying the enantiomeric excess. Additionally, these NMR techniques can be applied to large biomolecules.[26]

4) Circular Dichroism

Circular dichroism is a spectroscopic technique that involves the differential absorption of left-handed circularly polarized light and right-hand circularly polarized light. Chiral compounds interact with the two circularly polarized light differently causing the speed and the wavelength of the two polarizations to differ. There are many different types of CD methods, including photoelectron, vibrational, magnetic, and fluorescence CD.[27-29] These techniques have also been used as photometric detectors to complement chiral chromatography separation.[30] They have found an abundant use for biomolecules in detecting secondary and tertiary structures, determining

absolute configuration and analyzing metal protein interactions.[31-33] Quantification of chiral species is done with calibration curves, but the sample must have an enantiomeric excess for a signal to occur.

5) X-Ray Diffraction

X-ray diffraction techniques use the scattering of incident x-rays and measures the resulting diffraction patterns. The x-rays elastically scatter by interacting with electrons in a crystal, forming spherical waves that are then collected and analyzed.[34] The amplitude of the waves is proportional to the number of electrons, allowing the determination of the element.[34, 35] Information of the sample's electron density can be obtained based on the angles of the diffracted x-rays and intensities of the patterns. This technique has been the gold standard in molecular structure determination for almost a century. Amino acids and protein structures can also be determined, as well as hydrated protein crystals.[36, 37] However, this technique is only usable if a high quality crystal can be formed; although powdered x-ray diffraction can sometimes be used for materials that cannot form single crystals.[38] Absolute configuration can be determined directly by the x-ray scattering method or by using a chiral reference included in the crystal structure. The direct method depends on small differences in the intensities of the Friedel pairs, which is due to resonant scattering effects; however, this method breaks down for lighter atoms as their resonant scattering effects are small.[39-41] The chiral reference works similar to the other chiral analysis techniques where a reference of know chirality is covalently bonded, crystalized, or added by other means to form diastereomers.

6) Optical Rotation

Optical rotation is the process of rotating plane-polarized light by passing it through an optically active medium. Optical activity is measured using a polarimeter, where the rotation of the light can be measured in degrees. Enantiomers rotate the light in opposite directions but with equal magnitude depending on their handedness. An enantiomeric excess must be present for the optical activity to be measured. Likewise, racemic mixtures are unable to rotate the plane polarized light. Absolute configuration is established by the direction the light is rotated and the enantiomeric excess can be estimated by the degree of the rotation.[42] A standard of known absolute configuration is used to calibrate the angle and direction of rotation. Polarimeters can be used as detectors for chiral chromatography to establish absolute configuration.

7) Microwave Three-Wave Mixing

Rotational spectroscopy is a technique that is extremely sensitive to changes in the mass distribution of polar molecules in the gas phase; however, it cannot distinguish between two enantiomers.[43] Diastereomers are easily differentiated due to their differences in the moments of inertia, but enantiomers will have the same moments of inertia making them indistinguishable. It was shown that enantiomers can be identified using the rotational spectroscopic technique "microwave three-wave mixing".[44, 45] This technique distinguishes between enantiomers from the fact that the sign of the scalar triple product of the electric dipole moment components in the principal axis system ($\mu_a \times \mu_b \cdot \mu_c$) will always be opposite for enantiomers. This sign change can be measured as a phase difference in the free induction decay (FID) of 180°. Measurements are made in a three-level system joined by an a-, b-, and c-type rotational transition to form a three-

wave mixing cycle. A double resonant sum or difference frequency is generated using two orthogonally polarized excitation pulses and collecting the ensuing FID. Absolute configuration is determined via the phase of the FID, and the EE can be determined from the peak height. To date no group has been able to measure the absolute phase in a spectrometer, and absolute configuration is calibrated by using known samples. A key advantage to this technique is that it is highly selective and can be used on complex mixtures to establish the absolute configuration of a specific analyte.

II. Rotational Spectroscopy

1) Rotational Spectroscopy

Rotational spectroscopy is a technique that measures the transitions between the quantized rotational energy levels of a molecule.[43, 46] In the gas phase, molecules are free to rotate about their center of mass along three orthogonal axes, called the principal axes. The principal axes are defined such that the off-diagonal elements of the inertial tensor (products of inertia) are zero. For a molecule to have a pure rotational spectrum it must possess a permanent electric dipole moment. If the molecule has an electric dipole moment, or an electric dipole moment can be induced through a noncovalent interaction with another atom or molecule, then the electric field of electromagnetic radiation can interact with the molecule. The molecular rotational spectrum for an asymmetric top molecule is composed of three separate contributions that come from the interaction of the electric field of the light with the three components of the electric dipole moment in the principal axis system. These contributions are called the a-type, b-type, and c-type spectra and have different selection rules for allowed transitions between the quantized energy levels of the rotational kinetic energy. Due to the quantized energy levels, the frequency, v, of the light must match the difference

in energy, ΔE, of the rotational states:

$$\Delta E = h\nu \tag{1.1}$$

where *h* is Plank's constant. Therefore, a rotational spectrum depends on the molecule's moments-of-inertia and the electric dipole moment components along the principal axes. As a result, each molecule with a distinct geometry will have a unique rotational spectrum. This makes rotational spectroscopy a very effective technique for structure determination and chemical analysis.

As stated above, rotational spectra depend on the moments-of-inertia of a molecule, but more accurately, the rotational constants that describe a spectrum are inversely proportional to the moments-of-inertia:

$$A = \frac{h}{8\pi^2 I_a} \qquad B = \frac{h}{8\pi^2 I_b} \qquad C = \frac{h}{8\pi^2 I_C} \tag{1.2}$$

A, B, and C are the rotational constants of the molecule in Hz, and I_a, I_b, and I_c are the moments of inertia along the a, b, and c principal axes, respectively. By convention, A ≥ B ≥ C assumes that $I_a \leq I_b \leq I_c$. When $I_a = I_b = I_c$, it is known as a spherical top, and when $I_a = I_b$ or $I_b = I_c$ it is known as a symmetric top, an oblate and prolate symmetrical tops, respectively. In this dissertation the molecular systems studied are all asymmetric tops, where $I_a < I_b < I_c$. The transition frequencies are inherently described by the rotational constants of a molecule in the rigid rotor approximation:

$$\widehat{H}_{rot} = \frac{1}{\hbar^2}\left(A\hat{J}_a^2 + B\hat{J}_b^2 + C\hat{J}_c^2\right) \tag{1.3}$$

$\hat{J}_x$ is the total angular momentum operator along the principal axis, where x is either the a, b, or c axis. Rotating molecules experience centrifugal forces that pull the atoms apart and require additional constants to be fit. The analysis of a rotation spectrum will include comparing observed transitions to a model rotational Hamiltonian to fit the rotational and distortion constants. The most

commonly used Hamiltonian is the Watson reduced Hamiltonian, and in this dissertation only the quartic distortion constants for Watson's A reduction, Δ_J, Δ_{JK}, Δ_K, δ_J, and δ_K, will be used.[47] Moreover, other structural and electronic properties of a molecule can influence its corresponding spectral signatures and can also be included in the Hamiltonian. These include internal rotations[48, 49] and nuclear quadrupole interactions[49-51] which can couple to the angular momentum of the molecule to induce splitting of the rotational transitions. These structural and electronic properties can be calculated from a large array of free software packages available to reearchers.[52-54]

Incredibly, the magnitudes of the atom positions relative to the center of mass can be derived using rotational constants. Isotopically substituted atoms within the molecule will slightly alter the moments-of-inertia of the molecule, while not effecting the electronic structure in the Born-Oppenheimer approximation. This gives rise to a set of new rotational spectra for each isotopologue of the parent species. These can then be fit and Kraitchman's equations may be used to quantify the magnitudes of the atom positions:[55]

$$I'_{aa} = I_{aa} + \frac{\Delta m_n M}{(M+\Delta m_n)}(b^2 + c^2)$$

$$I'_{bb} = I_{bb} + \frac{\Delta m_n M}{(M+\Delta m_n)}(a^2 + c^2)$$

$$I'_{cc} = I_{cc} + \frac{\Delta m_n M}{(M+\Delta m_n)}(a^2 + b^2) \quad (1.4)$$

Here I'_{xx} (where x = a, b, or c) is the moment-of-inertia along the x principal axis, I_{xx} is the moment-of-inertia of the parent isotopic species, M is the total mass of the parent species, and Δm_n is the change in mass of the isotopically substituted atom, n. With three equations and three unknowns the system can be solved to yield magnitudes of the a, b, and c coordinates. However, errors can arise due to differences in the zero-point vibrations.[56, 57] If one of the atomic coordinates is close

to one of the principal axes ($x \leq 0.1$ Å), the solution can result in imaginary coordinates with high uncertainties. In this work, imaginary coordinates are set to 0 for the purpose of structure determination.

Intensities of rotational transitions are dependent on the magnitude of the electric dipole moment components, the population difference between rotational energy states, and the number density of the molecular species. As stated above, the projection of the electric dipole moment on to the principal axes, μ_a, μ_b, and μ_c, allows for three separate contributions to the rotational spectrum. For these contributions to the rotational spectrum to occur, it is necessary that the dipole moment component be nonzero in a direct absorption measurement. The intensities scale with the dipole moment component squared in the weak pulse limit of a Fourier transform microwave (FTMW) measurement. Furthermore, transition intensities are related to the difference in populations between two energy levels, where populated energy levels of a molecule are described by a Boltzmann distribution for a sample at thermal equilibrium. The distribution is dependent on the rotational temperature of the gas. An increase in rotational temperature allows for higher energy states to be populated. At higher temperatures, the peak transition intensity is observed at higher frequencies, while at lower temperatures the lower energy levels are populated, and the peak transition intensity is observed at lower frequencies. Molecular size can affect the spacing between the energy levels of a molecule, such that smaller molecules have larger spacing while larger molecules have smaller spacing.

Computational methods are now ubiquitous in rotational spectroscopy studies. Different *ab initio* calculations and computational methods that are traditionally used are Møller-Plesset (MP2) and density functional theory (DFT). A basis set is also chosen with the method, where a

basis set is defined as a set of one electron functions that are weighted in a linear combination to construct molecular orbitals.[58] Increasing the number of basis functions allows for a more accurate representation of the molecular orbital. These are used to predict the three-dimensional structure and electronic properties of the molecular system in study. Typically, geometry optimization calculations are conducted on many different conformations of the molecular system. From the theoretically optimized structures, rotational constants can be calculated from the calculated moments-of-inertia and compared to the experimental rotational constants. The accuracy of the predicted structures depends on the method and basis set used, but typical percent errors for rotational constants of a monomer species is less than 1%. Additionally, the electric dipole moment components, nuclear quadruple coupling constants, and zero-point vibrational energies can also be calculated. The development of computational methods is still an area of ongoing research that has greatly improved both the accuracy and computational expense. In the presented work, all computational calculations will be done using Gaussian09 and Gaussian16 software.[59, 60]

The large amount of structural data that can be gained from rotational spectroscopy combined with its unique sensitivity to changes in mass distribution make it an ideal technique for chemical analysis and benchmarking of quantum chemical methods. However, this technique is limited to molecules in the gas phase, which would not allow for the measurement of large biomolecules.

2) Instrumentation in Rotational Spectroscopy

The Varian brothers and Dr. Hansen at Stanford University invented the klystron, the first vacuum tube that generated microwave radiation.[61] The klystron quickly became the microwave

source for all early rotational spectroscopy experiments. Rotational spectroscopy advanced greatly with military research into radar during World War II. Many of the scientists working on radar and microwave technology established labs after the war to continue research efforts in the field of rotational spectroscopy. Developments included exploration into extended frequency ranges from cm to mm and sub-mm wavelengths,[62, 63] observations of nuclear quadrupole hyperfine structure resulting in transitional splitting,[49-51] and Stark modulated rotational spectra.[64-66] The Stark modulated rotational spectrometers use an applied D.C. electric field within the waveguide of an adsorption cell, inducing degenerate rotational energy levels to split. From these splittings, the electric dipole moment components of molecules can be accurately measured. Early microwave spectrometers used absorption cells to measure rotational transitions. These worked by passing the microwave through a gas and detecting the reduction of the amplitude of the light. Later, instruments used induced coherent spontaneous emission of radiation using short pulses to measure emissions spectra rather than absorption.[67, 68] Both of these techniques suffered from the Boltzmann distribution of the peak intensities rotational transitions as described in section 1.1, for they were done on room temperature gases. Not until the advent of supersonic molecular beam sources could the gasses be cooled to a few Kelvin. The first to utilize this were Smalley, Ramakrishna, Wharton and Levy, who used it for high-resolution fluorescence spectroscopy.[69, 70] The cooling reduced the vibrational and rotational states to the lowest energy levels, which greatly simplified spectra. Furthermore, this design allowed for the subsequent studies into weakly bound noncovalent complexes.[71] The complexes are produced by the expansion of a mixture of pressurized gases through a small, usually 1 mm diameter hole, into the vacuum chamber of a spectrometer. In rotational spectroscopy, the cooling lowered the partition function shifting the

peak rotational intensities to lower frequencies.

Fourier transform nuclear magnetic resonance (FT-NMR) was developed in the 1960s, and a basis for FTMW spectroscopy was developed in the 1970s.[72] The Flygare group then created the first spectrometer using FTMW techniques,[73] which gave huge advantages in sensitivity. The gaseous molecules of interest were excited with a short excitation pulse to polarize the molecules to induce background-free coherent emission. The ensuing free induction decay (FID) signal was collected over time and Fourier transformed to the frequency domain, revealing a high-resolution rotational spectrum. As with the earlier FT-NMR, Fourier transform techniques can average the FIDs to increase the signal-to-noise ratio of a spectrum by a factor of $\sqrt{N}$, where N is the number of FID acquisitions. Thus, to double the signal-to-noise ratio of a spectrum, four times the number of FIDs need to be collected.

Moreover, one great advantage of the Balle-Flygare spectrometer design was the use of a Fabry-Perot optical cavity.[74] In this design, the gas is expanded into a vacuum with highly reflective mirrors within the cavity. Once the gas passes the mirrors, a microwave pulse is coupled through the mirrors perpendicular to the nozzle to polarize the gas. The cavity is set to amplify a resonant frequency to intensify the emission signal. A major limitation with this design was the very small bandwidth, with a frequency range of less than 1 MHz. Additionally, the cavity mirrors must be adjusted each measurement to cover a new frequency range. Ultimately, the acquisition process requires a great amount of time to a collect a sufficient number of transitions over relatively large bandwidth. Since the inception of the Balle-flygare spectrometer, improvements have been made to automate the tuning of the mirrors for broadband spectral collection,[75] as well as increasing the sensitivity and resolution,[76, 77] and incorporating double resonance techniques using

two cavities.[78]

The Balle-Flygare design dominated rotational spectroscopy until 2006 with the invention of the chirped-pulsed Fourier transform microwave (CP-FTMW) spectrometer.[79] This spectrometer allowed for broadband, 6 GHz or more, of bandwidth to be acquired with every FID acquisition. A microwave chirp, a linear frequency sweep, is first generated using an arbitrary waveform generator (AWG). This chirp covers the whole bandwidth of the spectrum being acquired and typically is 1-4 μs long in duration. A high-power traveling wave tube amplifier (TWT) is used to provide enough power to each frequency in the chirp. The chirp is then broadcasted across the vacuum chamber by a microwave horn antenna, whereby multiple supersonic molecular beam nozzle sources expand the gas perpendicular to the chirp. The gas is then polarized by the chirp and the ensuing FID is collected by a receiving microwave horn antenna where it is directly digitized by a high speed (>40 GHz) oscilloscope. This decreases sample consumption and acquisition time compared to the Balle-Flygare instrument. However, the Balle-Flygare spectrometer still held an advantage in sensitivity from its use of passive amplification within the cavity, making it complimentary to the CP-FTMW technique.

The high resolution and large bandwidth of CP-FTMW spectrometers make it possible to study complex mixtures, the conformational landscape of molecules, reaction dynamics, and many other molecular systems. Relative transition intensities in the CP-FTMW technique are more reliable than Balle-Flygare spectrometer with about 15-30% accuracy.[79, 80] The relative transition intensities are appropriate for measuring the relative abundance between two different species in this work. Rotational spectroscopy's extreme sensitivity to changes in the mass distribution, the invention of the CP-FTMW spectrometer, and the range of systems that can be measured have

allowed rotational spectroscopy to become a viable option for quantitative chemical analysis of volatile compounds.

3) Noncovalent Complexing in Rotational Spectroscopy

Noncovalent bonds are weak and typically 1-5 kcal/mol, which allow short lived interaction to occur, creating the means for dynamic biological processes. These interactions are of immense importance for biological systems, as noncovalent interactions influence the three-dimensional structure of large molecules, such as proteins and nucleic acids. High resolution gas phase spectroscopy allows for these fundamental interactions to be investigated without matrix effects. As stated in section 1.2, molecules are not the only system that can be analyzed using rotational spectroscopy. Hydrogen bonded small biological molecules were the first noncovalent complexes to be analyzed by rotational spectroscopy.[81, 82] These were measured by absorption techniques where the gasses were introduced into the cell. Observations of these noncovalently bound molecules were very few in number until the 1970s. The use of supersonic molecular beams allowed for the weakly bound complexes via hydrogen bonding or Van der Waals forces to be created and studied.[71, 83]

CP-FTMW spectrometers have also increased the means to study these complexes.[84] The large bandwidth of these instruments allows for many transitions to be observed, permitting for spectral data not intended in the experiment to be observed and analyzed. This has led to the observation of ever increasing water clusters,[85, 86] acid-water complexes,[87, 88] dimers,[89] trimers,[90] and more. Chiral molecular recognition, an interaction between two chiral compounds that results

in the energetic favorability of one enantiomer over the other, has been observed in rotational spectra.[91, 92] A "three-point interaction" model is used to describe how chiral recognition can occur with non-bonding interactions.[93] The effects of chiral recognition is of great importance in pharmacological studies, whereby different enantiomers can have different pharmacological effects in the human body when metabolized. In this dissertation, noncovalently bound complexes will be used to perform quantitative analysis using rotational spectroscopy.

III. Dissertation Scope

The work presented in this thesis assesses the potential of chiral tag rotational spectroscopy, a chiral derivatization methodology using rotational spectroscopy, to perform chiral analysis. A potential advantage of chiral tag rotational spectroscopy is the ability to simplify chiral analysis, determination of enantiomeric excess and absolute configuration, all into one instrument. Chapter 2 will demonstrate that enantiomeric excess determinations are quantitatively accurate with high precision. Calibration curves using samples of known enantiomeric excess will be analyzed to validate accuracy of the technique. Statistical modeling of chiral tag rotational spectroscopy's precision will be shown with experimental results to further examine the source of errors in chiral tag measurements.

In Chapter 3, the reliability of quantum chemistry to establish the absolute configuration of chiral tag complexes with high confidence will be discussed. A benchmarking of the chiral tag complexes of verbenone noncovalently bonded with 3-butyn-2-ol will be used evaluate the reliability. Multiple methods will be used with two commonly used basis sets in rotational spectroscopy, Pople's 6-311G++(d,p) and Def2TZVP. The benchmarking will look at the accuracy

of the relative energies of isomers compared to that observed in the CP-FTMW spectroscopy measurement. This will assess the ability of the method and basis set to identify which isomers are expected to have the highest populations. Optimized structures from each method will be benchmarked to test the ability to give accurate rotational constants. Finally, the relative electric dipole moment components will be analyzed for increased confidence in assigning rotational spectra.

An example analysis of fenchyl alcohol will be performed in Chapter 4 with comparison to the accepted technique of vibrational circular dichroism, VCD. Fenchyl alcohol is a rigid molecule that has endo-exo isomerism. The sample is bought as the endo-isomer and quantification of the low abundance exo-diasteromer will be compared with VCD. Absolute configuration of the sample will be shown for both techniques, and the ability of chiral tag rotational spectroscopy to obtained extremely high confidence using ^{13}C-substitution structures for a chiral tag complex will also be shown. Advantages and disadvantages between the two techniques are highlighted.

A system that poses a challenge to high confidence assignment of absolute configuration is studied in Chapter 5. Carboxylic acids when noncovalently bound to the chiral tag can have isomers that are similar in rotational constants to the diastereomer complex. These isomers come from a 180° of the carboxylic acid functional group, and the two conformations from one of the diastereomer complexes have a corresponding structure from the other diastereomer complex. These predicted rotational constants are within the error of theoretical vs experimental determination and can lower confidence in the assignment of the complex. Multiple methods for gaining higher confidence will be assessed from determination of complexation energy to study binding preference, complexation of different chiral tags, and use of an isotopically labeled tag to

gain specific information on atom positions in the complex.

Ultimately the applicability of chiral tag is limited to smaller molecules due to the decrease in sensitivity from the rotational partition function. Furthermore, as molecules become larger the computational chemistry cost increases due to the many isomers of the chiral tag complexes that can be created, posing a problem for practical analytical chemistry use. Chapter 6 will explore the use of covalent modification of the analyte for the purpose of chiral analysis by rotational spectroscopy. This has the advantage of decreased computational time because theoretical conformational searches for monomers have already been developed. Furthermore, it can reduce sensitivity loss from the fractional complex formation of the analyte. FRD-903, a perfluorinated carboxylic acid, will be reacted with a chiral tag and the potential for covalent modification to increase size range for chiral analysis by rotational spectroscopy will be discussed.

IV. References

1. Nguyen, L. A.; He, H.; Pham-Huy, C., Chiral drugs: an overview. *Int J Biomed Sci* **2006,** *2* (2), 85-100.

2. Gleiser, M.; Walker, S. I., Life's chirality from prebiotic environments. *International Journal of Astrobiology* **2012,** *11* (4), 287-296.

3. Ribeiro, A. R.; Maia, A. S.; Cass, Q. B.; Tiritan, M. E., Enantioseparation of chiral pharmaceuticals in biomedical and environmental analyses by liquid chromatography: An overview. *Journal of Chromatography B* **2014,** *968*, 8-21.

4. Xiao, Y.; Ng, S.-C.; Tan, T. T. Y.; Wang, Y., Recent development of cyclodextrin chiral stationary phases and their applications in chromatography. *Journal of Chromatography A* **2012,** *1269*, 52-68.

5. Xie, S.-M.; Yuan, L.-M., Recent progress of chiral stationary phases for separation of enantiomers in gas chromatography. *Journal of Separation Science* **2017,** *40* (1), 124-137.

6. Morrison, C.; J Smith, F.; Tomaszewski, T.; Stawiarska, K.; Biziuk, M., Chiral gas chromatography as a tool for investigations into illicitly manufactured methylamphetamine. *Chirality* **2011,** *23* (7), 519-522.

7. Eiceman, G. A.; Hill, H. H.; Davani, B.; Gardea-Torresday, J., Gas Chromatography. *Analytical Chemistry* **1996,** *68* (12), 291-308.

8. Myrgorodska, I.; Javelle, T.; Meinert, C.; Meierhenrich, U. J., Enantioresolution and quantification of monosaccharides by comprehensive two-dimensional gas chromatography. *Journal of Chromatography A* **2017,** *1487*, 248-253.

9. Sciarrone, D.; Schipilliti, L.; Ragonese, C.; Tranchida, P. Q.; Dugo, P.; Dugo, G.; Mondello, L., Thorough evaluation of the validity of conventional enantio-gas chromatography in the analysis of volatile chiral compounds in mandarin essential oil: A comparative investigation with multidimensional gas chromatography. *Journal of Chromatography A* **2010,** *1217* (7), 1101-1105.

10. Kadokami, K.; Tanada, K.; Taneda, K.; Nakagawa, K., Novel gas chromatography–mass spectrometry database for automatic identification and quantification of micropollutants. *Journal of Chromatography A* **2005,** *1089* (1), 219-226.

11. Vielhauer, O.; Zakhartsev, M.; Horn, T.; Takors, R.; Reuss, M., Simplified absolute metabolite quantification by gas chromatography-isotope dilution mass spectrometry on the basis of commercially available source material. *J Chromatogr B Analyt Technol Biomed Life Sci* **2011,** *879* (32), 3859-70.

12. Barhate, C. L.; Regalado, E. L.; Contrella, N. D.; Lee, J.; Jo, J.; Makarov, A. A.; Armstrong, D. W.; Welch, C. J., Ultrafast Chiral Chromatography as the Second Dimension in Two-Dimensional Liquid Chromatography Experiments. *Analytical Chemistry* **2017,** *89* (6), 3545-3553.

13. Dugo, P.; Russo, M.; Sarò, M.; Carnovale, C.; Bonaccorsi, I.; Mondello, L., Multidimensional liquid chromatography for the determination of chiral coumarins and furocoumarins in Citrus essential oils. *Journal of Separation Science* **2012,** *35* (14), 1828-1836.

14. He, R.; Mai, B.; Fan, J.; Jiang, Y.; Chen, G.; Guo, D.; Chen, G.; Yao, X.; Gao, H.; Zhang, W., Identification, Quantification, and Stereoselective Degradation of Triazole Fungicide Cyproconazole in Two Matrixes through Chiral Liquid Chromatography-Tandem Mass Spectrometry. *Journal of Agricultural and Food Chemistry* **2019,** *67* (38), 10782-10790.

15. Nikolai, L. N.; McClure, E. L.; MacLeod, S. L.; Wong, C. S., Stereoisomer quantification of the β-blocker drugs atenolol, metoprolol, and propranolol in wastewaters by chiral high-performance liquid chromatography–tandem mass spectrometry. *Journal of Chromatography A* **2006,** *1131* (1), 103-109.

16. West, C., Recent trends in chiral supercritical fluid chromatography. *TrAC Trends in Analytical Chemistry* **2019,** *120*, 115648.

17. Speybrouck, D.; Lipka, E., Preparative supercritical fluid chromatography: A powerful tool for chiral separations. *Journal of Chromatography A* **2016,** *1467*, 33-55.

18. Lemasson, E.; Bertin, S.; West, C., Use and practice of achiral and chiral supercritical fluid chromatography in pharmaceutical analysis and purification. *Journal of Separation Science* **2016,** *39* (1), 212-233.

19. Lesellier, E., Retention mechanisms in super/subcritical fluid chromatography on packed columns. *Journal of Chromatography A* **2009,** *1216* (10), 1881-1890.

20. Kessler, H.; Gehrke, M.; Griesinger, C., Two-Dimensional NMR Spectroscopy: Background and Overview of the Experiments [New Analytical Methods (36)]. *Angewandte Chemie International Edition in English* **1988,** *27* (4), 490-536.

21. Wenzel, T. J.; Chisholm, C. D., Assignment of absolute configuration using chiral reagents and NMR spectroscopy. *Chirality* **2011,** *23* (3), 190-214.

22. Seco, J. M.; Quiñoá, E.; Riguera, R., Assignment of the Absolute Configuration of Polyfunctional Compounds by NMR Using Chiral Derivatizing Agents. *Chemical Reviews* **2012,** *112* (8), 4603-4641.

23. Holzgrabe, U., Quantitative NMR spectroscopy in pharmaceutical applications. *Progress in Nuclear Magnetic Resonance Spectroscopy* **2010,** *57* (2), 229-240.

24. Pérez-Trujillo, M.; Monteagudo, E.; Parella, T., 13C NMR Spectroscopy for the Differentiation of Enantiomers Using Chiral Solvating Agents. *Analytical Chemistry* **2013,** *85* (22), 10887-10894.

25. Wenzel, T. J.; Morin, C. A.; Brechting, A. A., Lanthanide-chiral resolving agent mixtures as chiral NMR shift reagents. *The Journal of Organic Chemistry* **1992,** *57* (13), 3594-3599.

26. Güntert, P., Automated structure determination from NMR spectra. *European Biophysics Journal* **2008,** *38* (2), 129.

27. Ranjbar, B.; Gill, P., Circular Dichroism Techniques: Biomolecular and Nanostructural Analyses- A Review. *Chemical Biology & Drug Design* **2009,** *74* (2), 101-120.

28. Janssen, M. H. M.; Powis, I., Detecting chirality in molecules by imaging photoelectron circular dichroism. *Physical Chemistry Chemical Physics* **2014,** *16* (3), 856-871.

29. Stephens, P. J.; Devlin, F. J.; Pan, J.-J., The determination of the absolute configurations of chiral molecules using vibrational circular dichroism (VCD) spectroscopy. *Chirality* **2008,** *20* (5), 643-663.

30. Tran, C. D.; Grishko, V. I.; Huang, G., Chiral detection in high-performance liquid chromatography by vibrational circular dichroism. *Analytical chemistry* **1994,** *66* (17), 2630-2635.

31. Greenfield, N. J., Using circular dichroism spectra to estimate protein secondary structure. *Nature protocols* **2006,** *1* (6), 2876-2890.

32. Manavalan, P.; Johnson, W. C., Sensitivity of circular dichroism to protein tertiary structure class. *Nature* **1983,** *305* (5937), 831-832.

33. Quintanar, L.; Rivillas-Acevedo, L., Studying metal ion–protein interactions: electronic absorption, circular dichroism, and electron paramagnetic resonance. In *Protein-Ligand Interactions*, Springer: 2013; pp 267-297.

34. Stanjek, H.; Häusler, W., Basics of X-ray Diffraction. *Hyperfine Interactions* **2004,** *154* (1), 107-119.

35. Smyth, M. S.; Martin, J. H., x ray crystallography. *Mol Pathol* **2000,** *53* (1), 8-14.

36. Garman, E. F., Developments in X-ray Crystallographic Structure Determination of Biological Macromolecules. *Science* **2014,** *343* (6175), 1102-1108.

37. Savage, H.; Wlodawer, A., [11] Determination of water structure around biomolecules using x-ray and neutron diffraction methods. In *Methods in Enzymology*, Academic Press: 1986; Vol. 127, pp 162-183.

38. Harris, K. D. M.; Tremayne, M.; Kariuki, B. M., Contemporary Advances in the Use of Powder X-Ray Diffraction for Structure Determination. *Angewandte Chemie International Edition* **2001,** *40* (9), 1626-1651.

39. Flack, H. D.; Bernardinelli, G., The use of X-ray crystallography to determine absolute configuration. *Chirality* **2008,** *20* (5), 681-690.

40. Flack, H.; Bernardinelli, G., The use of X-ray crystallography to determine absolute configuration. *Chirality: The Pharmacological, Biological, and Chemical Consequences of Molecular Asymmetry* **2008,** *20* (5), 681-690.

41. Albright, A. L.; White, J. M., Determination of absolute configuration using single crystal X-ray diffraction. In *Metabolomics tools for natural product discovery*, Springer: 2013; pp 149-162.

42. Polavarapu, P. L., Optical rotation: Recent advances in determining the absolute configuration. *Chirality* **2002,** *14* (10), 768-781.

43. Townes, C. H.; Schawlow, A. L., *Microwave Spectroscopy*. Dover Publications: 2013.

44. Patterson, D.; Doyle, J. M., Sensitive Chiral Analysis via Microwave Three-Wave Mixing. *Physical Review Letters* **2013,** *111* (2), 023008.

45. Alvin Shubert, V.; Schmitz, D.; Schnell, M., Enantiomer-sensitive spectroscopy and mixture analysis of chiral molecules containing two stereogenic centers – Microwave three-wave mixing of menthone. *Journal of Molecular Spectroscopy* **2014,** *300*, 31-36.

46. Bernath, P. F., *Spectra of Atoms and Molecules*. Oxford University Press: 2016.

47. Watson, J. K. G., Determination of Centrifugal Distortion Coefficients of Asymmetric-Top Molecules. III. Sextic Coefficients. *The Journal of Chemical Physics* **1968,** *48* (10), 4517-4524.

48. Lin, C. C.; Swalen, J. D., Internal Rotation and Microwave Spectroscopy. *Reviews of Modern Physics* **1959,** *31* (4), 841-892.

49. Wilson, E. B., Microwave spectroscopy in chemistry. *Science* **1968,** *162* (3849), 59-66.

50. Good, W. E., The Inversion Spectrum of Ammonia. *Physical Review* **1946,** *70* (3-4), 213-218.

51. Gordy, W., Microwave spectroscopy. Introductory paper: quadrupole couplings, dipole moments and the chemical bond. *Discussions of the Faraday Society* **1955,** *19*, 14-29.

52. Western, C. M., PGOPHER: A program for simulating rotational, vibrational and electronic spectra. *Journal of Quantitative Spectroscopy and Radiative Transfer* **2017,** *186*, 221-242.

53. Pickett, H. M., The fitting and prediction of vibration-rotation spectra with spin interactions. *Journal of Molecular Spectroscopy* **1991,** *148* (2), 371-377.

54. Kisiel, Z., Assignment and Analysis of Complex Rotational Spectra. In *Spectroscopy from Space*, Demaison, J.; Sarka, K.; Cohen, E. A., Eds. Springer Netherlands: Dordrecht, 2001; pp 91-106.

55. Kraitchman, J., Determination of Molecular Structure from Microwave Spectroscopic Data. *American Journal of Physics* **1953,** *21* (1), 17-24.

56. Costain, C. C., Determination of Molecular Structures from Ground State Rotational Constants. *The Journal of Chemical Physics* **1958,** *29* (4), 864-874.

57. Jagod, M.-F.; Oka, T., Inertial defects of planar symmetric top molecules. *Journal of Molecular Spectroscopy* **1990,** *139* (2), 313-327.

58. Lehtola, S.; Blockhuys, F.; Van Alsenoy, C., An Overview of Self-Consistent Field Calculations Within Finite Basis Sets. *Molecules* **2020,** *25* (5), 1218.

59. Frisch, M. J.; Trucks, G. W.; Schlegel, H. B.; Scuseria, G. E.; Robb, M. A.; Cheeseman, J. R.; Scalmani, G.; Barone, V.; Petersson, G. A.; Nakatsuji, H.; Li, X.; Caricato, M.; Marenich, A. V.; Bloino, J.; Janesko, B. G.; Gomperts, R.; Mennucci, B.; Hratchian, H. P.; Ortiz, J. V.; Izmaylov, A. F.; Sonnenberg, J. L.; Williams; Ding, F.; Lipparini, F.; Egidi, F.; Goings, J.; Peng, B.; Petrone, A.; Henderson, T.; Ranasinghe, D.; Zakrzewski, V. G.; Gao, J.; Rega, N.; Zheng, G.; Liang, W.; Hada, M.; Ehara, M.; Toyota, K.; Fukuda, R.; Hasegawa, J.; Ishida, M.; Nakajima, T.; Honda, Y.; Kitao, O.; Nakai, H.; Vreven, T.; Throssell, K.; Montgomery Jr., J. A.; Peralta, J. E.; Ogliaro, F.; Bearpark, M. J.; Heyd, J. J.; Brothers, E. N.; Kudin, K. N.; Staroverov, V. N.; Keith, T. A.; Kobayashi, R.; Normand, J.; Raghavachari, K.; Rendell, A. P.; Burant, J. C.; Iyengar, S. S.; Tomasi, J.; Cossi, M.; Millam, J. M.; Klene, M.; Adamo, C.; Cammi, R.; Ochterski, J. W.; Martin, R. L.; Morokuma, K.;

Farkas, O.; Foresman, J. B.; Fox, D. J. *Gaussian 16 Rev. C.01*, Wallingford, CT, 2016.

60. M. J. Frisch, G. W. T., H. B. Schlegel, G. E. Scuseria, M. A. Robb, J. R. Cheeseman, G. Scalmani, V. Barone, G. A. Petersson, H. Nakatsuji, X. Li, M. Caricato, A. Marenich, J. Bloino, B. G. Janesko, R. Gomperts, B. Mennucci, H. P. Hratchian, J. V. Ortiz, A. F. Izmaylov, J. L. Sonnenberg, D. Williams-Young, F. Ding, F. Lipparini, F. Egidi, J. Goings, B. Peng, A. Petrone, T. Henderson, D. Ranasinghe, V. G. Zakrzewski, J. Gao, N. Rega, G. Zheng, W. Liang, M. Hada, M. Ehara, K. Toyota, R. Fukuda, J. Hasegawa, M. Ishida, T. Nakajima, Y. Honda, O. Kitao, H. Nakai, T. Vreven, K. Throssell, J. A. Montgomery, Jr., J. E. Peralta, F. Ogliaro, M. Bearpark, J. J. Heyd, E. Brothers, K. N. Kudin, V. N. Staroverov, T. Keith, R. Kobayashi, J. Normand, K. Raghavachari, A. Rendell, J. C. Burant, S. S. Iyengar, J. Tomasi, M. Cossi, J. M. Millam, M. Klene, C. Adamo, R. Cammi, J. W. Ochterski, R. L. Martin, K. Morokuma, O. Farkas, J. B. Foresman, and D. J. Fox *Gaussian 09, Revision A.02*, Gaussian, Inc.: Wallingford, CT, 2016.

61. Gordy, W., Early events and some later developments in microwave spectroscopy. *Journal of Molecular Structure* **1983,** *97*, 17-32.

62. Gilliam, O. R.; Johnson, C. M.; Gordy, W., Microwave Spectroscopy in the Region from Two to Three Millimeters. *Physical Review* **1950,** *78* (2), 140-144.

63. Burrus, C. A.; Gordy, W., Millimeter and submillimeter wave spectroscopy. *Physical Review* **1956,** *101* (2), 599.

64. Dakin, T. W.; Good, W. E.; Coles, D. K., Resolution of a Rotational Line of the OCS Molecule and Its Stark Effect. *Physical Review* **1946,** *70* (7-8), 560-560.

65. Jr., K. B. M.; Hughes, R. H.; Jr., E. B. W., A Stark-Effect Microwave Spectrograph of High Sensitivity. *Review of Scientific Instruments* **1949,** *20* (11), 821-826.

66. Baird, D. H.; Fristrom, R. M.; Sirvetz, M. H., Stark Effect Absorption Cells for Microwave Spectroscopy. *Review of Scientific Instruments* **1950,** *21* (10), 881-881.

67. Dicke, R. H., Coherence in Spontaneous Radiation Processes. *Physical Review* **1954,** *93* (1), 99-110.

68. Dicke, R. H.; Romer, R. H., Pulse Techniques in Microwave Spectroscopy. *Review of Scientific Instruments* **1955,** *26* (10), 915-928.

69. Smalley, R. E.; Wharton, L.; Levy, D. H., The fluorescence excitation spectrum of rotationally cooled NO2. *The Journal of Chemical Physics* **1975,** *63* (11), 4977-4989.

70. Smalley, R.; Ramakrishna, B.; Levy, D.; Wharton, L., Laser spectroscopy of supersonic molecular beams: Application to the NO2 spectrum. *The Journal of Chemical Physics* **1974,** *61* (10), 4363-4364.

71. Novick, S. E.; Davies, P.; Harris, S. J.; Klemperer, W., Determination of the structure of ArHCl. *The Journal of Chemical Physics* **1973,** *59* (5), 2273-2279.

72. McGurk, J. C.; Schmalz, T. G.; Flygare, W. H., Fast passage in rotational spectroscopy: Theory and experiment. *The Journal of Chemical Physics* **1974,** *60* (11), 4181-4188.

73. Ekkers, J.; Flygare, W. H., Pulsed microwave Fourier transform spectrometer. *Review of Scientific Instruments* **1976,** *47* (4), 448-454.

74. Balle, T. J.; Flygare, W. H., Fabry–Perot cavity pulsed Fourier transform microwave spectrometer with a pulsed nozzle particle source. *Review of Scientific Instruments* **1981,** *52* (1), 33-45.

75. Chuang, C.; Hawley, C. J.; Emilsson, T.; Gutowsky, H. S., Computer-based controller and averager for the Balle-Flygare spectrometer. *Review of Scientific Instruments* **1990,** *61* (6), 1629-1635.

76. Grabow, J.-U.; Palmer, E. S.; McCarthy, M. C.; Thaddeus, P., Supersonic-jet cryogenic-resonator coaxially oriented beam-resonator arrangement Fourier transform microwave spectrometer. *Review of Scientific Instruments* **2005,** *76* (9), 093106.

77. Grabow, J. U.; Stahl, W.; Dreizler, H., A multioctave coaxially oriented beam-resonator arrangement Fourier-transform microwave spectrometer. *Review of Scientific Instruments* **1996,** *67* (12), 4072-4084.

78. Martinache, L.; Jans-bürli, S.; Vogelsanger, B.; Kresa, W.; Bauder, A., Microwave-microwave double-resonance experiments with pulsed molecular beams in crossed fabry-perot cavities. *Chemical Physics Letters* **1988,** *149* (4), 424-428.

79. Brown, G. G.; Dian, B. C.; Douglass, K. O.; Geyer, S. M.; Shipman, S. T.; Pate, B. H., A broadband Fourier transform microwave spectrometer based on chirped pulse excitation. *Review of Scientific Instruments* **2008,** *79* (5), 053103.

80. Park, G. B.; Field, R. W., Perspective: The first ten years of broadband chirped pulse Fourier transform microwave spectroscopy. *The Journal of Chemical Physics* **2016,** *144* (20), 200901.

81. Costain, C. C.; Srivastava, G. P., Microwave Rotation Spectra of Hydrogen-Bonded Molecules. *The Journal of Chemical Physics* **1964,** *41* (6), 1620-1627.

82. Srivastava, G. P.; Goyal, M. L., Microwave absorption in the hydrogen-bonded molecule CF3COOH-HCOOH. *Journal of Physics B: Atomic and Molecular Physics* **1968,** *1* (6), 1212-1217.

83. Novick, S. E.; Janda, K. C.; Holmgren, S. L.; Waldman, M.; Klemperer, W., Centrifugal distortion in ArHCl. *The Journal of Chemical Physics* **1976,** *65* (3), 1114-1116.

84. Juanes, M.; Saragi, R. T.; Caminati, W.; Lesarri, A., The Hydrogen Bond and Beyond: Perspectives for Rotational Investigations of Non-Covalent Interactions. *Chemistry–A European Journal* **2019,** *25* (49), 11402-11411.

85. Pérez, C.; Lobsiger, S.; Seifert, N. A.; Zaleski, D. P.; Temelso, B.; Shields, G. C.; Kisiel, Z.; Pate, B. H., Broadband Fourier transform rotational spectroscopy for structure determination: The water heptamer. *Chemical Physics Letters* **2013,** *571*, 1-15.

86. Pérez, C.; Muckle, M. T.; Zaleski, D. P.; Seifert, N. A.; Temelso, B.; Shields, G. C.; Kisiel, Z.; Pate, B. H., Structures of Cage, Prism, and Book Isomers of Water Hexamer from Broadband Rotational Spectroscopy. *Science* **2012,** *336* (6083), 897-901.

87. Schnitzler, E. G.; Seifert, N. A.; Kusuma, I.; Jäger, W., Rotational Spectroscopy of p-Toluic Acid and Its 1:1 Complex with Water. *The Journal of Physical Chemistry A* **2017,** *121* (45), 8625-8631.

88. Huang, W.; Thomas, J.; Jäger, W.; Xu, Y., Tunnelling and barrier-less motions in the 2-fluoroethanol–water complex: a rotational spectroscopic and ab initio study. *Physical Chemistry Chemical Physics* **2017,** *19* (19), 12221-12228.

89. McGuire, B. A.; Martin-Drumel, M.-A.; McCarthy, M. C., Electron Donor–Acceptor Nature of the Ethanol–CO2 Dimer. *The Journal of Physical Chemistry A* **2017,** *121* (33), 6283-6287.

90. Kannangara, P.; Peebles, R. A.; Peebles, S. A.; Pate, B. In *Studying CO 2 Solvent Properties by Microwave Spectroscopic Investigation of Fluoroethylene... CO 2... CO 2 Trimers*, 73rd International Symposium on Molecular Spectroscopy, 2018; p WE03.

91. Domingos, S. R.; Pérez, C.; Kreienborg, N. M.; Merten, C.; Schnell, M., Dynamic chiral self-recognition in aromatic dimers of styrene oxide revealed by rotational spectroscopy. *Communications Chemistry* **2021,** *4* (1), 32.

92. Seifert, N. A.; Pérez, C.; Neill, J. L.; Pate, B. H.; Vallejo-López, M.; Lesarri, A.; Cocinero, E. J.; Castaño, F., Chiral recognition and atropisomerism in the sevoflurane dimer. *Physical Chemistry Chemical Physics* **2015,** *17* (28), 18282-18287.

93. Davankov, V. A., The nature of chiral recognition: Is it a three-point interaction? *Chirality* **1997,** *9* (2), 99-102.

Chapter 2

Quantitative Enantiomeric Excess Determinations by Chiral Tag Rotational Spectroscopy

I. Introduction

As stated in the previous chapter, the ability to determine enantiomeric excess (EE) of a chiral molecule is of great importance for industrial and medicinal applications.[1-6] For example, pharmaceutical manufacturers need to verify their products are of the correct absolute configuration and enantiopurity to ensure governmental regulations are met.[7-9] Moreover, the number of single-enantiomer chiral pharmaceuticals have increased in recent years due to chiral switching. Chiral switching is a process where a single enantiomer of an already approved racemate pharmaceutical is brought to market as a separate drug sometimes marketed as more effective, longer lasting.[10-12] These single enantiomer drugs can lead to lower doses and decreased toxicity from drug-drug interactions, as well as in some cases, lesser adverse physiological effects from the other enantiomer.[13-14] Enantiopure pharmaceuticals require the lower abundant enantiomer to be quantified and labeled as an impurity. However, this level of quality assurance cannot be performed with typical achiral analytical methods.

In this chapter, a new technique using rotational spectroscopy will be shown to distinguish between enantiomers. This technique is dubbed "chiral tagging rotational spectroscopy" and works in a similar manner to NMR where chiral derivatization is used to convert enantiomers into diastereomers. The methodology used to measure the EE of an analyte using chiral tag rotational spectroscopy will be described. The accuracy and precision of the method are demonstrated using calibration curves, and the basis for the analytical formulas used in characterizing the measurement uncertainty are presented using experimental results and modeling. Variations in measurement

methodology to decrease fluctuations between measurements, thus decreasing uncertainty, is also explored.

II. Experimental

1) Chemicals

Commercial samples of (*R*)-3-methylcyclohexanone (3-MCH), racemic 3-MCH, (-)-isopulegol, (+)-isopulegol, and (1*S*)-(-)-verbenone were bought. All 3-MCH and isopulegol samples were obtained from MilliporeSigma. The reported EE from the certificate of analysis of the (*R*)-3MCH was 99.6%. The certificate of analysis reported the EE of (+)-isopulegol and (-)-isopulegol were 99.3% and 100%, respectively. The reference samples used to generate the calibration curves were prepared by either mixing the two enantiopure isopulegol samples or mixing the racemic and enantiopure 3-MCH samples to the desired EE. The reference mixture EE was calculated by volumetric and gravimetric analysis. (1*S*)-(-)-verbenone used in this study was purchased from MilliporeSigma with a reported EE of 53.6%. Finally, the chiral tags used in this study were (*S*)-(-)-propylene oxide, racemic propylene oxide, (*S*)-(-)-3-butyn-2-ol (butynol), and racemic butynol. Propylene oxide was obtained from TCI, while the butynol samples were purchased from MilliporeSigma. Certificate of analysis for propylene oxide and 3-MCH did not report an EE for both samples. However, the enantiopurity of the propylene oxide and butynol samples were measured in separate chiral tag rotational spectroscopy measurements conducted by another graduate student, Channing West. The enantiopurity with 1 sigma errors of the(*S*)-(-)-propylene oxide was found to be 99.68% ± 0.06% and 98.35% ± 0.11% for (*S*)-(-)-butynol.

2) Instrument Methodology

All molecular rotational measurements were performed on a 2-8 GHz CP-FTMW spectrometer. Information regarding the measurement technique and design of the 2-8 GHz CP-FTMW broadband spectrometer have been presented previously by Pérez et. al (2013).[15]

Chiral tag rotational spectroscopy uses the strategy of converting enantiomers to diastereomers by the addition of a new chiral center of known stereochemistry. As discussed previously in Chapter 1, NMR is the best example of a technique that uses an internal chiral reference. In NMR, the analyte is either covalently bonded with a chiral derivatizing agent or non-covalently bonded to form long-lived molecular complexes with a chiral resolving agent to determine EE.[16,17] Rotational spectroscopy achieves similar chiral resolution through non-covalent interactions with a small chiral molecule, the chiral tag, and the analyte to form a 1:1 complex. These complexes are formed in the pulsed jet expansion in molecular beam spectrometers.[18,19] This jet serves two functions: efficiently cooling the gas to a rotational temperature of ~1 K to reduce the partition function and increase the measurement sensitivity and generate the chiral tag complexes when the chiral tag is seeded into the Ne carrier gas.

Once the chiral tag complexes are formed, they are measured using broadband Fourier-transform rotational spectroscopy. The high spectral resolution of this technique allows for the diastereomer complexes and the noncomplexed monomers of the chiral tag and analyte to be completely resolved. The two complexes will have unique spectral features arising from the differences in their mass distributions and resulting rotational constants. Moreover, the large bandwidth used in the measurements allows for many transitions associated with the different

diastereomer complexes to be observed and analyzed for a high accuracy EE determination. For a complete EE determination, the absolute configuration, must be established. Absolute configuration is determined through the comparison of the experimentally observed and theoretical calculated rotational parameters. These parameters include the molecular rotational constants and the electric dipole moment components of the chiral tag complex.

Chiral tag rotational spectroscopy is performed by placing the analyte in the nozzle of the CP-FTMW spectrometer that is then heated to give a vapor pressure of ~1 Torr. The chiral tag is introduced at a 0.1% concentration mixture in neon to be used for adiabatic expansion in the spectrometer. The propylene oxide mixture was prepared and stored in a compressed gas cylinder. For the butynol tag, the mixture was made in a stainless-steel external reservoir. A small beaker containing 100 μL of butynol was placed in the reservoir with an inlet for the regulated Ne carrier gas and an outlet to allow mixing of the tag and neon. Separate reservoirs and Teflon gas lines connecting the reservoir to the spectrometer were used for enantiopure and racemic butynol to avoid contamination. The seeded carrier gas was pulsed into the spectrometer with a backing pressure of 2 atm at a rate of 3.3 Hz. For each pulse of gas, eight FIDs were collected. The optimized nozzle temperatures for the analytes were 50°C for isopulegol, 35°C for 3-MCH, and 60°C for the verbenone samples after testing different temperature and backing pressure conditions.

Samples for the calibration curves were prepared using a 250 μL syringe (SGE Analytical Science) and a 1 mL syringe (Thermo Scientific). 1mL solutions of 5, 10, 30, 55, and 90% EE were prepared with (-)-isopulegol and (*R*)-3-MCH, and 5 mL of 80% EE was made. Both racemic and enantiopure tag spectra are needed to perform an EE determination. Spectra were averaged for

400,000 FID acquisitions. Furthermore, the enantiopure (*R*)-(+)-3-MCH was ran for 900,000 FID acquisitions to increase the sensitivity to quantify the low abundant diastereomer complex. Only one chiral tag measurement was made for each EE, except for the 80% EE samples that was used to test the reproducibility of the method. The switch over between racemic and enantiopure measurements required cleaning of the instrument to avoid cross contamination that could affect the accuracy of the EE determination. Different methods of instrument cleaning were performed to determine the effect on the uncertainty of the measurement using verbenone in this study. First, after the enantiopure spectrum was obtained, the verbenone sample was heated to 80ºC, while neon was connected directly to the nozzles and allowed to flow over the sample by pulsing into the chamber to drive out any leftover butynol. Then the sample in the external reservoir was replaced and placed back into the system, and the spectrum was recorded for over a million FID acquisitions. The second method of replacing the sample involved taking the spectrometer apart after the enantiopure spectrum and thoroughly cleaning the instrument. This process included breaking vacuum, cleaning and refilling the nozzles, replacing the Teflon lines that connected the reservoir to the nozzles, replacing the sample in the reservoir, and reestablishing vacuum. Finally, the last measurement sought to determine the effect of a low signal-to-noise ratio on the determined EE. In this measurement only two of the five nozzles were filled with the verbenone sample. One nozzle was used to take a measurement with racemic butynol. After the measurement, the butynol sample was replaced, and the line to the other nozzle was connected. A spectrum of 200,000 FID acquisitions was collected for each butynol tag.

3) Computational Chemistry Methods

Quantum chemical estimates of the rotational spectroscopy parameters of the 1:1 analyte to chiral tag complexes were performed to identify absolute configuration. The quantum chemical calculations were performed with Gaussian09 software using dispersion corrected density functional theory (DFT) using Grimme's D3 correction with Becke-Johnson damping. [20-22] Geometry optimizations were performed using B3LYPD3BJ def2TZVP level of theory and were run by collaborator Dr. Luca Evangelisti. Many non-covalent conformations of the chiral tag complexes were generated and optimized, using a hydrogen bond as the expected dominant interaction. The lowest energy conformations of the3-MCH-butynol diastereomer complexes are shown in Figure 2.1, and in Figure 2.2 the propylene oxide-isopulegol lowest energy diastereomeric complexes are shown. The rotational parameters were experimentally fit using Pickett's SPCAT/SPFIT and Kisiel's PROSPE program package.[23,24]

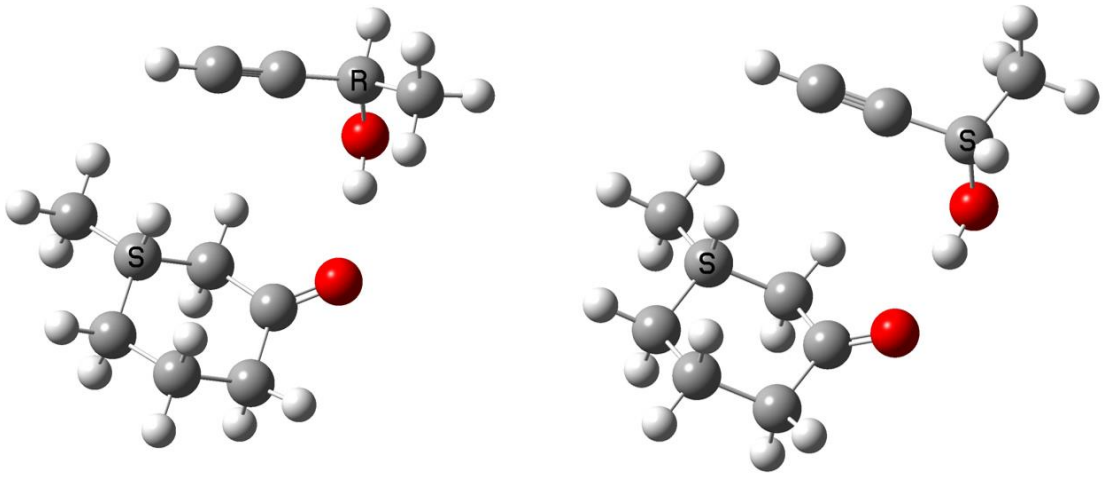

Figure 2.1: Lowest Energy complexes for (S)-(-)3-MCH noncovalently bonded to butynol. The structures were optimized with B3LYPD3BJ def2TZVP level of theory.

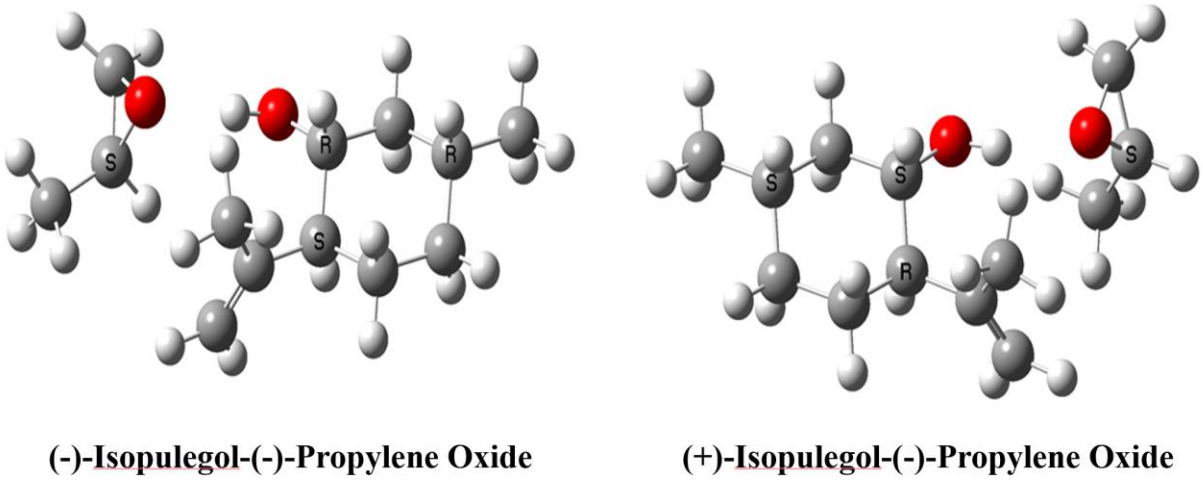

(-)-Isopulegol-(-)-Propylene Oxide **(+)-Isopulegol-(-)-Propylene Oxide**

Figure 2.2: Calculated complex structures for the two enantiomers of isopulegol and (-)-(S)-propylene oxide. These structures were calculated using B3LYPD3BJ with def2TZVP basis set.

III. Results and Discussion

1) Quantitative Analysis of the Chiral Tag Rotational Spectrum

Definitions of Analyte and Tag Enantiomeric Excess

In these equations the chirality is expressed with optical rotations, (+/-) rather than Cahn-Ingold-Prelog priority rules, (*R*/*S*). Both have limitation, such as the optical rotation of the sample must be measured to assign a +/-, and *R*/*S* designation becomes confused when the molecule has multiple chiral centers.

The concentration, or the number density, is proportional to the enantiomer fractions for the analyte enantiomers and can be written in terms of total analyte concentration as

$$[(-) - Analyte] = f_{-}[Analyte] \tag{2.1}$$

$$[(+) - Analyte] = f_+[Analyte] = (1 - f_-)[Analyte] \quad (2.2)$$

Where $0 \leq f_- \leq 1$. If the fractional enantiomeric excess of the analyte is

$$ee_{analyte} = f_+ - f_- = 1 - 2f_- \quad (2.3)$$

Note that the quantity is positive when the (+)-analyte is in excess ($f_- < 0.5$), and negative when (-)-analyte is in excess ($f_- > 0.5$). It is common to specify the percent enantiomeric excess, EE, where

$$EE_{analyte} = 100 \times ee_{analyte} \quad (2.4)$$

Similarly, for the chiral tag sample we define:

$$[(-) - Tag] = \delta_-[Tag] \quad (2.5)$$

$$[(+) - Tag] = (1 - \delta_-)[Tag] \quad (2.6)$$

So that

$$ee_{tag} = 1 - 2\delta_- \quad (2.7)$$

EE determinations by Chiral Tag Rotational Spectroscopy

The analysis of the chiral tag rotational spectrum to determine enantiomeric excess is based on the formulation provided in this section. A major goal of this work is to demonstrate the quantitative validity of the produced results. It is assumed that the number density of the two diastereomer chiral tag complexes are formed in a 1:1 ratio within the pulsed jet expansion is related to the number densities of the analyte and chiral tag by

$$I_{Homo} = C'_{Homo}([(+) - \text{Analyte}]\big[[(+) - \text{Tag}] + [(-) - \text{Analyte}][(-) - \text{Tag}]\big) \quad (2.8)$$

$$I_{Hetero} = C'_{Hetero}([(-) - \text{Analyte}][[(+) - \text{Tag}] + [(+) - \text{Analyte}][(-) - \text{Tag}]) \quad (2.9)$$

I_{Homo} and I_{Hetero} are the signal intensities, the number densities are denoted in brackets, and C'_{Hetero} and C'_{Homo} are the proportionality constants between the chiral tag complex concentration and the signals. The proportionality constants include effects from the spectroscopy, electric dipole moments, partition function, and instrument response, as well as variation in the number density due to chiral recognition and cooling. Substituting Eqs. 2.1, 2.2, 2.3 and 2.4:

$$I_{Homo} = C'_{Homo}[Analyte][Tag][(1 - f_{-})(1 - \delta_{-}) + (f_{-}\delta_{-})] =$$

$$C_{Homo}[(1 - f_{-})(1 - \delta_{-}) + (f_{-}\delta_{-})] \quad (2.10)$$

$$I_{Hetero} = C'_{Hetero}[Analyte][Tag][(1 - f_{-})(\delta_{-}) + f_{-}(1 - \delta_{-})] =$$

$$C_{Hetero}[(1 - f_{-})(\delta_{-}) + f_{-}(1 - \delta_{-})] \quad (2.11)$$

Where C_{Homo} and C_{Hetero} now contain the total concentration, or the number density, of both the tag and analyte. In the measurement, the instrument response is calibrated using a racemic tag sample, where $\delta = 0.5$:

$$I_{Homo}^{Rac} = \left(\frac{C_{Homo}}{2}\right)((1 - f_{-}) + f_{-}) = \left(\frac{C_{Homo}}{2}\right) \quad (2.12)$$

$$I_{Hetero}^{Rac} = \left(\frac{C_{Hetero}}{2}\right)((1 - f_{-}) + f_{-}) = \left(\frac{C_{Hetero}}{2}\right) \quad (2.13)$$

The second step in the EE determination repeats the chiral tag measurement with a high enantiopurity tag sample where $\delta_{-} \approx 0$ for enantiopure (+)-tag sample and $\delta_{-} \approx 1$ for the enantiopure (-)-tag sample. In addition, a common measurement methodology includes changing the analyte sample in the spectrometer between racemic and enantiopure measurements. After the spectrometer is rebuilt, the overall signal levels for both homochiral and heterochiral tag

complexes can change by an overall scale factor. For example, the tension on the solenoid valves may be different causing different total amounts to be injected into the spectrometer on each sample injection cycle.

$$I_{Homo}^{Pure} = \left[C_{Homo}[(1-f_{\_})(1-\delta_{\_}) + (f_{\_}\delta_{\_})]\right] \cdot \lambda \tag{2.14}$$

$$I_{Hetero}^{Pure} = \left[C_{Hetero}[(1-f_{\_})(\delta_{\_}) + f_{\_}(1-\delta_{\_})]\right] \cdot \lambda \tag{2.15}$$

Where λ accounts for the overall signal level variation between racemic and enantiopure measurements. To perform the enantiomeric excess determination, normalized signal intensities are used

$$N_{Homo} = \frac{I_{Homo}^{Pure}}{I_{Homo}^{Rac}} = 2\lambda[(1-f_{\_})(1-\delta_{\_}) + (f_{\_}\delta_{\_})] \tag{2.15}$$

$$N_{Hetero} = \frac{I_{Hetero}^{Pure}}{I_{Hetero}^{Rac}} = 2\lambda[(1-f_{\_})(\delta_{\_}) + f_{\_}(1-\delta_{\_})] \tag{2.16}$$

The ratio of these normalized signals is

$$R = \frac{N_{Homo}}{N_{Hetero}} = \frac{(1-f_{\_})(1-\delta_{\_}) + f_{\_}\delta_{\_}}{(1-f_{\_})(\delta_{\_}) + f_{\_}(1-\delta_{\_})} \tag{2.17}$$

Now consider the following quantity

$$\frac{R-1}{R+1} \tag{2.18}$$

where

$$R - 1 = \frac{\left(1-2f_{\_}\right)(1-2\delta_{\_})}{\left(1-f_{\_}\right)(\delta_{\_}) + f_{\_}(1-\delta_{\_})} \tag{2.19}$$

$$R + 1 = \frac{1}{(1 - f\_)(\delta\_) + f\_(1 - \delta\_)} \tag{2.20}$$

So that

$$\frac{R - 1}{R + 1} = (1 - 2f\_)(1 - 2\delta\_) = (ee_{analyte})(ee_{tag}) \tag{2.21}$$

using Eq. 2.3 and 2.7. Thus, the ratio of the two normalized signals shows a dependence on the enantiomeric excess of both the tag and analyte. Consequently, the ratio of two signals from heterochiral and homochiral complexes needs to be corrected by the ee_{tag} to give an accurate determination of the enantiomeric excess of the analyte.

Statistical Analysis of a Chiral Tag Measurement

In a chiral tag measurement, many transitions for both complexes are observed and can be used to derive many individual EE determinations. A mean and the measurement uncertainty can then be calculated to give a quantitative analysis of the enantiomeric excess of the analyte. The EE determinations can then be visualized in a histogram. The width of this histogram is related to the uncertainty of the mean measured EE, which can be related to the fluctuation in measurement intensities. In Fourier transform microwave spectroscopy, the measurement is proportional to the electric field strength of the excitation pulse and the number density of the molecular species. Both these quantities fluctuate from differences in noise power from the microwave amplifier and the amount of sample injected in the pulsed jet, respectively. From measurements in the broadband spectrometer, it has been found that:

$$\left(\frac{\sigma_I}{I}\right) = c \tag{2.22}$$

Where σ_I is the standard deviation of measurement intensity, *I* is the mean intensity, and *c* is a constant relative intensity fluctuation. Typically, *c* is between 1-10%, so that c = 0.01-0.1. As *R* is related to the intensity of the transitions from Eqs. 2.15-2.17, the measurement fluctuation in *R* is

$$\left(\frac{\sigma_R}{R}\right) = \sqrt{\left(\frac{\sigma_{I_{Homo}}^{Pure}}{I_{Homo}^{Pure}}\right)^2 + \left(\frac{\sigma_{I_{Homo}}^{Rac}}{I_{Homo}^{Rac}}\right)^2 + \left(\frac{\sigma_{I_{Hetero}}^{Pure}}{I_{Hetero}^{Pure}}\right)^2 + \left(\frac{\sigma_{I_{Hetero}}^{Rac}}{I_{Hetero}^{Rac}}\right)^2} = \sqrt{4c^2} = 2c$$

$$\sigma_R = 2Rc \tag{2.23}$$

The ratio, R, is related to the product of the ee of the analyte and the tag, $ee_{Product,}$ from Eq. 2.21. The uncertainty of the product is

$$\sigma_{ee_{Product}} = \sqrt{\left[\frac{\partial ee_{Product}}{\partial R}\right]^2 \cdot (\sigma_R)^2} \tag{2.24}$$

The partial differential with respect to the ratio, *R*

$$\frac{\partial ee_{Product}}{\partial R} = \frac{\partial}{\partial R}\left(\frac{R-1}{R+1}\right) = \frac{R-1}{(R+1)^2} - \frac{1}{R+1} \tag{2.25}$$

Now substituting this differential

$$\sigma_{ee_{Product}} = \left|\frac{R-1}{(R+1)^2} - \frac{1}{R+1}\right| \cdot 2Rc \tag{2.26}$$

Now in a chiral tag measurement, the ee_{tag} and σ_{Tag} will have been known from another measurement. These results can then be used to determine the uncertainty in the analytes ee, such

that

$$\frac{\sigma_{ee_{Product}}}{ee_{Product}} = \sqrt{\left(\frac{\sigma_{Tag}}{ee_{Tag}}\right)^2 + \left(\frac{\sigma_{Analyte}}{ee_{Analyte}}\right)^2} \tag{2.27}$$

When the high enantiopurity tag is used (ee ≈ 1) and is determined to a high accuracy ($\sigma_{Tag} \approx 0$), the expression is then dominated by the analyte uncertainty so that:

$$\frac{\sigma_{ee_{Product}}}{ee_{tag}ee_{Analyte}} \approx \frac{\sigma_{ee_{Product}}}{ee_{Analyte}} \approx \frac{\sigma_{ee_{Analyte}}}{ee_{Analyte}} \tag{2.28}$$

Or

$$\sigma_{ee_{Product}} \approx \left|\frac{R-1}{(R+1)^2} - \frac{1}{R+1}\right| \cdot 2Rc \approx \sigma_{ee_{Analyte}} \tag{2.29}$$

This equation gives a method to estimate the expected uncertainty from many individual ee determinations from a single chiral tag measurement. In the analysis, assuming equal number of transitions, *N*, for both the homochiral and heterochiral complexes are being used, then the analysis can be viewed as making *N* different ee determinations. Selecting a single transition from the homochiral spectrum and calculating the ee it makes with *N* heterochiral transitions gives a mean ee determination and a standard deviation. This standard deviation is expected to be the same for each of the *N* transitions used from the homochiral spectrum to estimate the mean ee. The uncertainty described by the *N* estimates of the analyte ee is then described by the standard error:

$$SE = \frac{\sigma_{ee_{Analyte}}}{\sqrt{N}} \tag{2.30}$$

This yields a simple representation for results of a chiral tag measurement: a histogram using *N*

transitions, the ee of the analyte as the mean ee of all ee determinations, and the measurement uncertainty represented by the standard error.

A statistical model of chiral tag rotational spectroscopy measurements is used to demonstrate the data analysis principles described above and modeled by Dr. Pate. The model is based on the observation that the signal fluctuations in Fourier transform rotational spectroscopy is proportional to the intensity of the transition, Eq. 2.22. The model chooses transitions from a normal distribution with a standard deviation proportional to the mean intensity value. Results of simulations of EE determination by chiral tag are discussed below. Fig. 2.3 shows the histograms for simulations of EE= 0, 25, 50, 75, 90, 95% using a 5% intensity fluctuation and assuming an enantiopure tag ($ee_{tag} \approx 1$). Each histogram is simulated using $N_{pairs} = 49$, for a total of 2401 individual ee determinations. The width of the histogram as seen in Fig. 2.3 decreases with increasing tag enantiopurity of the tag. The closer the ratio *R* is to 1, the analyte is racemic, and the larger the uncertainty is as shown in Eq. 2.29. Alternatively, the larger *R* is, the more enantiopure the analyte, the left side of the product in Eq. 2.29 approaches 0 and the uncertainty is reduced.

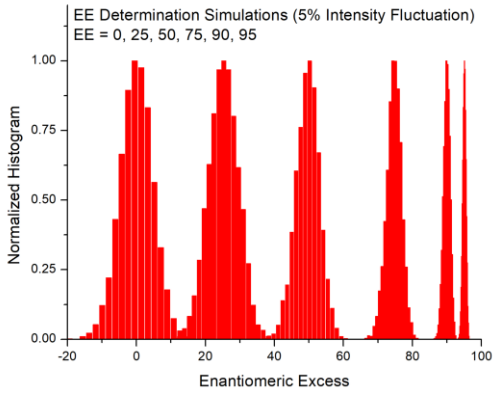

Figure 2.3: Simulated histograms results for a chiral tag measurement using a 5% relative intensity fluctuation for EE = 0, 25, 50, 75, 90, 95%.

The effect of percent intensity fluctuation is shown in Fig. 2.4. Intensity fluctuations for 2.5, 5, and 10% are used with N_{pairs} = 49. When the analyte is racemic, R =1, and the uncertainty of the measurement is a measurement of the intensity fluctuation. This agrees with Eq. 2.26. The width of the histogram is linearly dependent on the percentage intensity fluctuation. This is illustrated by EE = 60, where the uncertainty is 1.5, 3, and 6 for the 2.5, 5, and 10% curves. The data points in red are experimental uncertainty from the calibration curve of 3-MCH tagged with butynol below. An intensity fluctuation of 5% is shown to be a good characterization for the spectrometer. Figure 2.5 shows the effect of the number of transitions used, N, on the measurement uncertainty for a chiral tag measurement. This figure shows simulated results for an analyte of EE = 80 and using a 5% intensity fluctuation. The simulation was performed as the number of transitions, N, used from each spectrum is increased up to N=100 and for each N, the spectrum simulation is performed 1000 times. The blue data points represent the average of the histogram width, or the standard deviation of the ee determinations, for all 1000 simulations. This demonstrates that the uncertainty of a chiral tag measurement is determined by the intensity fluctuation of the spectrometer. In all cases, from N = 1-100 the width, or standard deviation, of the histogram is 1.8. The red data points represent the standard deviation of the calculated EE for all 1000 simulations, using N transitions. This is a measurement of the measurement uncertainty in replicate experiments, and the black curve through the red data points is the standard error calculated as the histogram width over $\sqrt{N}$. Measurement reproducibility can be described by the width of a histogram and the number of transitions used to construct the histogram.

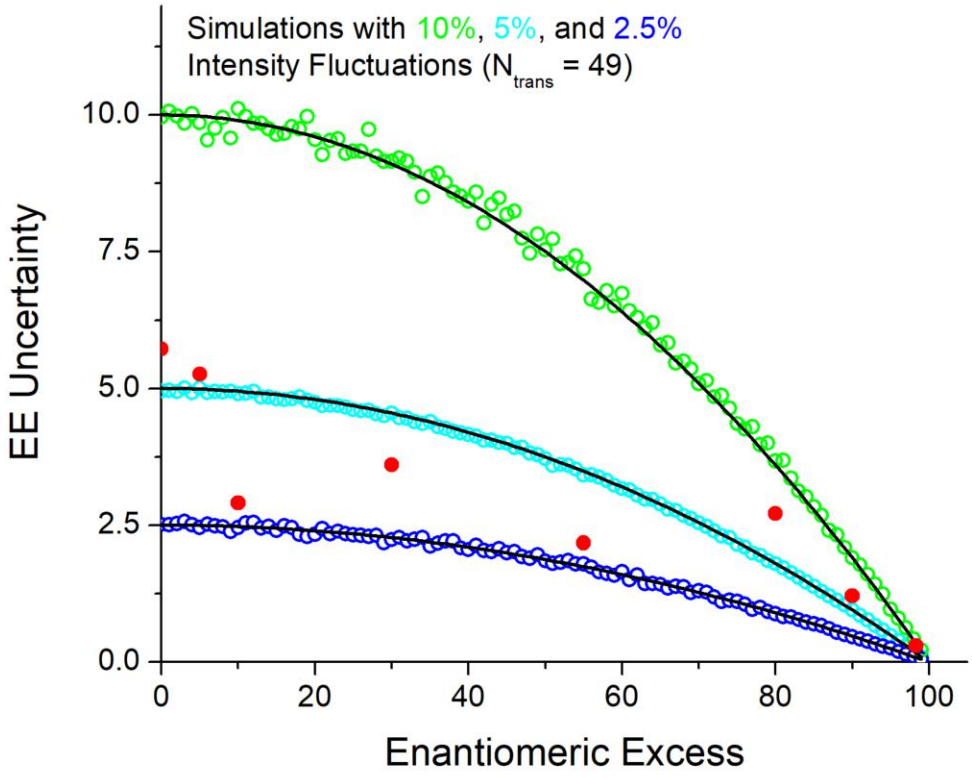

Figure 2.4 The results of using different intensity fluctuations to examine the effect on the EE uncertainty as the enantiopurity of the sample increases. The red data points are experimental data obtained in the 3-MCH calibration curve.

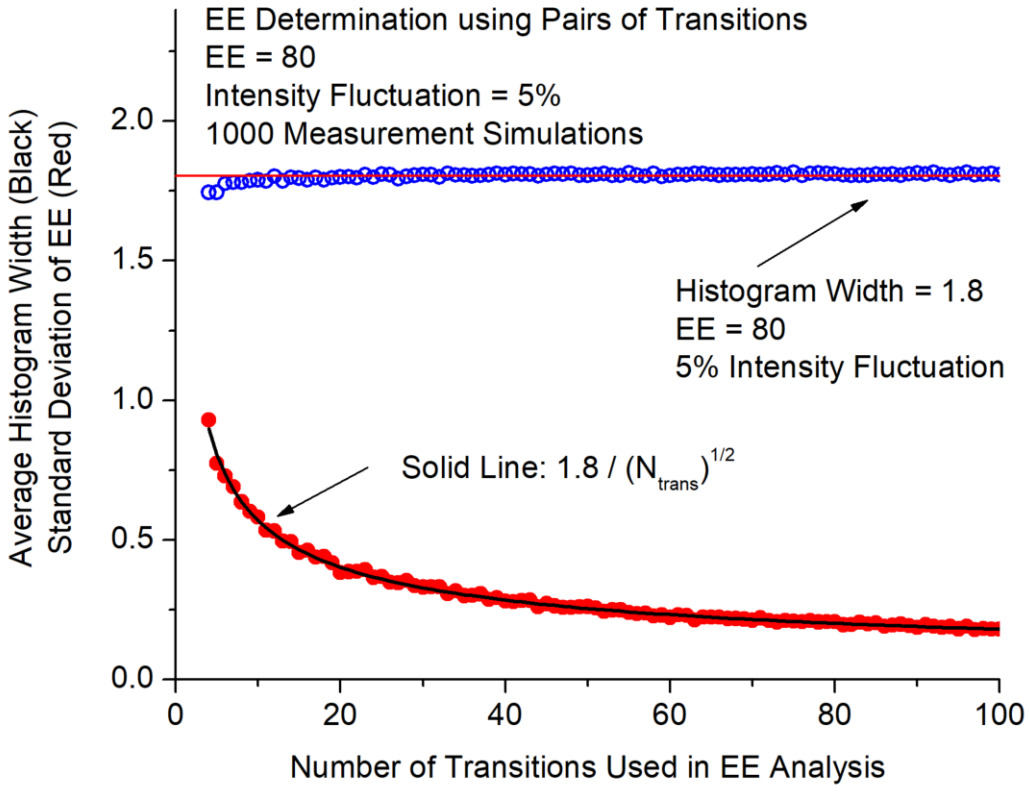

Figure 2.5: 1000 simulated chiral tag measurement results using different number of transitions from N=1-100. The Blue data is the average of the histogram width, for all 1000 simulations. The red data is the standard deviation of the calculated ee for 100 measurements. The solid black line is 1.8 over $\sqrt{N}$.

2) Experimental Chiral Tag Enantiomeric Excess Determinations

The first step in a chiral tag rotational spectroscopy measurement is to identify and fit the spectra belonging to the two diastereomer complexes. Table 2.1 and 2.2 below give the comparison of the lowest energy isomers for verbenone and 3-MCH, respectively. The theoretical and experimental rotational constants for isopulegol chiral tagged with propylene oxide are shown in the appendix (Table A7). Furthermore, to increase confidence in the identification of the complexes, carbon substitution structures were performed using Kraitchman's analysis shown in Figure A3, A4, A5 and A6. In the process of forming the non-covalent bond between the tag and the analyte, the tag may find many low energy conformations around the analyte leading to multiple homo- and heterochiral complexes. This can have the adverse effect of lowering the signal levels of the complexes and decreasing the sensitivity. In the case of 3-MCH, four different isomers of the diastereomer tags were observed and for verbenone four heterochiral and homochiral complexes were fit. Theoretical and experimental fit rotational parameters are given in the appendix for the higher energy isomers.

The effect of different sampling techniques was performed on a sample of (1*S*)-(-)-verbenone tagged with butynol. In the resulting spectra, four heterochiral complexes and four heterochiral complexes were observed. Table A10, gives the theoretical and experimental rotational parameter for each complex and Table A11 provides the observed rotational parameters. Once the spectra were obtained, the 49 strongest transitions of the homochiral and the heterochiral complexes were used to calculate the ee in two of the methods. The 25 strongest transitions were used in the lower sensitivity measurement. First a full instrument cleaning was performed which requires the breakdown of the instrument and replacing the sample. 2 million FIDs were collected,

and as shown in the left histogram of Fig. 2.6, the mean calculated ratio was 0.544 ± 0.0744 with a large histogram width. The uncertainty are 1 sigma errors represented by the standard error of the measurement. Next, only one nozzle was used to collect data, and only 200,000 FIDs were collected. The corresponding histogram was constructed using 25 transitions. This histogram is shown in the middle in Fig. 2.6. The mean calculated ratio was lower at 0.532 ± 0.0154 and the standard deviation was large at 0.077. The right histogram in Figure 2.6 is the histogram constructed from the verbenone-butynol spectra when the sample was heated with a neon purge between the two butynol samples and a deeper average of 1.5M FIDs was collected. A mean EE of 0.529 ± 0.00279 % was calculated using this chiral tag approach, which is in good agreement (after correcting for the ee of the tag, 0.983) with the 53.6% enantiomeric excess given by the certificate of analysis. The various sampling handlings had minimal effect on the mean EE calculated, yet the uncertainty greatly increased. In the purging method the instrument response function is not changed when switching between the different tags, but takes longer and consumes materials, both the sample and Ne. The method allowed for less uncertainty in the measurement because the intensity fluctuations were minimized between racemic and enantiopure tag measurements. This method does have drawbacks due to increased time from purging and sample is wasted in the process. The full cleaning method was lengthy as time was needed; to vent the chamber, clean, and reestablish a vacuum, while also needing more sample to refill the nozzles. When taking the instrument apart, the electric field structure in the chamber may differ between tag measurements effecting the instrument response function and causing higher percent intensity fluctuations. This is seen by the much larger width of the histogram compared to the purge. Finally, when using a single nozzle for each tag measurement, the time between the two measurements

was minimized. However, the electric field structure in the vacuum chamber around each nozzle may have differed due to the nozzles being at different physical positions in the chamber, causing a different instrument response function from nozzle to nozzle and potentially increasing the uncertainty in the measurement. Moreover, the lower number of FID averages shows that the longer measurements allow for the intensity fluctuations from the variation from the nozzle performance to average down and become less varied, decreasing the uncertainty as well as pulse-to-pulse power variations from the traveling wave tube microwave amplifier.

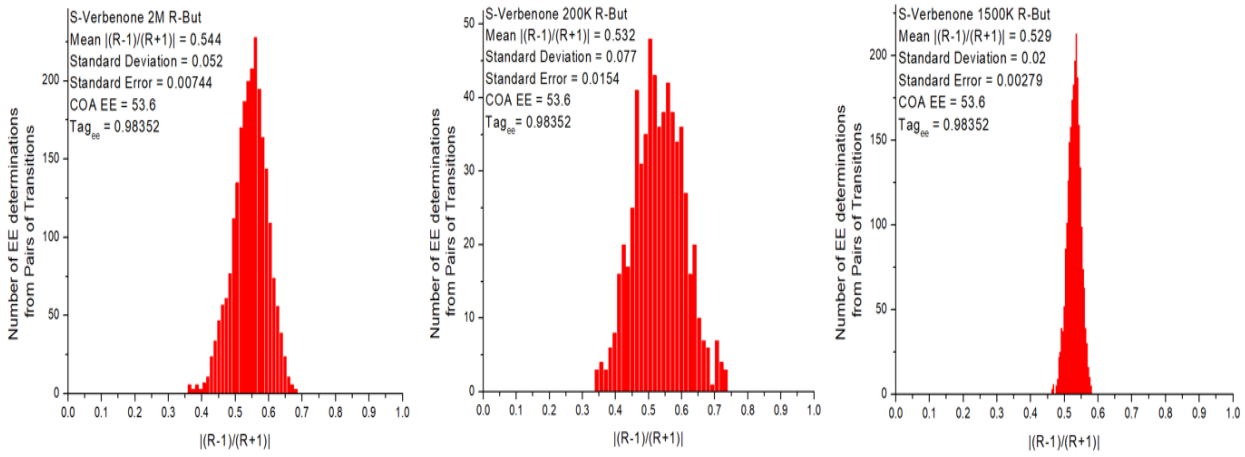

Figure 2.6: Histograms produced from various methodologies of sampling (S)-verbenone using the 25 strongest transitions. The left uses only one nozzle for each of the tags. The middle uses a method of taking apart and cleaning the instrument, and the right uses a method purging out excess tag between racemic and enantiopure tag measurements.

Table 2.1: Fit experimental rotational constants for the non-covalent complexes of verbenone and butynol and the corresponding theoretical constants.

Parameter	Verbenone Homochiral	Theoretical Verbenone Homochiral	Verbenone Heterochiral	Theoretical Verbenone Heterochiral
A/MHz	836.9427(16)	835	905.85816(81)	912.1
B/MHz	314.41418(43)	324	286.90405(35)	292.3
C/MHz	299.49708(44)	307.7	278.45467(34)	283.8
$\lvert\mu_{a,b,c}\rvert$/D	-	4.7/1.4/1.9	-	4.5/2.4/0.9
Δ_J/kHz	0.0622(14)		0.0329(11)	
Δ_{JK}/kHz	-0.1389(63)		0.0317(60)	
Δ_K/kHz	0.228(87)		-	
δ_J/kHz	0.0080(12)		0.00361(59)	
δ_K/kHz	-		-	
N	162		170	
RMS/kHz	4.88		6.07	

Table 2.2: Fit experimental rotational constants for the non-covalent complexes of 3-MCH and butynol and the corresponding theoretical constants.

Parameter	3-MCH Homochiral	Theoretical 3-MCH Homochiral	3-MCH Heterochiral	Theoretical 3-MCH Heterochiral
A/MHz	1185.8502(16)	1186.8	1094.3495(23)	1096.1
B/MHz	420.12945(87)	430.1	460.8011(11)	470.4
C/MHz	350.17283(86)	357.7	380.1642(11)	386.3
$\lvert\mu_{a,b,c}\rvert$/D		3.1/1.9/0.1		3.3/1.6/0.9
Δ_J/kHz	-0.06893(44)		-0.1144(73)	
Δ_{JK}/kHz	-0.127(15)		0.071(37)	
Δ_K/kHz	-0.114(69)		-0.47(12)	
δ_J/kHz	-0.0067(23)		-0.0239(42)	
δ_K/kHz	-0.366(80)		-0.34(12)	
N	196		134	
RMS/kHz	1.9		2.1	

Experimental results for the calibration curves using 3-MCH/butynol and isopulegol /propylene oxide are presented. In the next sections, derivations for determining EE and uncertainty are provided, as well as descriptions for statistical modeling used for the chiral tag measurement. Assumptions of the linear relationship for the number density of complexes produced in the pulse jet for both tag and analyte to derive the basic ee determination formula are supported by the experimental data. Samples of known EE of (*R*)-(+)-3-MCH were prepared, and an EE determination was made by chiral tag methodology using 25 transition pairs (*N*=25). The histograms for the 3-MCH tagged with butynol are shown in Fig. 2.7. These experimental results mirror the modeling presented in Figure 2.3. Larger enantiomeric excess samples contained smaller histogram widths and less uncertainty in the measurement. The value of (R-1)/(R+1) for each measurement is presented in Table 2.3 along with standard errors. The table also gives the EE calculated by gravimetric analysis with the respective masses reported in the appendix. As noted in Eq. 2.21, the values have not been correct by the tag ee, and the σ are the errors reported in Eq. 2.30. The data from the ee determinations was plotted with the 3σ error bars and fit in Fig. 2.8, weighted using the errors. The data is not corrected by the ee_{tag}, indicating the slope of the line fit through the data is equal to the ee_{tag} by Eq. 2.21 and should be linear with respect to ee. The calibrated tag ee (ee_{tag} = 0.983) and the slope are in good agreement.

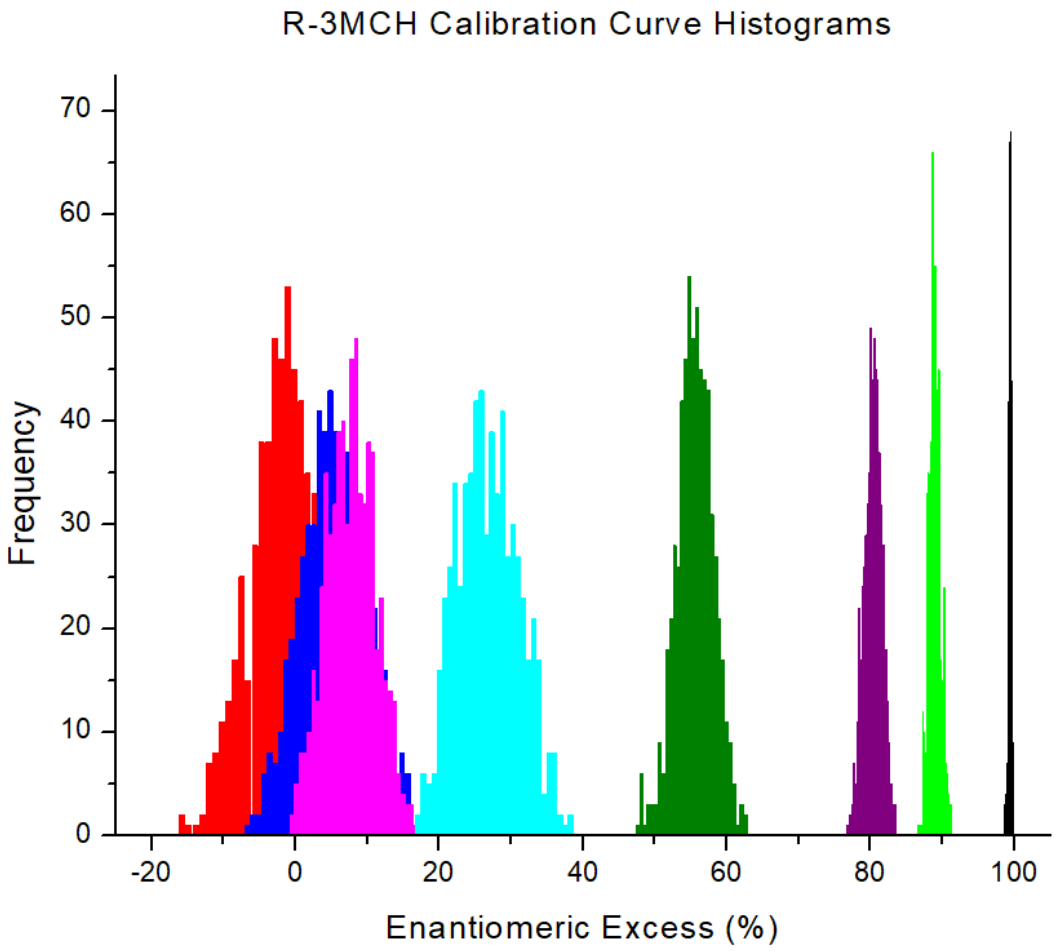

Figure 2.7: Experimental results of the 3-MCH calibration curve data. The Measured EE were EE = 0, 5, 10, 30, 55, 80, 90%, and enantiopure.

Table 2.3: Chiral tag analysis of prepared (R)-3-methylcyclohexanone samples. Enantiomeric excess values of the prepared samples and the absolute value of the ratios calculated by chiral tag with standard errors, used to create the calibration curve.

Enantiomeric Excess by Gravimetric analysis[1]	**|(R-1) / (R+1)|**	**Standard Error**
0	0.0089	0.00906
0.05242	0.059	0.00839
0.09811	0.101	0.00497
0.29175	0.292	0.00479
0.53851	0.534	0.00425
0.79377	0.783	0.00206
0.89188	0.878	0.00171
0.996	0.978	0.000408

1. Enantiomeric excess calculated by correcting for the enantiomeric excess provided in the certificate of analysis. (R)-3-methylcyclohexanone's enantiomeric excess was provided as 99.6%.

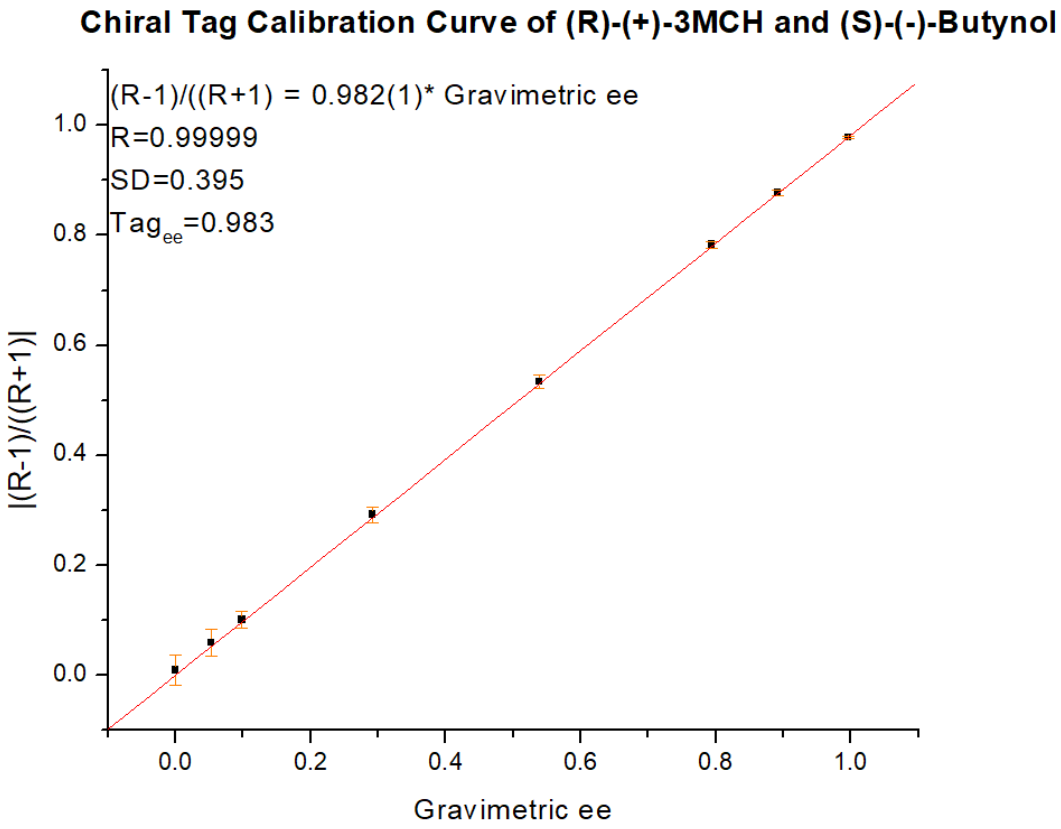

Figure 2.8: Calibration Curves of 3-methylcyclohexanone A) showing the calculated ee of the analyte by gravimetric analysis plotted against the absolute value of the mean calculated ratio. Here the slope of the calibration curve is expected to be the ee of the tag. Fits were fit through the origin and the error bars shown are 3σ.

The next measurement performed was to test the reproducibility of the chiral tag results. The same sample of EE = 80% was measured four times. Fig. A1 shows the results of the replicate measurements with 3σ error bars. The different ee determinations were made on consecutive days with a complete instrument cleaning and sample replacement. Over the four replicates, the average ratio was 0.779 with the tag corrected EE of 79.2% compared to the gravimetric value of 79.62%. The standard deviation of the four replicates was 0.00294 and the mean standard error for the four measurements was 0.00416. This result shows that the EE uncertainty estimated from the histogram analysis in a single measurement was a good characterization of the measurement reproducibility.

A calibration curve using isopulegol and propylene oxide was also constructed. Table 2.4 shows the results following the same format as Table 2.3. The spectroscopic analysis for these complexes has been described in the appendix in Table A7. The calibration curve is shown in Figure 2.9 and the plots of the data constructed similarly to Fig. 2.8. The data was in good agreement with the propylene oxide ee ($ee_{tag} = 0.996$). Six replicate measurements were performed on the EE = 80% sample, Fig. A2. The mean ratio of the replicates was 0.805 (tag corrected ee of 80.6%) and the EE by volumetric analysis was 80.1%. The standard deviation was 0.00673 and the mean standard error for the measurements was 0.00370. Again, these measurements support the results from the statistical modeling.

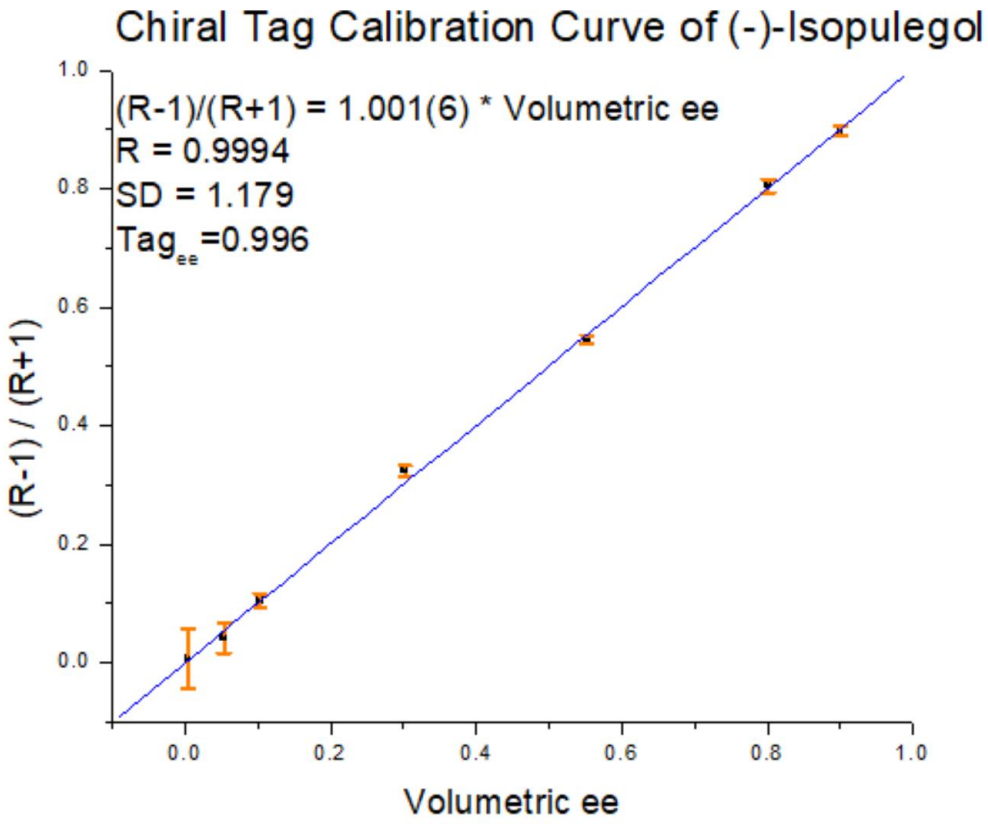

Figure 2.9: Calibration Curves of Isopulegol showing the calculated ee of the analyte by volumetric analysis plotted against the absolute value if the mean calculated ratio. Here the slope of the calibration curve is expected to be the ee of the tag. The fit was fit through the origin and the error bars shown are 3σ.

Table 2.4: Chiral tag analysis of prepared (-)-isopulegol samples. Enantiomeric excess values of the prepared samples and the ratios calculated by chiral tag with standard errors, used to create the calibration curve.

Enantiomeric Excess by Volume [1]	(R-1) / (R+1)	Standard Error
0.0035	0.00703	0.0171
0.0532	0.042	0.00853
0.103	0.105	0.00372
0.302	0.324	0.00273
0.552	0.546	0.00234
0.801	0.805	0.00384
0.900	0.898	0.00257

1. Enantiomeric excess calculated using the enantiomeric excess provided in the certificate of analysis and the volume used to create the samples. (-)-Isopulegol enantiomeric ratio was 100% by GC, and (+)-isopulegol was 99.3% by GC.

IV. Conclusion

The above work has demonstrated the ability of the chiral tag methodology to provide quantitative chiral analysis of a sample. The experimental results and their theoretical justifications were reported to support the method's ability to yield accurate results, and statistically meaningful uncertainties. Rotational spectroscopy coupled with chiral tagging allows for an easy method of adding an internal reference stereocenter to an analyte, which alters the mass distribution of the enantiomers allowing them to be completely spectroscopically resolved. This allows for a small number of tags to have broad applicability, such as a hydrogen bond donor and accepter as

demonstrated in this work. In contrast with chiral resolving agents used in NMR, many different resolving agents are required based on the structure and functional groups of the analyte. If the rotational parameters have already been fit and identified, the process of fitting and running quantum chemical calculations can be skipped. Once the spectroscopy is known, the results can be applied for any future measurement of the same tag and analyte. Furthermore, the spectral resolution rotational spectroscopy brings can allow for simultaneous analysis of many impurities or diastereomers with molecules that contain multiple stereocenters. Consequently, the greater the sample complexity the smaller the signals of the chiral tag complexes. The complexity of a measurement is also increased if the analyte forms many isomers of the chiral tag complexes. This can create greater uncertainty in the EE determination as shown in this work. This effect can be offset based on the vapor pressure of the constituent molecules in the mixture, allowing for different parts of the sample to be measured separately. Moreover, signal can be acquired more quickly and with greater sensitivity with the use of cavity-enhanced spectrometers. Finally, one major limitation of rotational spectroscopy is the range of molecules that can be measured due to the molecular size of the analyte. Proteins and other large biologically relevant molecules cannot be volatized without thermal decomposition for a chiral tag measurement.

V. References

1. 1. Federsei, H.-J., *The impact of chirality on drug manufacturing on the industrial scale.* Endeavour, 1994. **18**(4): p. 163-172.

2. Jeschke, P., *Current status of chirality in agrochemicals.* Pest Management Science, 2018. **74**(11): p. 2389-2404.
3. Wang, Z., et al., *Origami-Based Reconfigurable Metamaterials for Tunable Chirality.* Advanced Materials, 2017. **29**(27): p. 1700412.
4. Brooks, W.H., W.C. Guida, and K.G. Daniel, *The significance of chirality in drug design and development.* Current topics in medicinal chemistry, 2011. **11**(7): p. 760-770.
5. Nguyen, L.A., H. He, and C. Pham-Huy, *Chiral drugs: an overview.* International journal of biomedical science : IJBS, 2006. **2**(2): p. 85-100.
6. Zhou, Y., et al., *Chiral pharmaceuticals: Environment sources, potential human health impacts, remediation technologies and future perspective*. Environment International, 2018. 121: p. 523-537.
7. De Camp, W.H., *Chiral drugs: The FDA perspective on manufacturing and control.* Journal of Pharmaceutical and Biomedical Analysis, 1993. **11**(11): p. 1167-1172.
8. Gross, M., *Chapter 34. Significance of Drug Stereochemistry in Modern Pharmaceutical Research and Development*, in *Annual Reports in Medicinal Chemistry*, J.A. Bristol, Editor. 1990, Academic Press. p. 323-331.*FDA'S policy statement for the development of new stereoisomeric drugs.* Chirality, 1992. **4**(5): p. 338-340.
9. Agranat, I.; Caner, H.; Caldwell, J., Putting chirality to work: the strategy of chiral switches. *Nature Reviews Drug Discovery* **2002,** *1* (10), 753-768.
10. Asghar, W.; Pittman, E.; Jamali, F., Comparative efficacy of esomeprazole and omeprazole: Racemate to single enantiomer switch. *DARU Journal of Pharmaceutical Sciences* **2015,** *23* (1), 50.

11. Blaser, H.-U., Chirality and its implications for the pharmaceutical industry. *Rendiconti Lincei* **2013,** *24* (3), 213-216.
12. McConathy, J.; Owens, M. J., Stereochemistry in drug action. *Primary care companion to the Journal of clinical psychiatry* **2003,** *5* (2), 70.
13. Tucker, G. T., Chiral switches. *The Lancet* **2000,** *355* (9209), 1085-1087.
14. Townes, C. H.; Schawlow, A. L., *Microwave Spectroscopy*. Dover Publications: 2013.
15. Pérez, C., et al., *Broadband Fourier transform rotational spectroscopy for structure determination: The water heptamer.* Chemical Physics Letters, 2013. **571**: p. 1-15.
16. Pérez-Trujillo, M.; Monteagudo, E.; Parella, T., 13C NMR Spectroscopy for the Differentiation of Enantiomers Using Chiral Solvating Agents. *Analytical Chemistry* **2013,** *85* (22), 10887-10894.
17. Wenzel, T. J.; Morin, C. A.; Brechting, A. A., Lanthanide-chiral resolving agent mixtures as chiral NMR shift reagents. *The Journal of Organic Chemistry* **1992,** *57* (13), 3594-3599.
18. Smalley, R. E.; Wharton, L.; Levy, D. H., The fluorescence excitation spectrum of rotationally cooled NO2. *The Journal of Chemical Physics* **1975,** *63* (11), 4977-4989.
19. Smalley, R.-E.; Levy, D.-H.; Wharton, L., The fluorescence excitation spectrum of the HeI2 van der Waals complex. *The Journal of Chemical Physics* **1976,** *64* (8), 3266-3276.
20. Grimme, S., S. Ehrlich, and L. Goerigk, *Effect of the damping function in dispersion corrected density functional theory.* Journal of Computational Chemistry, 2011. **32**(7): p. 1456-1465.

21. Moellmann, J.; Grimme, S., DFT-D3 study of some molecular crystals. *The Journal of Physical Chemistry C* **2014,** *118* (14), 7615-7621.

22. Gaussian 09, Revision A.02, M. J. Frisch, G. W. Trucks, H. B. Schlegel, G. E. Scuseria, M. A. Robb, J. R. Cheeseman, G. Scalmani, V. Barone, G. A. Petersson, H. Nakatsuji, X. Li, M. Caricato, A. Marenich, J. Bloino, B. G. Janesko, R. Gomperts, B. Mennucci, H. P. Hratchian, J. V. Ortiz, A. F. Izmaylov, J. L. Sonnenberg, D. Williams-Young, F. Ding, F. Lipparini, F. Egidi, J. Goings, B. Peng, A. Petrone, T. Henderson, D. Ranasinghe, V. G. Zakrzewski, J. Gao, N. Rega, G. Zheng, W. Liang, M. Hada, M. Ehara, K. Toyota, R. Fukuda, J. Hasegawa, M. Ishida, T. Nakajima, Y. Honda, O. Kitao, H. Nakai, T. Vreven, K. Throssell, J. A. Montgomery, Jr., J. E. Peralta, F. Ogliaro, M. Bearpark, J. J. Heyd, E. Brothers, K. N. Kudin, V. N. Staroverov, T. Keith, R. Kobayashi, J. Normand, K. Raghavachari, A. Rendell, J. C. Burant, S. S. Iyengar, J. Tomasi, M. Cossi, J. M. Millam, M. Klene, C. Adamo, R. Cammi, J. W. Ochterski, R. L. Martin, K. Morokuma, O. Farkas, J. B. Foresman, and D. J. Fox, Gaussian, Inc., Wallingford CT, 2016.

23. Z. Kisiel, PROSPE, programs for rotational spectroscopy, http://info.ifpan.edu.pl/~kisiel/prospe.htm

24. Pickett, H. M., The fitting and prediction of vibration-rotation spectra with spin interactions. *Journal of Molecular Spectroscopy* **1991,** *148* (2), 371-377.

VI. Appendix A

Table A1: Calculated ratios from chiral tagging of the prepared 80% (-)-isopulegol EE sample. Replica 1-6 with corresponding ratios and the calculated enantiomeric excess, accounting for the enantiomeric fraction of the tag.

Replica	(R-1) / (R+1)	Enantiomeric Excess (%)
Run 1	0.809(3)	81.3(3)
Run 2	0.789(4)	80.2(4)
Run 3	0.808(2)	81.1(2)
Run 4	0.801(5)	80.5(5)
Run 5	0.817(4)	81.1(6)
Run 6	0.804(2)	81.1(5)

Table A2: Calculated ratios from chiral tagging of the prepared 80% EE (R)-3-methylcyclohexanone sample. Replica 1-4 with corresponding ratios and the calculated enantiomeric excess, accounting for the enantiomeric fraction of the tag.

Replica	(R-1) / (R+1)	Enantiomeric Excess (%)
Run 1	0.779(3)	79.2(3)
Run 2	0.782(4)	79.5(4)
Run 3	0.780(6)	79.3(6)
Run 4	0.775(3)	78.8(3)

Table A3: Heterochiral 3-mehtylcyclohexanone complexes theoretical rotational parameters and relative energies. All energies are relative to the lowest energy complex. All calculations were done with B3LYP def2tzvp with D3BJ dispersion correction level of theory.

Parameter	Complex 1	Complex 2	Complex 3	Complex 4
ΔEnergy /cm^{-1}	0.0	70.5	200.2	221.5
A /MHz	1091.1	1351.0	1263.4	1394.1
B/ MHz	470.4	395.6	375.0	380.0
C /MHz	386.3	373.8	344.9	365.7
$\lvert\mu_{A,B,C}\rvert$ /D	3.7/0.8/1.4	3.3/1.4/0.7	3.4/	3.5/1.2/1.32

Table A4: Homochiral 3-mehtylcyclohexanone complexes theoretical rotational parameters and relative energies. All energies are relative to the lowest energy complex. All calculations were done with B3LYP def2tzvp with D3BJ dispersion correction level of theory.

Parameter	Complex 1	Complex 2	Complex 3	Complex 4
ΔEnergy /cm^{-1}	0.0	91.4	200.0	260.0
A /MHz	1186.8	1238.2	1239.7	1559.9
B/ MHz	430.1	425.0	396.5	345.5
C /MHz	357.7	412.0	360.2	333.5
$\|\mu_{A,B,C}\|$ /D	3.6/1.4/0.8	3.6/1.1/0.07	3.4/0.2/2.1	3.5/1.3/1.4

Table A5: 3-methylcyclohexanone-butynol heterochiral final fits with rms errors.

Parameter	Complex 1	Complex 2	Complex 3	Complex 4
A/MHz	1094.3495(23)	1363.794(14)	1279.721(50)	1401.910(78)
B/MHz	460.8011(11)	381.8716(16)	375.46708(13)	372.7369(39)
C//MHz	380.1642(11)	362.1588(17)	350.48083(14)	359.0900(38)
ΔJ/KHz	-0.1144(73)	-0.3718(68)	-0.1416(62)	-0.173(78)
ΔJK/KHz	0.071(37)	3.147(55)	-1.717(65)	0.88(12)
ΔK/KHz	-0.47(12)	-9.1(28)		
δJ/KHz	-0.0239(42)	-0.0390(50)		-0.026(12)
δK/KHz	-0.34(12)	1.44(51)		
N	134	89	54	55
RMS/KHz	2.1	1.6	4.8	4.3

Table A6: 3-methylcyclohexanone-butynol homochiral final fits with rms errors.

Parameter	Complex 1	Complex 2	Complex 3	Complex 4
A/MHz	1185.8502(16)	1243.220(82)	1251.387(25)	1575.860(87)
B/MHz	420.12945(87)	410.9921(48)	402.1737(15)	339.6845(32)
C//MHz	350.17283(86)	399.3022(49)	374.6038(15)	328.2445(30)
ΔJ/KHz	-0.06893(44)	-0.278(11)	-0.1136(68)	-0.2046(55)
ΔJK/KHz	-0.127(15)	1.551(46)	-0.456(42)	1.527(91)
ΔK/KHz	-0.114(69)			
δJ/KHz	-0.0067(23)	-0.043(19)		-0.0427(79)
δK/KHz	-0.366(80)			
N	196	41	59	49
RMS/KHz	1.9	2.4	3.4	4.1

Table A7: Fit rotational constants for the non-covalent complex of isopulegol and propylene oxide.

PARAMETER	ISOPULEGOL RPO	ISOPULEGOL SPO
A/MHz	951.012(56)	1070.902(70)
B/MHz	305.52580(95)	290.54445(87)
C//MHz	263.49015(99)	249.62683(20)
ΔJ/KHz	0.0151(24)	0.0149(20)
ΔJK/KHz		
ΔK/KHz		
δJ/KHz		
δK/KHz		
N	78	86
RMS/KHz	5.3	6.1

Table A8: Gravimetric masses with calculated percent enantiomeric excess (EE). The EE was then corrected based off the R-3-methylcyclohexanone certificate of analysis.

Sample	Mass of empty cap and vial (g)	Mass of R-3MCH, cap, and vial (g)	Total mass (g)	Gravimetric EE (%)	Corrected Gravimetric EE(%)
90% EE	11.20198	12.03165	12.12199	90.18054	89.18856
80% EE	11.3089	12.0438	12.2245	80.26431	79.3814
55% EE	11.1389	11.64322	12.065	54.45632	53.8573
30% EE	11.1265	11.3982	12.0479	29.48774	29.16337
10% EE	11.17	11.2607	12.0843	9.920157	9.811036
5% EE	11.25547	11.3044	12.1764	5.313107	5.254663

Table A9: Sample preparation for the known enantiomeric excess samples for the (-)-isopulegol calibration curve. The Enantiomeric excess is corrected using the data from the certificate of analysis.

Sample	(-)-Isopulegol (μL)	(+)-Isopulegol (μL)	Corrected EE (%)
0% EE	500	500	0.35
5% EE	525	475	5.3325
10% EE	550	450	10.315
30% EE	650	350	30.245
55% EE	775	225	55.1575
80% EE	4500	500	400.35
90% EE	950	50	90.035

Table A10: Verbenone-butynol heterochiral final fits with rms errors.

Parameter	Complex 1	Complex 2	Complex 3	Complex 4
A/MHz	905.85816(81)	879.94543(84)	905.3498(12)	913.47679(27)
B/MHz	286.90405(35)	320.34351(36)	286.52859(41)	300.39373(78)
C//MHz	278.45467(34)	279.56130(38)	276.45786(43)	278.01924(75)
ΔJ/KHz	0.0329(11)	0.0277(11)	0.0237 (65)	0.0439(25)
ΔJK/KHz	0.0317(60)	0.0535(58)	0.1258(42)	-0.026(29)
ΔK/KHz	-	-	-	-
δJ/KHz	0.00361(59)	0.00425(63)	0.00178(94)	0.0014(16)
δK/KHz	-	-		-
N	170	183	137	121
RMS/KHz	6.07	5.79	4.92	3.56

Table A11: Verbenone-butynol homochiral final fits with rms errors.

Parameter	Complex 1	Complex 2	Complex 3	Complex 4
A/MHz	836.9427(16)	859.1653(14)	948.88846(67)	986.1931(10)
B/MHz	314.41418(43)	306.20216(43)	295.40012(29)	276.80869(37)
C//MHz	299.49708(44)	291.24858(49)	260.85724(28)	261.96346(37)
ΔJ/KHz	0.0622(14)	0.0262(17)	0.01751(84)	0.0347(10)
ΔJK/KHz	-0.1389(63)	0.0618(69)	0.1079(38)	0.0631(71)
ΔK/KHz	0.228(87)	-	-	-
δJ/KHz	0.0080(12)	-	0.00164(47)	-0.00122(63)
δK/KHz	-	-0.00086(37)	0.00035(23)	-
N	162	106	254	151
RMS/KHz	4.88	4.99	6.00	5.29

Table A12: Heterochiral verbenone-butynol complexes theoretical rotational parameters and relative energies. All energies are relative to the lowest energy complex. All calculations were done with B3LYP def2tzvp with D3BJ dispersion correction level of theory.

Parameter	Complex 1	Complex 2	Complex 3	Complex 4
ΔEnergy /cm^{-1}	0.0	22.8	24.4	130
A /MHz	912.1	876.6	905.5	918.1
B/ MHz	292.3	328.8	291.8	305.5
C /MHz	283.8	286.2	281.3	282.6
$\|\mu_{A,B,C}\|$ /D	4.5/2.4/0.9	4.8/1.8/1.3	4.6/0.1/2.5	4.6/1.8/1.8

Table A13: Homochiral verbenone-butynol complexes theoretical rotational parameters and relative energies. All energies are relative to the lowest energy complex. All calculations were done with B3LYP def2tzvp with D3BJ dispersion correction level of theory.

Parameter	Complex 1	Complex 2	Complex 3	Complex 4
ΔEnergy /cm^{-1}	0.0	43.1	53	171.5
A /MHz	835	861.4	951.4	994.4
B/ MHz	324	309.8	301.2	334.1
C /MHz	307.7	294.9	265.9	300.7
$\|\mu_{A,B,C}\|$ /D	4.7/1.4/1.9	4.7/0.2/2.3	4.7/2.2/0.5	4.4/2.6/1,0

Table A14: Table of C13 fits for complex 1 of the heterochiral verbenone-butynol complexes.

Parameter	C1	C2	C3	C4	C5
A /MHz	904.80(30)	905.06(29)	903.18(28)	902.67(33)	902.18(31)
B /MHz	285.86382(60)	285.76098(60)	286.35415(67)	285.41496(63)	286.49413(63)
C /MHz	277.57777(62)	277.35289(62)	277.66473(70)	277.18344(63)	277.96902(68)
N	41	43	42	39	35
RMS /KHz	6.6	6.6	7.2	8.5	5.3
Parameter	C6	C7	C8	C9	C10
A /MHz	899.70(37)	901.64(37)	904.01(30)	904.07(34)	892.13(31)
B /MHz	285.96118(61)	284.32898(72)	286.83839(62)	286.75206(66)	286.41495(73)
C /MHz	278.12010(62)	276.29695(67)	278.28170(63)	278.43074(66)	277.09667(76)
N	42	38	40	39	32
RMS /KHz	7.5	6.8	7.9	8	7.1
Parameter	C11	C12	C13	C14	
A /MHz	905.45(35)	906.05(30)	903.89(29)	898.57(30)	
B /MHz	284.76732(76)	282.78158(61)	285.42142(64)	285.72250(61)	
C /MHz	276.42654(72)	274.57184(61)	277.12648(68)	277.30180(62)	
N	34	47	40	41	
RMS /KHz	6.1	6.4	8.4	8.2	

Table A15: Table of C13 fits for complex 1 of the homochiral verbenone-butynol complexes.

Parameter	C1	C2	C3	C4	C5
A /MHz	835.71(17)	836.43(15)	834.47(15)	834.16(16)	833.77(15)
B /MHz	313.32932(88)	313.07475(78)	313.84953(78)	312.66160(76)	313.97707(81)
C /MHz	298.56399(86)	298.23729(76)	298.71996(73)	298.15727(70)	298.80681(82)
N	25	31	28	29	32
RMS /KHz	6.7	6.7	7.7	9.2	7.9
Parameter	C6	C7	C8	C9	C10
A /MHz	831.72(19)	832.29(14)	835.28(16)	835.14(16)	825.24(13)
B /MHz	313.36871(95)	311.75342(71)	314.28091(82)	314.27050(83)	313.92729(73)
C /MHz	299.20037(85)	297.09632(71)	299.40047(78)	299.39782(76)	297.61543(72)
N	27	31	26	28	32
RMS /KHz	5.1	5.8	8.9	6.4	7.9
Parameter	C11	C12	C13	C14	C5
A /MHz	837.05(14)	834.10(16)	834.85(14)	829.93(17)	
B /MHz	311.69732(68)	311.26522(81)	312.56659(73)	312.82969(88)	
C /MHz	297.03286(71)	296.34664(79)	297.86139(76)	298.22675(96)	
N	35	30	27	27	
RMS /KHz	6.9	9.4	7.7	8.6	

Table A16: Table of C13 fits for complex 1 of the homochiral 3-MCH-butynol complexes.

Parameter	C1	C2	C3	C4	C5	C6
A /MHz	1182.167(75)	1184.356(77)	1183.35(86)	1182.076(85)	1177.573(75)	1181.203(72)
B /MHz	419.1132(12)	416.7314(13)	419.4705(14)	416.4119(14)	418.0879(15)	419.7402(12)
C /MHz	349.1622(11)	347.7058(12)	349.9284(12)	347.7475(14)	348.0541(11)	349.5147(11)
N	35	42	43	39	39	43
RMS /KHz	4.4	5.2	3.1	3.6	2.5	2.5
Parameter	C7	C8	C9	C10	C11	
A /MHz	1166.986(71)	1185.376(75)	1185.817(74)	1182.294(75)	1173.152(70)	
B /MHz	418.8323(12)	416.8914(12)	413.26329(65)	418.1368(12)	418.7726(7726)	
C /MHz	347.9988(11)	347.922(11)	345.39043(74)	348.7226(11)	348.6499(11)	
N	47	47	45	45	46	
RMS /KHz	3.4	2.9	4.1	3.6	4.6	

Table A17: Table of C13 fits for complex 1 of the heterochiral 3-MCH-butynol complexes.

Parameter	C1	C2	C3	C4	C5	C6
A /MHz	1091.665(71)	1093.530(67)	1092.041(63)	1089.71(10)	1086.024(61)	1090.310(17)
B /MHz	459.5089(15)	456.7877(14)	459.9825(15)	456.9102(19)	458.9477(14)	460.4722(21)
C /MHz	378.9671(13)	377.4231(13)	379.8686(15)	377.6218(17)	377.9126(13)	379.52968(81)
N	24	25	23	18	24	20
RMS /KHz	4.6	5.2	4.4	4.1	7.4	9.1

Parameter	C7	C8	C9	C10	C11
A /MHz	1079.441(61)	1094.290(74)	1090.654(70)	1090.338(78)	1081.960(68)
B /MHz	458.9773(15)	456.6382(17)	455.2136(15)	458.4723(18)	459.3198(17)
C /MHz	377.3836(13)	377.3214(14)	376.3683(13)	378.2216(16)	378.2090(16)
N	24	20	27	22	19
RMS /KHz	5.2	6.4	5.7	5.4	5.9

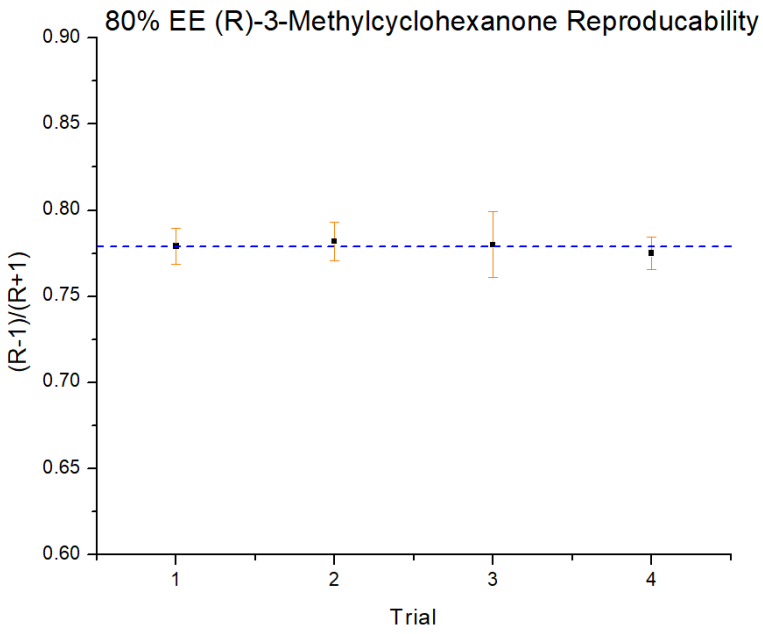

Figure A1: A plot showing the mean enantiomeric excess calculated using the chiral tagging method of a sample of 80% (R)-3-methylcyclohexanone was run four separate times. This plot shows the reproducibility of the chiral tagging method and the error bars shown are 3σ.

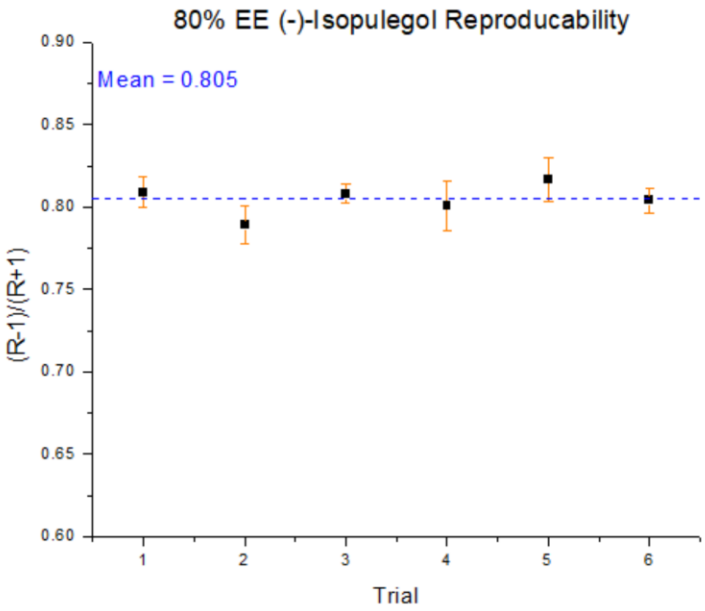

Figure A2: A graph showing the mean calculated enantiomeric excess of a sample of 80% EE (-)-isopulegol that was divided and run 6 separate times. The mean of the six measurements is shown with the dashed blue line, and the error bars shown are 3σ. This graph shows the reproducibility of the chiral tagging method.

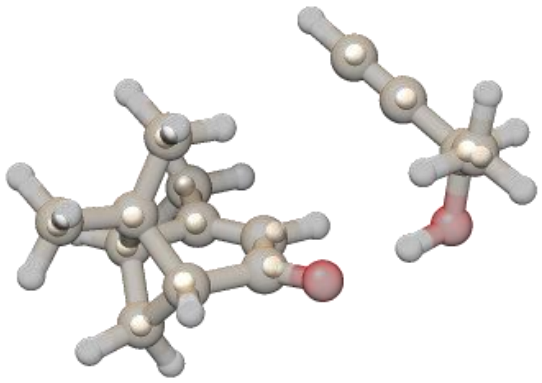

Figure A3: Substitution structure for complex 1 of the homochiral verbenone-butynol complexes using Kraitchman's equations.

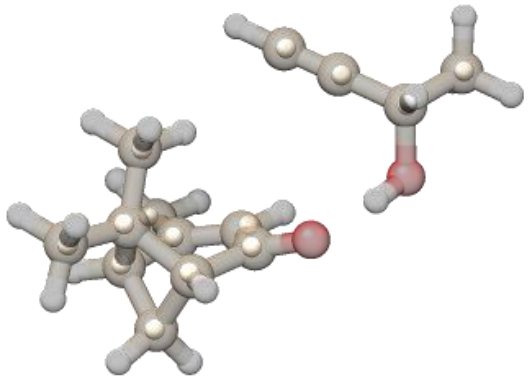

Figure A4: Substitution structure for complex 1 of the heterochiral verbenone-butynol complexes using Kraitchman's equations.

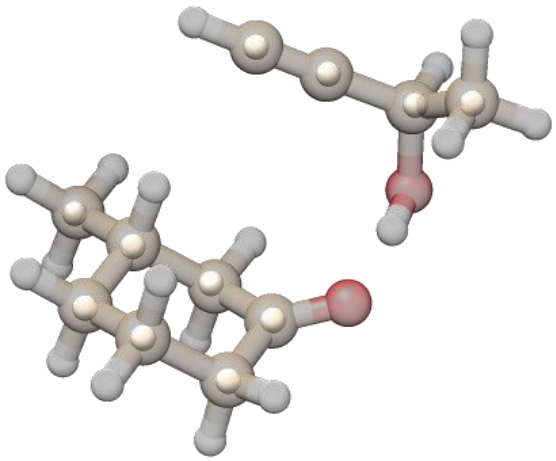

Figure A5: Substitution structure for complex 1 of the heterochiral 3-Methylcyclohexanone-butynol complexes using Kraitchman's equations. The transparent structure is the theoretical gaussian output.

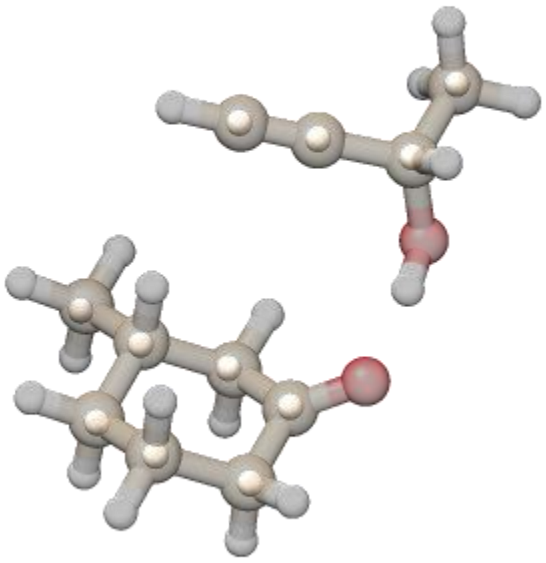

Figure A6: Substitution structure for complex 1 of the homochiral 3-Methylcyclohexanone-butynol complexes using Kraitchman's equations.

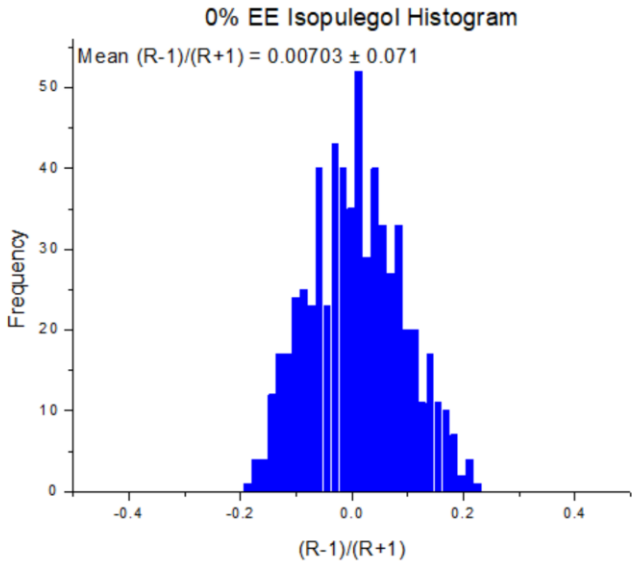

Figure A7: A histogram showing the distribution of enantiomeric excess calculated using the 25 strongest transitions of both the hetero- and homochiral complexes from the racemic isopulegol measurement. The mean and uncertainty are also reported on the graph.

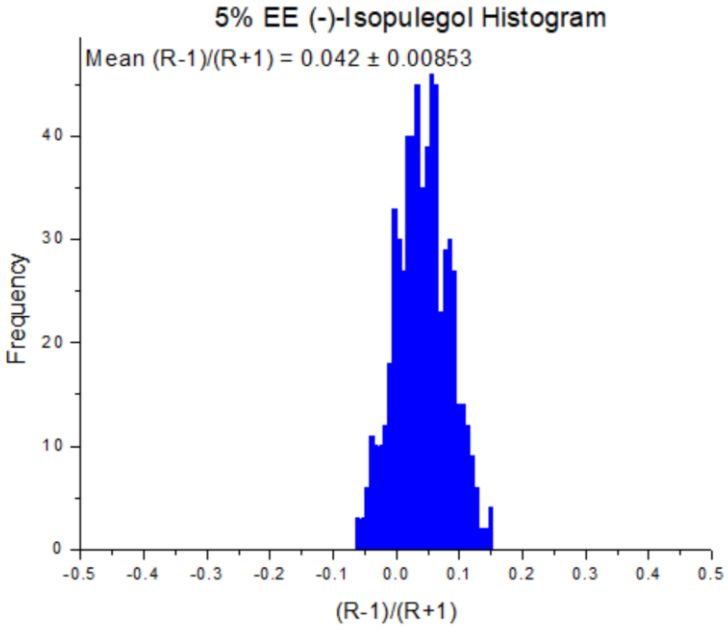

Figure A8: A histogram showing the distribution of enantiomeric excess calculated using the 25 strongest transitions of both the hetero- and homochiral complexes from the 5% EE isopulegol measurement. The mean and uncertainty are also reported on the graph.

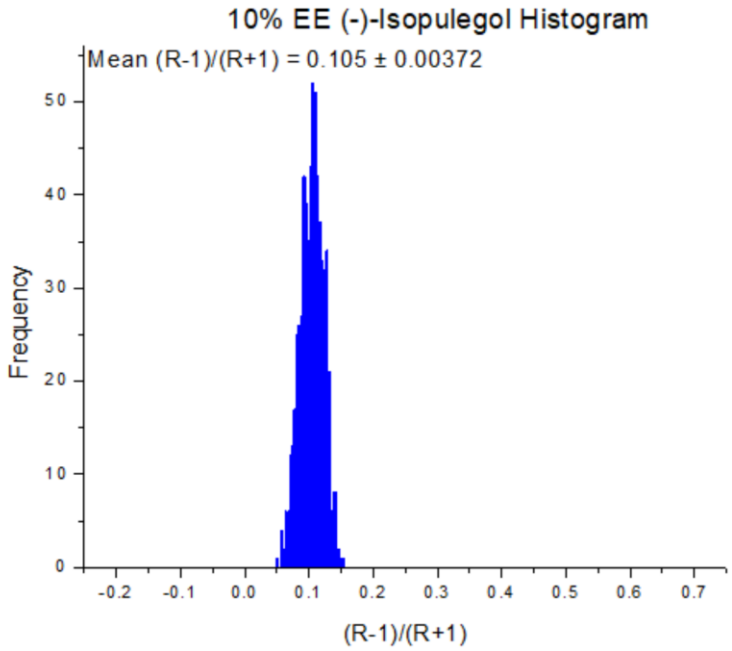

Figure A9: A histogram showing the distribution of enantiomeric excess calculated using the 25 strongest transitions of both the hetero- and homochiral complexes from the 10% EE isopulegol measurement. The mean and uncertainty are also reported on the graph.

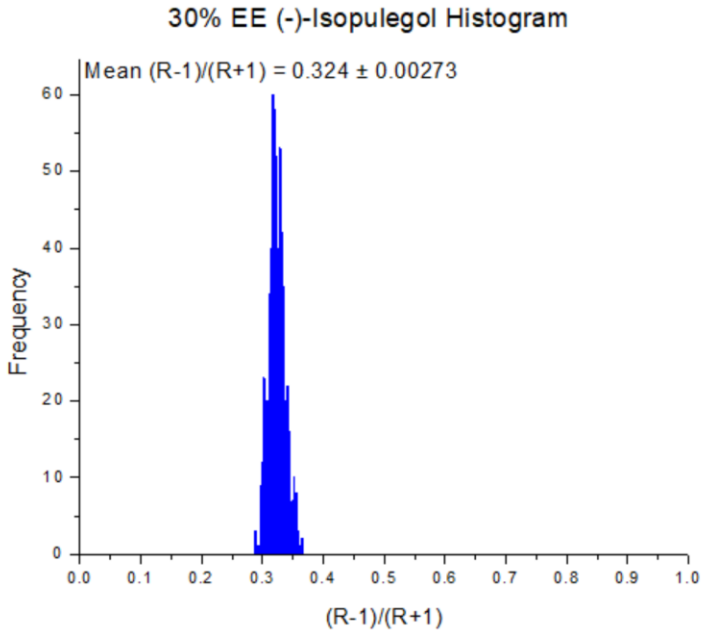

Figure A10: A histogram showing the distribution of enantiomeric excess calculated using the 25 strongest transitions of both the hetero- and homochiral complexes from the 30% EE isopulegol measurement. The mean and uncertainty are also reported on the graph.

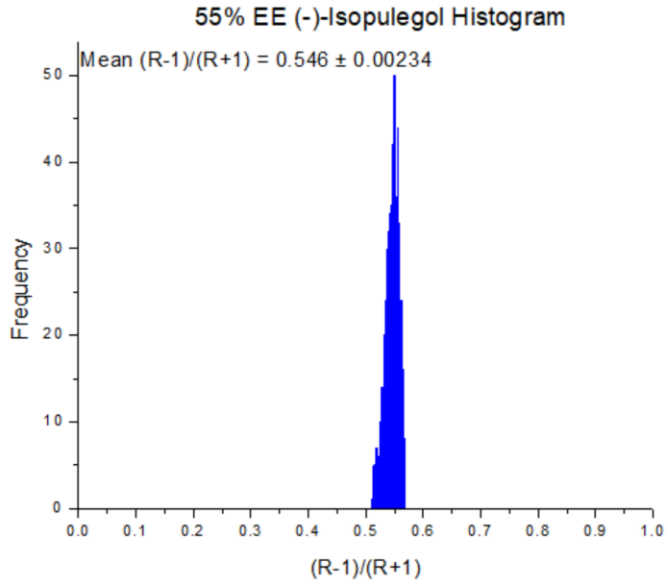

Figure A11: A histogram showing the distribution of enantiomeric excess calculated using the 25 strongest transitions of both the hetero- and homochiral complexes from the 55% EE isopulegol measurement. The mean and uncertainty are also reported on the graph.

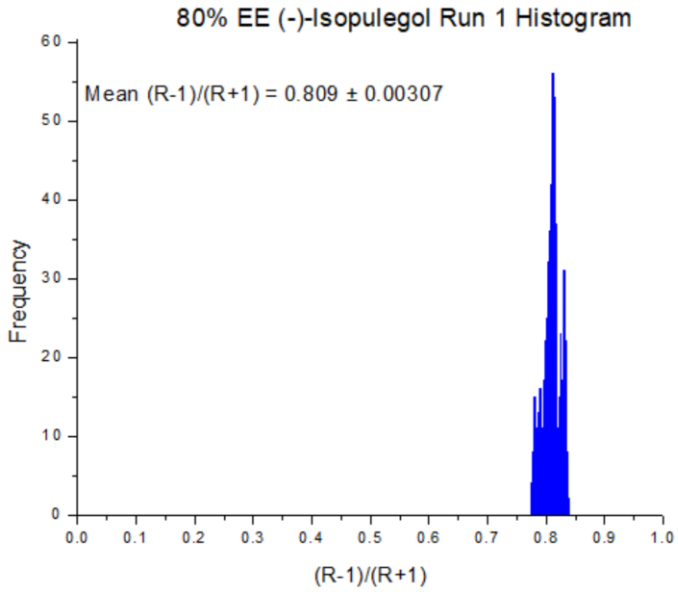

Figure A12: A histogram showing the distribution of enantiomeric excess calculated using the 25 strongest transitions of both the hetero- and homochiral complexes from the first 80% EE isopulegol measurement. The mean and uncertainty are also reported on the graph.

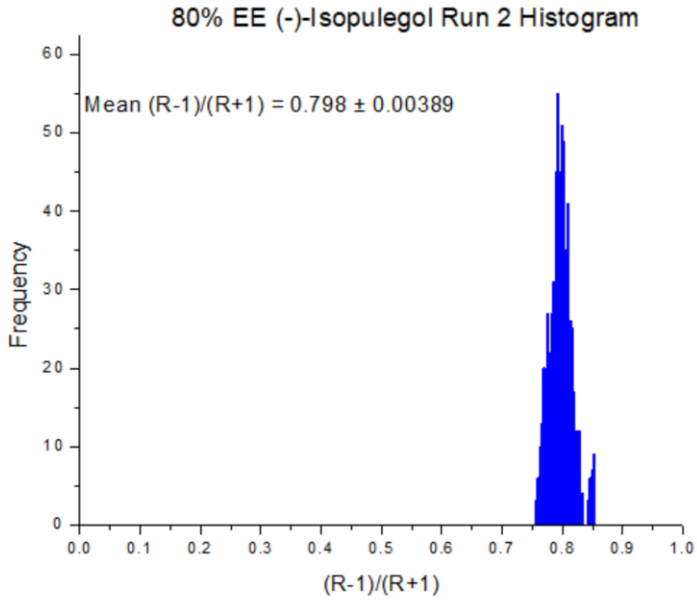

Figure A13: A histogram showing the distribution of enantiomeric excess calculated using the 25 strongest transitions of both the hetero- and homochiral complexes from the second 80% EE isopulegol measurement. The mean and uncertainty are also reported on the graph.

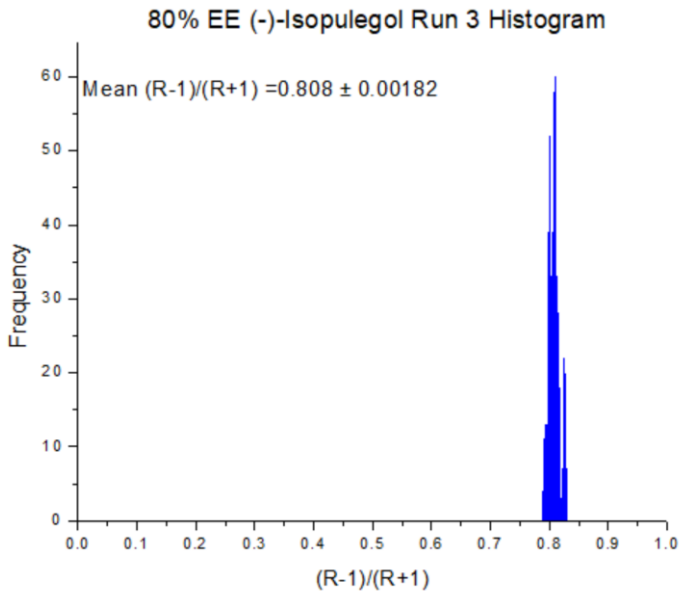

Figure A14: A histogram showing the distribution of enantiomeric excess calculated using the 25 strongest transitions of both the hetero- and homochiral complexes from the third 80% EE isopulegol measurement. The mean and uncertainty are also reported on the graph.

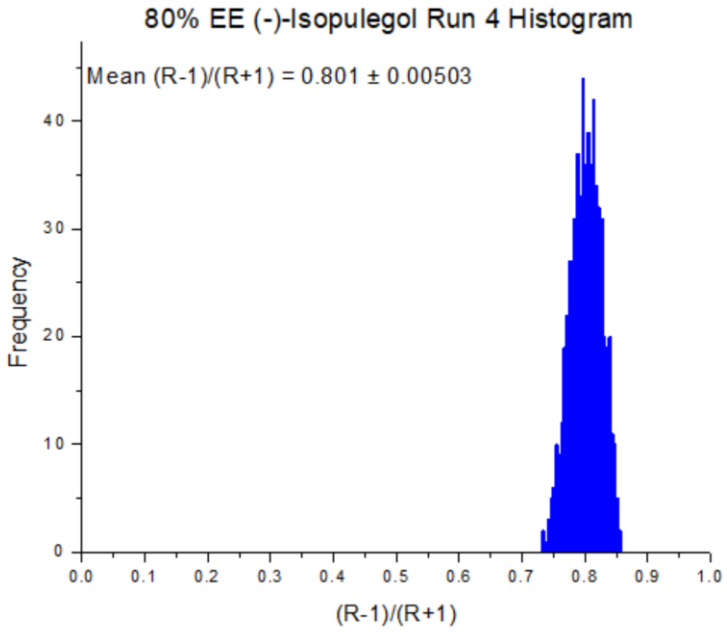

Figure A15: A histogram showing the distribution of enantiomeric excess calculated using the 25 strongest transitions of both the hetero- and homochiral complexes from the fourth 80% EE isopulegol measurement. The mean and uncertainty are also reported on the graph.

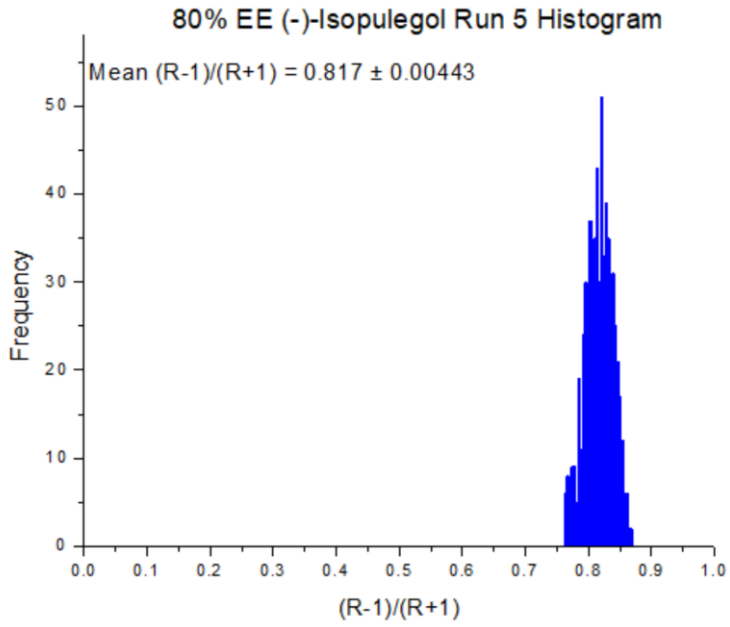

Figure A16: A histogram showing the distribution of enantiomeric excess calculated using the 25 strongest transitions of both the hetero- and homochiral complexes from the fifth 80% EE isopulegol measurement. The mean and uncertainty are also reported on the graph.

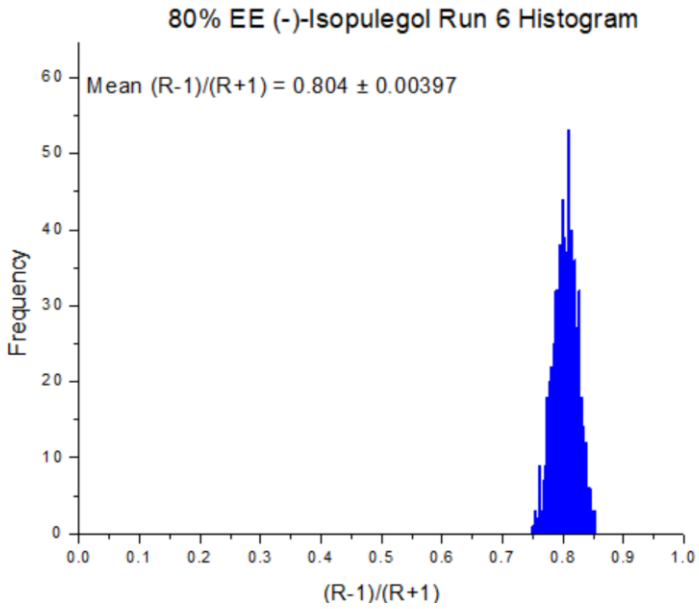

Figure A17: A histogram showing the distribution of enantiomeric excess calculated using the 25 strongest transitions of both the hetero- and homochiral complexes from the sixth 80% EE isopulegol measurement. The mean and uncertainty are also reported on the graph.

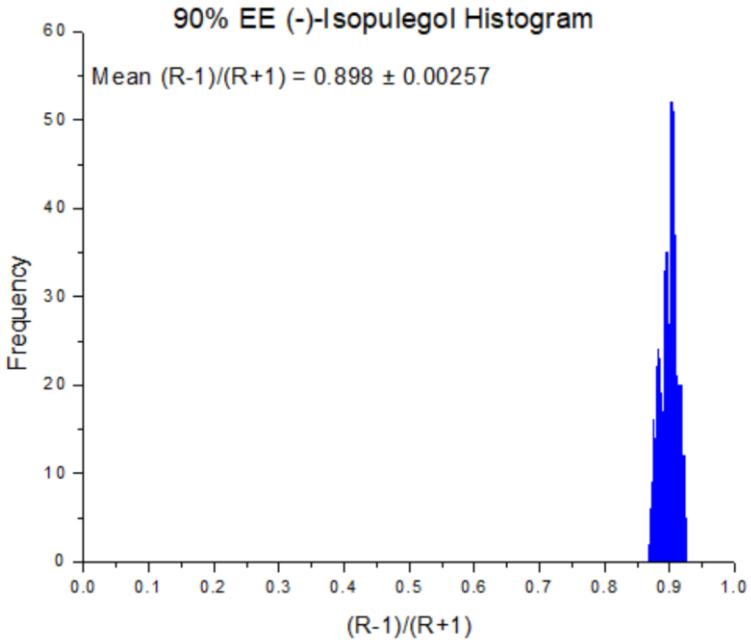

Figure A18: A histogram showing the distribution of enantiomeric excess calculated using the 25 strongest transitions of both the hetero- and homochiral complexes from the 90% EE isopulegol measurement. The mean and uncertainty are also reported on the graph.

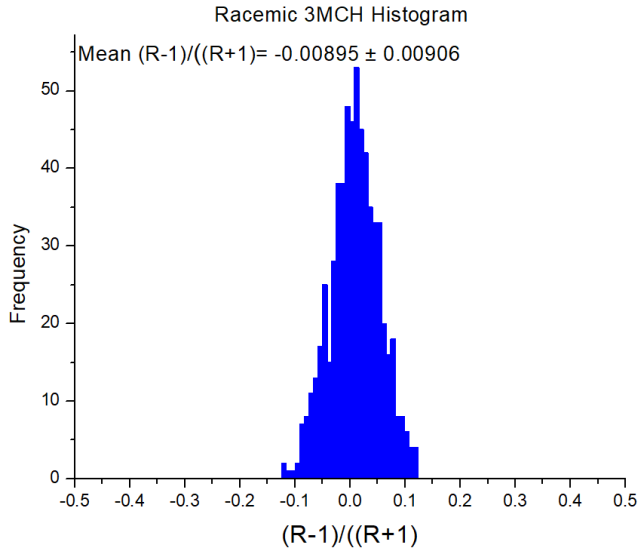

Figure A19: A histogram showing the distribution of enantiomeric excess calculated using the 25 strongest transitions of both the hetero- and homochiral complexes from the racemic 3-MCH measurement. The mean and uncertainty are also reported on the graph.

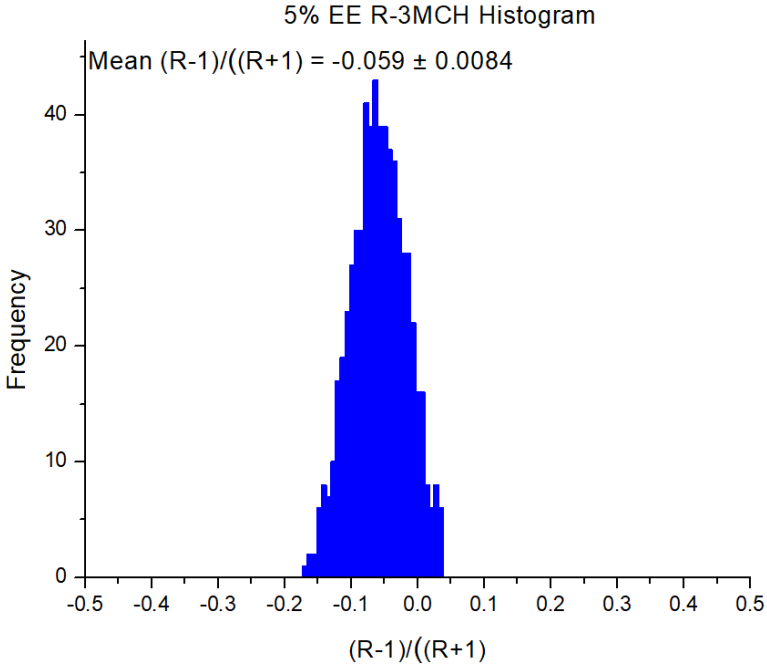

Figure A20: A histogram showing the distribution of enantiomeric excess calculated using the 25 strongest transitions of both the hetero- and homochiral complexes from the 5% EE 3-MCH measurement. The mean and uncertainty are also reported on the graph.

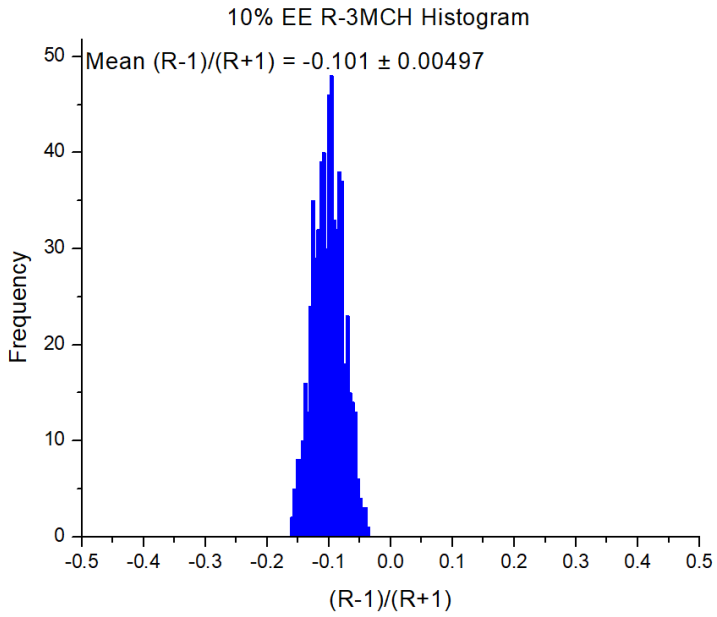

Figure A21: A histogram showing the distribution of enantiomeric excess calculated using the 25 strongest transitions of both the hetero- and homochiral complexes from the 10% EE 3-MCH measurement. The mean and uncertainty are also reported on the graph.

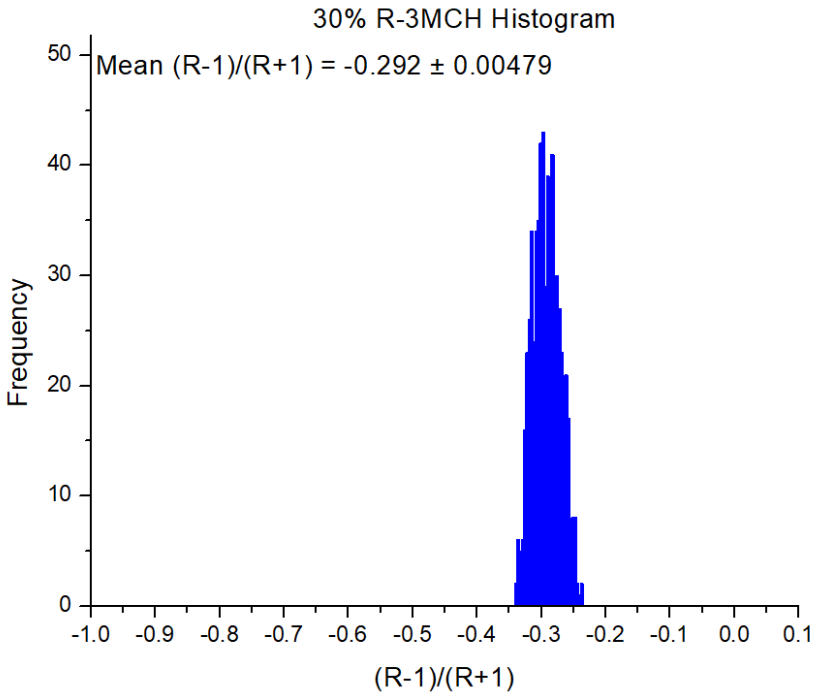

Figure A22: A histogram showing the distribution of enantiomeric excess calculated using the 25 strongest transitions of both the hetero- and homochiral complexes from the 30% EE 3-MCH measurement. The mean and uncertainty are also reported on the graph.

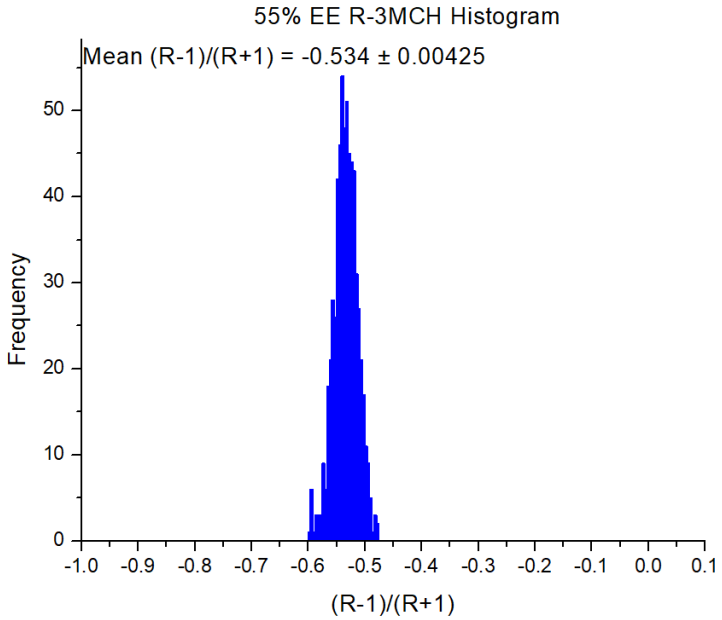

Figure A23: A histogram showing the distribution of enantiomeric excess calculated using the 25 strongest transitions of both the hetero- and homochiral complexes from the 55% EE 3-MCH measurement. The mean and uncertainty are also reported on the graph.

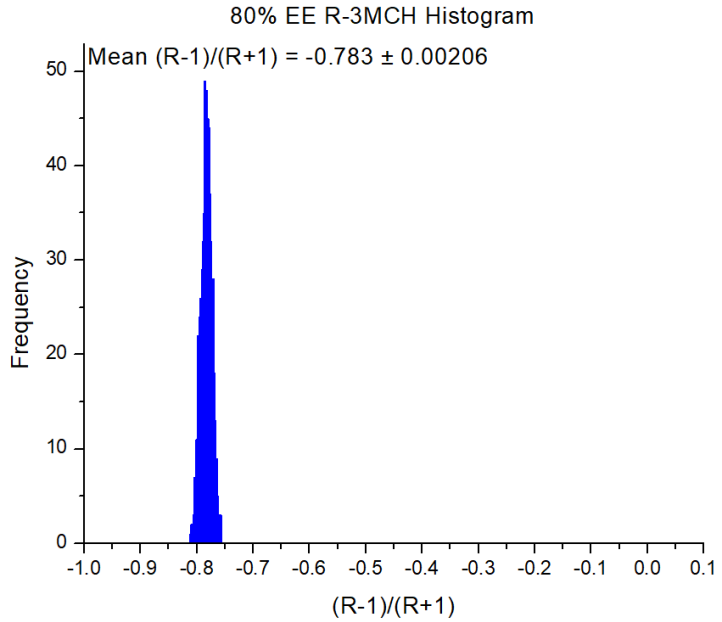

Figure A24: A histogram showing the distribution of enantiomeric excess calculated using the 25 strongest transitions of both the hetero- and homochiral complexes from the 80% EE 3-MCH measurement. The mean and uncertainty are also reported on the graph.

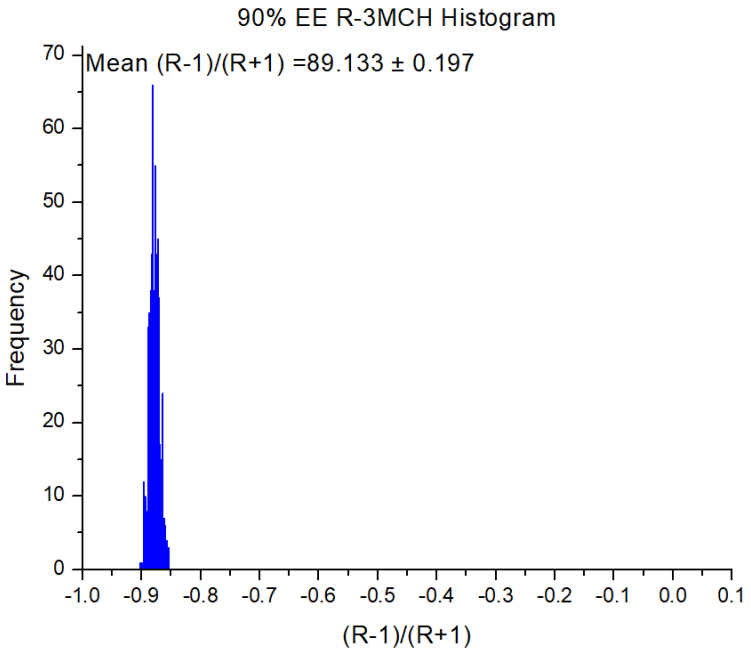

Figure A25: A histogram showing the distribution of enantiomeric excess calculated using the 25 strongest transitions of both the hetero- and homochiral complexes from the 90% EE 3-MCH measurement. The mean and uncertainty are also reported on the graph.

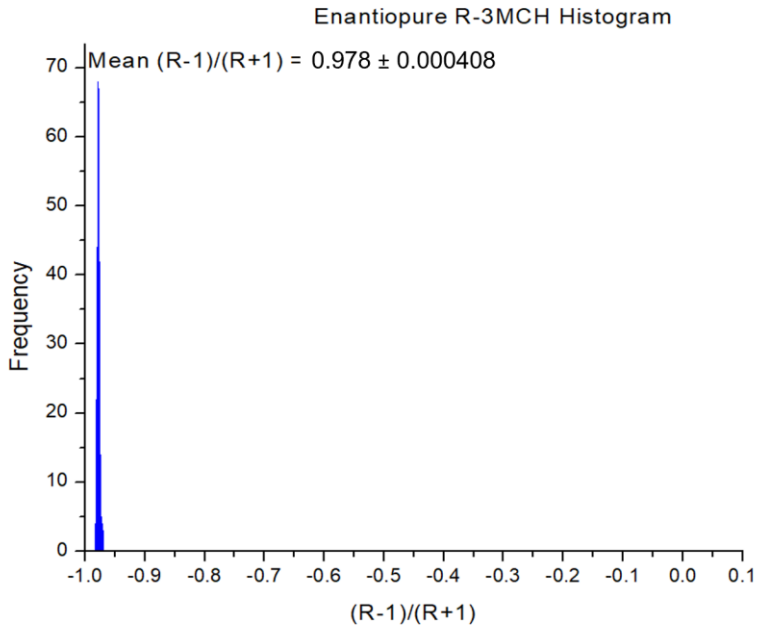

Figure A26: A histogram showing the distribution of enantiomeric excess calculated using the 25 strongest transitions of both the hetero- and homochiral complexes from the enantiopure EE 3-MCH measurement. The mean and uncertainty are also reported on the graph.

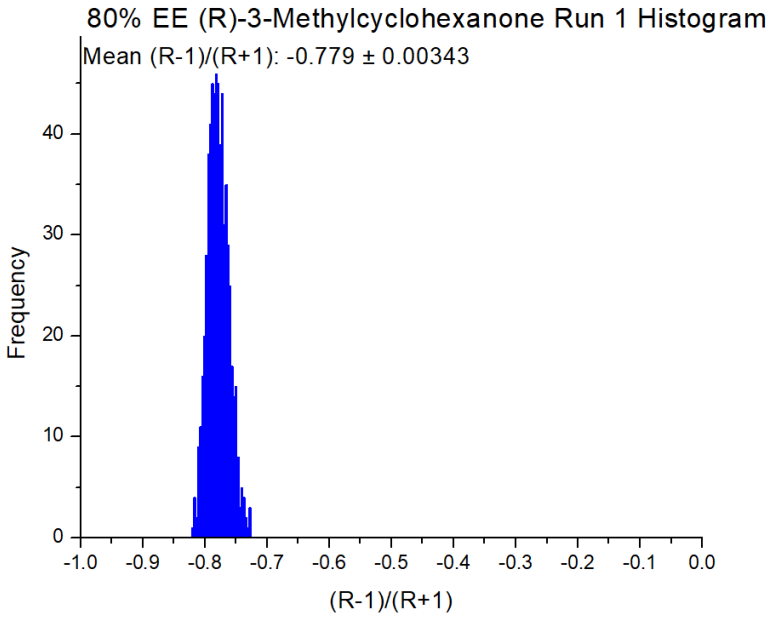

Figure A27: A histogram showing the distribution of enantiomeric excess calculated using the 25 strongest transitions of both the hetero- and homochiral complexes from the first 80% EE 3-MCH reproducibility measurement. The mean and uncertainty are also reported on the graph.

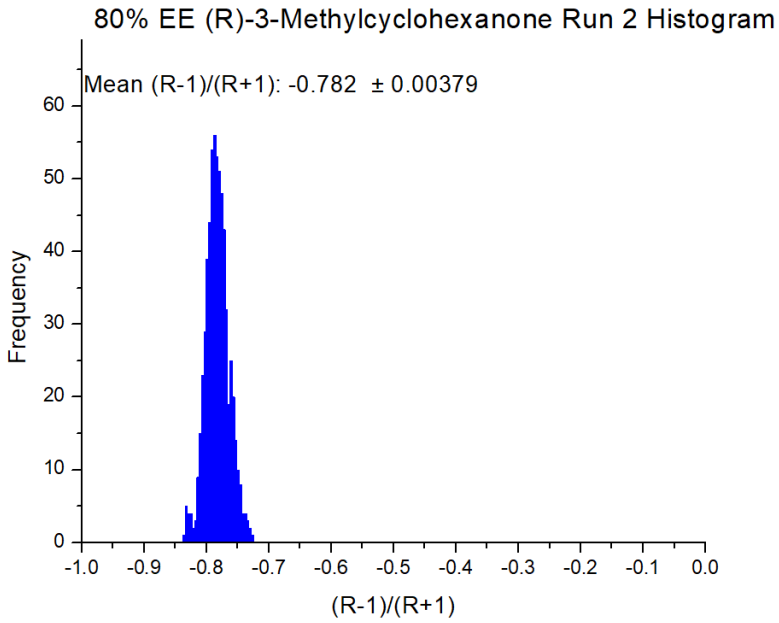

Figure A28: A histogram showing the distribution of enantiomeric excess calculated using the 25 strongest transitions of both the hetero- and homochiral complexes from the second 80% EE 3-MCH reproducibility measurement. The mean and uncertainty are also reported on the graph.

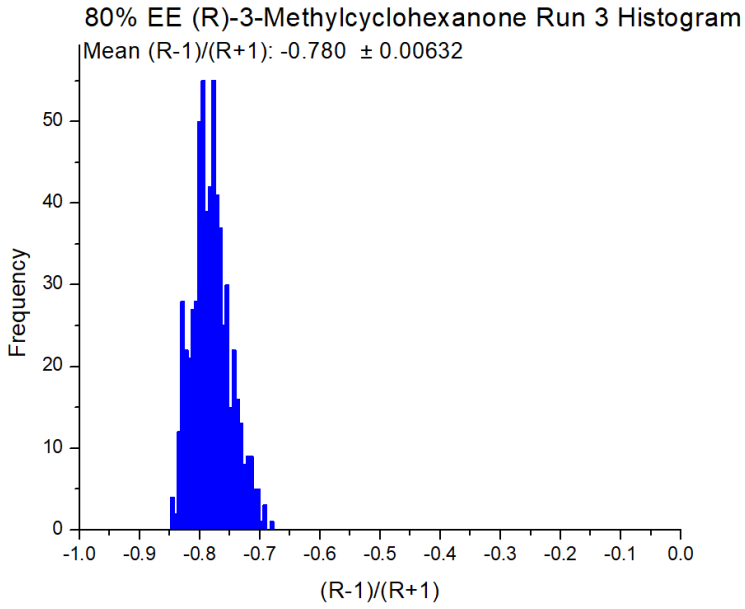

Figure A29: A histogram showing the distribution of enantiomeric excess calculated using the 25 strongest transitions of both the hetero- and homochiral complexes from the third 80% EE 3-MCH reproducibility measurement. The mean and uncertainty are also reported on the graph.

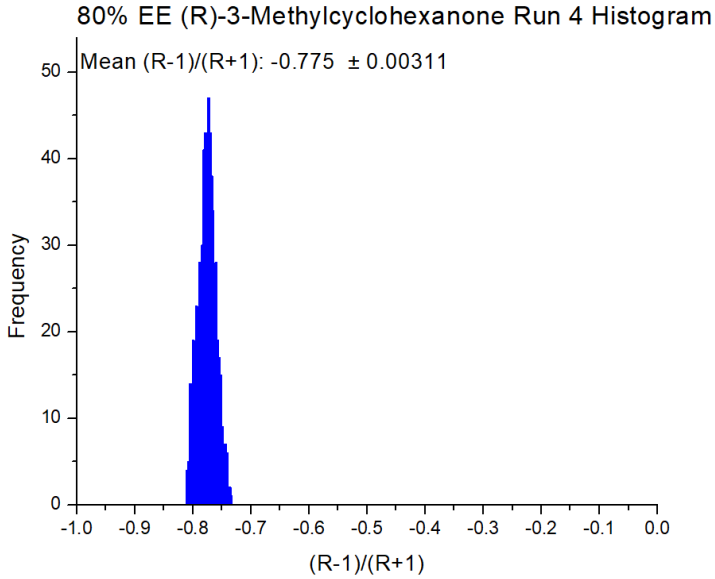

Figure A30: A histogram showing the distribution of enantiomeric excess calculated using the 25 strongest transitions of both the hetero- and homochiral complexes from the fourth 80% EE 3-MCH reproducibility measurement. The mean and uncertainty are also reported on the graph.

Chapter 3

Benchmarking Quantum Chemical Methods on the Hydrogen Bonded Complex of Verbenone and 3-Butyn-2-ol for Absolute Configuration Assignment

I. Introduction

In the previous chapter the method and accuracy of enantiomeric excess determinations from chiral tag rotational spectroscopy were studied. A complete chiral analysis must also provide the absolute configuration of the enantiomer in excess. Importantly, the absolute configuration must be reliable and the capacity of the technique to misassign stereochemistry understood. Here, the absolute configuration determination by chiral tag rotational spectroscopy will be discussed. To assign absolute configuration, theoretical calculations done by quantum chemical computational methods are used to obtain relative energies of chiral tag complexes, structures, and the electronic dipole moment. The accuracy of these quantum chemical calculations to make high-confidence absolute configuration assignments will be explored.

A large part of modern computational quantum chemistry is the prediction of molecular structure and the molecular energies. Theoretical descriptions of systems are often used in conjunction with experimental results to support conclusions. These theoretical descriptions need to have a certain degree of accuracy as well as having acceptable computationally costs. Benchmarking has become a common method of assessing the accuracy and identify shortcomings of computational methods. Many recent benchmarking results have focused on non-covalent interactions using dispersion-corrected DFT models.[1, 2] Empirical DFT methods generally have lower computational costs associated with them when compared to *ab initio* methods. A frequently used method to interpret spectra is the DFT-D3 method which calculates intra- and intermolecular

dispersionforces using an atom pairwise routine with a general form given in Eq 3.1.[3-5]

$$E_{disp} = -\frac{1}{2}\sum_{A\neq B}\sum_{n=6,8,10\,,..} s_n \frac{C_n^{AB}}{R_{AB}^n} f_{\text{damp}}(R_{AB}) \tag{3.1}$$

E_{disp} is the dispersion energy correction, *AB* are the atom pair, C_n^{AB} is the *n*th order dispersion correction term, R_{AB} is the internuclear distance, s_n is a global scaling factor, and f_{damp} is the damping function. Many of these benchmarking studies of dispersion corrected DFT methods are tested with molecules of biochemical and materials application due to the importance of dispersion interactions in these systems. Such benchmarking datasets are usually tested against references computed with coupled cluster methods.[1, 3]

In rotational spectroscopy, computational methods are used to predict the rotational constants; A, B, and C.[6-8] Rotational constants are calculated from the moments-of-inertia along the principal axes of a molecule; therefore, electronic structure optimizations from computational methods are needed to accurately determine the positions of the atoms within a molecule relative to its center of mass. To assign the absolute configuration in chiral tag rotational spectroscopy, the theoretical rotational constants need to be compared to experimental results. Furthermore, the electric dipole moments along the principal axes, μ_a, μ_b, and μ_c, contribute separately to the molecular rotational spectrum. These contributions are known as the *a*-type, *b*-type, and *c*-type spectra and arise from the interaction of the electric field of the microwave source with the three electric dipole moment components. The relative intensities of the rotational spectra from these spectra are determined by the respective square of the electric dipole moments components. Electric dipole moment vector direction can be used to support assignment made using theory and build confidence in absolute configuration determination. In addition, pulsed jet methods are used to rotationally cool gasses to increase measurement sensitivity in Fourier-transform microwave

spectrometers. In the pulsed jet expansion, higher energy conformations of the molecule are depopulated, leaving the lowest energy conformations present.[9, 10] Therefore, rotational spectroscopy relies on computational quantum chemistry to accurately determine the electronic structure and energies of molecular species.

Chirped-pulse Fourier transformation microwave spectroscopy (CP-FTMW) has made the acquisition of large bandwidth rotational spectra quick relative to cavity techniques. This has allowed for a plethora of rotational data to be gathered, such as, rotational transitions, fits, conformational landscapes of molecules in the pulsed jet, and Kraitchman coordinates of atom positions. All of these can be used to make an absolute configuration assignment. In chiral tag rotational spectroscopy, absolute configuration is determined by first making a measurement with the racemic tag to generate both the homochiral and heterochiral complexes. Measurement with the enantiopure tag is then made to break the complexes into two families. Spectroscopic parameters are then compared to theory to support the identification of the diastereomer complexes. In cases where there is enough sensitivity, a substitution structure can be made to provide exceptionally high confidence for absolute configuration assignment. The benchmarking of current computational methods used in rotational spectroscopy will be investigated to provide insight into the most accurate methods with consideration of the computational costs and time of each method for implementation in an analytical method. The study of the non-covalently bound 3-butyn-2-ol to verbenone via a hydrogen bond, shown in the previous chapter, will explore the comparison of the energetics of calculated from theory to the observed isomers in the pulsed jet expansion, accuracy of the atomic positions relative to the center of mass, and the accuracy of the relative electric dipole moments.

II. Experimental

1) Materials

Materials used in this experiment were obtained from commercial sources. (1*S*)-(-)-verbenone, (*S*)-(-)-3-butyn-2-ol (butynol), (*R*)-(+)-butynol and racemic butynol were purchased from MilliporeSigma.

2) Rotational Spectroscopy

Rotational spectra were recorded on a 2-8 GHz CP-FTMW with the instrument design and technique previously described by Perez *et al* (2013).[11] The sample of verbenone was loaded directly into the nozzles of the spectrometer and heated to 60 °C. A 50 mL beaker was loaded with 100 µL of butynol that was placed into a stainless-steel reservoir with an inlet and a pressure regulated outlet. Neon was used as a carrier gas and pressure regulated at 20 psig connected by Teflon lines to the reservoir. The pressure out of the reservoir was set to 10 psig to seed the carrier gas with butynol. The mixture of butynol and Ne were then connected to the spectrometer with additional Teflon gas lines. The mixture of verbenone, butynol, and Ne were then adiabatically expanded into the spectrometer to form non-covalent complexes. Spectra were taken using enantiopure (*R*)-(+)-butynol, enantiopure (*S*)-(-)-butynol and racemic butynol with (1*S*)-(-)-verbenone. A total of 2 million FIDs were averaged for enantiopure samples, and 1 million averages for the racemic sample. The corresponding spectra were then fit using JB95, Pickett's SPCAT/SPFIT and Kisiel's PROSPE program package.[12-14]

3) Experimental Data Set

The experimental data set for benchmarking is the chiral tag complex of verbenone and butynol, as stated above. This system was chosen because there is no conformational flexibility in the verbenone, leaving only conformational flexibility in the butynol, Figure 3.1. Given the simplicity of the conformational landscape, this work tests the accuracy of quantum chemistry in calculating the non-covalent interactions accurately. Eight spectra were assigned (Table A10-A11), and for five spectra there was sensitivity for ^{13}C isotopomers in natural abundance. Carbon atom positions were obtained from employing Kraitchman's analysis to the fit ^{13}C spectra. It is estimated that any other chiral tag complexes unassigned in the spectrum are less than 3% relative abundance, Figure 3.2.

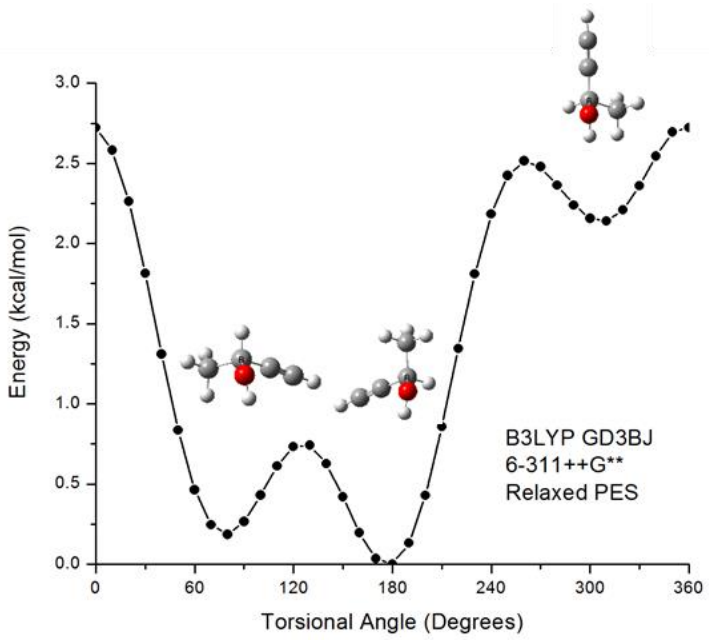

Figure 3.1: Potential energy surface generated by the varying of the torsion angle of the hydroxyl group of 3-buty-2-ol using B3LYPD3BJ with 6-311++G** method and basis set. Two distinct conformations of butynol are expected when the hydroxyl is almost anti to the hydrogen and methyl group of butynol.

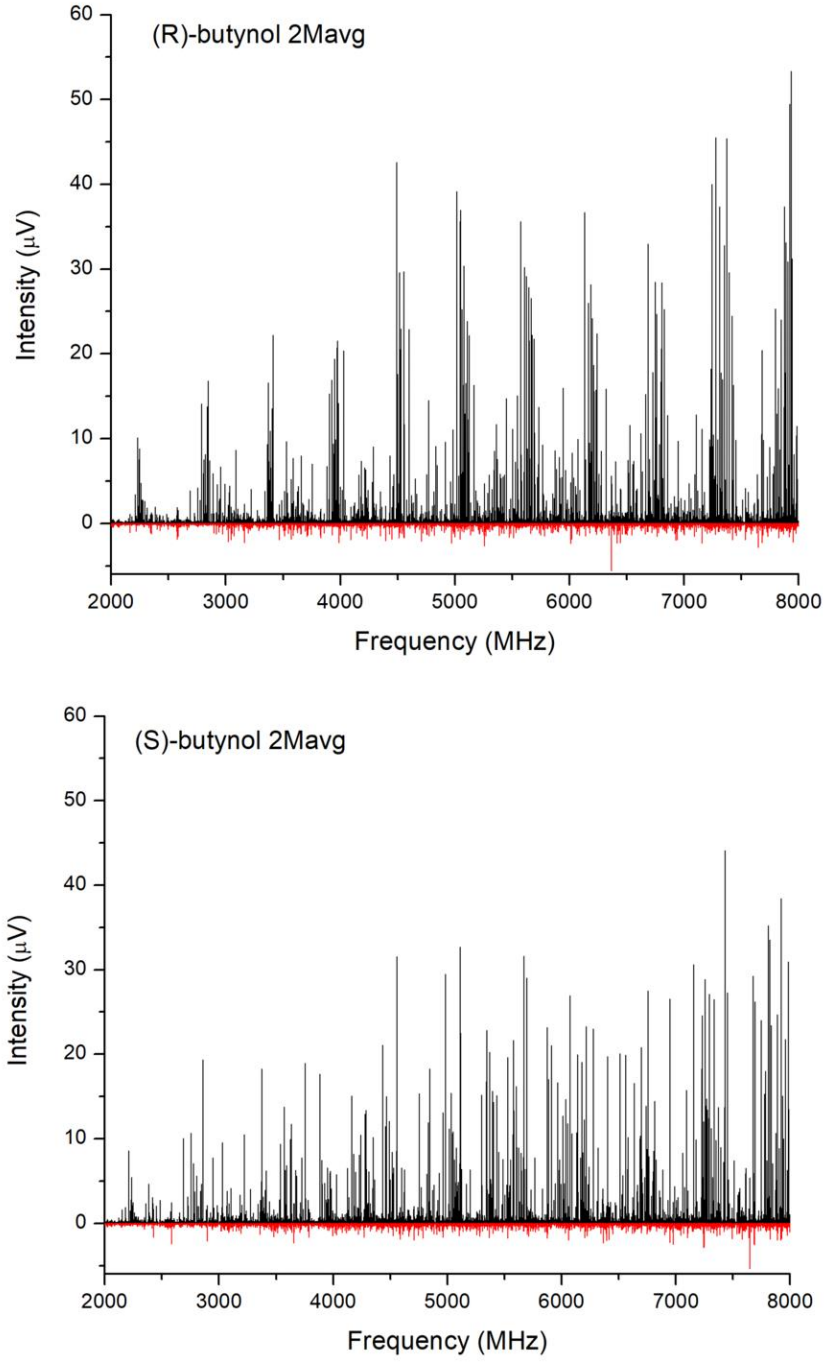

Figure 3.2: Two experimental spectra taken with 2 million averaged FID acquisitions for the (*S*)-verbenone tagged with (*R*)-butynol (top) and (*S*)-butynol (bottom). Plotted below both graphs are the residual lines, in red, left after cutting the spectra for the fit chiral tag complexes, and the verbenone monomer.

4) Restricted Isomer Search

A major challenge for identifying chiral tag complexes is the search of the potential energy surface to find low energy isomers. In this verbenone-butynol system, complexes consist of diastereomeric pairings of homochiral complexes, (*R*)-(+)-verbenone-(*R*)-(+)-butynol and (*S*)-(-)-verbenone-(*S*)-(-)-verbenone, and heterochiral complexes, (*R*)-(+)-verbenone-(*S*)-(-)-butynol and (*S*)-(-)-verbenone-(*R*)-(+)-butynol, and conformational isomers of each. A conformation search for the chiral tag is done by chemical intuition, unlike conformational searches of monomers, which can utilize molecular mechanics programs. In the case of butynol-verbenone, the hydroxyl group on the butynol will assume to form a hydrogen bond to the carbonyl oxygen of the verbenone to form the chiral tag complexes. The hydrogen bond can form on either the lone pairs on the carbonyl oxygen, the butynol can be above or below the ring of the verbenone, and the butynol can have two distinct conformers (Figure 3.1) where the hydrogen on the hydroxy group is anti to the hydrogen or to the methyl group. This gives 8 distinct conformers for both heterochiral and homochiral complexes. S and R labels refer to the stereochemistry of the butynol with all the verbenone being the (*R*)-enantiomer. Complexes denoted by 1 have the hydroxyl group on the butynol anti to the hydrogen, and 2 denotes the hydroxyl hydrogen is anti to the methyl group. An a or b have the hydrogen bond at the same lone pair on the carbonyl oxygen, the lone pair away from the bridge structure of the verbenone, and the butynol is positioned below and above the ring structure of the verbenone, respectively. A c or d denotes that the hydrogen bond is on the other lone pair of the carbonyl, the lone pair closer to the bridge structure, with the butynol positioned above and below the ring structure of verbenone, respectively. All eight complexes for the heterochiral and homochiral are displayed in Figure 3.3-3.6.

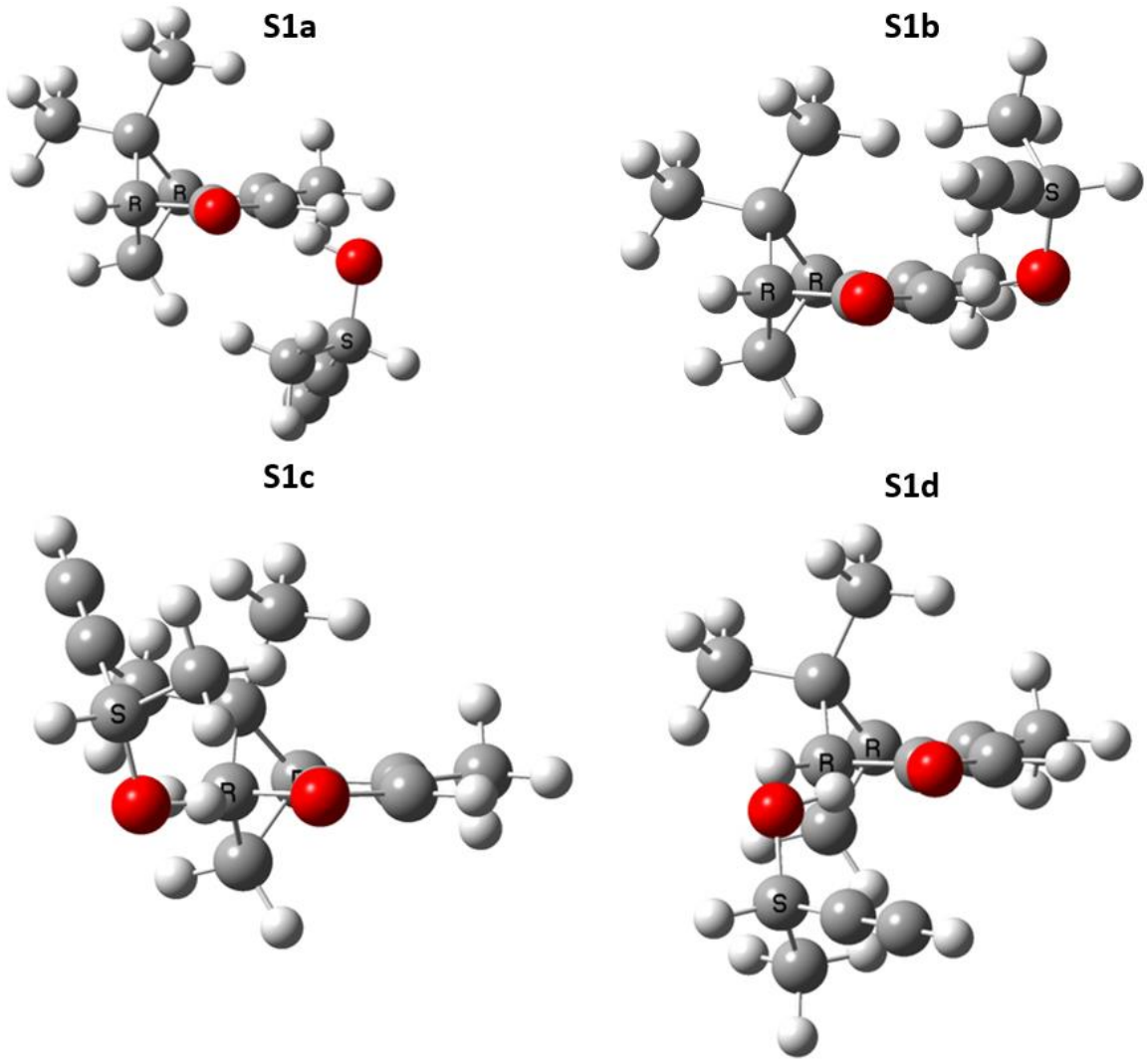

Figure 3.3: Heterochiral complexes of the four different positions the butynol can hydrogen bond to verbenone. These four complexes all have the same conformation of butynol with the hydroxyl group anti to the hydrogen on the butynol. All structures were optimized using B3LYPD3BJ def2TZVP method and basis set.

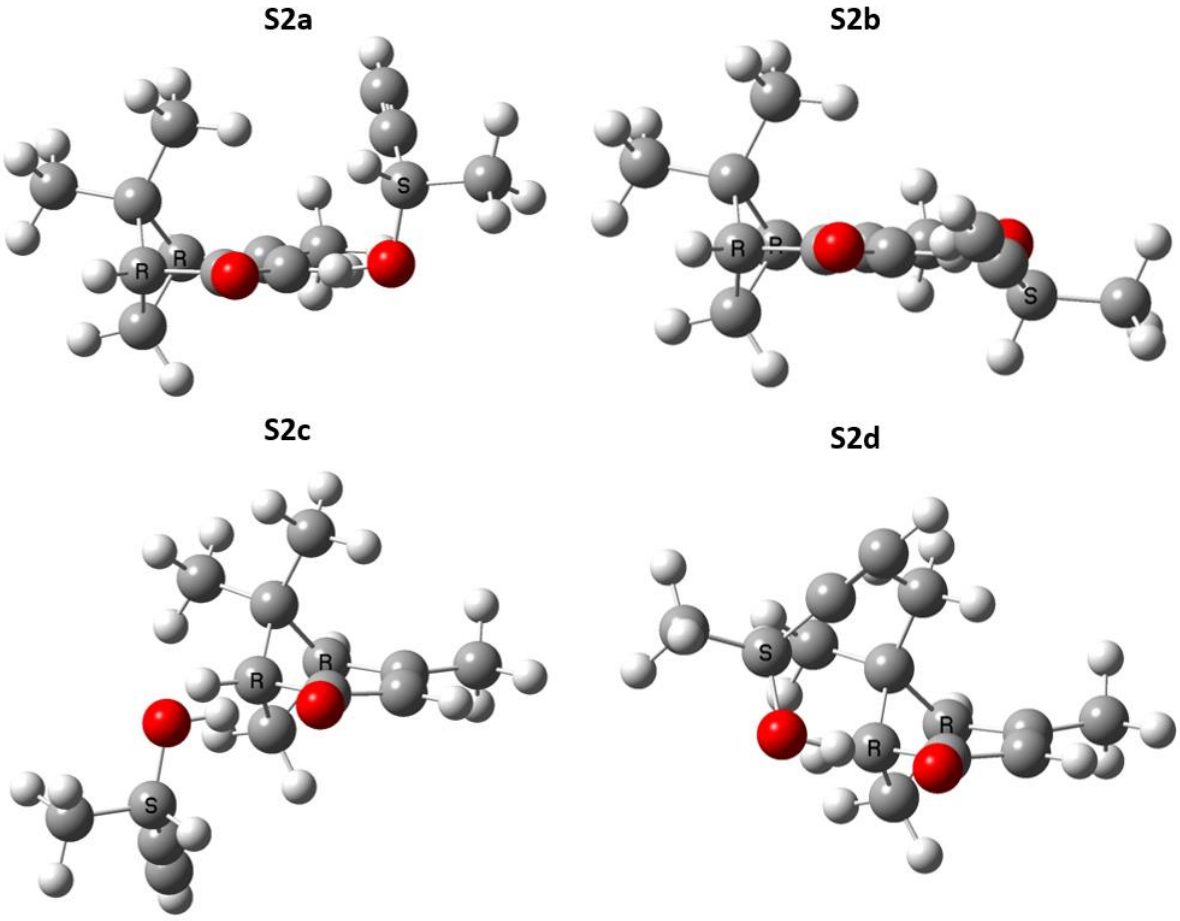

Figure 3.4: Heterochiral complexes of the four different positions the butynol can hydrogen bond to verbenone. These four complexes all have the same conformation of butynol with the hydroxyl group anti to the methyl group on the butynol. All structures were optimized using B3LYPD3BJ def2TZVP method and basis set.

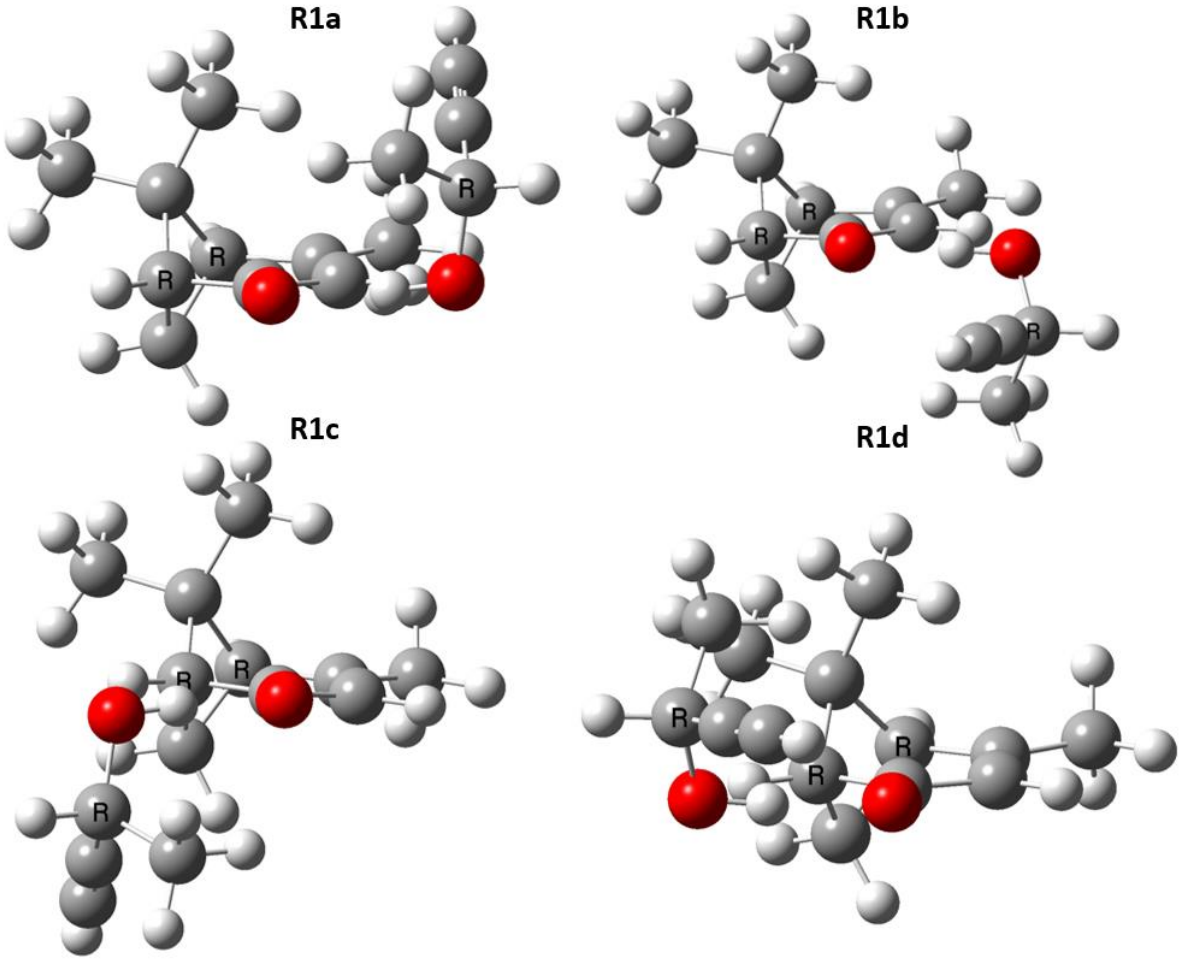

Figure 3.5: Homochiral complexes of the four different positions the butynol can hydrogen bond to verbenone. These four complexes all have the same conformation of butynol with the hydroxyl group anti to the hydrogen on the butynol. All structures were optimized using B3LYPD3BJ def2TZVP method and basis set.

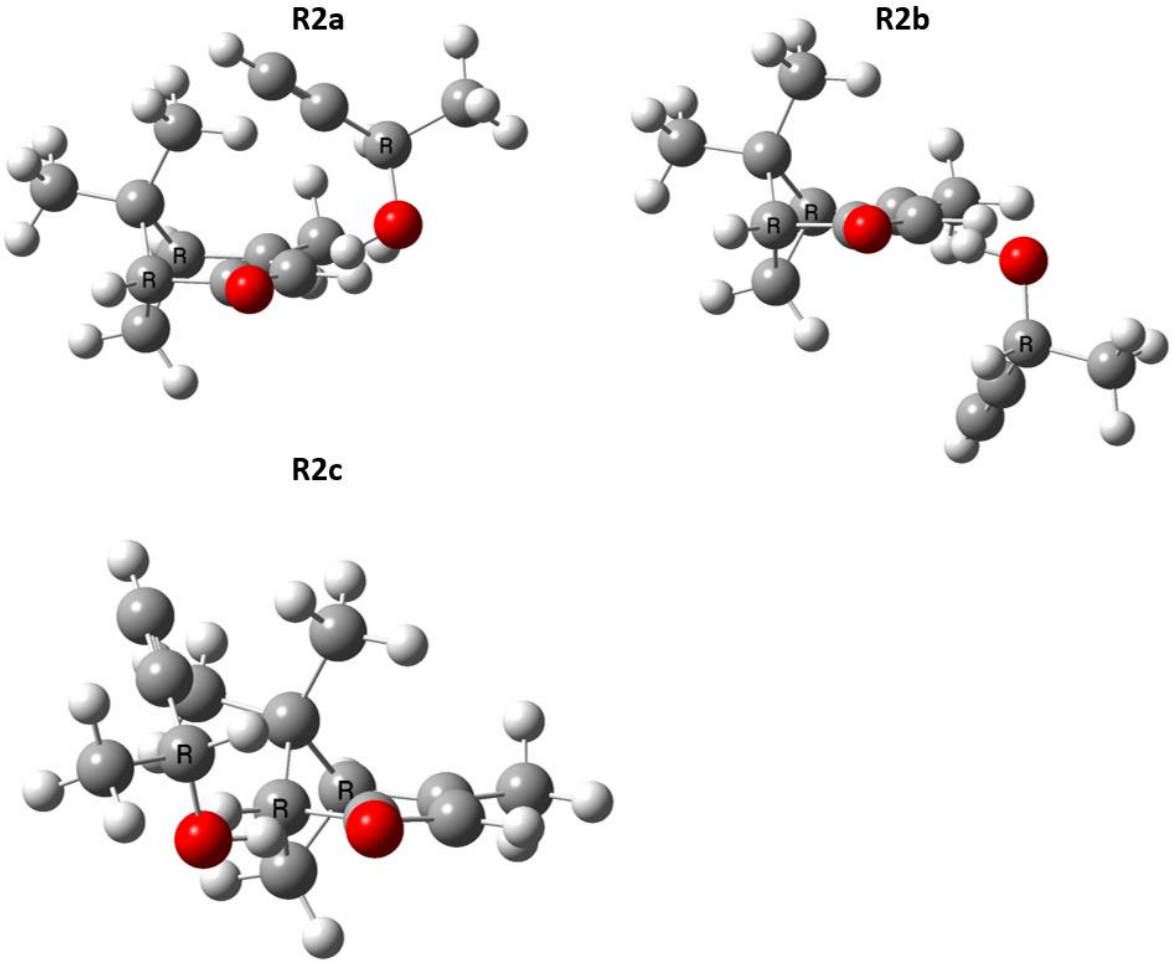

Figure 3.6: Homochiral complexes of the three different positions the butynol can hydrogen bond to verbenone, with R2d having optimized to the R2c structure for all methods used. These three complexes all have the same conformation of butynol with the hydroxyl group anti to the methyl group on the butynol. All structures were optimized using B3LYPD3BJ def2TZVP method and basis set.

5) Model Chemistries

The computational methods used in this paper were performed using Gaussian09 by our collaborator Dr. Luca Evangelisti and myself using Gaussian16 on UVA's computing cluster.[15, 16] Methods compared in this paper are B3LYPD3BJ, MP2, and a higher order DFT, B2PLYPD3. DFT without dispersion correction was excluded due a second point of contact that involves the non-covalent interaction of the alkyne group of butynol with verbenone (Figure 3.7). DFT calculations without dispersion correction fail to describe these interactions producing poor geometries and, therefore, poor estimates of the rotational constants, and are not suitable for analyzing chiral tag rotational spectra. Two basis sets were used, which were def2TZVP and Pople's 6311++G(d,p). All were run with the keyword *output=pickett* to calculate the rotational constants, electric dipole moment components, and atomic positions in the principal axis system.

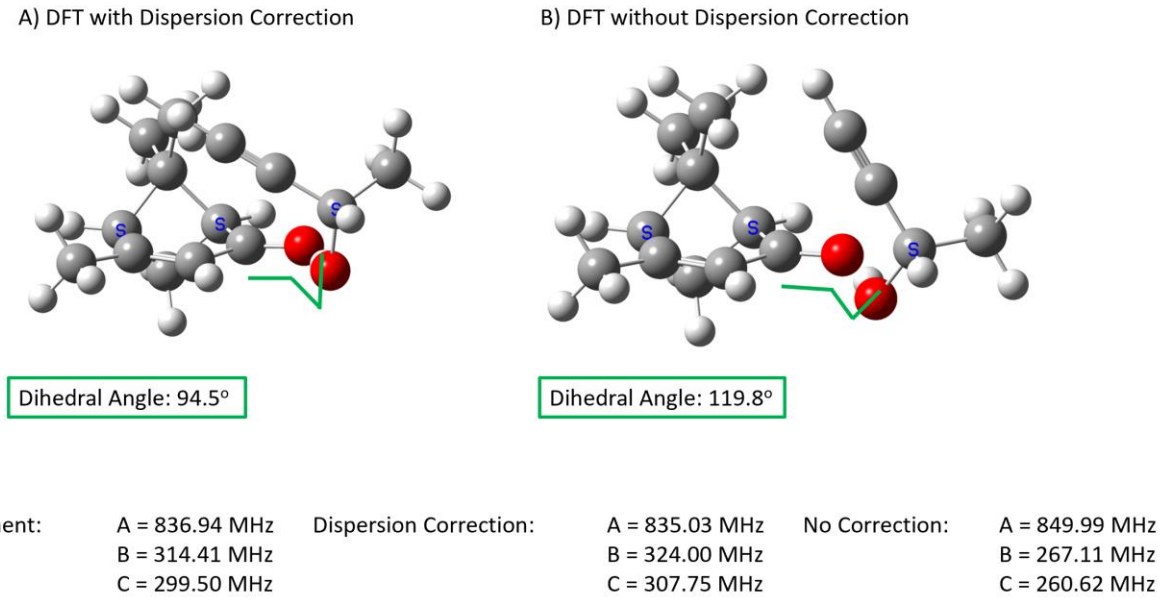

Figure 3.7: A comparison of DFT with dispersion correction (A) and without dispersion correction (B). The calculated dihedral angle from the carbon alpha to the carbonyl oxygen, the carbonyl oxygen, to the oxygen on the butynol and its alpha carbon is given for both structures. Furthermore, the experimental rotational constants and the theoretical constants are compared.

III. Results

1) Quantum Chemistry Equilibrium Geometries

Relative Energies

Experimentally, four of the heterochiral and homochiral complexes were observed in all three spectra. These were the S1a, S2c, S2a, and S2c isomers for the heterochiral complexes, and the R1a, R1c, R2b, and R2c isomers for the homochiral complexes. Five of these structures were verified with substitution coordinates, which were S2a, S2c, R1a, R1c, and R2c. An estimation of the relative populations of each of the complexes for homochiral and heterochiral isomers can be made by simulating each complex with SPCAT using the *ab initio* electric dipole moment component magnitudes and scaling the calculated intensity of each transition to the experimental intensity. The *ab initio* electric dipole moments were from the B3LYPD3BJ with def2TZVP basis set. Mean scaling factors are recorded and the percent composition for each isomer is calculated by dividing the isomers mean scale factor over the sum of scale factors. Tables B1 and B2 in the appendix show experimental percent compositions of the observed heterochiral “S” isomers and the homochiral “R” isomers in both enantiopure tag spectra and the racemic tag spectrum using 25 transitions, respectively. Moreover, Figure 3.8 shows the variation of the mean scale factor with number of transitions for each isomer in racemic spectrum. The solid line is the mean of all the means calculated with the different number transitions, and the dash line is one standard deviation above and below the mean. The mean using 25 is no more than 1% away from the mean scale factor and allows a better error estimate of how well we know these calculated scale factors. Since both isomers are observed in the racemic measurement, an estimate of the relative amounts of the homochiral and heterochiral is present. Summing over all the scale factors of the both the

heterochiral and homochiral isomers in Tables B1 and B2, the relative amount of homochiral complexes is calculated to be 48.8% and 51.2% for the heterochiral complexes.

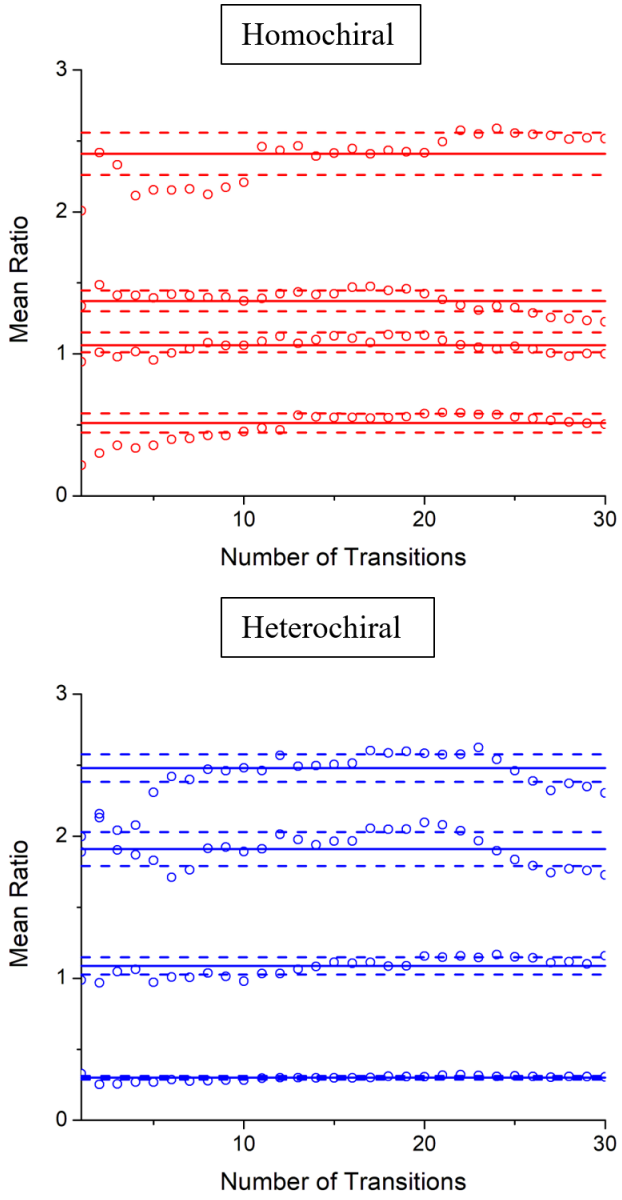

Figure 3.8: Experimentally calculated scaling factors used to determine the percent composition of each isomer for the homochiral complexes (top) and heterochiral complexes (bottom). The solid lines are the average mean scaling factors and the dashed lines are one standard deviation above and below the average.

Assuming thermal equilibrium, the theoretically predicted relative energy of a higher energy isomer, P_n, to the lowest energy isomer, P_0, is related by a Boltzmann factor, Eq 3.2.

$$\frac{P_n}{P_0} = e^{\frac{-\Delta E}{k_b T}} \tag{3.2}$$

Where ΔE is the difference in energy of the two states k_b is Boltzmann's constant, and T is the temperature at thermal equilibrium. Taking the absolute value of the natural log of the Boltzmann factor gives

X

$$\left|\ln\left(\frac{P_n}{P_0}\right)\right| = \frac{\Delta E}{k_b T} \tag{3.3}$$

Therefore,

$$\left|\ln\left(\frac{P_n}{P_0}\right)\right| \propto \Delta E \tag{3.4}$$

In Figure 3.9 and Figure 3.10, the relative energies of each of the eight isomers computed with the different methods and basis sets are presented graphically and the Tables B3 and B4 give the numerical values. The energies are relative to the lowest energy isomer computed in that method and basis set combination. These are compared to the natural log of the ratio of each structure's experimentally determined scale factor to the most abundant structure determined experimentally. The most abundant structure would be the one with the largest scale factor. In some of the calculations, optimization at certain starting positions optimized to a different structure. For the heterochiral "S" isomers only the S2b structure using the Pople basis set optimized to a different energy structure, S2a. Again, the Pople basis set for the R1b optimized to the R1a structure, and all the methods except MP2 had the R2d structure optimize to the R2c structure.

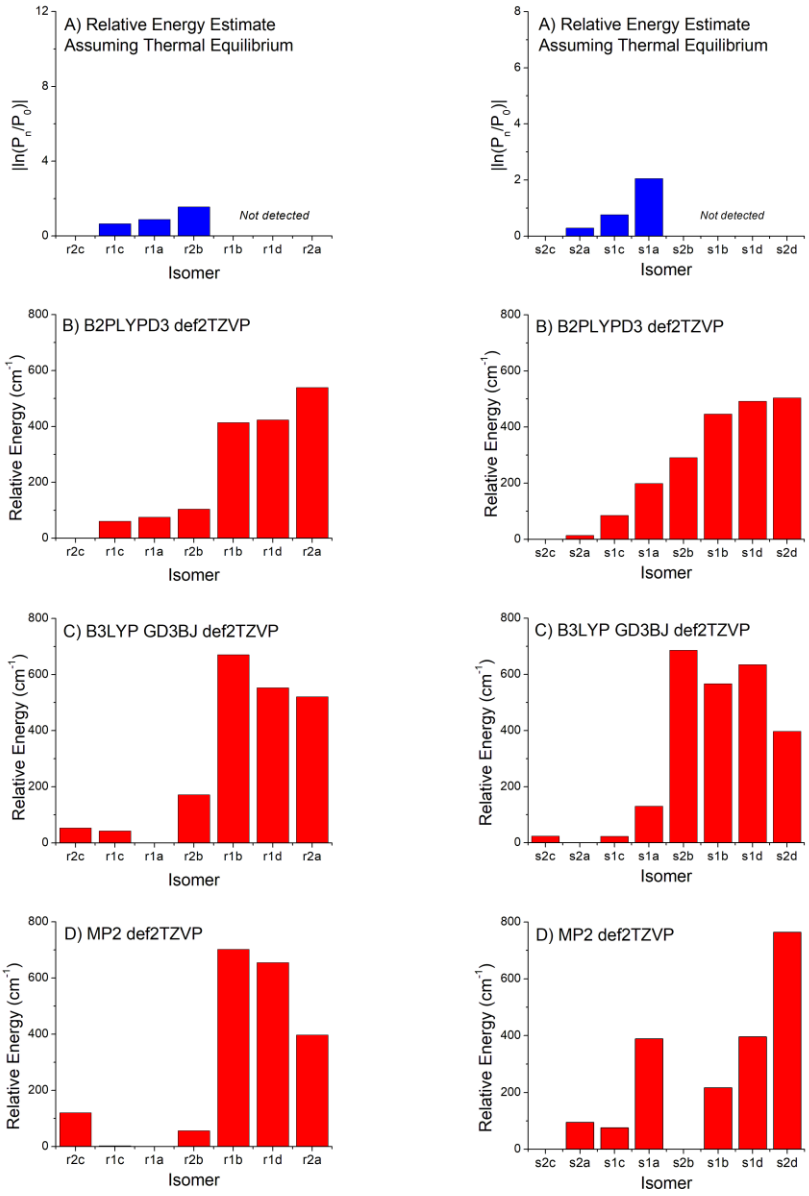

Figure 3.9: Top bar charts show the experimentally determined relative energy estimates for the observed complex for the homochiral (right) and heterochiral (left). Below are the bar charts of the relative energies calculated using B2PLYPD3, B3LYPD3BJ and MP2 methods all using the def2TZVP basis set.

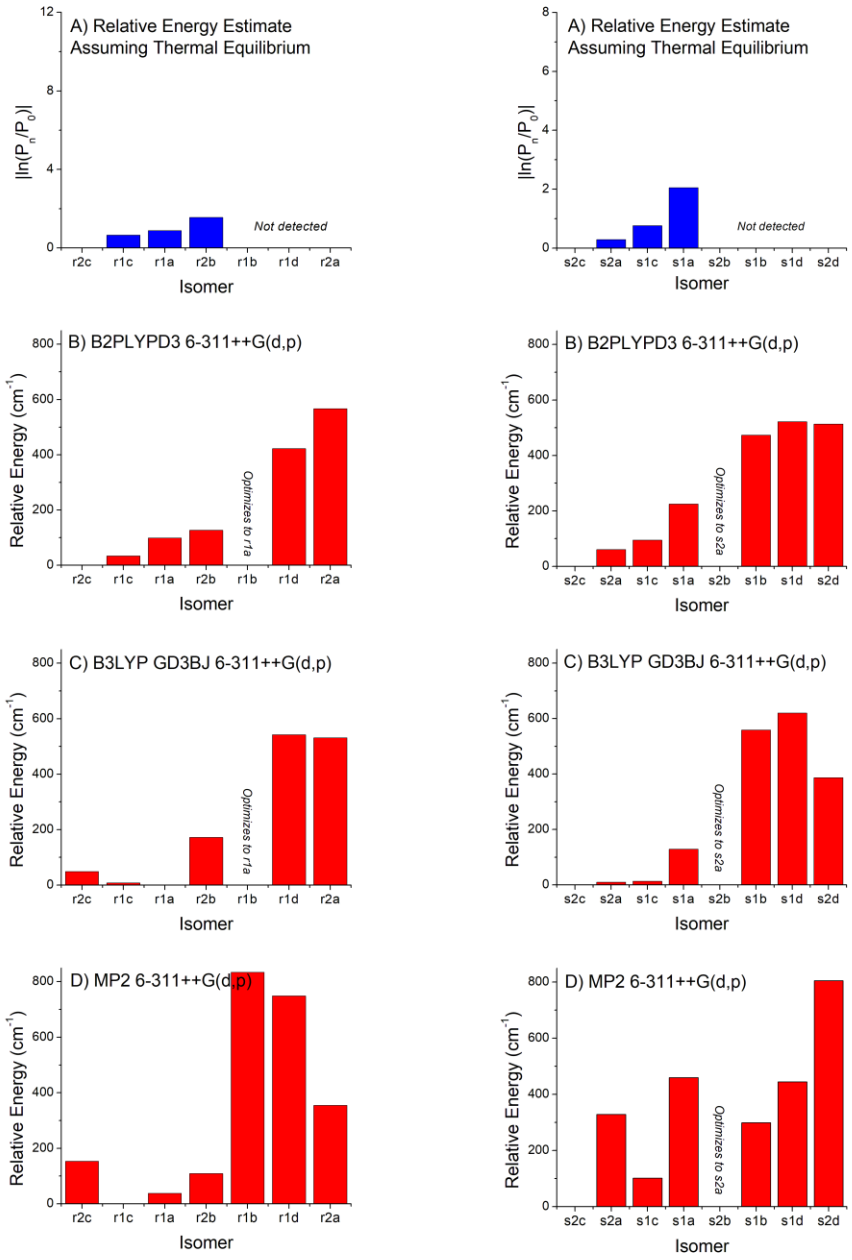

Figure 3.10: Top bar charts show the experimentally determined relative energy estimates for the observed complex for the homochiral (right) and heterochiral (left). Below are the bar charts of the relative energies calculated using B2PLYPD3, B3LYPD3BJ and MP2 methods all using the Pople basis set.

From these relative energies the expected geometries to be observed would be the lower energy isomer structures. For the B2PLYPD3 method, R1a, R1c, R2b, and R2c are calculated to be >300 cm^{-1} lower in energy then all the other isomers. Looking at the experimental relative energies assuming thermal equilibrium the B2PLYPD3 method captures the experimental relative populations observed in these measurements. S1c, S2a and S2c heterochiral structures were calculated to be the lowest energy isomers. S1a was ~200 cm^{-1} higher in energy than S2c, but ~100 cm^{-1} lower in energy than the next isomer, leaving it in a middle ground on whether it would be expected to be observed. Again, when assuming a thermal equilibrium, the experimental relative energies match very well with the predicted relative energies calculated with the B2PLYPD3 method. The def2TZVP basis set also appears to capture the observed experimental populations more accurately than the Pople basis set.

Experimentally and theoretically with the B2PLYPD3 method, the lowest energy isomer for the homochiral structures were R2c and S2c. However, the B3LYPD3BJ method calculated the R1a and S2a as the lowest energy isomers, using the def2TZVP basis set, and R1a and S2c for the Pople basis set. This method did not calculate the relative energies of the isomers accurately when compared to the experimentally observed results. The overall energies were not accurate in this method, but it did allow for the identification of the eight isomers observed. The other seven isomers in the table were ~300 cm^{-1} greater in energy than the highest energy isomers in the diastereomer families.

Finally, with the MP2 calculations, the lowest energy isomer changes around again, except the calculation of the S2c as the lowest energy heterochiral isomer. The homochiral species that was calculated to be the lowest energy isomer R1a and R1c for the def2TZVP and Pople basis sets,

respectively. Again, for the homochiral species the relative energies calculated by MP2 would suggest those that were experimentally observed. However, with the heterochiral isomers the S1b isomer becomes lower in energy then the S1a when using the def2tzvp basis set. With the Pople basis set S1b becomes lower then the S2a and S1a isomers. These results lead to altered expectations of which isomers would be expected to be observed in the chiral tag measurement.

Another issue that pertains to the relative energies is the effect of zero-point vibrational energies and the effect of an issue in quantum chemistry methodology. This issue is known as the basis set superposition error, BSSE, and arises during calculations of intermolecular interactions.[17] The BSSE is caused by the use of basis functions of one monomer by the other monomer to increase the basis functions at its disposal.[18] This is corrected by counterpoise method where all the calculations are redone using the mixed basis set, increasing computational costs. These calculations were all performed using the B3LYPD3BJ method with def2TZVP basis set to understand the effect these may have on relative energies. Figure 3.11 shows the bar graph of relative energies of the equilibrium structures, counterpoise corrected energies, and the zero-point vibration corrected relative energies. The numerical relative energies are tabulated in Table B5 in the appendix. In the counterposie corrected heterochiral graph the S2b structure optimized to the S2a structure. In this test case, all structures are very similar, just altered by the direction of the butynol when forming the hydrogen bond with verbenone. Since these structures are so similar it appears that the calculated relative energies from counterpoise and zero-point vibrational corrections does not alter the relative energies enough to suggest isomers may or may not be observed. This suggests that these effects may be able to be neglected for faster computational time for use in analytical chemistry applications.

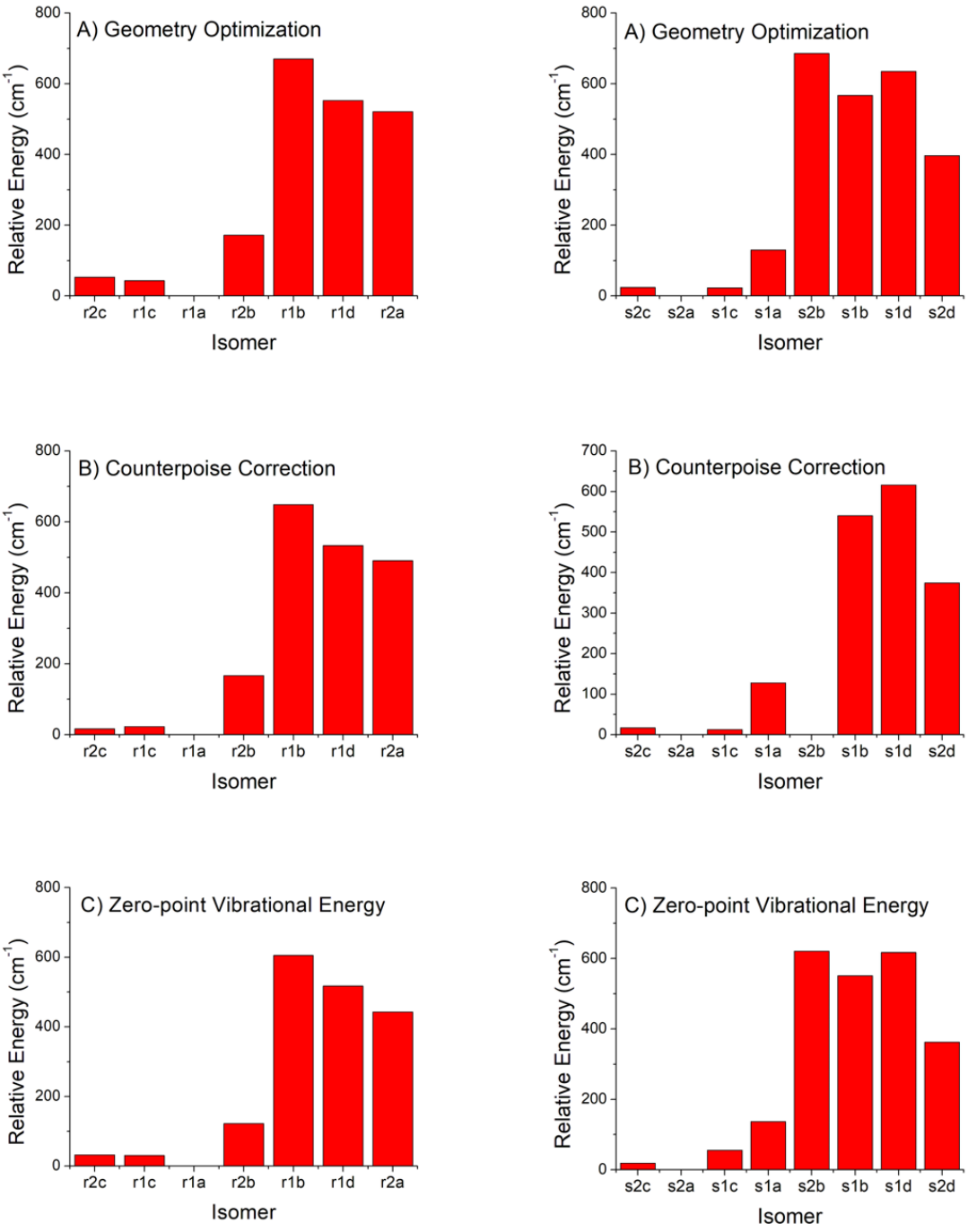

Figure 3.11: Relative energies of the equilibrium geometries (top), counterpoise corrected energies (middle), and zero-point vibrational energies (bottom). The left bar graphs are homochiral structures and the right are heterochiral structures.

Atomic Structures

As discussed in Chapter 1, Kraitchman's analysis is one of the most powerful structure determination tools available to rotational spectroscopy. It can be used to provide the magnitudes of the atomic coordinates in the principal axis system using the rotational constants from the parent isotope species and its isotopologues to gain what is known as the substitution structure, r_s.[19] There are well known faults with Kraitchman's analysis that have to do with the assumption of treating the vibrationally averaged structure of each isotopic substitution as constant.[20] The change in mass of each isotopologue does change the zero-point vibrational wavefunction of the molecule and can impact large molecules with low-frequency vibrational modes. Moreover, an atom too close to one of the principal axes, ≤ 0.1 Å, can result in imaginary coordinates due the fact that it produces a small change in the moment-of-inertia, but the change in vibrational frequency can be large. The method used to treat this problem was to replace the imaginary coordinates with zero. Atomic coordinates for each of the five structures calculated *via* Kraitchman's analysis are presented at the end of this chapter in Tables B6-B10 of appendix B. Since the measurement only had enough sensitivity to observe the ^{13}C spectra for 5 of the eight structures at natural abundance, S2c, S2a, R1a, R1c, and R2c are used for this analysis.

From these five structures, the difference in the a, b, and c atomic coordinates are plotted against the magnitude of the theory coordinate with a histogram showing the distribution of errors to the right for all three methods. Figures 3.12 and 3.13. In every method the errors were large for coordinates that were close to a principal axis, due to the zero-point vibrational motion mentioned above. For both basis sets, B2PLYPD3 method again is the most accurate as shown by the narrow width of errors around zero in the histogram. The B3LYPD3BJ method is less accurate, but most

of the coordinates are still within 0.04 Å to the experimentally determined coordinate. Computational time and memory requirements are substantially reduced compared to the higher level B2PLYPD3 for only a slightly less accurate atomic coordinate. MP2 proved to have the largest errors in atomic coordinates, while having a similar computational cost as B2PLYPD3. The def2tzvp basis set also produces less error on atomic coordinates then the Pople for all three methods, and significantly more with MP2. The MP2 calculations are in better agreement with the experimental geometries for the S1c, R1c, S2c and R2c structures based on rotational constants then for the R1a, S1a, R2b, and S2a structures. The 1c and 2c complexes all have the triple bond of butynol pointing towards the bicyclic structure of verbenone, while the other complexes have the alkyne group of butynol pointing towards the double bond in verbenone. In the latter structures, the butynol is closer towards the verbenone, which is most likely due to the overestimation of the dispersion forces for π-electron interactions as previously reported with MP2.[21-23]

Another way to compare the atomic coordinates calculated from the theoretical structures and the substitution coordinates was to compare the difference in distance from the center of mass (experimental – theory) against the distance away from the center of mass of the theoretically calculated coordinates, Figures 3.14 and 3.15. Again, the effects of zero-point vibrational motion on the atoms close to center of mass cause the experimentally calculated coordinate to be less than the theoretically predicted coordinate for each method. The atoms further away we can see a systematic compression, where the theory calculates the atoms to be closer to the center of mass. The error from the compression is lower with the B2PLYPD3 method, followed by the B3LYPD3BJ, and then the MP2. The error from the atom position of the S2a and R1a geometries is very apparent in the Pople basis set.

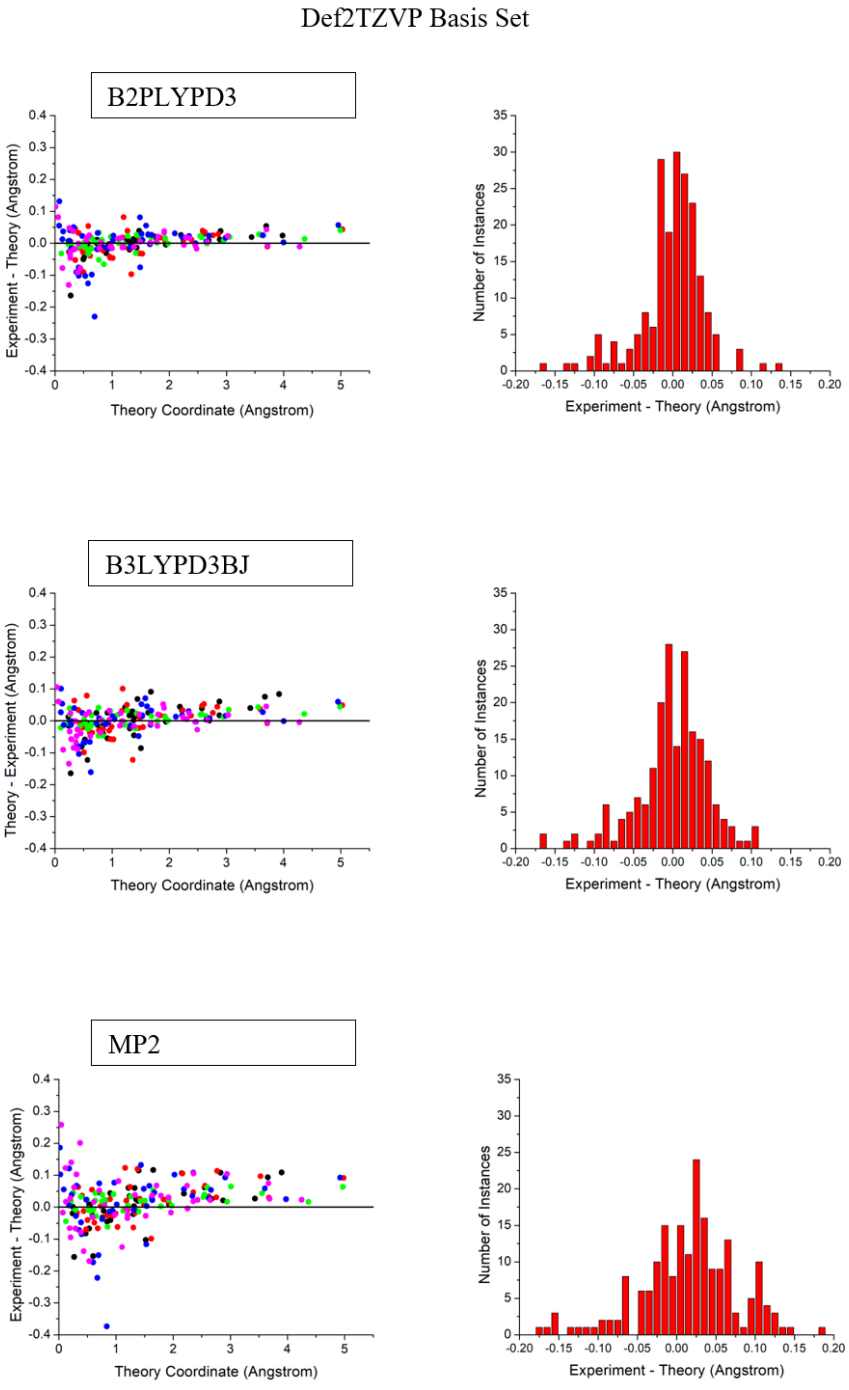

Figure 3.12: Difference in magnitudes of the a, b, and c coordinates for the B2PLYPD3 (top), B3LYPD3BJ (middle), and MP2 (bottom) vs the magnitude of the theory coordinate. The differences are arranged in a histogram to the right of each plot. The black dots are errors from R1a, the red dots from S2a, the blue dots from R1c, the green dots from S2c, and the magenta dots from R2c.

Pople Basis Set

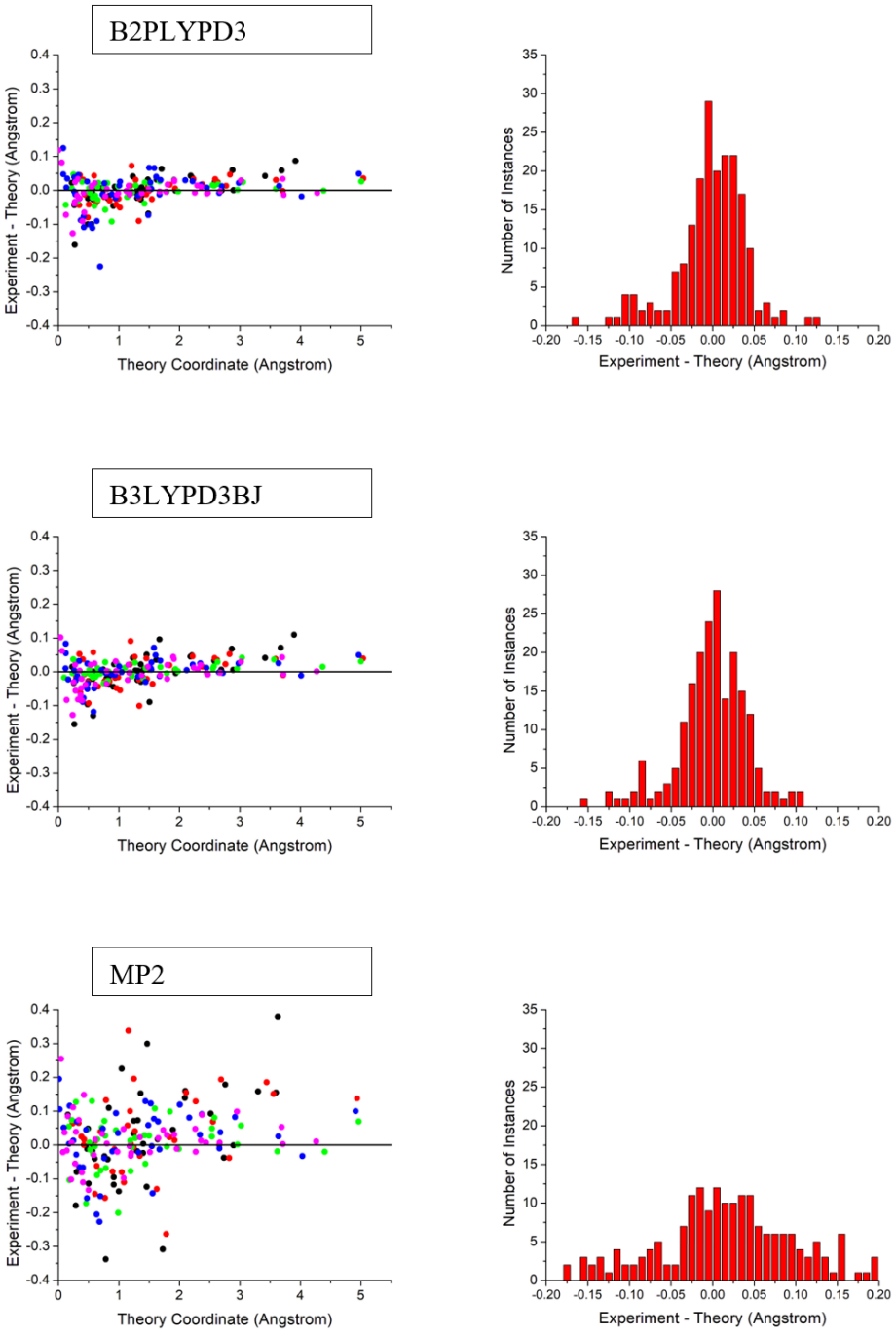

Figure 3.13: Difference in magnitudes of the a, b, and c coordinates for the B2PLYPD3 (top), B3LYPD3BJ (middle), and MP2 (bottom) vs the magnitude of the theory coordinate. The differences are arranged in a histogram to the right of each plot. The black dots are errors from R1a, the red dots from S2a, the blue dots from R1c, the green dots from S2c, and the magenta dots from R2c.

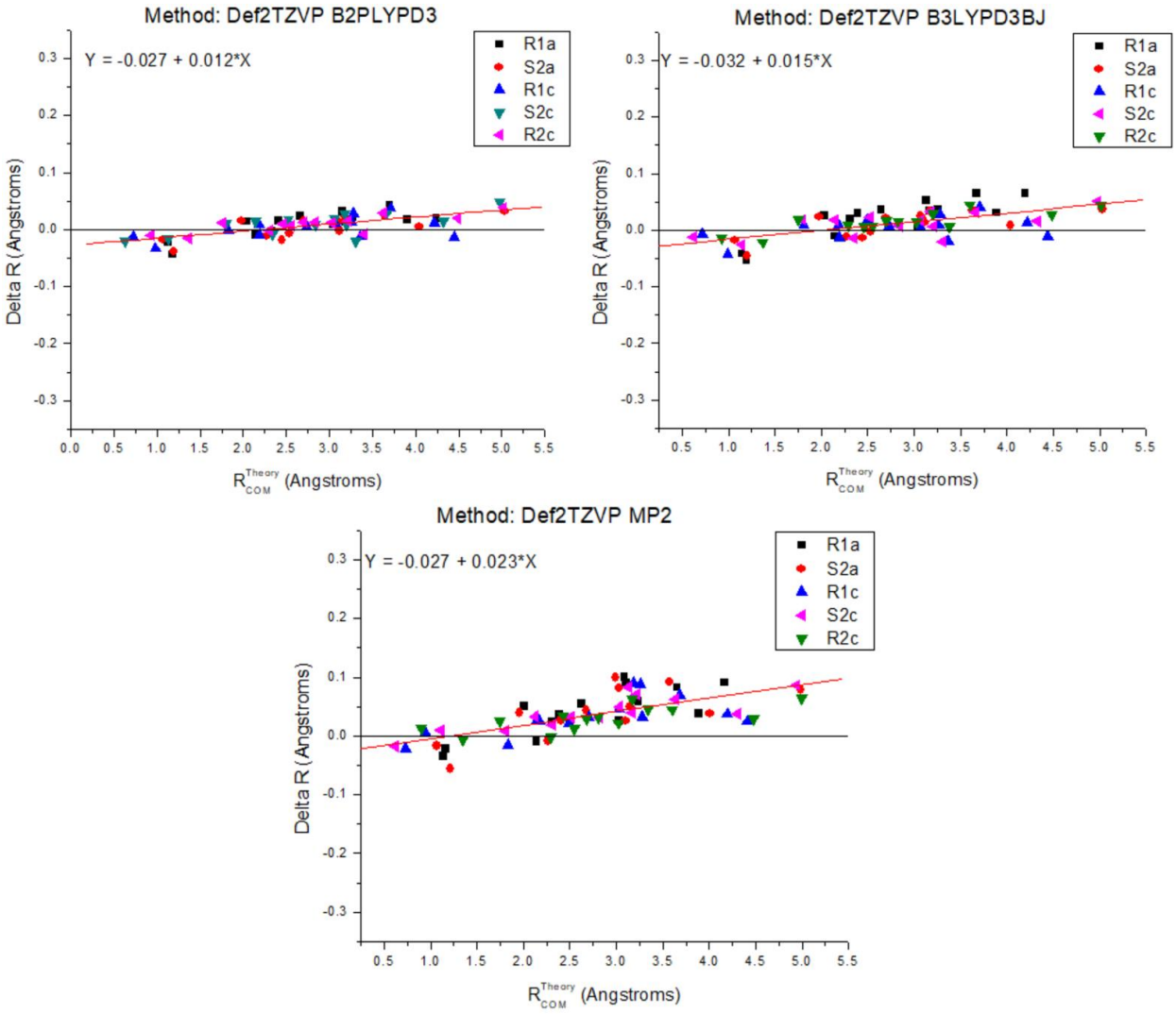

Figure 3.14: A plot of the difference in experimental carbon atom distance and theoretical carbon atom distance from the center of mass against the distance from the center of mass of the theoretical coordinate. These plots are all for theoretical methods using the def2TZVP basis set. A linear line is fit through all data points, and the fit constants are stated on the graph.

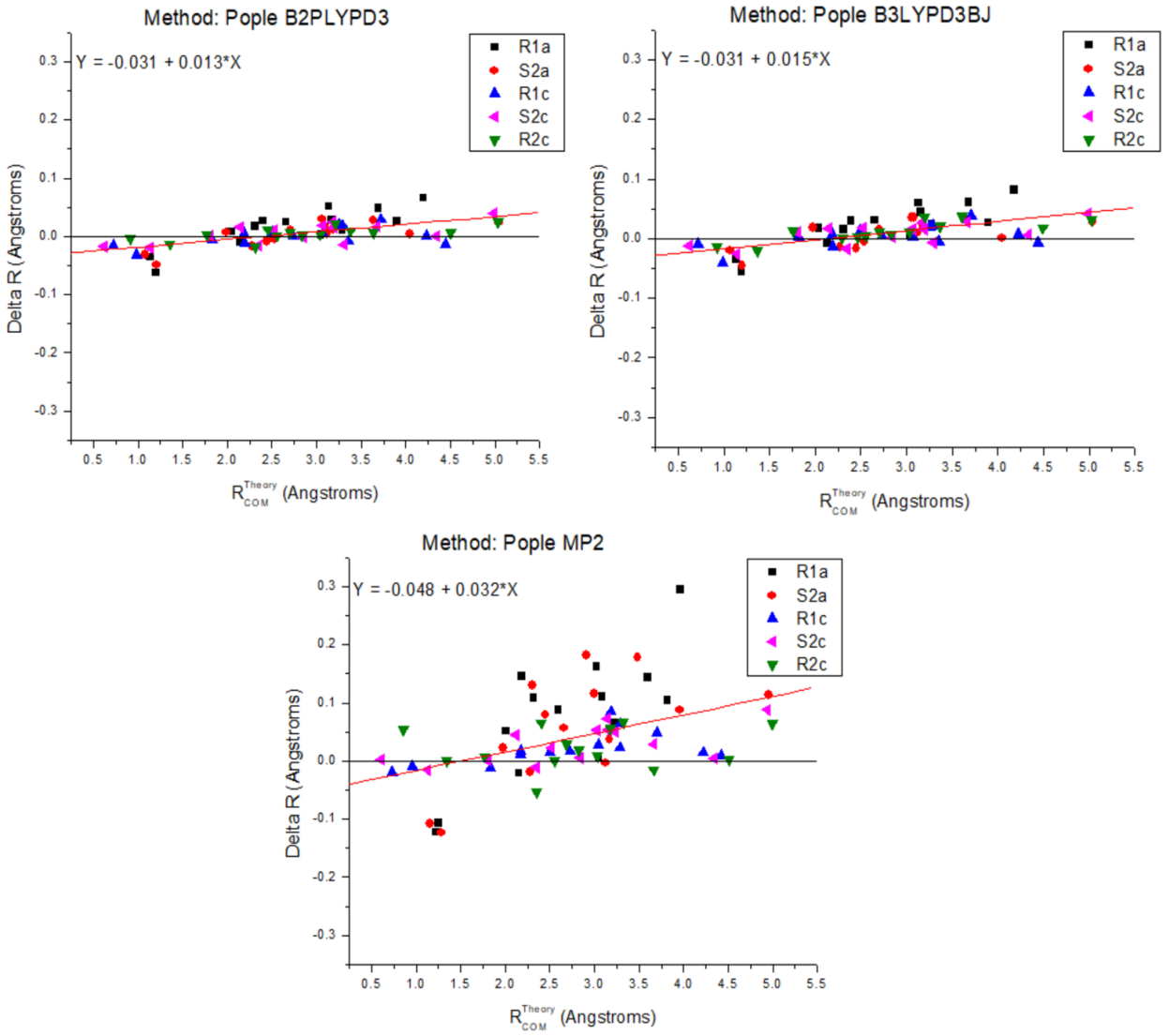

Figure 3.15: A plot of the difference in experimental carbon atom distance and theoretical carbon atom distance from the center of mass against the distance from the center of mass of the theoretical coordinate. These plots are all for theoretical methods using the Pople 6311G++(d,p) basis set. A linear line is fit through all data points, and the fit constants are stated on the graph.

2) Spectroscopic Parameters from Equilibrium Geometries

Rotational Constants

In appendix A of Chapter 1, the final fits with centrifugal distortion constants and theoretical calculated structures using B3LYPD3BJ with def2TZVP basis set were shown in Tables A10-A13. The fit A, B, and C rotational constants are again presented in Tables B11-B14 for each of the observed heterochiral and homochiral species along with the theoretically calculated rotational constants for every method and basis set combination with their corresponding percent errors. Table 3.1 and Table 3.2 show a summary of those table with the average percent error and standard deviation for the three methods and the two basis sets. The mean percent errors are lower for the B2PLYPD3 and B3LYPD3BJ when using the Pople basis set, but the standard deviations for the rotational constants are higher. Errors with the MP2 as discussed previously were reduced with the use of the def2TZVP basis set.

Table 3.1: Mean percent error and standard deviation for each rotational constant using the three different methods and the def2TZVP basis set.

def2TZVP		
B2PLYPD3		
Rotational Constant	Mean Percent Error (%)	Standard Deviation
A	-0.425	0.234
B	-1.42	0.315
C	-1.45	0.283
B3LYP GD3BJ		
Rotational Constant	Mean Percent Error (%)	Standard Deviation
A	-0.246	0.426
B	-1.90	0.694
C	-1.80	0.626
MP2		
Rotational Constant	Mean Percent Error (%)	Standard Deviation
A	-0.941	0.199
B	-3.61	0.831
C	-3.39	0.678

Table 3.2: Mean percent error and standard deviation for each rotational constant using the three different methods and the Pople basis set.

6-311++G(d,p) Pople basis set		
B2PLYPD3		
Rotational Constant	Mean Percent Error (%)	Standard Deviation
A	0.129	0.269
B	-1.28	0.529
C	-1.26	0.364
B3LYP GD3BJ		
Rotational Constant	Mean Percent Error (%)	Standard Deviation
A	0.0537	0.482
B	-1.70	0.763
C	-1.47	0.717
MP2		
Rotational Constant	Mean Percent Error (%)	Standard Deviation
A	0.491	1.24
B	-3.89	2.59
C	-3.47	1.76

Electric Dipole Moment

The accuracy of the calculated relative electric dipole moment components was analyzed for each experimentally observed structure. In the absence of a Stark effect measurement, the individual magnitudes of the electric dipole moments could not be measured experimentally, but the relative strengths can be estimated. This analysis was done by simulating the rotational spectra of each complex three times using Pickett's SPCAT program with 1 Debye dipole moments for each μ_a, μ_b, and μ_c. The .cat output are then processed through a program that compares frequency of transitions vs frequency in a corresponding spectrum. Intensities from the spectrum and the transition strengths from the .cat file are then used to find a scaling factor. The top 25 scale factors, if there are that many transitions, are then used to calculate a mean and standard deviation, Tables B15 and B16. A ratio of the dipole moments was calculated by dividing the dipole moment component scale factor by the largest scale factor. The results show

that the calculated relative squares of the dipole moments components are closer to equal for every method and basis set combination. Large standard deviations come from variations in the electric field of the excitation pulse, which is not normalized out in this calculation. They are all in good agreement with experimental results for measured relative strengths, with not one outperforming against any other. Thus, electric dipole moment considerations favor a faster choice of method and basis set to use for chiral tagging measurements in the case of verbenone-butynol complex. Figure 3.16, show a graphical comparison of the relative dipole strengths calculated with B3LYPD3BJ with def2TZVP basis to the experimentally determined relative strengths.

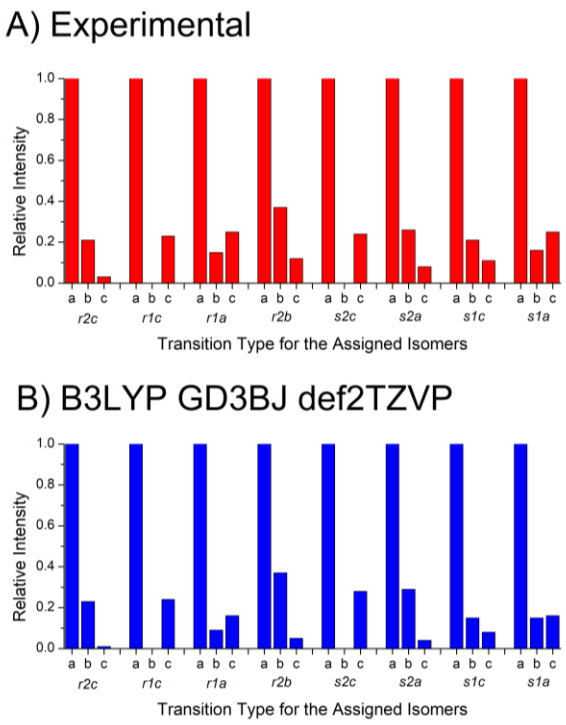

Figure 3.16: The experimentally calculated relative electric dipole strengths referenced to the strongest electric dipole component for each isomer (top). The relative squares of the dipole moment components for each isomer calculated from the B3LYPD3BJ with the def2TZVP basis set (bottom).

IV. Discussion

Each method used in the work is accessed on its ability to provide accurate information on the chiral tag complexes for the purpose of identifying absolute configuration. For five of these structures the absolute configuration is verified with ^{13}C atom position, allowing for the accuracy of the theory to be assessed. A key consideration of this analysis is the feasibility of implementation into an analytical technique where computational results will be needed on a short time scale. The B2PLYPD3 proved to be the most accurate across the board, except for the relative strengths of the squares of the electric dipole where every method performed well. Most notably, the calculated relative energies of the isomers accurately reflected experimental observations, assuming a thermal equilibrium. The B3PLYPD3BJ method did not predicted the most abundant isomers with the def2TZVP basis set, and only predicted the heterochiral most abundant isomer with the Pople basis set. However, the energies of the four isomers experimentally observed for both homochiral and heterochiral complexes were predicted to be observed by the method and would allow for the assignment of the spectra. MP2 was able to predict the lowest energy heterochiral, but unable to predict the homochiral lowest energy structure. Moreover, MP2 calculated the S1b structure, which was not observed for the heterochiral complexes, to be lower in energy than two of the observed isomers. B2PLYPD3 had similar computation costs as MP2 and required substantially more time and memory than the B3LYPD3BJ method. The preferred choice would be B3LYPD3BJ method as it would allow for the identification of the all the observed isomer in a fraction of the time (30 min run times compared to a day or more using 16 cores). If studies require accurate energies, then the B2PLYPD3 method should be used.

Similarly, the comparison of the calculated atomic structures with Kraitchman substitution

coordinates showed that the B2PLYPD3 method was the most accurate at calculating the coordinates. The zero-point vibrational motion for atoms close to a principal axis produce the largest errors in coordinates seen in every method. B3LYPD3BJ proved to be less accurate then the B2PLYPD3, but more accurate then the MP2. A majority of the errors in the atomic coordinates were between 0.05 and -0.05 Å for B2PLYPD3 and B3LYPD3BJ methods. Again, the B3LYPD3BJ has the accuracy and speed that would favor its use in an analytical setting. The accuracy of atomic coordinates helps lead to the accuracy of the spectroscopic parameters used in rotational spectroscopy. Rotational constants are calculated using the moments-of-inertia and we find a similar accuracy for the methods. The strengths of the relative squares of the electric dipole moment components were very similar across every method. This is probably due to the fact that the major component of the electric dipole moment comes from the hydrogen bond between the carbonyl oxygen and hydroxyl groups. Every structure had very similar position of these groups, but changes in the dihedral, shown in Figure 3.7, caused the difference in structural accuracy between methods. This allows the electric dipole information to be used as an additional way of gaining confidence in assigning the absolute configuration.

Finally, the difference in accuracy of the two basis sets used in this work will be considered. In terms of computational cost, the Pople basis set is less computationally expensive, but not to the same magnitude as the choice of method. Relative energies calculated with the def2TZVP method were more accurate in the B2PLYPD3 method than with the Pople. Similarly, the atomic coordinates for every method gave a narrower histogram of errors for every method. None more apparent than with the MP2 method, where the large errors produced with the Pople basis set were reduced with the def2TZVP basis set. The rotational constant accuracy slightly favored the Pople,

but the basis set did produce a larger standard deviation. Overall, the improved accuracy from the def2TZVP basis set at the cost of a little more time is suggested.

This benchmarking of the verbenone-butynol complexes was a way to assess the accuracy of the different levels of theory used for use in an analytical method. This work is limited though, as the system studied was rigid and had an obvious attachment site for the butynol. With verbenone there were eight attachments sites to screen with the buytnol positioned around the carbonyl oxygen. In the absence of a clear hydrogen bond site, the performance of the quantum chemical method for chiral tag technique is not understood. A more rigorous isomer search would need to be carried out. The accuracy of the quantum chemistry to calculate the non-covalent interactions that create these complexes needs to be studied carefully. Moreover, in this work the sensitivity was able to be increased a lot by the 2 million average spectra collected with both enantiopure butynol tags. This allowed for observation of ^{13}C species of the complexes for verification of absolute configuration determination. In many cases in an analytical setting this will not be available due to sample limits. Therefore, the importance of the accurate quantum chemical calculations is paramount for chiral tag rotational spectroscopy. Molecular size limits in rotational spectroscopy can also limit this technique. Molecules must be thermally stable and measured in the gas phase. Large molecules also have reduced sensitivity due to the large number of rotational states that may be occupied and take a further hit in sensitivity from the need for complex formation.

V. Conclusion

Chiral tag rotational spectroscopy relies on the ability of quantum chemical computational

methods to provide accurate information of the relative energies, structure, and spectroscopic parameters. The benchmarking of the verbenone-butynol chiral tag complexes allows us to access the ability of the dispersion corrected DFT, higher level DFT and MP2 methods to identify the diastereomer complexes for absolute configuration assignment. Absolute configuration determination with chiral tag rotational spectroscopy requires the identification of the lowest energy isomers, accurate rotational constants, and accurate electric dipole information. Moreover, the accuracy in the structures is enough to differentiate between the structures. The B2PLYPD3 and B3LYPD3BJ methods were able to identify the lowest energy isomers and contained a < 2% average error in the rotational constants. Electric dipole information was very accurate across all methods and basis sets and could allow for additional confidence in assigning absolute configuration. The speed and accuracy of the B3LYPD3BJ would make it the preferred method to use in an analytical method. Overall, the def2TZVP proved more accurate then the Pople basis set with little additional computational costs.

VI. References

1. Jurečka, P.; Černý, J.; Hobza, P.; Salahub, D. R., Density functional theory augmented with an empirical dispersion term. Interaction energies and geometries of 80 noncovalent complexes compared with ab initio quantum mechanics calculations. *Journal of Computational Chemistry* **2007,** *28* (2), 555-569.

2. Grimme, S.; Antony, J.; Ehrlich, S.; Krieg, H., A consistent and accurate ab initio parametrization of density functional dispersion correction (DFT-D) for the 94 elements H-Pu. *The Journal of Chemical Physics* **2010,** *132* (15), 154104.

3. Schröder, H.; Creon, A.; Schwabe, T., Reformulation of the D3(Becke–Johnson) Dispersion Correction without Resorting to Higher than C6 Dispersion Coefficients. *Journal of Chemical Theory and Computation* **2015,** *11* (7), 3163-3170.

4. Grimme, S., Accurate description of van der Waals complexes by density functional theory including empirical corrections. *Journal of computational chemistry* **2004,** *25* (12), 1463-1473.

5. Grimme, S.; Ehrlich, S.; Goerigk, L., Effect of the damping function in dispersion corrected density functional theory. *Journal of computational chemistry* **2011,** *32* (7), 1456-1465.

6. Spada, L.; Tasinato, N.; Vazart, F.; Barone, V.; Caminati, W.; Puzzarini, C., Noncovalent Interactions and Internal Dynamics in Pyridine–Ammonia: A Combined Quantum-Chemical and Microwave Spectroscopy Study. *Chemistry – A European Journal* **2017,** *23* (20), 4876-4883.

7. Puzzarini, C., Rotational spectroscopy meets theory. *Physical Chemistry Chemical Physics* **2013,** *15* (18), 6595-6607.

8. Heim, Z. N.; Amberger, B. K.; Esselman, B. J.; Stanton, J. F.; Woods, R. C.; McMahon, R. J., Molecular structure determination: Equilibrium structure of pyrimidine (m-C4H4N2) from rotational spectroscopy (reSE) and high-level ab initio calculation (re) agree within the uncertainty of experimental measurement. *The Journal of Chemical Physics* **2020,** *152* (10), 104303.

9. Kuş, N.; Sharma, A.; Peña, I.; Bermúdez, M. C.; Cabezas, C.; Alonso, J. L.; Fausto, R., Conformers of β-aminoisobutyric acid probed by jet-cooled microwave and matrix isolation infrared spectroscopic techniques. *The Journal of Chemical Physics* **2013,** *138* (14), 144305.

10. Ruoff, R. S.; Klots, T. D.; Emilsson, T.; Gutowsky, H. S., Relaxation of conformers and isomers in seeded supersonic jets of inert gases. *The Journal of Chemical Physics* **1990,** *93* (5), 3142-3150.

11. Pérez, C.; Lobsiger, S.; Seifert, N. A.; Zaleski, D. P.; Temelso, B.; Shields, G. C.; Kisiel, Z.; Pate, B. H., Broadband Fourier transform rotational spectroscopy for structure determination: The water heptamer. *Chemical Physics Letters* **2013,** *571*, 1-15.

12. Pickett, H. M., The fitting and prediction of vibration-rotation spectra with spin interactions. *Journal of Molecular Spectroscopy* **1991,** *148* (2), 371-377.

13. Kisiel, Z. PROSPE, programs for rotational spectroscopy. http://info.ifpan.edu.pl/~kisiel/prospe.htm.

14. Plusquellic, D. F., User Guide to JB95. exe Spectral Fitting Program v1. 02.4, 1/30/01 http://physics. nist. gov/SpectralFitGUI. **2016**.

15. M. J. Frisch, G. W. T., H. B. Schlegel, G. E. Scuseria, M. A. Robb, J. R. Cheeseman, G. Scalmani, V. Barone, G. A. Petersson, H. Nakatsuji, X. Li, M. Caricato, A. Marenich, J. Bloino, B. G. Janesko, R. Gomperts, B. Mennucci, H. P. Hratchian, J. V. Ortiz, A. F. Izmaylov, J. L. Sonnenberg, D. Williams-Young, F. Ding, F. Lipparini, F. Egidi, J. Goings, B. Peng, A. Petrone, T. Henderson, D. Ranasinghe, V. G. Zakrzewski, J. Gao, N. Rega, G. Zheng, W. Liang, M. Hada, M. Ehara, K. Toyota, R. Fukuda, J. Hasegawa, M. Ishida, T. Nakajima, Y. Honda, O. Kitao, H. Nakai, T. Vreven, K. Throssell, J. A. Montgomery, Jr., J. E. Peralta, F. Ogliaro, M.

Bearpark, J. J. Heyd, E. Brothers, K. N. Kudin, V. N. Staroverov, T. Keith, R. Kobayashi, J. Normand, K. Raghavachari, A. Rendell, J. C. Burant, S. S. Iyengar, J. Tomasi, M. Cossi, J. M. Millam, M. Klene, C. Adamo, R. Cammi, J. W. Ochterski, R. L. Martin, K. Morokuma, O. Farkas, J. B. Foresman, and D. J. Fox *Gaussian 09, Revision A.02*, Gaussian, Inc.: Wallingford, CT, 2016.

16. Frisch, M. J.; Trucks, G. W.; Schlegel, H. B.; Scuseria, G. E.; Robb, M. A.; Cheeseman, J. R.; Scalmani, G.; Barone, V.; Petersson, G. A.; Nakatsuji, H.; Li, X.; Caricato, M.; Marenich, A. V.; Bloino, J.; Janesko, B. G.; Gomperts, R.; Mennucci, B.; Hratchian, H. P.; Ortiz, J. V.; Izmaylov, A. F.; Sonnenberg, J. L.; Williams; Ding, F.; Lipparini, F.; Egidi, F.; Goings, J.; Peng, B.; Petrone, A.; Henderson, T.; Ranasinghe, D.; Zakrzewski, V. G.; Gao, J.; Rega, N.; Zheng, G.; Liang, W.; Hada, M.; Ehara, M.; Toyota, K.; Fukuda, R.; Hasegawa, J.; Ishida, M.; Nakajima, T.; Honda, Y.; Kitao, O.; Nakai, H.; Vreven, T.; Throssell, K.; Montgomery Jr., J. A.; Peralta, J. E.; Ogliaro, F.; Bearpark, M. J.; Heyd, J. J.; Brothers, E. N.; Kudin, K. N.; Staroverov, V. N.; Keith, T. A.; Kobayashi, R.; Normand, J.; Raghavachari, K.; Rendell, A. P.; Burant, J. C.; Iyengar, S. S.; Tomasi, J.; Cossi, M.; Millam, J. M.; Klene, M.; Adamo, C.; Cammi, R.; Ochterski, J. W.; Martin, R. L.; Morokuma, K.; Farkas, O.; Foresman, J. B.; Fox, D. J. *Gaussian 16 Rev. C.01*, Wallingford, CT, 2016.

17. Brauer, B.; Kesharwani, M. K.; Martin, J. M. L., Some Observations on Counterpoise Corrections for Explicitly Correlated Calculations on Noncovalent Interactions. *Journal of Chemical Theory and Computation* **2014,** *10* (9), 3791-3799.

18. Richard, R. M.; Bakr, B. W.; Sherrill, C. D., Understanding the Many-Body Basis Set Superposition Error: Beyond Boys and Bernardi. *Journal of Chemical Theory and Computation* **2018,** *14* (5), 2386-2400.

19. Kraitchman, J., Determination of Molecular Structure from Microwave Spectroscopic Data. *American Journal of Physics* **1953,** *21* (1), 17-24.

20. Costain, C. C., Determination of Molecular Structures from Ground State Rotational Constants. *The Journal of Chemical Physics* **1958,** *29* (4), 864-874.

21. Riley, K. E.; Hobza, P., Assessment of the MP2 Method, along with Several Basis Sets, for the Computation of Interaction Energies of Biologically Relevant Hydrogen Bonded and Dispersion Bound Complexes. *The Journal of Physical Chemistry A* **2007,** *111* (33), 8257-8263.

22. Tkatchenko, A.; Jr., R. A. D.; Head-Gordon, M.; Scheffler, M., Dispersion-corrected Møller–Plesset second-order perturbation theory. *The Journal of Chemical Physics* **2009,** *131* (9), 094106.

23. Lochan, R. C.; Head-Gordon, M., Computational studies of molecular hydrogen binding affinities: The role of dispersion forces, electrostatics, and orbital interactions. *Physical Chemistry Chemical Physics* **2006,** *8* (12), 1357-1370.

VII. Appendix B

Table: B1: Mean scale factors, standard deviation of the mean scale factor, and percent composition for each heterochiral isomers in three experimental spectra using 25 transitions.

"S" Isomers in R-butynol		
Isomer	Mean Scale	Percent Composition
s1a	0.737	5.60%
s1c	2.59	19.50%
s2a	4.23	31.90%
s2c	5.70	43.00%

"S" Isomers in S-butynol		
Isomer	Mean Scale	Percent Composition
s1a	0.221	5.70%
s1c	0.762	19.50%
s2a	1.24	31.80%
s2c	1.68	43.10%

"S" Isomers in RS-butynol		
Isomer	Mean Scale	Percent Composition
s1a	0.313	5.40%
s1c	1.15	20.00%
s2a	1.84	31.90%
s2c	2.46	42.70%

Table B2: Mean scale factors, standard deviation of the mean scale factor, and percent composition for each homochiral isomers in three experimental spectra using 25 transitions.

"R" Isomers in R-butynol		
Isomer	Mean Scale	Percent Composition
R1a	0.845	20.51%
R1c	1.03	25.03%
R2b	0.33	8.06%
R2c	1.91	46.39%

"R" Isomers in S-butynol		
Isomer	Mean Scale	Percent Composition
R1a	2.308	20.39%
R1c	2.729	24.11%
R2b	0.88	7.80%
R2c	5.40	47.69%

"R" Isomers in RS-butynol		
Isomer	Mean Scale	Percent Composition
R1a	1.090	19.83%
R1c	1.34	24.36%
R2b	0.40	7.30%
R2c	2.67	48.51%

Table B3: Relative energies of the eight heterochiral complexes, using different computational methods and basis sets. All energies are relative to lowest energy isomer calculated and rounded to the nearest whole number.

	Relative Energies (cm^{-1})			
Method*,‡	S1a	S1b	S1c	S1d
def2 B2PLYPD3	199	446	85	492
def2 B3LYP	102	102	110	110
def2 B3LYPD3BJ	130	567	23	635
def2 MP2	389	217	76	396
Pople B2PLYPD3	225	473	95	522
Pople B3LYP	110	110	102	107
Pople B3LYPD3BJ	129	559	13	620
Pople MP2	460	299	102	445

	S2a	S2b	S2c	S2d
def2 B2PLYPD3	14	291	0	504
def2 B3LYP	2	115	0	0
def2 B3LYPD3BJ	0	686	24	397
def2 MP2	95	-	0	764
Pople B2PLYPD3	61	-	0	513
Pople B3LYP	11	-	0	2
Pople B3LYPD3BJ	10	-	0	387
Pople MP2	329	-	0	805

-Structures with dashes optimized to another structures position. S2b optimized to S2a in this table.
**def2 stands for the def2TZVP basis set and Pople is the 6311G++(d,p) basis set.*
‡*Relative energies that are equal mean the structures optimized to the same structure.*

Table B4: Relative energies of the eight homochiral complexes, using different computational methods and basis sets. All energies are relative to lowest energy isomer calculated and rounded to the nearest whole number.

	Relative Energies (cm^{-1})			
Method*,‡	R1a	R1b	R1c	R1d
def2 B2PLYPD3	75	414	61	423
def2 B3LYP	117	106	104	100
def2 B3LYPD3BJ	0	670	43	553
def2 MP2	54	637	151	692
Pople B2PLYPD3	99	-	34	422
Pople B3LYP	92	-	87	83
Pople B3LYPD3BJ	0	-	8	542
Pople MP2	119	749	182	759

	R2a	R2b	R2c	R2d
def2 B2PLYPD3	539	104	0	-
def2 B3LYP	0	3	4	-
def2 B3LYPD3BJ	521	172	53	-
def2 MP2	0	-	5	355
Pople B2PLYPD3	567	127	0	-
Pople B3LYP	10	0	7	-
Pople B3LYPD3BJ	531	172	49	-
Pople MP2	82	-	0	274

-Structures with dashes optimized to another structures position.R1b optimized to R1a for the Pople basis sets except with the MP2 method. R2b optimized to the R2a structure using the MP2 method. R2d optimized to R2c in this table for all methods except MP2.

**def2 stands for the def2TZVP basis set and Pople is the 6311G++(d,p) basis set.*

‡*Relative energies that are equal mean the structures optimized to the same structure.*

Table B5: Calculated relative energies using B3LYPD3BJ with def2TZVP basis set for the equilibrium structure, the counterpoise corrected equilibrium structure, and the zero-point vibrational correction.

Homochiral Complex

	Equilibrium Energy	Counter Poise Energy	Zero-Point Energy
R1a	0	0	0
R1b	670.04	648.28	605.08
R1c	43.11	22.76	30.73
R1d	553.10	533.26	517.29
R2a	521.43	490.39	442.89
R2b	171.52	166.96	122.24
R2c	52.96	16.66	32.48

Heterochiral Complex

	Equilibrium Energy	Counter Poise Energy	Zero-Point Energy
S1a	129.90	128.09	136.51
S1b	566.74	540.13	550.87
S1c	22.76	12.68	55.75
S1d	635.20	616.02	617.15
S2a	0	0	0
S2b	685.81	0*	621.10
S2c	24.36	16.94	19.09
S2d	397.23	374.24	362.34

Table B6: Atomic coordinates in the principal axis system calculated using Kraitchman's equations for the complex R1a.

Carbon	a(Å)	Error(Å)	b(Å)	Error(Å)	c(Å)	Error(Å)
C1	2.231	0.014	0.547	0.056	0.773	0.040
C2	2.612	0.010	0.559	0.049	0.245	0.112
C3	1.657	0.016	1.283	0.021	0.386	0.072
C4	2.699	0.011	0.538	0.053	1.319	0.022
C5	1.385	0.020	1.406	0.019	0.572	0.049
C6	1.272	0.027	0.221	0.150	1.937	0.018
C7	3.459	0.007	1.277	0.020	1.337	0.020
C8	0.110	0.265	0.727	0.040	0.821	0.036
C9	0.0675*i	0.430	0.748	0.039	0.863	0.034
C10	1.511	0.016	2.895	0.008	0.463	0.058
C11	3.750	0.007	0.212*i	0.121	0.183*i	0.140
C12	4.007	0.007	1.377	0.021	0.445	0.068
C13	2.937	0.009	0.799	0.032	0.943	0.027
C14	2.257	0.014	1.417	0.021	1.768	0.018

Table B7: Atomic coordinates in the principal axis system calculated using Kraitchman's equations for the complex S2a.

Carbon	a(Å)	Error(Å)	b(Å)	Error(Å)	c(Å)	Error(Å)
C1	2.398	0.019	0.10878*i	0.423	0.817	0.057
C2	2.624	0.005	0.573	0.022	0.407	0.031
C3	1.856	0.023	1.314	0.033	0.256*i	0.176
C4	2.787	0.018	0.736	0.068	1.202	0.043
C5	1.307	0.037	1.202	0.040	0.915	0.054
C6	1.443	0.040	0.301	0.179	1.934	0.030
C7	3.708	0.016	0.635	0.088	1.496	0.039
C8	0.442	0.105	0.965	0.048	0.460	0.103
C9	0.0832*i	0.633	0.400	0.129	0.972	0.054
C10	1.284	0.038	2.659	0.018	1.239	0.045
C11	3.627	0.015	0.421	0.130	0.278	0.197
C12	5.076	0.009	0.260*i	0.182	0.231*i	0.204
C13	2.884	0.016	0.615	0.072	0.920	0.050
C14	2.267	0.021	1.520	0.030	1.496	0.033

Table B8: Atomic coordinates in the principal axis system calculated using Kraitchman's equations for the complex R1c.

Carbon	a(Å)	Error(Å)	b(Å)	Error(Å)	c(Å)	Error(Å)
C1	1.821	0.014	1.179	0.022	0.329	0.080
C2	2.370	0.010	0.227	0.106	0.805	0.030
C3	0.306	0.079	0.624	0.039	0.138	0.175
C4	0.957	0.029	0.410	0.066	1.494	0.019
C5	2.449	0.012	1.176	0.025	0.356	0.084
C6	2.311	0.012	0.981	0.028	1.778	0.016
C7	1.949	0.016	2.672	0.012	0.122	0.283
C8	0.110	0.251	0.761	0.036	0.557	0.050
C9	1.371	0.018	1.671	0.015	0.296	0.085
C10	3.713	0.006	1.945	0.012	0.571	0.042
C11	3.743	0.006	0.223	0.110	0.053	0.463
C12	4.272	0.006	1.123	0.025	0.364	0.078
C13	3.049	0.008	0.240	0.107	1.166	0.022
C14	2.462	0.012	0.300	0.094	2.250	0.013

Table B9: Atomic coordinates in the principal axis system calculated using Kraitchman's equations for the complex S2c.

Carbon	a(Å)	Error(Å)	b(Å)	Error(Å)	c(Å)	Error(Å)
C1	1.717	0.023	1.303	0.030	0.128	0.312
C2	2.371	0.016	0.261	0.141	0.874	0.043
C3	0.284	0.158	0.502	0.089	0.180	0.251
C4	0.928	0.040	0.206	0.175	1.540	0.024
C5	2.652	0.013	1.022	0.035	0.141	0.258
C6	2.245	0.016	1.414	0.025	1.567	0.024
C7	1.651	0.019	2.716	0.012	0.452	0.079
C8	0.339	0.105	0.781	0.045	0.718	0.050
C9	1.660	0.023	1.544	0.024	0.544	0.072
C10	4.001	0.009	1.657	0.022	0.301	0.126
C11	3.664	0.011	0.376	0.104	0.267	0.147
C12	5.015	0.007	0.314	0.121	0.129*i	0.293
C13	3.003	0.013	0.428	0.094	1.046	0.039
C14	2.461	0.016	0.465	0.079	2.127	0.019

Table B10: Atomic coordinates in the principal axis system calculated using Kraitchman's equations for the complex R2c.

Carbon	a(Å)	Error(Å)	b(Å)	Error(Å)	c(Å)	Error(Å)
C1	1.293	0.006	1.212	0.007	0.0749*i	0.106
C2	2.588	0.003	0.521	0.013	0.623	0.011
C3	0.516	0.014	0.157*i	0.047	0.769	0.010
C4	1.702	0.005	0.112*i	0.069	1.788	0.004
C5	2.964	0.003	0.659	0.011	0.227	0.033
C6	1.116	0.007	1.382	0.005	1.452	0.005
C7	0.997	0.007	2.564	0.003	0.716	0.010
C8	0.598	0.011	1.201	0.006	0.079	0.084
C9	1.978	0.003	1.528	0.004	0.544	0.012
C10	4.384	0.002	0.801	0.009	0.685	0.010
C11	3.600	0.002	0.510	0.016	0.296	0.027
C12	5.033	0.001	0.418	0.018	0.284	0.026
C13	3.076	0.002	0.831	0.009	0.551	0.013
C14	2.660	0.003	1.944	0.004	0.790	0.009

Table B11: Table of the experimental rotational constants and rotational constants computed from different method and basis sets with percent errors for the S1a and S1c complexes.

	A (MHZ)	B (MHz)	C (MHZ)	Error A (%)	Error B (%)	Error C (%)
S1a Fit	913.4767(27)	300.39373(78)	278.01924(75)	-	-	-
def2 B2PLYPD3	919.9490466	304.0724698	281.2147	-0.71	-1.22	-1.15
def2 B3LYP	920.3395953	252.1683657	234.8562946	-0.75	16.05	15.53
def2 B3LYPD3BJ	918.1223955	305.5393775	282.5830183	-0.51	-1.71	-1.64
def2 MP2	921.3818634	312.7854856	289.5312737	-0.87	-4.13	-4.14
Pople B2PLYPD3	912.7081971	304.5726636	281.6333744	0.08	-1.39	-1.30
Pople B3LYP	917.3429282	246.7737991	230.9372226	-0.42	17.85	16.93
Pople B3LYPD3BJ	917.2001993	304.4166226	280.7331982	-0.41	-1.34	-0.98
Pople MP2	907.2611792	313.8862066	290.0345835	0.68	-4.49	-4.32
S1c Fit	879.94543(84)	320.34351(36)	279.56130(38)	-	-	-
def2 B2PLYPD3	881.3893	325.5700	284.0115	-0.16	-1.63	-1.59
def2 B3LYP	878.0542	269.9898	251.3065	0.21	15.72	10.11
def2 B3LYPD3BJ	876.6153	328.7519	286.2212	0.38	-2.62	-2.38
def2 MP2	890.4967	327.7264	286.0488	-1.20	-2.30	-2.32
Pople B2PLYPD3	878.0902	323.6408	282.5357	0.21	-1.03	-1.06
Pople B3LYP	876.8704	264.7651	247.1553	0.35	17.35	11.59
Pople B3LYPD3BJ	873.0696	328.1221	285.6074	0.78	-2.43	-2.16
Pople MP2	887.2806	323.3626	282.9468	-0.83	-0.94	-1.21

def2 stands for the def2TZVP basis set and Pople is the 6311G++(d,p) basis set.

Table B12: Table of the experimental rotational constants and rotational constants computed from different method and basis sets with percent errors for the S2a and S2c complexes.

	A (MHZ)	B (MHz)	C (MHZ)	Error A (%)	Error B (%)	Error C (%)
S2a Fit	905.85816(81)	286.90405(35)	278.45467(34)	-	-	-
def2 B2PLYPD3	911.9642	290.8667	282.8038	-0.67	-1.38	-1.56
def2 B3LYP	902.2712	250.7907	247.8435	0.40	12.59	10.99
def2 B3LYPD3BJ	912.0502	292.3047	283.7847	-0.68	-1.88	-1.91
def2 MP2	914.0981	298.8733	287.6974	-0.91	-4.17	-3.32
Pople B2PLYPD3	906.6422	290.8140	282.0733	-0.09	-1.36	-1.30
Pople B3LYP	895.0202	245.2397	239.0619	1.20	14.52	14.15
Pople B3LYPD3BJ	909.3900	291.8744	282.7370	-0.39	-1.73	-1.54
Pople MP2	888.7292	305.4369	291.3064	1.89	-6.46	-4.62
S2c Fit	905.3497(13)	286.52860(41)	276.45786(43)	-	-	-
def2 B2PLYPD3	906.3113	291.6156	280.9230	-0.11	-1.78	-1.61
def2 B3LYP	902.9971	255.6908	244.9186	0.26	10.76	11.41
def2 B3LYPD3BJ	905.4867	291.8294	281.2872	-0.02	-1.85	-1.75
def2 MP2	912.3976	297.3812	285.7957	-0.78	-3.79	-3.38
Pople B2PLYPD3	903.2630	290.4595	279.7258	0.23	-1.37	-1.18
Pople B3LYP	898.7138	252.0314	236.2408	0.73	12.04	14.55
Pople B3LYPD3BJ	903.5686	291.1586	280.6798	0.20	-1.62	-1.53
Pople MP2	905.6097	295.2917	283.2753	-0.03	-3.06	-2.47

def2 stands for the def2TZVP basis set and Pople is the 6311G++(d,p) basis set.

Table B13: Table of the experimental rotational constants and rotational constants computed from different method and basis sets with percent errors for the R1a and R1c complexes.

	A (MHZ)	B (MHz)	C (MHZ)	Error A (%)	Error B (%)	Error C (%)
R1a Fit	836.9427(16)	314.41418(43)	299.49708(44)	-	-	-
def2 B2PLYPD3	839.1768	320.1425	304.9318	-0.27	-1.82	-1.81
def2 B3LYP	849.9895	267.1131	260.6158	-1.56	15.04	12.98
def2 B3LYPD3BJ	835.0281	324.0044	307.7472	0.23	-3.05	-2.75
def2 MP2	842.5535	328.4835	310.8422	-0.67	-4.47	-3.79
Pople B2PLYPD3	830.8842	322.1322	305.7865	0.72	-2.45	-2.10
Pople B3LYP	850.9309	256.3397	250.0671	-1.67	18.47	16.50
Pople B3LYPD3BJ	831.6089	324.0386	307.2242	0.64	-3.06	-2.58
Pople MP2	813.9498	341.1055	319.3891	2.75	-8.49	-6.64
R1c Fit	859.1653(14)	306.20216(43)	291.24858(49)	-	-	-
def2 B2PLYPD3	863.3462	309.6967	294.9572	-0.49	-1.14	-1.27
def2 B3LYP	874.8017	264.2460	253.2447	-1.82	13.70	13.05
def2 B3LYPD3BJ	861.4464	309.8432	294.9080	-0.27	-1.19	-1.26
def2 MP2	869.7668	315.9432	300.6089	-1.23	-3.18	-3.21
Pople B2PLYPD3	858.9889	308.7918	293.9368	0.02	-0.85	-0.92
Pople B3LYP	873.3680	261.2586	250.4894	-1.65	14.68	13.99
Pople B3LYPD3BJ	858.4270	309.8731	294.7314	0.09	-1.20	-1.20
Pople MP2	861.8630	312.6406	297.6083	-0.31	-2.10	-2.18

def2 stands for the def2TZVP basis set and Pople is the 6311G++(d,p) basis set.

Table B14: Table of the experimental rotational constants and rotational constants computed from different method and basis sets with percent errors for the R2b and R2c complexes.

	A (MHZ)	B (MHz)	C (MHZ)	Error A (%)	Error B (%)	Error C (%)
R2b Fit	986.1931(10)	276.80869(37)	261.96346(37)	-	-	-
def2 B2PLYPD3	992.4291	279.3791	264.4954	-0.63	-0.93	-0.97
def2 B3LYP	969.8174	242.8416	229.8231	1.66	12.27	12.27
def2 B3LYPD3BJ	994.3639	279.3251	263.8725	-0.83	-0.91	-0.73
def2 MP2	994.3356	288.6200	273.1882	-0.83	-4.27	-4.28
Pople B2PLYPD3	987.1087	279.3392	264.7318	-0.09	-0.91	-1.06
Pople B3LYP	958.1527	233.5709	226.6327	2.84	15.62	13.49
Pople B3LYPD3BJ	991.1885	278.3477	262.5322	-0.51	-0.56	-0.22
Pople MP2	983.2421	288.3765	272.6743	0.30	-4.18	-4.09
R2c Fit	948.88846(67)	295.40012(29)	260.85724(28)	-	-	-
def2 B2PLYPD3	952.2759	299.7174	265.0199	-0.36	-1.46	-1.60
def2 B3LYP	926.7140	267.2203	246.5677	2.34	9.54	5.48
def2 B3LYPD3BJ	951.4194	301.2210	265.9371	-0.27	-1.97	-1.95
def2 MP2	958.7905	302.9004	267.8163	-1.04	-2.54	-2.67
Pople B2PLYPD3	949.3443	297.9432	263.8388	-0.05	-0.86	-1.14
Pople B3LYP	922.1018	263.6947	243.9131	2.82	10.73	6.50
Pople B3LYPD3BJ	948.5893	300.3020	264.8895	0.03	-1.66	-1.55
Pople MP2	953.8186	299.5812	266.7258	-0.52	-1.42	-2.25

def2 stands for the def2TZVP basis set and Pople is the 6311G++(d,p) basis set.

Table B15: Table of the mean scale factor for each dipole moment component between a SCAT output and experimentally observed transitions using N transitions with a calculated standard deviation for heterochiral complexes. The experimental and computational calculated relative squares of the dipole moments are also shown for the def2TZVP and Pople's 6311G++(d,p) basis sets using different methods.

Complex	S1a			S1c		
Dipole Component	μ_a	μ_b	μ_c	μ_a	μ_b	μ_c
N	25	6	5	25	16	16
Mean Scale Factor	14.93	2.39	3.66	54.51	11.29	6.07
Standard Deviation	3.45	0.58	1.48	22.09	7.14	2.59
Mean Experimental Ratio	1.00	0.16	0.25	1.00	0.21	0.11
def2 B2PLYPD3	1.00	0.16	0.16	1.00	0.15	0.07
def2 B3LYP	1.00	0.12	0.05	1.00	0.03	0.03
def2 B3LYPD3BJ	1.00	0.15	0.16	1.00	0.15	0.08
def2 MP2	1.00	0.14	0.19	1.00	0.17	0.08
Pople B2PLYPD3	1.00	0.16	0.19	1.00	0.17	0.09
Pople B3LYP	1.00	0.11	0.05	1.00	0.03	0.04
Pople B3LYPD3BJ	1.00	0.17	0.17	1.00	0.16	0.09
Pople MP2	1.00	0.15	0.24	1.00	0.18	0.09
Complex	S2a			S2c		
Dipole Component	μ_a	μ_b	μ_c	μ_a	μ_b	μ_c
N	25	16	9	25	-	16
Mean Scale Factor	78.949	20.17	6.397	127.172	-	30.548
Standard Deviation	36.937	16.772	2.424	42.134	-	19.312
Mean Experimental Ratio	1.00	0.26	0.08	1.00	0.00	0.24
def2 B2PLYPD3	1.00	0.29	0.05	1.00	0.00	0.29
def2 B3LYP	1.00	0.02	0.04	1.00	0.00	0.15
def2 B3LYPD3BJ	1.00	0.29	0.04	1.00	0.00	0.28
def2 MP2	1.00	0.29	0.06	1.00	0.00	0.30
Pople B2PLYPD3	1.00	0.31	0.06	1.00	0.00	0.33
Pople B3LYP	1.00	0.00	0.16	1.00	0.00	0.14
Pople B3LYPD3BJ	1.00	0.31	0.05	1.00	0.00	0.31
Pople MP2	1.00	0.31	0.10	1.00	0.00	0.37

def2 stands for the def2TZVP basis set and Pople is the 6311G++(d,p) basis set.

Table B16: Table of the mean scale factor for each dipole moment component between a SCAT output and experimentally observed transitions using N transitions with a calculated standard deviation for homochiral complexes. The experimental and computational calculated relative squares of the dipole moments are also shown for the def2TZVP and Pople's 6311G++(d,p) basis sets using different methods.

Complex	R1a			R1c		
Dipole Component	μ_a	μ_b	μ_c	μ_a	μ_b	μ_c
N	25	9	16	25	-	25
Mean Scale Factor	35.12	5.49	8.89	65.71	-	15.64
Standard Deviation	22.28	2.65	5.69	14.66	-	8.67
Mean Experimental Ratio	1.00	0.15	0.25	1.00	-	0.23
def2 B2PLYPD3	1.00	0.16	0.16	1.00	0.08	0.16
def2 B3LYP	1.00	0.12	0.05	1.00	0.02	0.10
def2 B3LYPD3BJ	1.00	0.15	0.16	1.00	0.09	0.16
def2 MP2	1.00	0.14	0.19	1.00	0.09	0.19
Pople B2PLYPD3	1.00	0.16	0.19	1.00	0.08	0.19
Pople B3LYP	1.00	0.11	0.05	1.00	0.00	0.09
Pople B3LYPD3BJ	1.00	0.17	0.17	1.00	0.08	0.18
Pople MP2	1.00	0.10	0.26	1.00	0.02	0.28
Complex	R2b			R2c		
Dipole Component	μ_a	μ_b	μ_c	μ_a	μ_b	μ_c
N	25	16	4	25	25	2
Mean Scale Factor	21.93	8.08	2.60	117	25.17	3.23
Standard Deviation	11.5	3.69	0.271	38.93	13.12	0.41
Mean Experimental Ratio	1.00	0.37	0.12	1.00	0.21	0.03
def2 B2PLYPD3	1.00	0.36	0.06	1.00	0.24	0.01
def2 B3LYP	1.00	0.23	0.02	1.00	0.13	0.01
def2 B3LYPD3BJ	1.00	0.37	0.05	1.00	0.23	0.01
def2 MP2	1.00	0.35	0.09	1.00	0.26	0.01
Pople B2PLYPD3	1.00	0.39	0.08	1.00	0.27	0.01
Pople B3LYP	1.00	0.20	0.02	1.00	0.14	0.01
Pople B3LYPD3BJ	1.00	0.39	0.06	1.00	0.25	0.01
Pople MP2	1.00	0.37	0.13	1.00	0.33	0.01

def2 stands for the def2TZVP basis set and Pople is the 6311G++(d,p) basis set.

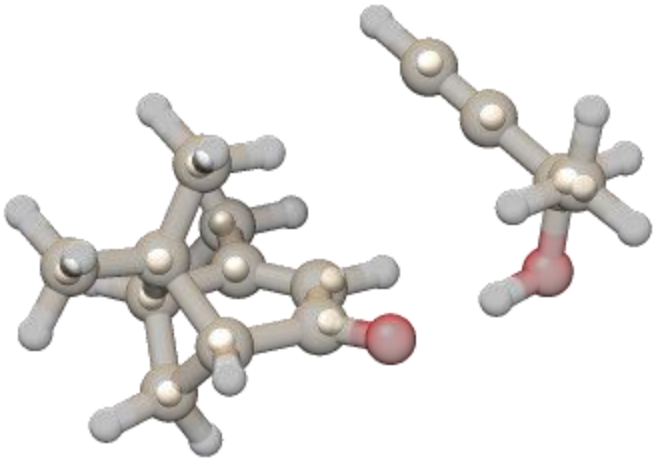

Figure B1: Kraitchman substitution structure for the R1a complex. The transparent structure is the theoretically calculated structure using B3LYPD3BJ with def2TZVP basis set, and the solid white spheres are the experimentally determined coordinates of the carbons.

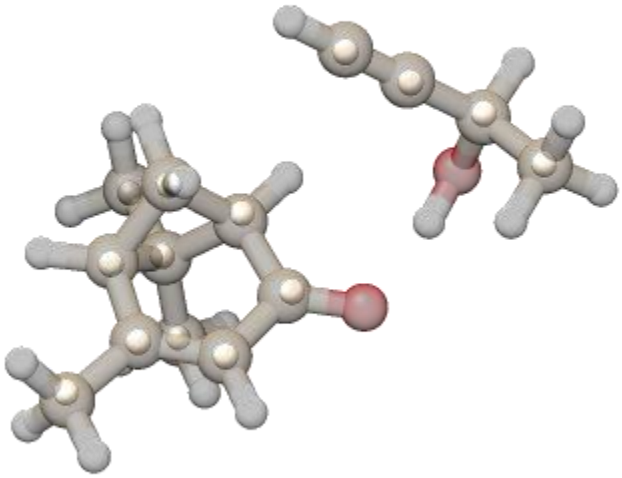

Figure B2: Kraitchman substitution structure for the R1c complex. The transparent structure is the theoretically calculated structure using B3LYPD3BJ with def2TZVP basis set, and the solid white spheres are the experimentally determined coordinates of the carbons.

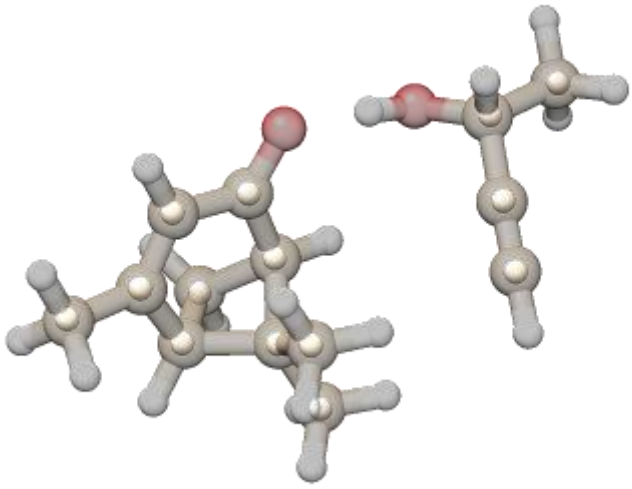

Figure B3: Kraitchman substitution structure for the R2c complex. The transparent structure is the theoretically calculated structure using B3LYPD3BJ with def2TZVP basis set, and the solid white spheres are the experimentally determined coordinates of the carbons.

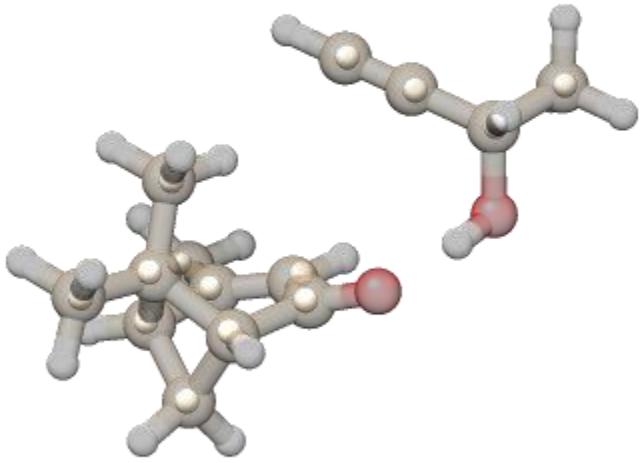

Figure B4: Kraitchman substitution structure for the S2a complex. The transparent structure is the theoretically calculated structure using B3LYPD3BJ with def2TZVP basis set, and the solid white spheres are the experimentally determined coordinates of the carbons.

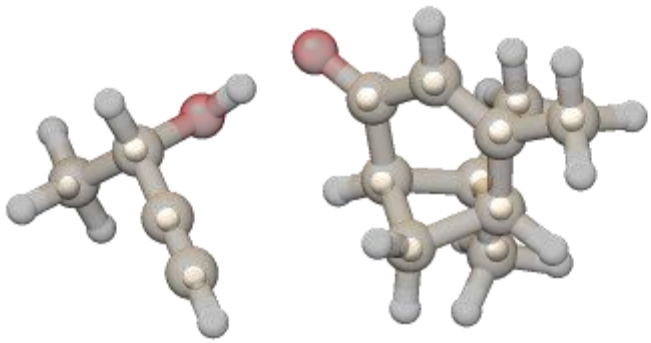

Figure B5: Kraitchman substitution structure for the S2c complex. The transparent structure is the theoretically calculated structure using B3LYPD3BJ with def2TZVP basis set, and the solid white spheres are the experimentally determined coordinates of the carbons.

Table B17: Table of atomic coordinates for the R1a chiral tag complex calculated using B2PLYPD3 with the def2TZVP basis set.

Atom	a	b	c
1	-2.20551	0.561826	-0.78861
2	-2.58642	-0.57087	0.238295
3	-1.6305	1.30313	0.474502
4	-2.69021	0.541996	1.317757
5	-1.37184	-1.398	0.571498
6	-1.26508	0.248537	-1.9418
7	-3.43982	1.262611	-1.34872
8	-0.27389	0.726511	0.814118
9	-0.24336	-0.73736	0.89408
10	-1.47204	-2.88352	0.507635
11	3.69648	-0.03817	0.026522
12	3.982976	1.368406	-0.49537
13	2.898882	-0.80625	-0.9459
14	2.247566	-1.43077	-1.74748

Table B18: Table of atomic coordinates for the R1a chiral tag complex calculated using B3LYPD3BJ with the def2TZVP basis set.

Atom	a	b	c
1	-2.1866	0.553252	-0.80046
2	-2.57284	-0.57538	0.232549
3	-1.63171	1.306893	0.467033
4	-2.69814	0.545205	1.302202
5	-1.35534	-1.39273	0.585275
6	-1.22916	0.236514	-1.93977
7	-3.419	1.242265	-1.38237
8	-0.27435	0.739765	0.828921
9	-0.23857	-0.72333	0.918168
10	-1.44253	-2.87797	0.521409
11	3.674656	-0.02011	0.009342
12	3.923259	1.375042	-0.56772
13	2.876487	-0.84013	-0.91763
14	2.223857	-1.50283	-1.67698

Table B19: Table of atomic coordinates for the R1a chiral tag complex calculated using MP2 with the def2TZVP basis set.

Atom	a	b	c
1	-2.18862	-0.5437	0.78508
2	-2.55061	0.586572	-0.24397
3	-1.63149	-1.30518	-0.46852
4	-2.67347	-0.52923	-1.31635
5	-1.32518	1.386519	-0.58308
6	-1.23768	-0.24041	1.927916
7	-3.43245	-1.21667	1.349381
8	-0.26588	-0.75987	-0.80272
9	-0.20568	0.701707	-0.90386
10	-1.39621	2.874092	-0.53024
11	3.656584	0.026657	-0.00392
12	3.898551	-1.35252	0.598846
13	2.829315	0.844673	0.899498
14	2.150555	1.519962	1.651502

Table B20: Table of atomic coordinates for the R1a chiral tag complex calculated using B2PLYPD3 with the Pople basis set.

Atom	a	b	c
1	-2.18828	0.573733	-0.79174
2	-2.58704	-0.56841	0.223258
3	-1.62535	1.305894	0.486472
4	-2.69939	0.53878	1.313475
5	-1.37644	-1.4053	0.565545
6	-1.23093	0.264989	-1.93812
7	-3.41688	1.284654	-1.36374
8	-0.27123	0.721085	0.837629
9	-0.24671	-0.74778	0.909134
10	-1.47953	-2.89459	0.486892
11	3.691527	-0.02143	0.001201
12	3.919862	1.390469	-0.54511
13	2.877443	-0.82405	-0.93275
14	2.22138	-1.48578	-1.70492

Table B21: Table of atomic coordinates for the R1a chiral tag complex calculated using B3LYPD3BJ with the Pople basis set.

Atom	a	b	c
1	-2.18628	0.568192	-0.79354
2	-2.57938	-0.57099	0.230567
3	-1.62166	1.307315	0.482611
4	-2.69288	0.541513	1.315712
5	-1.36344	-1.40206	0.571117
6	-1.23126	0.254958	-1.94115
7	-3.41837	1.273606	-1.36647
8	-0.26531	0.725558	0.835378
9	-0.23783	-0.74169	0.907621
10	-1.46037	-2.88967	0.491227
11	3.678802	-0.01477	-0.0042
12	3.897699	1.391786	-0.57483
13	2.868736	-0.83712	-0.9211
14	2.209108	-1.5065	-1.67213

Table B22: Table of atomic coordinates for the R1a chiral tag complex calculated using MP2 with the Pople basis set.

Atom	a	b	c
1	-2.09178	0.564837	-0.81561
2	-2.51932	-0.5996	0.155346
3	-1.63966	1.301139	0.499774
4	-2.73653	0.48963	1.247462
5	-1.3118	-1.40249	0.571611
6	-1.04613	0.300962	-1.89203
7	-3.30087	1.243151	-1.46061
8	-0.28892	0.76016	0.916321
9	-0.22561	-0.70968	1.000096
10	-1.35834	-2.89595	0.47412
11	3.594892	0.042333	-0.08119
12	3.62717	1.40104	-0.7828
13	2.758456	-0.91632	-0.8334
14	2.097624	-1.72501	-1.46891

Table B23: Table of atomic coordinates for the R1c chiral tag complex calculated using B2PLYPD3 with the def2TZVP basis set.

Atom	a	b	c
1	-1.80029	1.188067	-0.34691
2	-2.35458	0.263577	0.802079
3	-0.3971	0.598933	0.056763
4	-0.96754	0.410877	1.488935
5	-2.45514	-1.15914	0.318521
6	-2.29295	0.997267	-1.77289
7	-1.9115	2.667918	0.007534
8	-0.24109	-0.77723	-0.55015
9	-1.3825	-1.66917	-0.31683
10	-3.72005	-1.91148	0.553508
11	3.700366	0.269019	-0.13074
12	4.282871	-1.10835	-0.44225
13	3.026444	0.267105	1.179555
14	2.479356	0.252156	2.255256

Table B24: Table of atomic coordinates for the R1c chiral tag complex calculated using B3LYPD3BJ with the def2TZVP basis set.

Atom	a	b	c
1	1.801123	1.179705	0.377044
2	2.346486	0.284392	-0.80275
3	0.394311	0.596772	-0.03255
4	0.953261	0.449597	-1.47416
5	2.452711	-1.15147	-0.35662
6	2.305938	0.94945	1.793873
7	1.908282	2.669695	0.061804
8	0.244505	-0.79779	0.537284
9	1.387947	-1.67862	0.272374
10	3.717419	-1.89294	-0.61886
11	-3.69802	0.256317	0.143713
12	-4.27661	-1.13859	0.391036
13	-3.03138	0.324558	-1.16736
14	-2.48982	0.367068	-2.23814

Table B25: Table of atomic coordinates for the R1c chiral tag complex calculated using MP2 with the def2TZVP basis set.

Atom	a	b	c
1	-1.78503	1.2032	-0.26682
2	-2.3516	0.199768	0.799269
3	-0.38476	0.608262	0.121148
4	-0.98087	0.307322	1.521569
5	-2.42657	-1.18178	0.215897
6	-2.24367	1.106142	-1.71024
7	-1.91873	2.650112	0.188231
8	-0.20483	-0.70891	-0.58882
9	-1.3327	-1.63484	-0.43412
10	-3.68693	-1.96219	0.36978
11	3.668433	0.290201	-0.07015
12	4.248934	-1.04157	-0.53298
13	2.944993	0.117467	1.200807
14	2.356427	-0.04211	2.254424

Table B26: Table of atomic coordinates for the R1c chiral tag complex calculated using B2PLYPD3 with the Pople basis set.

Atom	a	b	c
1	1.804016	1.188499	0.352706
2	2.359947	0.266244	-0.80194
3	0.397157	0.602453	-0.05581
4	0.970276	0.41764	-1.49157
5	2.458213	-1.16262	-0.32256
6	2.296895	0.989884	1.782405
7	1.918526	2.6741	0.003611
8	0.237199	-0.77876	0.548229
9	1.380042	-1.67484	0.312031
10	3.726561	-1.91847	-0.5576
11	-3.70932	0.262822	0.125712
12	-4.27994	-1.1252	0.429292
13	-3.0197	0.27404	-1.17912
14	-2.46979	0.275944	-2.25705

Table B27: Table of atomic coordinates for the R1c chiral tag complex calculated using B3LYPD3BJ with the Pople basis set.

Atom	a	b	c
1	-1.80124	1.181489	-0.3774
2	-2.34997	0.283089	0.803165
3	-0.39123	0.599846	0.036417
4	-0.955	0.44863	1.479882
5	-2.45285	-1.15554	0.353176
6	-2.30349	0.950352	-1.79922
7	-1.91153	2.674949	-0.06049
8	-0.23815	-0.7964	-0.53655
9	-1.38269	-1.68163	-0.27595
10	-3.72075	-1.90119	0.609177
11	3.700186	0.254076	-0.13665
12	4.270953	-1.14746	-0.38518
13	3.019483	0.322185	1.168894
14	2.47035	0.368985	2.238198

Table B28: Table of atomic coordinates for the R1c chiral tag complex calculated using MP2 with the Pople basis set.

Atom	a	b	c
1	1.790969	1.202836	0.290321
2	2.357009	0.219889	-0.80079
3	0.387276	0.608146	-0.10082
4	0.977172	0.336232	-1.51512
5	2.442206	-1.1794	-0.24491
6	2.263125	1.078926	1.734124
7	1.918383	2.665166	-0.13888
8	0.211758	-0.72855	0.58686
9	1.348275	-1.65089	0.406335
10	3.710265	-1.95616	-0.42281
11	-3.68978	0.278362	0.074403
12	-4.26169	-1.07585	0.4973
13	-2.94998	0.154886	-1.19825
14	-2.37297	0.045269	-2.27006

Table B29: Table of atomic coordinates for the R2c chiral tag complex calculated using B2PLYPD3 with the def2TZVP basis set.

Atom	a	b	c
1	-1.27068	1.215006	0.074249
2	-2.57015	0.524386	0.639954
3	-0.51318	0.020773	0.765994
4	-1.68395	-0.0361	1.787017
5	-2.95541	-0.64305	-0.22987
6	-1.11594	1.413015	-1.42568
7	-0.97713	2.541425	0.768267
8	-0.61695	-1.20644	-0.1113
9	-1.97928	-1.50923	-0.56308
10	-4.37051	-0.76766	-0.68011
11	3.572244	-0.51893	-0.25202
12	4.992428	-0.42873	0.289067
13	3.056389	0.820981	-0.58504
14	2.661336	1.928981	-0.85608

Table B30: Table of atomic coordinates for the R2c chiral tag complex calculated using B3LYPD3BJ with the def2TZVP basis set.

Atom	a	b	c
1	-1.26048	-1.21544	-0.07177
2	-2.56662	-0.52813	-0.63402
3	-0.51116	-0.01861	-0.77224
4	-1.68719	0.029619	-1.78885
5	-2.95083	0.641826	0.234947
6	-1.09722	-1.40658	1.429138
7	-0.96579	-2.54438	-0.7625
8	-0.616	1.214064	0.100434
9	-1.97751	1.510598	0.558745
10	-4.36227	0.759893	0.694644
11	3.557209	0.513764	0.256949
12	4.988558	0.434708	-0.26388
13	3.041767	-0.82856	0.576615
14	2.645475	-1.93201	0.83653

Table B31: Table of atomic coordinates for the R2c chiral tag complex calculated using MP2 with the def2TZVP basis set.

Atom	a	b	c
1	-1.25971	1.20741	0.067424
2	-2.54897	0.526121	0.651642
3	-0.49242	0.020968	0.752055
4	-1.65002	-0.03592	1.785138
5	-2.94689	-0.63814	-0.20918
6	-1.12707	1.396025	-1.43271
7	-0.95663	2.532839	0.752937
8	-0.60535	-1.20078	-0.12364
9	-1.97354	-1.50776	-0.55594
10	-4.36758	-0.7625	-0.64175
11	3.556735	-0.51946	-0.25085
12	4.969672	-0.38599	0.292138
13	3.011487	0.807985	-0.58245
14	2.598672	1.921189	-0.85197

Table B32: Table of atomic coordinates for the R2c chiral tag complex calculated using B2PLYPD3 with the Pople basis set.

Atom	a	b	c
1	-1.27912	-1.21896	-0.07651
2	-2.57446	-0.52074	-0.65127
3	-0.50935	-0.02393	-0.76068
4	-1.6752	0.042024	-1.79265
5	-2.96282	0.648955	0.221763
6	-1.13578	-1.42162	1.428554
7	-0.98507	-2.54899	-0.77359
8	-0.61371	1.20421	0.122031
9	-1.98175	1.512632	0.566375
10	-4.38513	0.779477	0.663162
11	3.59567	0.517671	0.249057
12	5.006953	0.393086	-0.31749
13	3.051449	-0.80955	0.597257
14	2.642082	-1.91225	0.88248

Table B33: Table of atomic coordinates for the R2c chiral tag complex calculated using B3LYPD3BJ with the Pople basis set.

Atom	a	b	c
1	-1.26582	-1.21773	-0.06493
2	-2.57248	-0.52945	-0.634
3	-0.51034	-0.02444	-0.77238
4	-1.68818	0.023307	-1.7929
5	-2.95504	0.648178	0.231577
6	-1.10412	-1.40123	1.441111
7	-0.97313	-2.55446	-0.75032
8	-0.61349	1.214858	0.096293
9	-1.97676	1.518016	0.55388
10	-4.36983	0.772907	0.691309
11	3.564276	0.510861	0.261812
12	5.002724	0.424037	-0.24744
13	3.034739	-0.8306	0.56824
14	2.631267	-1.93654	0.816993

Table B34: Table of atomic coordinates for the R2c chiral tag complex calculated using MP2 with the Pople basis set.

Atom	a	b	c
1	-1.2725	-1.21829	-0.08284
2	-2.53935	-0.51426	-0.69858
3	-0.4709	-0.02175	-0.71765
4	-1.59428	0.064951	-1.79257
5	-2.9625	0.642164	0.172385
6	-1.19329	-1.43777	1.42351
7	-0.95339	-2.53926	-0.78441
8	-0.60187	1.188074	0.182739
9	-1.98981	1.500565	0.571887
10	-4.40438	0.773478	0.555274
11	3.618736	0.523505	0.222405
12	4.963679	0.291165	-0.45655
13	3.018772	-0.75973	0.640113
14	2.57925	-1.84512	0.990562

Table B35: Table of atomic coordinates for the S2a chiral tag complex calculated using B2PLYPD3 with the def2TZVP basis set.

Atom	a	b	c
1	-2.38667	-0.19683	0.839585
2	-2.58445	0.612481	-0.49784
3	-1.83859	-1.32958	-0.10534
4	-2.7621	-0.755	-1.21455
5	-1.26843	1.184429	-0.95722
6	-1.4745	0.353842	1.924815
7	-3.71879	-0.58137	1.476702
8	-0.41021	-1.01137	-0.48814
9	-0.20829	0.354326	-0.98319
10	-1.20239	2.624271	-1.33589
11	3.600663	-0.43593	0.272784
12	5.032503	-0.00274	-0.00778
13	2.855688	0.629733	0.965582
14	2.254782	1.512042	1.528818

Table B36: Table of atomic coordinates for the S2a chiral tag complex calculated using B3LYPD3BJ with the def2TZVP basis set.

Atom	a	b	c
1	-2.3819	0.184333	-0.84356
2	-2.57658	-0.60994	0.506064
3	-1.83879	1.331148	0.091003
4	-2.76223	0.76578	1.205964
5	-1.25667	-1.17102	0.972433
6	-1.46556	-0.3778	-1.92077
7	-3.71562	0.555847	-1.4877
8	-0.40803	1.023121	0.481532
9	-0.20324	-0.33687	0.990628
10	-1.1835	-2.60664	1.361402
11	3.589822	0.428116	-0.28755
12	5.026873	0.003428	-0.00598
13	2.840178	-0.65171	-0.95064
14	2.23368	-1.53949	-1.48522

Table B37: Table of atomic coordinates for the S2a chiral tag complex calculated using MP2 with the def2TZVP basis set.

Atom	a	b	c
1	-2.35172	-0.20526	0.842734
2	-2.55694	0.621661	-0.47683
3	-1.83198	-1.33263	-0.11694
4	-2.75633	-0.73272	-1.20898
5	-1.24343	1.18194	-0.94283
6	-1.41674	0.318053	1.917163
7	-3.67824	-0.58036	1.489325
8	-0.40595	-1.02754	-0.50034
9	-0.1903	0.337214	-0.99193
10	-1.16098	2.625566	-1.3033
11	3.530236	-0.43327	0.304061
12	4.984748	-0.03947	0.110755
13	2.770889	0.681396	0.89533
14	2.161613	1.619235	1.376674

Table B38: Table of atomic coordinates for the S2a chiral tag complex calculated using B2PLYPD3 with the Pople basis set.

Atom	a	b	c
1	-2.38021	0.20404	-0.84763
2	-2.59126	-0.61241	0.487476
3	-1.83946	1.336441	0.10766
4	-2.77392	0.755765	1.210271
5	-1.27612	-1.18891	0.957503
6	-1.45478	-0.34473	-1.92884
7	-3.71036	0.59173	-1.49756
8	-0.41098	1.015811	0.50168
9	-0.2132	-0.35522	0.996735
10	-1.2116	-2.63535	1.329737
11	3.596838	0.433486	-0.28541
12	5.040835	0.010284	-0.03411
13	2.83757	-0.64624	-0.9453
14	2.233937	-1.54602	-1.48433

Table B39: Table of atomic coordinates for the S2a chiral tag complex calculated using B3LYPD3BJ with the Pople basis set.

Atom	a	b	c
1	-2.38341	0.195992	-0.84543
2	-2.58385	-0.61015	0.500316
3	-1.83695	1.337021	0.100255
4	-2.76472	0.763903	1.213362
5	-1.26289	-1.18076	0.96347
6	-1.46452	-0.36255	-1.92785
7	-3.71851	0.577562	-1.49013
8	-0.4053	1.019917	0.490228
9	-0.20387	-0.34777	0.988588
10	-1.19323	-2.62374	1.339842
11	3.589267	0.428783	-0.29356
12	5.036675	0.011912	-0.03713
13	2.831704	-0.6589	-0.93783
14	2.221081	-1.55623	-1.45667

Table B40: Table of atomic coordinates for the S2a chiral tag complex calculated using MP2 with the Pople basis set.

Atom	a	b	c
1	-2.26911	0.240634	-0.89538
2	-2.55511	-0.63484	0.382416
3	-1.83309	1.346013	0.136394
4	-2.82493	0.696609	1.144285
5	-1.26625	-1.19818	0.927478
6	-1.24754	-0.23691	-1.91998
7	-3.55698	0.621606	-1.62639
8	-0.42566	1.045207	0.604554
9	-0.22969	-0.33516	1.082451
10	-1.18419	-2.65911	1.245352
11	3.441442	0.420764	-0.34396
12	4.938432	0.133184	-0.31926
13	2.69042	-0.77182	-0.78735
14	2.112095	-1.78311	-1.15822

Table B41: Table of atomic coordinates for the S2c chiral tag complex calculated using B2PLYPD3 with the def2TZVP basis set.

Atom	a	b	c
1	-1.69091	1.315831	-0.07305
2	-2.3484	0.253275	0.88657
3	-0.3745	0.479649	0.143367
4	-0.94436	0.074905	1.530161
5	-2.6473	-1.01352	0.128733
6	-2.22567	1.489692	-1.48601
7	-1.59568	2.692423	0.577951
8	-0.41485	-0.74902	-0.73705
9	-1.66318	-1.51442	-0.64248
10	-3.99822	-1.62912	0.260304
11	3.639284	-0.32607	-0.28269
12	4.958224	0.415747	-0.12076
13	2.98614	-0.53046	1.021864
14	2.461348	-0.69484	2.096263

Table B42: Table of atomic coordinates for the S2c chiral tag complex calculated using B3LYPD3BJ with the def2TZVP basis set.

Atom	a	b	c
1	1.684671	1.317099	0.101128
2	2.340877	0.274465	-0.88533
3	0.369587	0.477267	-0.12656
4	0.933415	0.105597	-1.52547
5	2.649028	-1.00727	-0.15394
6	2.227394	1.461859	1.515242
7	1.580556	2.707842	-0.52018
8	0.419167	-0.77263	0.725782
9	1.672723	-1.52675	0.610278
10	4.002103	-1.61161	-0.30243
11	-3.63643	-0.33619	0.270194
12	-4.95523	0.417663	0.139934
13	-2.98703	-0.4975	-1.04114
14	-2.46418	-0.62575	-2.11437

Table B43: Table of atomic coordinates for the S2c chiral tag complex calculated using MP2 with the def2TZVP basis set.

Atom	a	b	c
1	-1.67138	1.312418	-0.02543
2	-2.33588	0.222341	0.888078
3	-0.35611	0.478855	0.174482
4	-0.93936	0.019648	1.536805
5	-2.62469	-1.01362	0.085695
6	-2.18909	1.530651	-1.43523
7	-1.58434	2.662442	0.673448
8	-0.38714	-0.70676	-0.75583
9	-1.62893	-1.48671	-0.69451
10	-3.97607	-1.63507	0.179927
11	3.605274	-0.30865	-0.29512
12	4.922623	0.399123	-0.02905
13	2.910378	-0.60091	0.969407
14	2.353331	-0.83874	2.025467

Table B44: Table of atomic coordinates for the S2c chiral tag complex calculated using B2PLYPD3 with the Pople basis set.

Atom	a	b	c
1	1.686585	1.319626	0.080666
2	2.355029	0.265129	-0.88577
3	0.372541	0.476162	-0.14558
4	0.950466	0.081227	-1.5363
5	2.659887	-1.00833	-0.13286
6	2.218247	1.487478	1.500417
7	1.585319	2.704046	-0.56361
8	0.416498	-0.76037	0.730347
9	1.672495	-1.52095	0.634978
10	4.019196	-1.61725	-0.2626
11	-3.65105	-0.33052	0.279158
12	-4.96616	0.423047	0.107336
13	-2.98095	-0.52913	-1.02025
14	-2.45365	-0.69009	-2.09748

Table B45: Table of atomic coordinates for the S2c chiral tag complex calculated using B3LYPD3BJ with the Pople basis set.

Atom	a	b	c
1	1.684152	1.317577	0.11826
2	2.346356	0.286953	-0.88233
3	0.367447	0.478252	-0.12521
4	0.937563	0.122994	-1.5302
5	2.654224	-1.00629	-0.1638
6	2.223873	1.443918	1.539518
7	1.579876	2.719775	-0.48677
8	0.416473	-0.78462	0.713387
9	1.673307	-1.53786	0.593049
10	4.012419	-1.60805	-0.31341
11	-3.63904	-0.34426	0.263316
12	-4.96554	0.402962	0.135593
13	-2.97828	-0.47909	-1.04702
14	-2.44946	-0.58362	-2.12248

Table B46: Table of atomic coordinates for the S2c chiral tag complex calculated using MP2 with the Pople basis set.

Atom	a	b	c
1	-1.64745	1.324743	-0.02245
2	-2.3406	0.248326	0.892874
3	-0.34982	0.457328	0.176449
4	-0.94478	0.010995	1.543576
5	-2.66195	-0.98678	0.089361
6	-2.16412	1.556894	-1.43737
7	-1.52808	2.678447	0.679144
8	-0.40561	-0.73302	-0.75708
9	-1.67295	-1.48533	-0.69566
10	-4.03402	-1.57952	0.185359
11	3.638753	-0.30646	-0.29584
12	4.914945	0.471419	0.002674
13	2.920096	-0.63327	0.951774
14	2.370184	-0.91003	2.00762

Chapter 4

Chiral Analysis of Fenchyl Alcohol by Chiral Tag and VCD

I. Introduction

In the previous chapters, the justification and experimental evidence for the determination of enantiomeric excess was given, and the accuracy of the corresponding computational quantum chemical methods for high confidence absolute configuration determination was discussed. In this chapter, the chiral tag method will be applied to a test molecule, fenchyl alcohol, and another spectroscopy based chiral analysis technique, vibrational circular dichroism (VCD), will also be conducted on the same sample for comparison with an accepted chiral analysis technique. The VCD experiments were performed by Jordan Nafie at BioTools Inc. (Jupiter, FL, USA). Furthermore, this project was performed as an undergraduate physical chemistry lab project with many of the students contributing to the work presented in this chapter.

VCD is a relatively new technique with its first observation in the 1970s and later commercialized in the late 1990s.[1-4] Circular dichroism is the measurement of the difference in absorption of left-handed circularly polarized light and right-handed circularly polarized light. VCD measures the difference of absorption of vibrational transitions by the two forms of circularly polarized light by chiral molecules. Enantiomers will have equal and opposite magnitude intensities for each transition, so that a racemic mixture of molecules will cause no net signal. Originally, the theoretical predictions of VCD spectra were not very accurate until 1985 when Stephens published a new theoretical derivation for predicting VCD spectra that has now become routine for the method.[5] The greater accuracy of predicting VCD spectra and its wide range of

sampling have allowed VCD to be used in a wide range of analytical applications. Samples for VCD measurements can be solid, liquid, or gas phase.[6-9] One of the largest uses of VCD is in biochemical studies measuring the secondary structures of amino acids in proteins, polypeptides, and other large biomolecules.[10-13] Circular dichroism has also been integrated with chiral chromatography to determine the absolute configuration of chiral molecules after separation.[14, 15]

As VCD was a relatively recently discovered technique that has been able to establish itself in terms of chiral analytical capabilities, the comparison with chiral tag rotational spectroscopy can help understand the advantages and disadvantages in certain analytical applications. The techniques share some similarities that will support application of chiral tag as a common analytical technique. Firstly, the use of quantum chemistry calculations for the prediction of spectra or rotational parameters are common between the methods.[16, 17] Furthermore, both quantum chemical calculations need to be applied to the conformational landscape of the system to aid in identification. VCD spectra use a Boltzmann-weighted average of each individual conformation's VCD spectra in order to predict the experimental spectrum.[18] Rotational spectroscopy typically uses seeded molecular beams to cool the molecules to the lowest energy structures, but with large molecules or molecules with alkyl chains the number of conformations can be large. Secondly, they are both Fourier transform spectroscopy techniques that allow for increased sensitivity by averaging the signal through many measurements to reduce random noise. Finally, they both have reduced intensities from the parent technique they are using. VCD intensities are about four to five orders of magnitude smaller than the parent IR transition, and chiral tag rotational spectroscopy are also a fraction, ~1-20%, of the monomer transition signal

intensity.[19, 20] Even though both techniques share the common attributes above, many of these are applied differently for the two techniques.

II. Experimental

1) Chemicals

In this study, (1*R*)-endo-(+)-fenchyl alcohol and (1*S*)-endo-(-)-fenchyl alcohol were purchased from MilliporeSigma. The certificate of analysis reported a purity of 98.5% for (1*R*)-endo-(+)-fenchyl-alcohol with a measured optical rotation of 10.3°. No certificate of analysis was provided for (1*S*)-endo-(-)-fenchyl alcohol. The label of the vial for the (1*S*)-endo-fenchyl alcohol specified that the identification of the product had not been validated. The propylene oxide used in the chiral tag analysis was purchased from TCI. Both racemic and enantiopure (*R*)-(+)-propylene oxide were used.

2) Methods

The samples of (1*R*)-(+)-endo-fenchyl alcohol and (1*S*)-endo-(-)-fenchyl alcohol were measured separately in the CP-FTMW spectrometer previously described. Samples were loaded directly into the four nozzles for the (1*R*)-endo-(+)-fenchyl alcohol and three for the (1*S*)-endo-(-)-fenchyl alcohol, due to the small sample amount, and placed into the spectrometer. A backing pressure of 2 atmospheres absolute pressure was used with neon as the carrier gas, and samples were heated to 50°C. Monomer spectra of both samples were collected as a 1000 FID average and

400,000 FID average of the (1*R*)-endo-(-)-fenchyl and 100,000 FID average of the (1*S*)-endo-(-)-fenchyl alcohol. Different number of averages were obtained to give a better understanding of the timing required to measure relative abundances of diastereomers in the samples, and because the (1*S*)-endo-fenchyl alcohol came in small vials and was run until the sample was exhausted. To chiral tag the molecules, the samples were loaded into the nozzles, heated to 50°C, and run with a backing pressure of 2 atmospheres with a 0.1% mixture of propylene oxide in neon from the chiral tag complexes with racemic and enantiopure (*R*)-(+)-propylene oxide. For the sample of (1*R*)-endo-(+)-fenchyl alcohol, a 300,000 FID average spectrum was collected for both the racemic and enantiopure tag. The sampling methodology followed the purging of the tag with neon between samples as discussed in Chapter 1. Another 1 million FID average spectrum for the racemic propylene oxide and (*R*)-(+)-propylene oxide was also collected for high confidence absolute configuration determination with a Kraitchman substitution analysis. The same propylene oxide gas mixtures were used with the (1*S*)-endo-(-)-fenchyl alcohol sample, and a 10,000 FID average spectrum of the racemic and the enantiopure chiral tag spectra were collected. Subsequently, 100,000 FID average spectra of both the racemic and the enantiopure propylene oxide tag spectra were collected.

The samples were sent to BioTools where the VCD measurements were collected and analyzed by Dr. Jordan Nafie. Both samples of fenchyl alcohol were dissolved in carbon tetrachloride to achieve a concentration of 17 mg / 200 μL. A spectrum of the solvent was collected in addition to the two samples on a BioTools chiralIR-2x^{TM} VCD spectrometer. The spectrometer takes both the IR and the VCD spectrum of the sample at a resolution of 4 cm^{-1}. The solvent spectrum was then subtracted out of both sample spectra. The sample spectra were scaled on the

frequency axis by 0.981, as scaling factors are normally used for theoretical predicted IR spectra.[21] The experimental and theoretical spectra were then compared using BioTool's CompareVOA™ software.

3) Computational Chemistry

Geometry optimizations were run on Gaussian09 for fenchyl alcohol and fenchyl's diastereomer by Dr. Luca Evangelisti, Figure 4.1.[22] The optimizations were performed using the B3LYP method and def2TZVP basis set with D3BJ dispersion correction. The VCD spectra were also predicted using Gaussian09 for fenchyl alcohol. Chiral tag complexes of (*R*)-endo-(+)-fenchyl alcohol with both (*S*)-(-)- and (*R*)-(+)-propylene oxide were optimized. The heterochiral, (+)-(-) combinations, and homochiral, (+)-(+) and (-)-(-) combinations, using B3LYP method with def2TZVP basis set and D3BJ dispersion correction were run. Many different tag orientations of the two diastereomer complexes were optimized with the two lowest energy complexes displayed in Figure 4.2. The theoretical rotational constants are provided in Table 4.1. All rotational spectra were fit using Pickett's SPCAT/SPFIT programs and Kisiel's PROPOSE package.[23, 24]

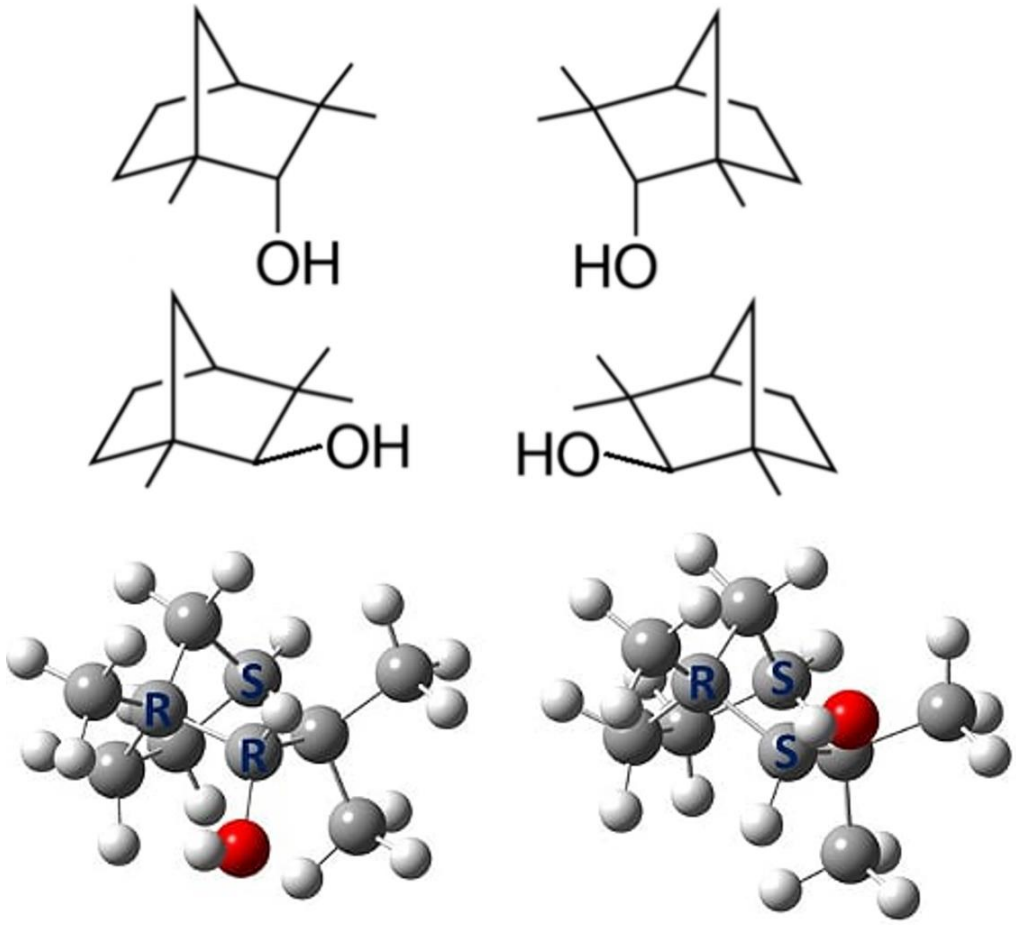

Figure 4.1: Top skeletal structures represent endo-fenchyl alcohol and its enantiomer, and the bottom skeletal structures represent exo-fenchyl alcohol and corresponding enantiomer. The bottom structures are endo-fenchyl alcohol, left, and exo-fenchyl alcohol, right, optimized in Gaussian09 using B3LYPD3BJ with def2TZVP basis set.

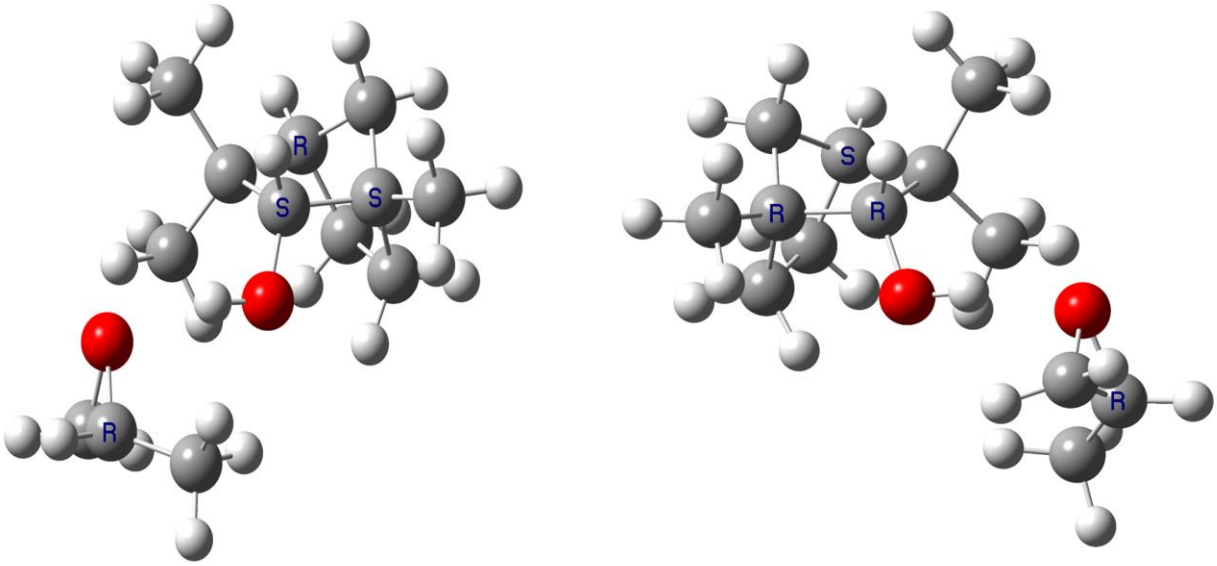

Figure 4.2: Strongest observed theoretical structures for fenchyl alcohol chiral tagged with (*R*)-(+)-propylene oxide. Left is the chiral tag complex for the heterochiral species and right is the chiral tag complex of the homochiral species.

Table 4.1: Theoretical rotational parameters calculated by B3LYPD3BJ with def2TZVP basis set for homochiral and heterochiral complexes.

Complex	Homochiral 1	Homochiral 2	Homochiral 3	Homochiral 4
A / MHz	945.0051	882.31	942.12	969.72
B / MHz	348.2616	408.47	361.07	358.45
C / MHz	324.238	355.93	316.89	332.02
μ_a (D)	2.502218	-1.89	1.95	2.87
μ_b (D)	-0.1107	-0.28	0.59	0.32
μ_c (D)	0.334171	0.49	0.77	-1.41
Complex	Homochiral 5	Homochiral 6		
A / MHz	904.02	1002.31		
B / MHz	374.70	342.13		
C / MHz	332.99	307.90		
μ_a (D)	-2.00	2.09		
μ_b (D)	0.36	0.82		
μ_c (D)	0.38	0.77		
Complex	Heterochiral 1	Heterochiral 2	Heterochiral 3	Heterochiral 4
A / MHz	939.57	985.77	880.29	916.72
B / MHz	354.17	334.03	400.20	363.14
C / MHz	309.25	302.05	350.66	323.45
μ_a (D)	2.30	2.48	-1.87	-1.94
μ_b (D)	-0.31	-0.34	0.01	0.23
μ_c (D)	0.54	0.57	0.44	0.35

III. Results

From the spectra of the fenchyl alcohol monomer, two conformations of fenchyl alcohol were fit, while only one structure of the fenchyl epimer, exo-fenchyl alcohol, was fit (Table 4.2 and Table 4.3). The second conformation of the fenchyl arose from the torsional angle of the hydroxyl group, while the epimer abundance was too small for any other conformation to be observed except the lowest energy structure. Despite sensitivity differences, the epimer was observed in both the 1000 and 400,000 average spectra of the (1*R*)-endo-(+)-fenchyl alcohol and the 100,000 average spectra of the (1*S*)-endo-(-)-fenchyl alcohol sample (Figure 4.3). The relative

abundance of the epimer in each spectrum was determined using the same scaling method where predicted transitions from SPCAT are scaled to experimental peak intensities described in Chapter 3, using all electric dipole moments components (Table 4.4). In both spectra, the calculated percent epimer abundance was about 3%, with the (*R*)-endo-(+)-fenchyl alcohol sample having a 3.2% abundance calculated in the 1000 and 400,000 average spectra, and a calculated 2.8% abundance from the 100,000 average spectrum of the (*S*)-endo-fenchyl-alcohol.

Table 4.2: Experimental fits for the observed endo-fenchyl alcohol conformations and the corresponding theoretical rotational constants calculated using B3LYPD3BJ level of theory with a def2TZVP basis set.

	Endo-Fenchyl Conformer 1		Endo-Fenchyl Conformer 2	
Complex	Theoretical	Experimental	Theoretical	Experimental
A / MHz	1528.11	1520.2243(20)	1515.09	1509.57403(57)
B / MHz	1096.28	1097.3666(23)	1102.21	1101.1536(19)
C / MHz	988.64	983.7042(17)	978.30	974.8878(17)
μ_a (D)	1.00	-	0.04	-
μ_b (D)	-0.04	-	1.63	-
μ_c (D)	-0.78	-	0.19	-
ΔE / cm^{-1}	0	-	64	-

Table 4.3: Experimental fit for the observed exo-fenchyl alcohol spectrum and the corresponding theoretical rotational constants calculated using B3LYPD3BJ level of theory with a def2tzvp basis set.

	Theoretical	Experimental
A / MHz	1499.25	1494.8834(64)
B / MHz	1204.04	1201.8109(39)
C / MHz	903.63	901.9053(23)
μ_a (D)	-1.07	-
μ_b (D)	0.45	-
μ_c (D)	0.68	-

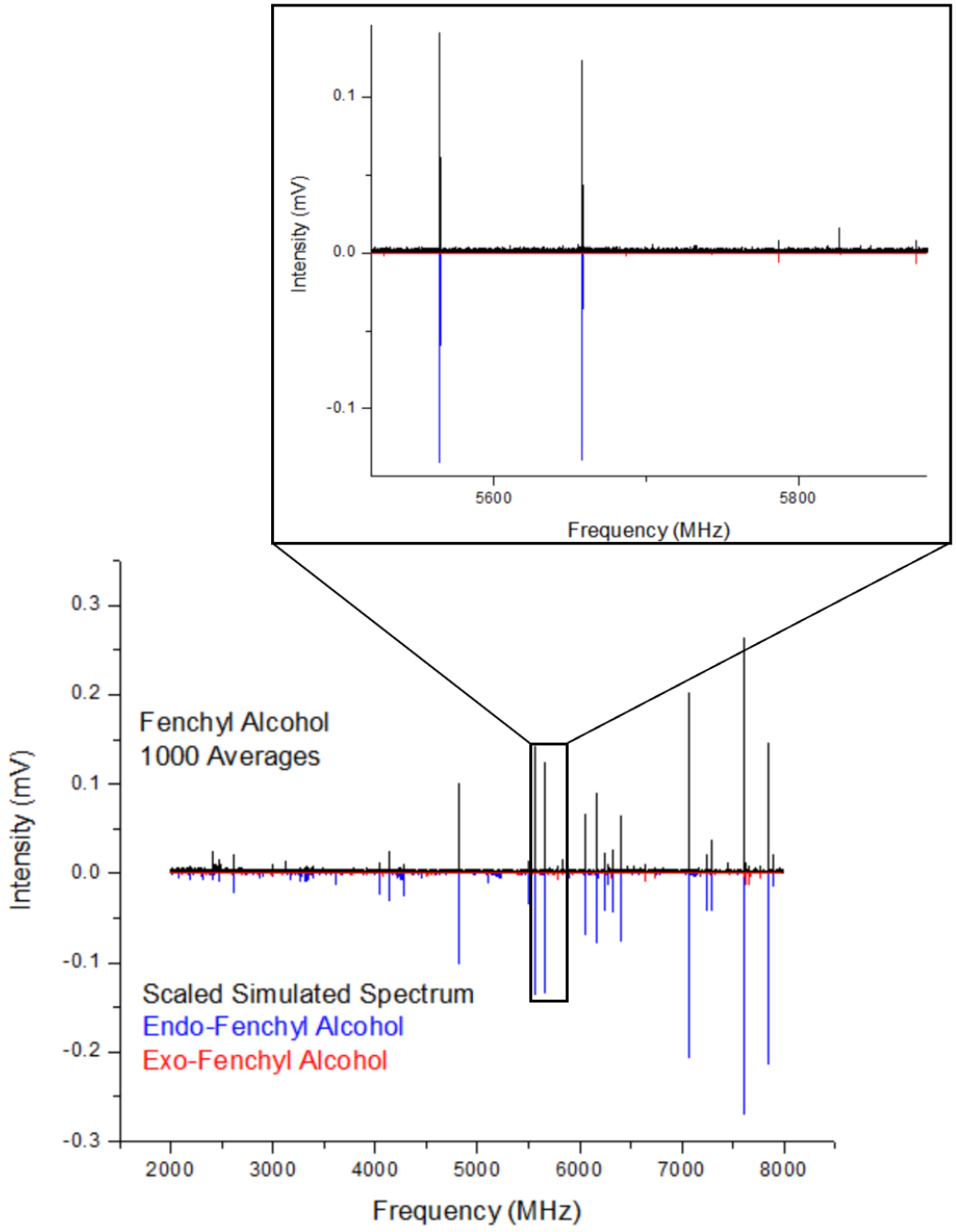

Figure 4.3: Experimental spectrum of the (1*R*)-endo-(+)-fenchyl alcohol spectrum with the scaled simulated rotational spectra of the endo- and exo-fenchyl alcohol (bottom), and a zoomed in part of the spectrum shown in the black box of transitions of both species (top).

Table 4.4: The tabulated mean scale factors for each species observed in the fenchyl alcohol spectrum with corresponding standard deviations from N lines. The fraction refers to the fractional abundance of each species for the different spectra listed.

1000 Average (1*R*)-endo-(+)-fenchyl Alcohol			
Species	Exo	Endo 1	Endo 2
N	5	19	5
Mean scale	6.694	194.388	6.726
Standard deviation	2.447	138.879	1.343
Fraction	0.032	0.935	0.032
400K Average (1*R*)-endo-(+)-fenchyl Alcohol			
Species	Exo	Endo 1	Endo 2
N	17.000	22.000	11.000
Mean scale	6.005	172.000	5.225
Standard deviation	2.199	133.000	2.656
Fraction	0.033	0.939	0.029
100k Average (1*S*)-endo-(-)-fenchyl Alcohol			
Species	Exo	Endo 1	Endo 2
N	17	23	9
Mean scale	3.942	132.522	4.706
Standard deviation	1.618	101.038	1.755
Fraction	0.028	0.939	0.033

Theoretical IR spectra for both diastereomers were calculated and compared (Figure 4.4). The diastereomer spectra displayed distinct intense peaks that could be used to identify the diastereomers based on their IR spectra. However, with low abundance of one diastereomer, the distinct feature almost vanishes. Figure 4.4 shows the predicted IR spectrum of a 97:3 endo- to exo-fenchyl alcohol spectrum. Below the experimental IR spectrum is compared to the calculated 97:3 diastereomer mix IR spectrum that has been scaled by 0.981. No abundance from the experimental IR spectra was obtained.

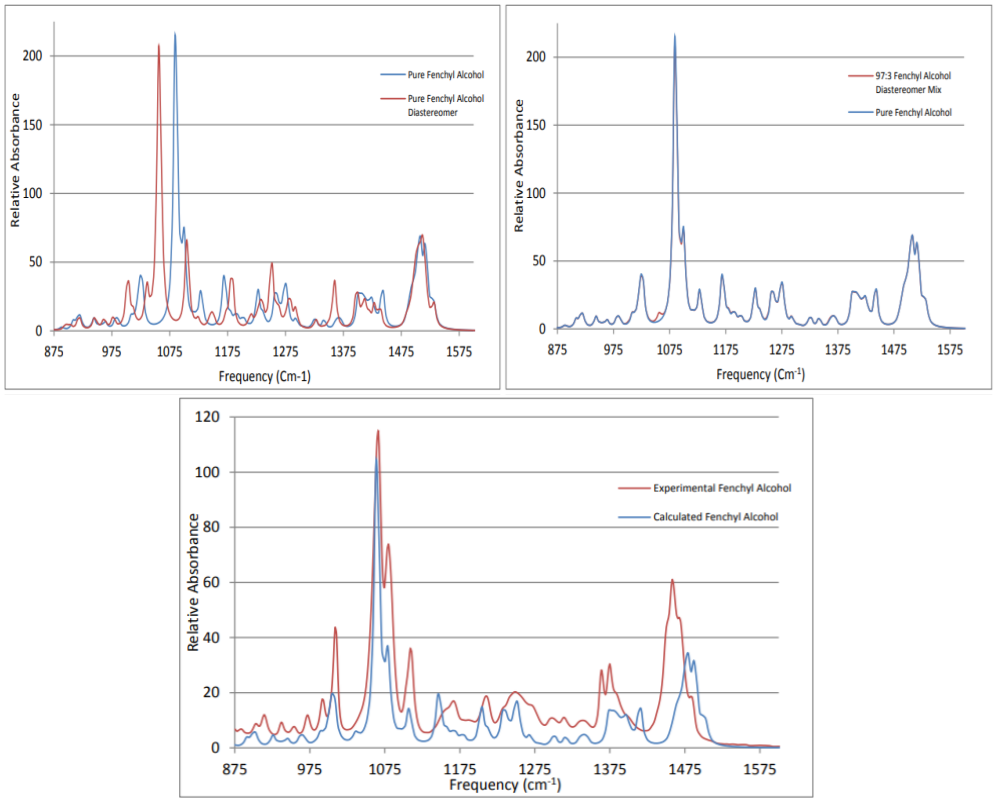

Figure 4.4: The top left spectrum depicts the two theoretical calculated IR spectra of the pure fenchyl and its epimer. The top right spectrum a Boltzmann weighted 97:3 ratio of the endo-fenchyl alcohol to its epimer. The bottom spectrum is a comparison of the experimental spectrum of fenchyl alcohol, and the Boltzmann weighted theoretical spectrum.

The two 300,000 average chiral tag measurements of (1*R*)-endo-(+)-fenchyl alcohol were taken to obtain an enantiomeric excess and establish absolute configuration. The 1 million average spectra were used to find the different isomers for both homochiral and heterochiral complexes and obtain ^{13}C sensitivity for a Kraitchman's analysis to validate the absolute configuration of the homochiral species. Two sets of spectra were differentiated by switching the tag from racemic to enantiopure. This created two groups of fit complexes, where some increased in intensity and others decreased. The rotational constants are then compared to theoretical rotational constants produced from the computational chemistry to assign absolute configuration. Six homochiral

complex isomers were fit (Table 4.5) and four heterochiral complex isomers were fit (Table 4.6) with the corresponding percent errors all less than 2%. For higher confidence in the absolute configuration determination, the substitution structure of homochiral 1 complex was found. Carbon atom positions are displayed with the theoretical homochiral 1 complex overlayed (Figure 4.5). Chiral tag rotational spectroscopy's ability to compare all carbon atomic coordinates in a structure to those generated by quantum chemistry greatly increases the confidence of spectral assignments. Using the species with the most intense spectra, homochiral 1 and heterochiral 1, the enantiomeric excess of the two samples of fenchyl was calculated. Figure 4.6 shows 3 histograms: the top is from the enantiomeric excess determination of the 10,000 average spectra of (1*S*)-endo-(-)-fenchyl alcohol, the middle is from the 100,000 average spectra of the same sample. An enantiomeric excess of 79.8% and 81.25% were calculated with the (1*R*)-endo-(+)-fenchyl alcohol in excess for the sample sold by MilliporeSigma as (1*S*)-endo-(-)-fenchyl alcohol. The bottom histogram in Figure 4.5 is the calculated enantiomeric excess from (1*R*)-endo-(+)-fenchyl alcohol with an enantiomeric excess of 83.5% with the (1*R*)-endo-(+)-fenchyl alcohol in excess.

Figure 4.5: Carbon atom positions calculated using Kraitchman's equations shown as solid blue spheres, overlayed with the theoretically predicted structure for homochiral 1 complex.

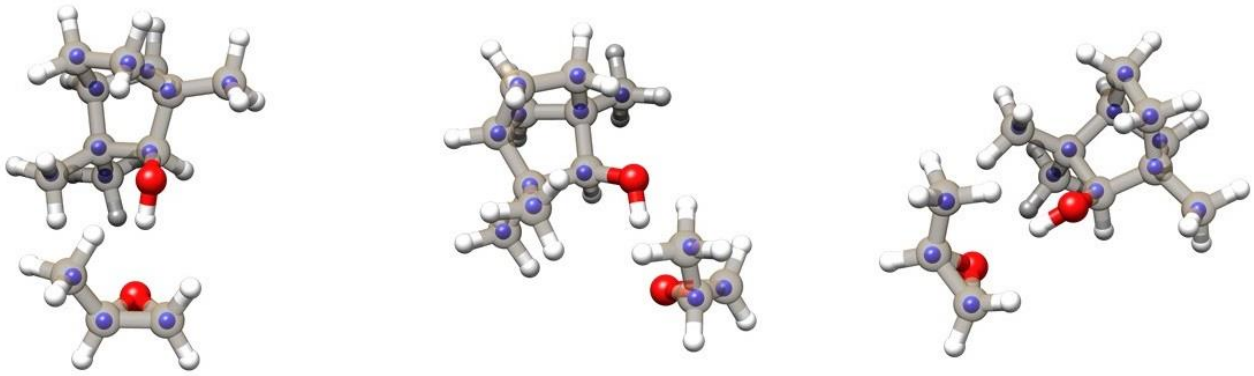

Table 4.5: Experimental fits for the overserved homochiral complexes of (1*R*)-endo-(+)-fenchyl alcohol hydrogen bonded to (*R*)-(+)-propylene oxide.

Complex	Homochiral 1	Percent Error (%)	Homochiral 2	Percent Error (%)
A / MHz	943.79(17)	-0.13	880.901(10)	-0.16
B / MHz	344.4071(12)	-1.12	401.5258(11)	-1.73
C / MHz	320.7456(13)	-1.09	350.7132(12)	-1.49
Δ_J/kHz	0.0276(35)		0.0433(59)	
Δ_{JK}/kHz	0.239(13)		0.367(30)	
Δ_K/kHz	-		-	
δ_J/kHz	-		-	
δ_K/kHz	-		-	
RMS /KHz	3.2		7.6	
N	93		75	
Complex	Homochiral 3	Percent Error (%)	Homochiral 4	Percent Error (%)
A / MHz	942.080(79)	-0.55	968.5026(20)	-0.13
B / MHz	355.5793(13)	0.14	357.02169(73)	-0.40
C / MHz	312.2493(13)	1.41	330.67890(76)	-0.41
Δ_J/kHz	0.0365(46)		0.0797(29)	
Δ_{JK}/kHz	0.213(53)		0.193(18)	
Δ_K/kHz	-		-	
δ_J/kHz	-		-	
δ_K/kHz	-		-	
RMS /KHz	4.3		4.8	
N	65		109	
Complex	Homochiral 5	Percent Error (%)	Homochiral 6	Percent Error (%)
A / MHz	905.996(78)	0.22	998.7139(25)	-0.36
B / MHz	368.8703(13)	-1.58	337.63311(91)	-1.33
C / MHz	328.4561(13)	-1.38	304.32256(89)	-1.18
Δ_J/kHz	0.0383(49)		0.0380(35)	
Δ_{JK}/kHz	0.173(28)		0.185(34)	
Δ_K/kHz	-		-	
δ_J/kHz	-		-	
δ_K/kHz	-		-	
RMS /KHz	4.5		98	
N	74		5	

Table 4.6: Experimental fits for the overserved heterochiral complexes of (1*R*)-endo-(+)-fenchyl alcohol hydrogen bonded to (*S*)-(-)-propylene oxide.

Complex	Heterochiral 1	Percent Error (%)	Heterochiral 2	Percent Error (%)
A / MHz	939.860(66)	0.03	979.87(12)	-0.60
B / MHz	350.7011(11)	-0.99	331.0475(11)	-0.90
C / MHz	306.7929(11)	-0.80	300.1914(12)	-0.62
Δ_J/kHz	0.0232(36)		0.0343(34)	
Δ_{JK}/kHz	0.175(17)		0.195(28)	
Δ_K/kHz	-		-	
δ_J/kHz	-		-	
δ_K/kHz	-		-	
RMS /KHz	3.6		2.6	
N	90		78	
Complex	Heterochiral 3	Percent Error (%)	Heterochiral 4	Percent Error (%)
A / MHz	879.673(66)	-0.07	913.78(11)	-0.32
B / MHz	394.3426(14)	-1.49	363.8805(15)	0.20
C / MHz	346.6308(15)	-1.16	324.3188(15)	0.27
Δ_J/kHz	0.0267(64)		0.2447(54)	
Δ_{JK}/kHz	0.208(58)		3.323(43)	
Δ_K/kHz	-		-	
δ_J/kHz	-		0.0127(48)	
δ_K/kHz	-		-	
RMS /KHz	5.6		10	
N	62		61	

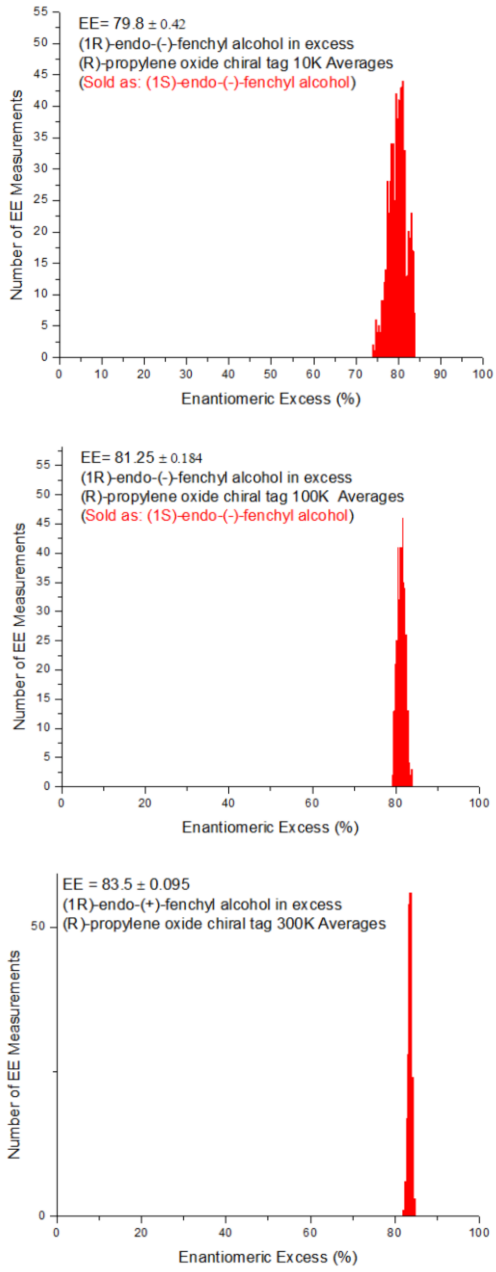

Figure 4.6: Histograms generated by chiral tag rotational spectroscopy to calculate the enantiomeric excess of endo-fenchyl alcohol. The top histogram is a 10K average of the (*S*)-fenchyl sample, the middle is the histogram of the 100K (*S*)-fenchyl sample, and the bottom is the histogram of the 400K (*R*)-fenchyl sample

The resulting VCD spectra of both samples are shown in the top spectrum of Figure 4.7 with the spectra being multiplied by 500,000. Both samples have the same spectra meaning they have the same absolute configuration. The enantiomer would have a spectrum similar in magnitude, but opposite in sign due to the greater absorption of the opposite circular polarized light. Enantiomeric excess would be determined from the peak height of the spectrum compared to a calibration curve of known enantiomeric excess samples as the presences of the opposite enantiomer would diminish the spectrum to zero if the sample was racemic. The theoretical (1*R*)-endo-(+)-fenchyl alcohol VCD spectrum is also compared to the experimental spectrum to confirm that the absolute configuration of the fenchyl alcohol was the *R* enantiomer. The BioTools CompareVOA™ software was used to calculate a similarity value of 85.8% for the (1*R*)-endo-(+)-fenchyl-alcohol enantiomer and 4.4% for the (1*S*)-endo-fenchyl alcohol enantiomer. This gives an enantiomeric similarity index of 81.4. CompareVOA™ also computed a 99% confidence that both spectra were (1*R*)-endo-(+)-fenchyl alcohol.

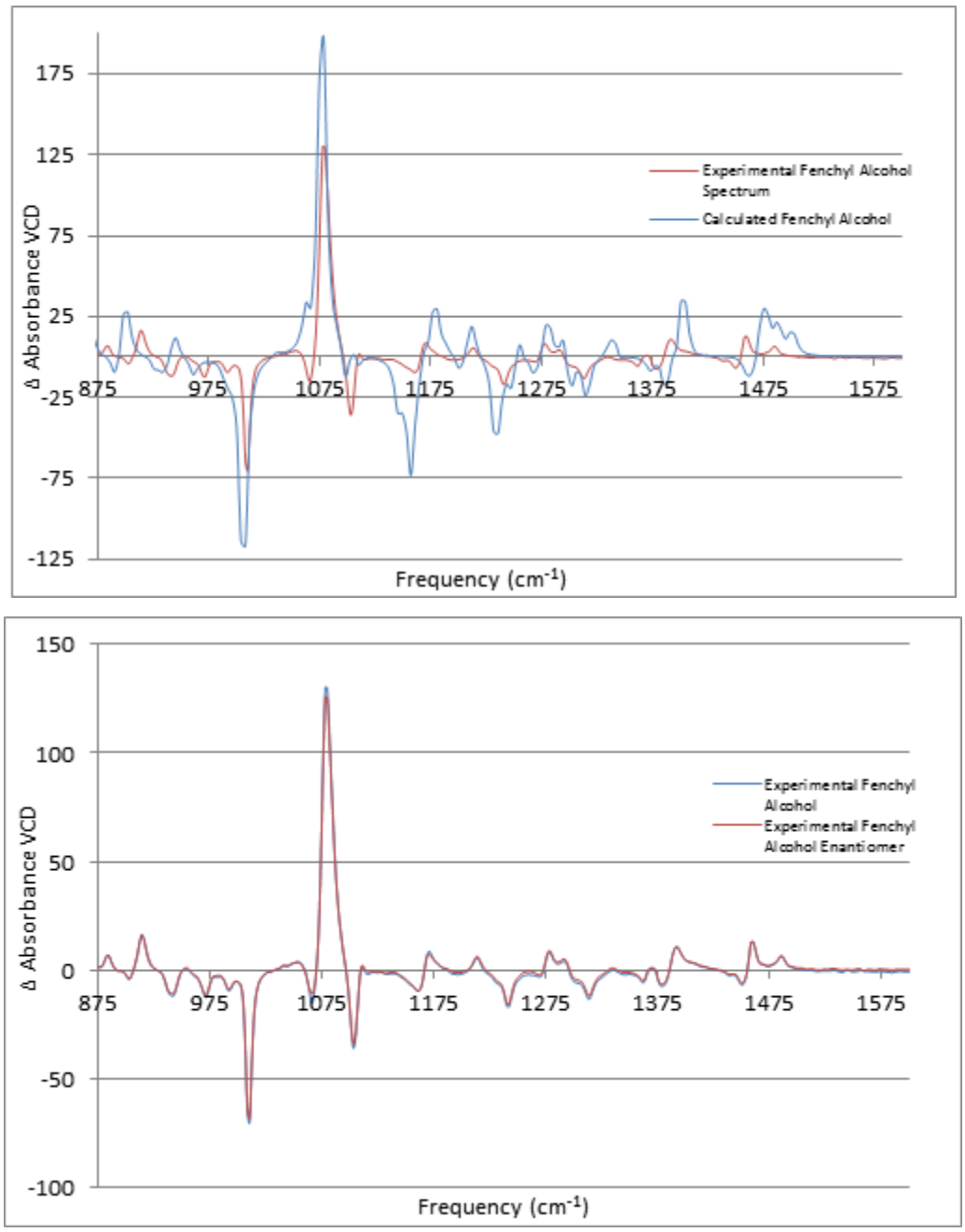

Figure 4.7: VCD spectra for the experimental (R)-fenchyl alcohol compared to its theoretical predicted VCD spectrum, scaling the frequency by 0.981 (top), and the experimental spectrum of both samples of enantiomers (bottom).

IV. Discussion

A complete analysis of a chiral sample would involve the measurement of the abundance of all stereoisomers, enantiomers, and diastereomers. In this test case of fenchyl alcohol, there were two diastereomers corresponding to the endo and exo forms, where the hydroxyl group is axial and equatorial. Many analytical techniques can discriminate between diastereomers with no need for special instrumentation or reagents. Both the theoretical predicted rotational constants and the theoretical IR spectra for both diastereomers indicate there are distinct characteristic frequencies for both and possible to detect. However, the very low abundance of one of the diastereomers does not allow the characteristic frequency in the IR to be observed using the commercial FT-IR spectrometer. The weighted experimental spectrum with a 3% abundance of the exo-fenchyl alcohol showed very little difference to the endo-fenchyl alcohol with a slight peak at about 1050 cm^{-1} corresponding to the strongest transition in the frequency range measured. This small peak cannot be seen in either of the IR spectra of the fenchyl alcohol samples. In the case of rotational spectroscopy, there are many different characteristic frequencies that can be observed in the CP-FTMW spectrum for both the endo and exo structures. The frequencies do not overlap with each other which allows for percent abundance to be calculated. These abundances were calculated at 3.2% abundance in the (1*R*)-endo-(+)-fenchyl alcohol and 2.8% abundance in the (1*S*)-endo-(-)-fenchyl alcohol. In the case of the (1*R*)-endo-(+)-fenchyl alcohol sample, the same percent abundance was shown when the measurement was run with 1000 averages, which took ~40 seconds to collect, and 400,000 averages, which took about four hours to collect. This shows that 40 seconds is a sufficiently long measurement for rotational spectroscopy to determine an accurate relative abundance of the components when the relative abundance is as low as 3%. If the relative

abundance had been lower, possibly below <1%, then the time required to signal average to achieve better sensitivity will increase. Moreover, electric dipole moments and conformational flexibility of the molecule also factor into the signal's intensity. The IR can be run in the same amount of time, but the low abundance diastereomer impurity could not be quantified or identified in the spectrum.

The other part of the chemical analysis of the stereoisomers of a sample is the determination of the absolute configuration of the dominant enantiomer and to quantify enantiomeric excess of the enantiomer. VCD was able to quantify the absolute configuration of both the samples with high confidence. With the theoretical spectra of the (+)-enantiomer of endo-fenchyl alcohol being shown in Figure 4.7, it was obvious as to which enantiomer was in excess. However, to calculate the enantiomeric excess, a calibration curve must be made where the peak height from the acquired VCD spectrum is used to quantify enantiomeric excess. In chiral tag rotational spectroscopy, the absolute configuration is determined in the 10,000, 100,000, and 300,000 average spectra. The 1 million average spectra taken with the chiral tag was also collected to validate the assignment of absolute configuration. It is worth noting that both methods agree that the sample obtained from MilliporeSigma as (1*S*)-endo-(-)-fenchyl alcohol was actually the (1*R*)-endo-(+)-fenchyl alcohol enantiomer. In addition, chiral tag rotational spectroscopy was able to quantify the enantiomeric excess with 10,000 averages as well without the need for a calibration of know samples of the analyte. The calculated enantiomeric excess for the (1*R*)-endo-(+)-fenchyl alcohol was 83.5% and for the sample that was sold as (1*S*)-endo-(-)-fenchyl alcohol the calculated enantiomeric excess was 79.8% and 81.25%. The lower sensitivity of the 10,000 average is shown by the larger width of the histogram and the larger calculated error. The three sigma of this error is within 1 sigma of

the 81.25% enantiomeric excess calculated in the 100,000 averages spectrum. The enantiomeric excess of the tag does need to be calibrated to be able to determine the enantiomeric excess. Strategies for calibrating an enantiomeric excess have been studied by other members of the lab, but the general method is either by the "autotag" spectrum, where the tag forms diastereomer complexes with itself, or in the case of propylene oxide, the dimers do not have strong electric dipole moments, and the tag is complexed with another tag that does have an autotag spectrum. Propylene oxide was complexed with the butynol chiral tag, for the butynol forms strong dimer spectra that allow for the chiral tagging of itself and enantiomeric excess of propylene oxide to be done in the same spectrum. Further note that the tags can be calibrated and used for multiple measurements. A primary difference between the VCD and chiral tag measurements was the time required to collect the spectra. The 10,000 average spectrum took 6 minutes to collect, the 100,000 took 1 hour, and the 300,000 average took 3 hours to collect. The VCD as stated above took 18 hours per sample and another 18 hours to collect the solvent spectrum. Even the longer chiral tag rotational spectroscopy measurements offer a large time savings compared to a VCD measurement along with the ability to quantify the enantiomeric excess with no need for an analyte reference.

For both techniques, the diastereomers must undergo a conformational search in order to obtain accurate results. In the case of the IR spectroscopy the conformation contributes to the overall experimental spectrum and the theoretical IR spectra need to be Boltzmann weighted to correspond with what is experimentally observed. Similarly, in rotational spectroscopy, all of the conformers need to be identified in order to get an accurate relative abundance. In this test case, there were three conformations corresponding to the torsional angle of the hydroxyl as the rest of the molecule was very rigid with the bicyclic structure and lack of an alkyl carbon chain. The three

conformers were Boltzmann weighted to give the theoretical IR spectrum. In rotational spectroscopy the three conformations were run to calculate their rotational constants and dipole moment components for both the diastereomers, but only the two conformations were observed for the endo-fenchyl alcohol and only one for the exo-fenchyl alcohol. The same is the case with the chiral discrimination techniques for the respective spectroscopies where the computational chemistry for the VCD spectrum and the chiral tag complexes needs to be performed. VCD spectra can be computed without the need to find additional structures. These can be computed at the same time as the IR, generally saving time on computational costs. Again, a Boltzmann weighting needs to be performed to calculate the VCD spectra for the system. The chiral tag method requires a survey of the different 3-dimensional tag configurations that can result in unique spectra. CP-FTMW use of a seeded molecular beam allows for many of the conformations to be cooled out, and only the lowest energy conformations will be observed in the experimental spectrum. The fenchyl alcohol test case shows that a large portion of these isomers can still be observed, which can reduce sensitivity due to the diastereomer complex being spread over a number of spectra. However, once the system is measured, the computational chemistry does not need to be performed again for either case. As shown in Chapter 3, the increase in accuracy from less computational taxing methods, and the continued development of computational chemistry has allowed this step to become considerably easier. These advancements plus the increased use of computational chemistry in industry would allow for these techniques to be more accessible for routine analytical chemical analysis.[25]

V. Conclusion

VCD is a relatively new spectroscopy based chiral analysis technique that has grown to producing commercial instruments with a wide variety of analytical applications being found. A comparison of the chiral tag method to VCD would aid in understanding the advantageous and disadvantage of this technique in terms of analytical capability. In this study, it was shown that the IR and VCD spectroscopic techniques have trouble identifying and quantifying low abundance impurities of stereoisomers in a spectrum. Rotational spectroscopy had no issue detecting a diastereomer impurity of about 3% in approximately 40 seconds, and the less sensitive measurement is further validated by the longer 400,00 average spectrum that calculated the same percent abundance. It is worth noting that this is the time it takes to run the measurement after the sample has been loaded in the CP-FTMW spectrometer. Currently the CP-FTMW spectrometer used in this study does not have a user-friendly sampling system, while the ease of use of commercially available IR/VCD spectrometers is well known. Another worthwhile difference between the methods is the need to purify samples for IR spectroscopy. For example, a reaction mixture cannot be measured by IR with meaningful interpretation, while rotational spectroscopy can identify components of a reaction mixture without further purification. Molecules with similar vibrational modes would produce overlapping spectra, whereas the molecules each would have different set of rotational constants with distinct frequencies that can be resolved on the CP-FTMW spectrometer. This also has the added advantage of identifying products of less desirable reaction products that could occur during the reaction.

In terms of chiral analysis, both methods could determine the absolute configuration of the dominant enantiomer in the sample. Both samples of fenchyl alcohol sold by MilliporeSigma

were correctly labeled as (1R)-endo-(+)-fenchyl alcohol. However, the chiral tag method was able to quantify an enantiomeric excess as well. Chiral tag was able to measure an enantiomeric excess and an absolute configuration determination in a measurement time of 6 minutes. The measured enantiomeric excess of the (1R)-endo-(+)-fenchyl alcohol by chiral tag was 83.5% and the sample sold as (1S)-endo-(-)-fenchyl alcohol was 81.25%. Since they were the same dominant enantiomer, the samples were essentially the same with a slight difference in diastereomer impurity and enantiomeric excess, but the (1S)-endo-(-)-fenchyl alcohol cost about 3000 times as much. VCD was able to determine absolute configuration determination in 18 hours not including the 18-hour measurement of the solvent. VCD could determine absolute configuration if there were known standards of the analyte being measured to compare peak heights to. Rotational spectroscopy can determine the enantiomeric excess of a new compound with no need for standards of the newly produced compound. The ability of chiral tag to quantify an accurate enantiomeric excess does depends on the calibration of the tag enantiomeric excess because, as discussed in Chapter 1, the measured ratios are a product of the tag enantiomeric excess and the analyte's enantiomeric excess.

A big difference also in the two techniques is the ability to measure large molecules. VCD works on large chiral molecules, such as proteins and nucleic acids, which rotational spectroscopy cannot. Many applications of VCD are in studies of secondary structures of large biomolecules, which has led to a much greater use of VCD. As molecules increase in molecular size, rotational energy levels become denser and shift to lower frequencies due to decreasing rotational constants. Large molecules, such as proteins or molecules that are thermally unstable, cannot be measured for they will decompose when trying to volatilize. Solid samples that can produce a vapor pressure, like fenchyl alcohol, can be measured through rotational spectroscopy techniques.

VI. References

1. Holzwarth, G.; Hsu, E. C.; Mosher, H. S.; Faulkner, T. R.; Moscowitz, A., Infrared circular dichroism of carbon-hydrogen and carbon-deuterium stretching modes. Observations. *Journal of the American Chemical Society* **1974,** *96* (1), 251-252.

2. Nafie, L.; Cheng, J.; Stephens, P., Vibrational circular dichroism of 2, 2, 2-trifluoro-1-phenylethanol. *Journal of the American Chemical Society* **1975,** *97* (13), 3842-3843.

3. Nafie, L. A.; Keiderling, T.; Stephens, P., Vibrational circular dichroism. *Journal of the American Chemical Society* **1976,** *98* (10), 2715-2723.

4. Polavarapu, P. L.; He, J., Peer Reviewed: Chiral Analysis Using Mid-IR Vibrational CD Spectroscopy. ACS Publications: 2004.

5. Stephens, P. J., Theory of vibrational circular dichroism. *The Journal of Physical Chemistry* **1985,** *89* (5), 748-752.

6. Nafie, L. A., Vibrational Circular Dichroism: A New Tool for the Solution-State Determination of the Structure and Absolute Configuration of Chiral Natural Product Molecules. *Natural Product Communications* **2008,** *3* (3), 1934578X0800300322.

7. Quesada-Moreno, M. M.; Virgili, A.; Monteagudo, E.; Claramunt, R. M.; Avilés-Moreno, J. R.; López-González, J. J.; Alkorta, I.; Elguero, J., A vibrational circular dichroism (VCD) methodology for the measurement of enantiomeric excess in chiral compounds in the solid phase and for the complementary use of NMR and VCD techniques in solution: The camphor case. *Analyst* **2018,** *143* (6), 1406-1416.

8. Diem, M.; Photos, E.; Khouri, H.; Nafie, L. A., Vibrational circular dichroism in amino acids and peptides. 3. Solution-and solid-phase spectra of alanine and serine. *Journal of the American Chemical Society* **1979,** *101* (23), 6829-6837.

9. Cianciosi, S. J.; Spencer, K. M.; Freedman, T. B.; Nafie, L. A.; Baldwin, J. E., Synthesis and gas-phase vibrational circular dichroism of (+)-(S, S)-cyclopropane-1, 2-2H2. *Journal of the American Chemical Society* **1989,** *111* (5), 1913-1915.

10. Rudd, T. R.; Nichols, R. J.; Yates, E. A., Selective Detection of Protein Secondary Structural Changes in Solution Protein−Polysaccharide Complexes Using Vibrational Circular Dichroism (VCD). *Journal of the American Chemical Society* **2008,** *130* (7), 2138-2139.

11. Baumruk, V.; Keiderling, T. A., Vibrational circular dichroism of proteins in water solution. *Journal of the American Chemical Society* **1993,** *115* (15), 6939-6942.

12. Ma, S.; Cao, X.; Mak, M.; Sadik, A.; Walkner, C.; Freedman, T. B.; Lednev, I. K.; Dukor, R. K.; Nafie, L. A., Vibrational circular dichroism shows unusual sensitivity to protein fibril formation and development in solution. *Journal of the American Chemical Society* **2007,** *129* (41), 12364-12365.

13. Kurouski, D., Advances of vibrational circular dichroism (VCD) in bioanalytical chemistry. A review. *Analytica chimica acta* **2017,** *990*, 54-66.

14. Said, M. E. A.; Bombarda, I.; Naubron, J. V.; Vanloot, P.; Jean, M.; Cheriti, A.; Dupuy, N.; Roussel, C., Isolation of the major chiral compounds from Bubonium graveolens essential oil by HPLC and absolute configuration determination by VCD. *Chirality* **2017,** *29* (2), 70-79.

15. Tran, C. D.; Grishko, V. I.; Huang, G., Chiral detection in high-performance liquid chromatography by vibrational circular dichroism. *Analytical chemistry* **1994,** *66* (17), 2630-2635.

16. Stephens, P. J.; Devlin, F. J.; Pan, J. J., The determination of the absolute configurations of chiral molecules using vibrational circular dichroism (VCD) spectroscopy. *Chirality: The Pharmacological, Biological, and Chemical Consequences of Molecular Asymmetry* **2008,** *20* (5), 643-663.

17. Kirchner, B.; Blasius, J.; Esser, L.; Reckien, W., Predicting Vibrational Spectroscopy for Flexible Molecules and Molecules with Non-Idle Environments. *Advanced Theory and Simulations* **2021,** *4* (4), 2000223.

18. Koenis, M. A.; Xia, Y.; Domingos, S. R.; Visscher, L.; Buma, W. J.; Nicu, V. P., Taming conformational heterogeneity in and with vibrational circular dichroism spectroscopy. *Chemical science* **2019,** *10* (33), 7680-7689.

19. Merten, C.; Xu, Y., Chirality Transfer in a Methyl Lactate–Ammonia Complex Observed by Matrix-Isolation Vibrational Circular Dichroism Spectroscopy. *Angewandte Chemie* **2013,** *125* (7), 2127-2130.

20. Nafie, L. A.; Diem, M.; Vidrine, D. W., Fourier transform infrared vibrational circular dichroism. *Journal of the American Chemical Society* **1979,** *101* (2), 496-498.

21. Laury, M. L.; Carlson, M. J.; Wilson, A. K., Vibrational frequency scale factors for density functional theory and the polarization consistent basis sets. *Journal of computational chemistry* **2012,** *33* (30), 2380-2387.

22. M. J. Frisch, G. W. T., H. B. Schlegel, G. E. Scuseria, M. A. Robb, J. R. Cheeseman, G. Scalmani, V. Barone, G. A. Petersson, H. Nakatsuji, X. Li, M. Caricato, A. Marenich, J. Bloino, B. G. Janesko, R. Gomperts, B. Mennucci, H. P. Hratchian, J. V. Ortiz, A. F. Izmaylov, J. L. Sonnenberg, D. Williams-Young, F. Ding, F. Lipparini, F. Egidi, J. Goings, B. Peng, A. Petrone, T. Henderson, D. Ranasinghe, V. G. Zakrzewski, J. Gao, N. Rega, G. Zheng, W. Liang, M. Hada, M. Ehara, K. Toyota, R. Fukuda, J. Hasegawa, M. Ishida, T. Nakajima, Y. Honda, O. Kitao, H. Nakai, T. Vreven, K. Throssell, J. A. Montgomery, Jr., J. E. Peralta, F. Ogliaro, M. Bearpark, J. J. Heyd, E. Brothers, K. N. Kudin, V. N. Staroverov, T. Keith, R. Kobayashi, J. Normand, K. Raghavachari, A. Rendell, J. C. Burant, S. S. Iyengar, J. Tomasi, M. Cossi, J. M. Millam, M. Klene, C. Adamo, R. Cammi, J. W. Ochterski, R. L. Martin, K. Morokuma, O. Farkas, J. B. Foresman, and D. J. Fox *Gaussian 09, Revision A.02*, Gaussian, Inc.: Wallingford, CT, 2016.

23. Kisiel, Z. PROSPE, programs for rotational spectroscopy. http://info.ifpan.edu.pl/~kisiel/prospe.htm.

24. Pickett, H. M., The fitting and prediction of vibration-rotation spectra with spin interactions. *Journal of Molecular Spectroscopy* **1991,** *148* (2), 371-377.

25. Lam, Y.-h.; Abramov, Y.; Ananthula, R. S.; Elward, J. M.; Hilden, L. R.; Nilsson Lill, S. O.; Norrby, P.-O.; Ramirez, A.; Sherer, E. C.; Mustakis, J.; Tanoury, G. J., Applications of Quantum Chemistry in Pharmaceutical Process Development: Current State and Opportunities. *Organic Process Research & Development* **2020,** *24* (8), 1496-1507.

VII. Appendix C

Figure C1: Experimental rotational constant fits for the ^{13}C isotopolgoues for homochiral 1 complex.

Atom	A	B	C	N	RMS (KHz)
1	941.19(4)	344.1691(2)	320.2771(2)	40	8.7
2	941.67(5)	343.6085(3)	319.8122(3)	40	10
3	941.84(5)	343.0292(4)	319.3289(4)	40	10
4	943.06(5)	344.2407(4)	320.6626(3)	40	11
5	943.15(6)	342.2818(4)	318.9768(4)	40	12.6
6	938.96(4)	342.4128(2)	319.4844(2)	32	8.2
7	938.82(2)	343.0880(2)	319.7789(2)	32	6.6
8	937.16(3)	344.3166(2)	320.0669(2)	30	7.7
9	932.18(2)	343.6055(1)	319.7378(1)	32	5.1
10	931.92(3)	343.4562(2)	318.7196(2)	30	5.3
11	943.67(3)	340.6310(2)	317.4727(2)	30	5.9
12	941.28(3)	340.7359(2)	317.4757(2)	30	6.2
13	939.23(4)	341.0281(2)	318.3370(2)	41	8.9

Figure C2: Experimentally determined atomic coordinates for homochiral 1 complex using Kraitchman's equations.

Atom	a	b	c
1	0.958	1.179	0.314
2	1.844	1.098	0.107
3	2.426	1.055	0.095
4	0.591	0.243	0.601
5	2.958	0	0.612
6	2.449	0.462	1.602
7	1.943	0.984	1.373
8	0	1.835	0.658
9	0.924	2.005	1.634
10	1.899	2.529	0.681
11	4.03	0.159	0.222
12	3.912	0.968	0.721
13	3.452	0	1.626

Chapter 5

Chiral Tagging of Carboxylic acids

I. Introduction

As discussed in Chapter 2 and 3, establishment of the absolute configuration with high confidence is the most challenging part of chiral analysis. The work presented in this chapter, utilizes a new method to increase confidence in assignment when rotational constants for diastereomer complexes are too similar. Isotope-labeled tags are studied for the use of atomic coordinate verification when substitution structures are not possible due to sample limits.

Carboxylic acids are essential for everyday life as they are present in amino acids,[1, 2] metabolites,[3] fatty acids,[4] foods,[5] pharmaceuticals,[1, 6] and much more. Previous work has shown carboxylic acid containing molecules are more likely to bind to proteins, making them highly used functional group in the pharmaceutical industry.[7] Carboxylic acids themselves are polar weak acids that form hydrogen bonds that contribute to their ability to interact with different therapeutic targets. Many of these applications are biochemical in nature, and therefore, many of these carboxylic acid containing molecules are chiral. As such, the need to quantify the enantiomeric excess as well absolute configuration is crucial.

A unique feature of carboxylic acids occurs during the chiral tagging of this functional group where the same chiral tag diastereomer complex with a 180° rotation of the carboxylic acid group and tag have nearly identical rotational constants as the corresponding diastereomer complex. In total there are four unique complexes that arise from the homochiral and heterochiral

pairs. The experimental rotational constants are within error of the theoretically predicted rotational constants from each other and makes assigning the absolute configuration less confident then with other chiral tag molecules. The aim of this project was to find a general method to confidently assign the absolute configuration of structures containing carboxylic acids. Various chiral tags were used to determine if different tag motifs could increase the difference in the rotational constants for the two pairs. Moreover, theoretical studies of the complexes were used to achieve higher confidence in the assignment. The carboxylic acid, 2-phenylpropionic acid was chosen in this analysis and tagged with the different chiral tags to study the carboxylic acids-chiral tag system.

II. Experimental

1) Materials

A sample of 2-phenylpropionic acid was purchased from MilliporeSigma in the racemic form and (*S*)-(+)-2-phenylpropionic enantiopure form. The chiral tags used in this study were (*S*)-(-)-propylene oxide, racemic propylene oxide, racemic propylene oxide-1,3-$^{13}C_2$, racemic and (*S*)-(-)-butynol. The parent isotope propylene oxide was obtained from TCI, while the butynol and ^{13}C labeled propylene oxide samples were purchased from MilliporeSigma.

2) Rotational Spectroscopic Study of 2-Phenylpropionic Acid

The sample of 2-phenylpropionic acid was loaded into the CP-FTMW spectrometer

directly from the manufacturer's vial with no additional work up. First, a monomer spectrum was collected by heating the sample reservoirs to 130°C with a backing pressure of ~2 atmospheres using neon. The spectrum was collected in the 2-8 GHz frequency range and in the 6-18 GHz range. Next, gas tanks of 0.1% mixtures of propylene oxide in neon were made, and the 2-phenylpropionic acid was chiral tagged using the previously discussed methodology with the racemic tag. Subsequently, the enantiopure (*S*)-(+)-2-phenylpropionic acid was tagged with (*S*)-(-)-propylene oxide under the same conditions. The next chiral tag used was butynol. Additional sample of racemic 2-phenylpropionic acid was loaded into the nozzles and heated to 130°C. To induce complexation with butynol, the 0.1% mixture was made in a stainless-steel external reservoir that housed a small beaker. 100 µL of butynol was placed in the beaker and neon was added via an inlet to the reservoir. An outlet on the reservoir was pressure regulated to allow mixing of the tag and neon. The seeded chiral tag gas was then pulsed with a backing pressure of 2 atm. Finally, the 0.1% propylene oxide-1,3-$^{13}C_2$ chiral tag mixture in neon was made similar to the parent isotope propylene oxide and introduced to the sample in the same conditions.

3) Computational Chemistry Calculations

Quantum chemical calculations for the monomer and noncovalent complexes were performed on the Gaussian16 software.[8] The theoretical structure and rotational constants for the 2-phenylpropionic acid monomer are shown in Figure 5.1. Chiral tag complexes for the homochiral species, the (-)-(-) and (+)-(+) combinations, and the heterochiral species, (+)-(-) and (-)-(+) combinations, are given in Figure 5.2-5.3 and Table 5.1. Rotational parameters and binding

energies for the complexes were calculated using counterpoise corrections and provided in Table 5.2. The rotational constants for 1,3-^{13}C propylene oxide noncovalent complexes are given in Table 5.3. All calculations used the B3LYPD3BJ method and def2TZVP basis set. All final fits and simulations for the rotational parameters were done using SPCAT/SPFIT and Kisiel's PROSPE package.[9, 10]

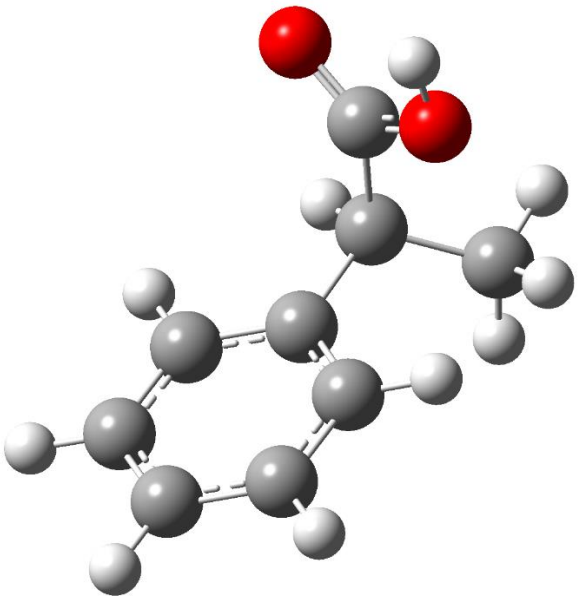

Figure 5.1: 2-phenylpropionic acid monomer theoretical structure optimized with a B3LYPD3BJ level of theory and def2tzvp basis set.

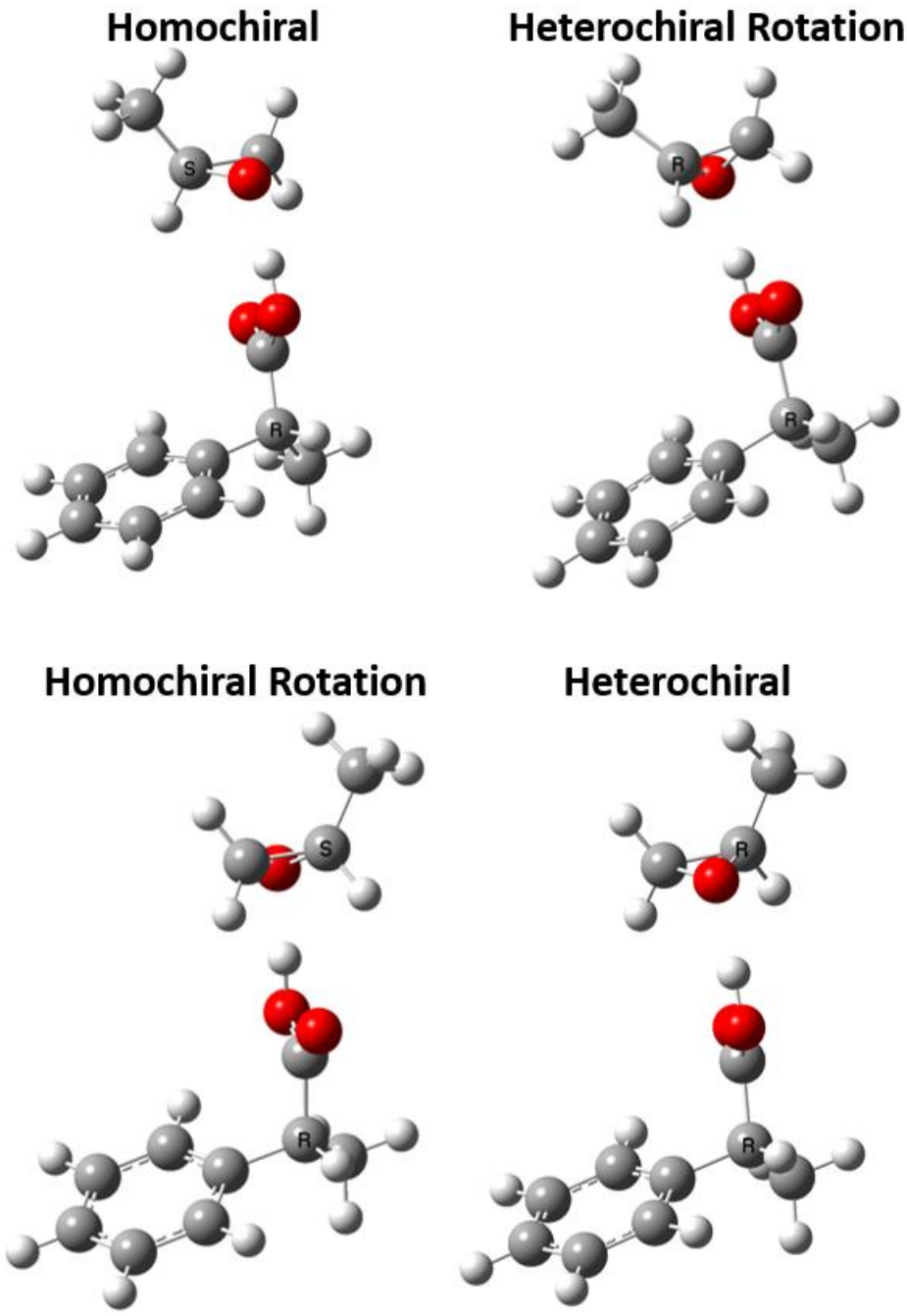

Figure 5.2: Theoretical structures of the noncovalent bound propylene oxide and 2-phenylpropionic acid using B3LYPD3BJ and def2tzvp basis set. Structures labeled heterochiral refer to the combinations of opposite sign optical activity, whereas homochiral structures refer to the combinations with the same sign of optical activity. The labeled rotation refers to the lowest energy optimized diastereomer complex structure after a 180° rotation.

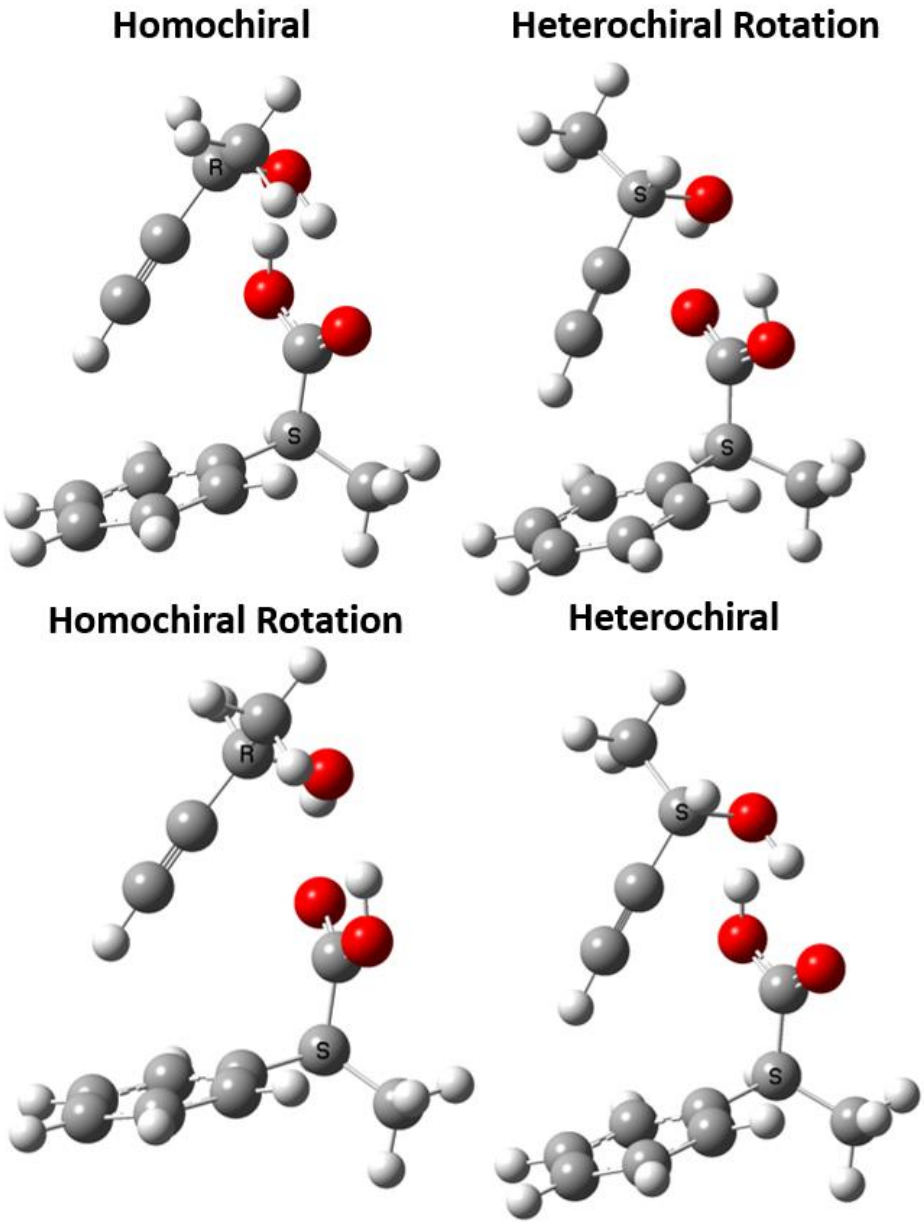

Figure 5.3: Theoretical structures of the noncovalent bound butynol and 2-phenylpropionic acid using B3LYPD3BJ and def2tzvp basis set. Structures labeled heterochiral refer to the combinations of opposite sign optical activity, whereas homochiral structures refer to the combinations with the same sign of optical activity. The labeled rotation refers to the lowest energy optimized diastereomer complex structure after a 180° rotation.

Table 5.1: Table of theoretical rotational parameters calculated using B3LYPD3BJ with def2TZVP basis set of the 2-phenylpropionic acid-propylene oxide complexes (top) and the 2-phenylpropionic acid-butynol complexes (bottom). Complexes include the lowest energy tag structures as well as the 180° rotation of the carboxylic acid group and tag.

PO Complex	Homochiral Rotation	Heterochiral	Heterochiral Rotation	Homochiral
A (MHz)	1168.0015	1162.1632	945.3539	958.6826
B (MHz)	257.6398	259.3680	289.0637	287.0324
C (MHz)	241.0804	241.5160	254.7053	253.4340
μ_a (D)	-1.43	-1.26	-1.12	1.15
μ_b (D)	-0.421	-0.532	-0.921	-0.835
μ_c (D)	0.258	-0.617	0.233	0.602
E (Hartrees)	-692.9028823	-692.9040413	-692.9029425	-692.904162
ΔE (cm^{-1})	281	27	268	0
Butynol Complex	Homochiral Rotation	Heterochiral	Heterochiral Rotation	Homochiral
A	725.6671	735.2231	733.711	723.7651
B	377.0952	372.897	375.2165	379.2183
C	296.2988	290.3417	293.0592	298.7285
μ_a (D)	1.13	1.03	1.17	-1.12
μ_b (D)	1.04	1.13	1	1.08
μ_c (D)	-0.674	0.309	-0.269	0.079
E (Hartrees)	-730.9987343	-730.9997777	-730.9986131	-730.9997186
ΔE (cm^{-1})	229	0	256	13

Table 5.2: Table of theoretical rotational parameters calculated using B3LYPD3BJ with def2tzvp basis set and using counterpoise correction of the 2-phenylpropionic acid-propylene oxide complexes(top) and the 2-phenylpropionic acid-butynol complexes (bottom). Complexes include the lowest energy tag structures as well as the 180° rotation of the carboxylic acid group and tag.

PO Complex	Homochiral Rotation	Heterochiral	Heterochiral Rotation	Homochiral
A (MHz)	1176.4416	1164.1560	951.4320	945.0001
B (MHz)	256.6292	258.8527	287.3397	289.9872
C (MHz)	240.5539	241.4030	253.6827	254.8250
μ_a (D)	-1.34	-1.31	-1.17	-1.14
μ_b (D)	-0.554	-0.513	-0.906	-0.898
μ_c (D)	0.260	-0.616	0.243	-0.607
E (Hartrees)	-692.9017764	-692.9029601	-692.9018339	-692.90303
ΔE (cm^{-1})	275	15	263	0
Raw Complexation Energy (kcal/mol)	-13.04	-12.65	-13.08	-12.69
Corrected Complexation Energy (kcal/mol)	-12.35	-11.97	-12.39	-12.01

Butynol Complex	Homochiral Rotation	Heterochiral	Heterochiral Rotation	Homochiral
A (MHz)	725.1906	734.1664	732.9758	723.0917
B (MHz)	375.7202	372.0038	374.1782	378.1203
C (MHz)	295.1883	289.6582	292.3579	297.9585
μ_a (D)	1.12	-1.02	-1.16	1.05
μ_b (D)	-1	-1.09	-0.969	-1.09
μ_c (D)	0.647	0.295	-0.248	0.108
E (Hartrees)	-730.9971861	-730.998256	-730.9971248	-730.99824
ΔE (cm^{-1})	235	0	248.27	4
Raw Complexation Energy (kcal/mol)	-15.61	-15.67	-15.82	-15.61
Corrected Complexation Energy (kcal/mol)	-14.7	-14.51	-14.89	-14.69

Table 5.3: Table of theoretical rotational parameters calculated using B3LYPD3BJ with def2tzvp basis set and using counterpoise correction of the 2-phenylpropionic acid-1,3-^{13}C propylene oxide complexes. Complexes include the lowest energy tag structures as well as the 180° rotation of the carboxylic acid group and tag.

1,3-^{13}C PO Complex	Homochiral Rotation	Heterochiral	Heterochiral Rotation	Homochiral
A (MHz)	1169.3239	1157.5521	942.4866	936.3895
B (MHz)	251.4459	253.6093	281.6800	284.2928
C (MHz)	235.7311	236.6044	248.6864	249.8342
μ_a (D)	-1.34	-1.31	-1.18	-1.15
μ_b (D)	-0.549	-0.504	-0.897	-0.888
μ_c (D)	0.257	-0.619	0.243	-0.610
E (Hartrees)	-692.9017764	-692.9029601	-692.9018339	-692.90303
ΔE (cm^{-1})	275	15	263	0

III. Results and Discussion

1) 2-Phenylproprionic Acid Monomer

The 2-phenylpropionic acid monomer spectra were collected with the 2-8 GHz and 6-18 GHz CP-FTMW spectrometer set ups. In the 6-18 GHz setup, a 1.6 million average spectrum was obtained. A Kraitchman substitution structure was also created and compared to the theoretical structure with both ^{13}C and ^{18}O isotopologues observed in natural abundance (Figure D1). The only conformationally flexible part of the molecule is the carboxylic acid group, which can rotate 180°, which becomes an issue for chiral tagging. However, only one conformation was observed. The lack of another observable spectrum from different conformations of the carboxylic acid group suggests the higher energy conformation was cooled into the lower energy conformation of the carboxylic acid in the seeded molecular beam. Theoretical constants for the two conformations are provided in Table D1, with experimentally fit rotational parameters also included, and Figure D2.

shows the experimental monomer spectrum with the one fit observed. As shown, the higher energy conformer is almost 400 cm^{-1} higher in energy in a much more energetically unfavorable geometry. The lower energy theoretical geometry has the hydroxyl oxygen at a 31.6° dihedral angle with the hydrogen on the adjacent carbon, while the higher energy conformation has the carbonyl oxygen at a 16° dihedral angle with the hydrogen. This much higher energy conformation may cool to the lower energy conformation of the chiral tag complexes leaving one structure for both diastereomer complexes to increase the confidence of assigning absolute configuration. However, possible favorable interaction within the chiral tag complex could allow for the other structure to exist, so the chiral tagging of 2-phenylpropionic acid was explored.

2) 2-Phenylpropionic Acid Chiral Tag

2-phenylpropionic acid was tagged with both racemic propylene oxide and enantiopure (*S*)-(-)-propylene oxide. As shown in Figure 5.2, the rotation of the carboxylic acid group produces two sets of isomers for each of the diastereomer complexes. The binding motif of the complexes are all the same with the hydroxyl hydrogen pointing towards the lone pair on the epoxide carbon of propylene oxide to form a hydrogen bond and the two hydrogens on the epoxide carbons point towards the carbonyl oxygen for some favorable electrostatic interactions. These form pairs that have very similar rotational constants between two of the diastereomer complexes. The rotational constants are shown in Table 5.1, their values are within 1% of each other, i.e. within the difference of theory and experiment that is normally observed in rotational constants of noncovalently bound complexes. Again, the energy of rotation of the carboxylic acid group is fairly high, > 250 cm^{-1}

relative to the lower energy conformation, for both diastereomer complexes. The energy difference is not as high as the rotation in the monomer of 2-phenlpropionic acid, suggesting the propylene oxide stabilizes this conformation of the 2-phenylproionic acid.

In the racemic spectrum, two complexes were observed and fit, and the rotational constants are reported in Table 5.4. This indicates that two of the conformations cool out in the pulsed jet regardless of the approximately 100 cm^{-1} reduction in energy of the conformation when chiral tagged with propylene oxide. A sample of (*S*)-(+)-2-phenylpropionic acid was then tagged with (*S*)-(-)-propylene oxide to validate that the rotational constants of the heterochiral complex did remain. Figure 5.4 shows a zoomed in part of the spectra of the racemic and the enantiopure propylene oxide tag of 2-phenylpropionic acid with corresponding fit homochiral and heterochiral

Table 5.4: The table of fit rotational parameters for complexes of propylene oxide and 2-phenylpropionic acid and butynol and 2-phenylpropionic acid.

Tag	Propylene Oxide		Butynol	
	Homochiral	Heterochiral	Homochiral	Heterochiral
A /MHz	944.0024(33)	1158.8601(35)	722.8016(17)	733.5281(15)
B /MHz	291.16263(67)	259.88255(66)	372.67577(98)	366.47906(91)
C /MHz	255.20900(69)	241.51474(70)	294.88785(74)	286.48955(67)
Δ_J (KHz)	0.1223(69)	0.0465(15)	0.0446(36)	0.0328(31)
Δ_{Jk} (KHz)	-1.105(23)	-0.659(17)	-0.072(24)	-0.016(16)
Δ_k (KHz)	---	---	---	---
δ_J (KHz)	0.0337(13)	0.0103(11)	0.0093(21)	0.0084(18)
δ_k (KHz)	---	---	---	---
RMS /kHz	5.67	4.87	5.56	10.51

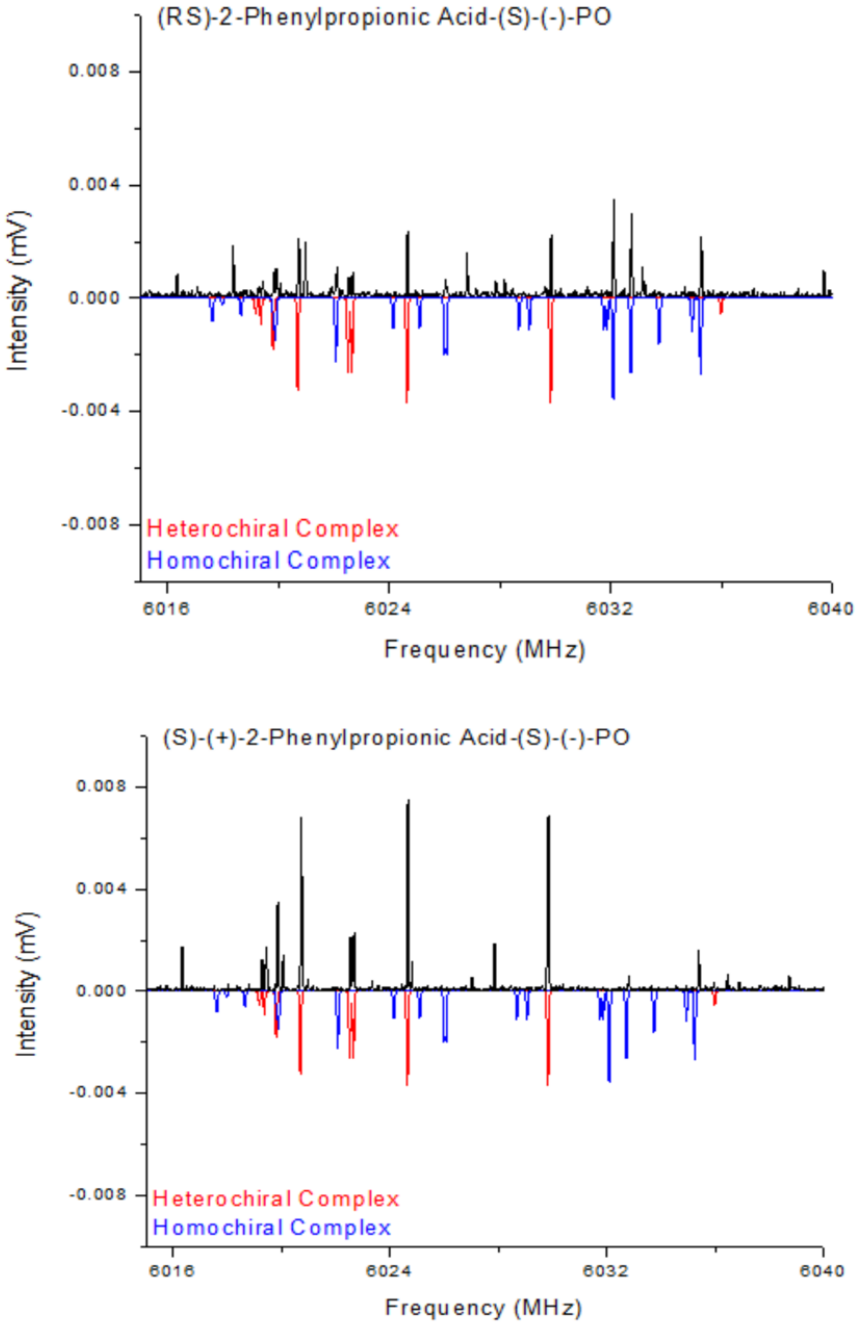

Figure 5.4: Zoomed in part of the chiral tag spectrum of 2-phenylpropionic acid with propylene oxide. Shown is the observation of the spectrum that disappears, on use of the enantiopure tag only one spectrum remains.

Simulations on the bottom. Both complexes are present in the racemic tag measurement, and only the heterochiral complex remains in the enantiopure spectrum. This further validates that these rotational constants belong to the heterochiral species and that the higher energy complexes are cooled out and not observed.

For analytical purposes, an analyte may not have an enantiopure commercial form readily available, especially if it is a reaction product being analyzed for the first time. Additionally, if the sample is not completely enantiopure, both spectra would still be observed. In the case of propylene oxide noncovalently bound to 2-phenylpropionic acid, the rotational constants are very similar, so a new chiral tag was chosen that potentially could cause a more substantial change in the rotational constants. Butynol was chosen since the alkyne group is linear and rigid and has the possibility of pointing in different directions with the hydroxyl hydrogen preferably being anti to the hydrogen on the asymmetric carbon of butynol. However, all theoretical structures have the hydrogen on the alkyne group pointing towards the top of the phenyl group for favorable electrostatic interactions with the pi electrons. The hydroxyl group on the butynol then rotates from anti to the hydrogen and anti to the methyl group. All structures have a double hydrogen bond motif between the hydrogen of the carboxylic acid to the hydroxyl oxygen of butynol and from the hydroxyl hydrogen on the butynol to the carbonyl oxygen on the carboxylic acid. The theoretical rotational constants are given in Table 5.1, but the predicted constants are all very similar. However, the structures that correspond to the rotation of the carboxylic acid group for the diastereomer complexes have constants closer to those of the other structure of the same diastereomer complex. The difference in rotational constants is greater (~2%) for the lowest energy diastereomer complex structures than the rotational constants for the propylene oxide complexes.

As before, the chiral tag lowers the energy difference between the two conformations of the carboxylic acid monomer. The racemic and enantiopure butynol chiral tag spectrum were collected and analyzed, and the disappearance of one of the spectra was observed. The experimentally fit rotational constants are found in Table 5.4 and again only two chiral tag complexes were observed in the spectrum. This also supports that the other conformation is cooled out in the pulsed jet and only the lower energy conformations will be observable in the chiral tag spectrum. Nevertheless, there are favorable interactions between functional groups on the chiral tags and the analyte other than the hydrogen bond that might be strong enough to stabilize the higher energy conformation of the carboxylic acid group leading to the observation of both structures.

The electronic properties of the molecule can be used to provide greater confidence in the assignment of rotational constants. However, the electric dipole moment components for these carboxylic acid complexes are all similar. Figure 5.5 and Figure 5.6 show the theoretical relative intensities of the squares of the electric dipole moment components for all four carboxylic acid complexes and the corresponding experimentally derived relative intensities. For the Propylene oxide complex the c electric dipole moment component for heterochiral complex increases confidence for that assignment, as the corresponding homochiral complex has weak predicted c-types. Similarly, the homochiral complex and its corresponding heterochiral complex c-type components increases confidence in the assignment. However, the butynol theoretical calculations predicted only one structure with a strong b-type spectrum, but both experimental scaling factors for the fit contained higher b-type mean scale factors. Overall, the dipole analysis does add some confidence to assigning the absolute configuration, but higher confidence is desired for practical analytical settings. Summary of the calculated scale factors can be found in the Table D2 and D3.

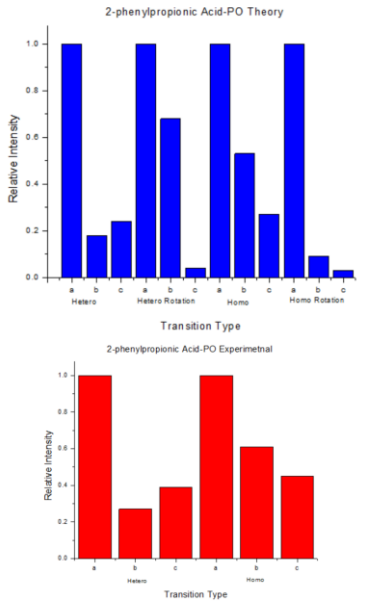

Figure 5.5: Relative intensities of the theoretical propylene oxide (PO) complexes (top) and the experimentally fit complexes (bottom). The structures labeled "rotation" involve a 180°rotation of the carboxylic acid functional group for the corresponding complex.

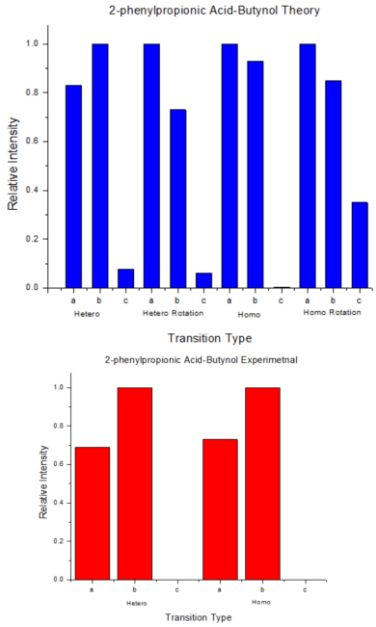

Figure 5.6: Relative intensities of the theoretical butynol complexes (top) and the experimentally fit complexes (bottom). The structures labeled "rotation" involve a 180°rotation of the carboxylic acid functional group for the corresponding complex

3) Counterpoise Corrected Calculations

This argument relies on energy calculations for the assignment of absolute configuration, so known issues in the calculations need to be examined. A counterpoise corrected calculation was performed which allows for the determination of complexation energies to determine the reason for the observation of only one of the conformers. Counterpoise corrected calculations are used when studying intermolecular interactions between multiple monomers to correct for the basis set superposition error, BSSE.[11] The BSSE is caused by the "borrowing" of basis functions of one monomer to stabilize itself, and likewise for the other monomer.[12] This usually results in overbound complexes, or a shortening of the intermolecular distances.[13-15] The common method to account for this is the Boys-Bernardi counterpoise method where both monomers are calculated with only its basis functions and then subtracted from the monomer calculated in the presence of the other monomers basis functions:[13, 16]

$$\Delta E_{BSSE}(A) = E_A(AB) - E_A(A) \qquad (5.1)$$

Where $\Delta E_{BSSE}(A)$ is the difference in energy due to basis set superposition error of monomer A, $E_A(AB)$ is the energy calculated of monomer A with both basis sets, and $E_A(A)$ is the energy of monomer A with only its basis functions. When calculating the energy of the monomer with the dimer basis functions, the basis functions of the other monomer are located on the atomic centers with the electrons and nuclear charges ignored, which are referred to as "ghost functions".[12, 13]

A significant difference in the complexation energy would increase the confidence that there would only be one conformation of the carboxylic acid group for both diastereomer complexes. The counterpoise corrections are presented in Table 5.2. The raw complexation energies are the energies calculated without counterpoise and the corrected complexation energies

are the energies with counterpoise corrected energies. Recent computational studies have suggested that an average of the raw and counterpoise corrected energies is more accurate as the raw complexation energies converge from above and the counterpoise energies converge from the bottom to experimental values as the basis function approaches a complete basis set limit.[11, 17] As can be seen for both butynol and propylene oxide complexes the binding energies both raw and corrected are very similar with the largest difference between all four species being ~0.4 kcal/mol. This is not a significant difference to account for the lack of observation of the conformation of the rotated species for either diastereomer complex. In both cases the binding energies for the rotated species are higher than that of the lower energy complexes, except in the case of the homochiral butynol chiral tag complex as they are equal in complexation energy. As the complexation energies was not enough to increase confidence in absolute configuration assignment, a new method to increase confidence was assessed.

4) Isotopically Labeled Chiral Tag

Ways to improve absolute configuration assignments for diastereomer pairs using theoretical and experimental spectroscopy results is a current area of research in the field of NMR.[18] As with theoretical rotational constants, calculated NMR shifts are subjected to systematic errors in the theoretical calculations. Many developed approaches aim to calculate the probability that a structure amongst a set of structures is the most likely candidate for each shift observed in an NMR spectrum.[19-22] Methods, such as CP3, use a difference measurement for the two calculated diastereomers to cancel systematic error compared to differences in the experimental shift.[23] NMR

has seen a large improvement and development of increasing accuracy of assigning structures using quantum chemical calculations. An important part of this area of research is that not only do the calculations help identify to which diastereomer an experimental spectrum might belong, but also aid in quantifying the confidence in each assignment.

In this section, concepts from NMR to increase the confidence of assigning theoretical structural data for diastereomers with experimental spectral data will be used. In switching from propylene oxide to 1,3-^{13}C-propylene oxide, principal moments-of-inertia are altered. These principal moments-of-inertia will increase or decrease relative to one another by using the isotopically labeled tag, and comparing the differences in moments-of-inertia between theory and experiment will improv the confidence in assigning absolute configuration to each diastereomer. Table 5.5 shows the experimentally fit rotational constants for the two observed spectra using the isotopically labeled propylene oxide racemic tag. Like NMR approaches, utilizing the differences in the theoretical moments-of-inertia will eliminate systematic errors from the theoretical calculations. The moments-of-inertia are calculated by solving Eq. 1.2 using experimental and theoretical rotational constants, Eq. 5.2.

$$I_x = \frac{\hbar^2}{2X} \tag{5.2}$$

I_x is the moment-of-inertia of the x principal axis (x = a, b, or c) and X denotes the respective rotational constant (X = A, B or C). This method uses the difference in the observed change in moments-of-inertias for propylene oxide and 1,3-^{13}C-propylene oxide and the difference in the theoretically calculated moments-of-inertias when using the different tags, Eq. 5.3

$$\Delta I_{obs,calc} = I_{obs,calc}^{propylene\ oxide} - I_{obs,calc}^{C^{13}-propylene\ oxide} \quad (5.3)$$

Figure 5.7 shows the two possible options for assigning the rotational constant to each of the pairs of diastereomer complexes for which the rotational constants were similar. Option 1 is the case where we assign the experimentally observed rotational constants with the A constant of the homochiral species is approximately 1160 MHz and the rotational constants with the A constant of the heterochiral species is approximately 950 MHz. Option 2 shows the result if one were to assign the rotational constants to the opposite diastereomer complex from option 1. The Ixx1 where (x = a, b, or c) is compared to the experimental rotational constants that have A ≈ 1160 MHz, and Ixx2 are the rotational constants for A ≈ 950 MHz. The difference in the shift in moments-of-inertia from switching to the isotopically labeled ^{13}C-propylene oxide has better (observed-calculated) agreement from both experimental spectra for option 2, where the predicted lowest energy conformations for both diastereomer complexes are assigned to the respective experimental

Table 5.5: Experimentally fit rotational constants of chiral tag complexes of 2-phenylpropionic acid using 1,3-^{13}C-propylene oxide as the chiral tag.

	Fit 1	Fit 2
A / MHz	1152.5386(36)	935.5500(26)
B / MHz	254.59764(56)	285.44354(63)
C / MHz	236.73357(60)	250.22488(66)
Δ_J (MHz)	0.0000458(12)	0.0001212(21)
Δ_{Jk} (MHz)	-0.000638(10)	-0.001089(14)
Δ_k (MHz)	-	0.00323(16)
δ_J (MHz)	0.0000100(10)	0.0000326(10)
δ_k (MHz)	-	0.00019(11)
RMS / kHz	4.1	2.5
N	141	206

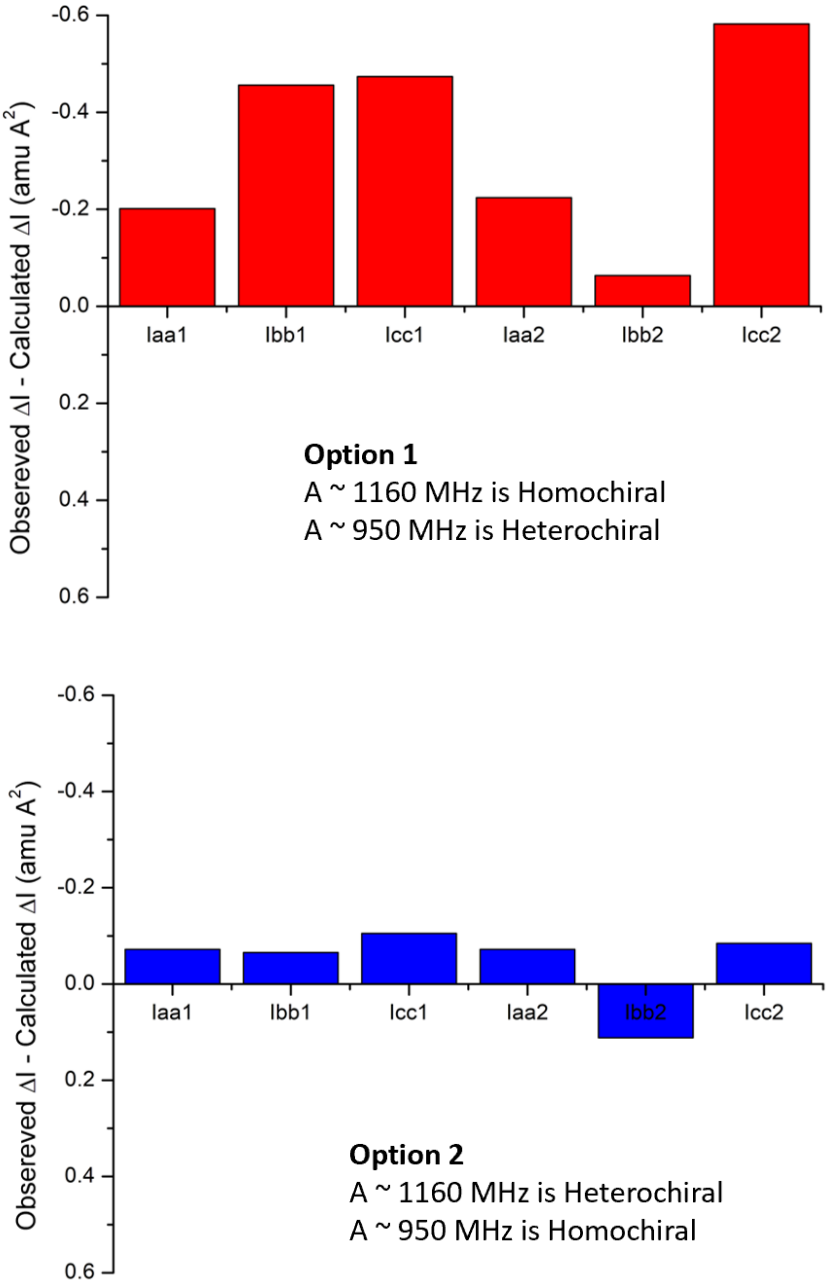

Figure 5.7: Calculation of the difference of the observed shifts in moments-of-inertia using the experimental and theoretical rotational constants. Option 1 and 2 correspond to choosing different conformations for heterochiral and homochiral structures that fit the experimental rotational constants.

rotational constants. Changes in the moments-of-inertia between the parent isotopologue propylene oxide and the 1,3-^{13}C-propylene oxide was as high as ~40 amu Å^2. The quantum chemistry calculations were able to predict the shifts in the moments-of-inertia to ~0.1 amu Å^2, giving high confidence that the assignment of the absolute configuration is correct.

IV. Conclusion

As seen from the theoretical optimization of the chiral tag complexes for both butynol and propylene oxide, diastereomer complex pairs with very similar rotational constants are predicted from the 180° rotation of the carboxylic acid group. This could lead to decreased confidence in the assignment of absolute configuration of the analyte in a chiral tag measurement of carboxylic acids. A large energy difference for the rotation of the carboxylic acid was calculated for the monomer with almost a 400 cm^{-1} energy difference. This energy difference is lowered by the noncovalent interactions between 2-phenylpropionic acid and the chiral tags, but the energy difference is still large, > 250 cm^{-1}. Observation of only two chiral tag complexes in the rotational spectrum does support that the formation of these conformations are cooled out in the seeded molecular beam. Still, different approaches were used to study the system of chiral tagging carboxylic acids to improve confidence in assignment.

Butynol was chosen as a different chiral tag to try to increase the difference in rotational constants between the diastereomer pairs. The rotational constants were altered slightly, but the constants were still within error. Instead of having two different pairs of rotational constants, all the four structures had similar values. This choice of chiral tag did not help to increase the

confidence on assigning absolute configuration of the carboxylic acid as all structures ended up having the alkyne hydrogen directed towards the electron density of the phenyl group, but it does not rule out the possibility that a different chiral tag would be able to achieve large discrimination between the pairs. A good chiral tag would be a small volatile chiral molecule that is relatively cheap, and there remains many candidates to be screened for use as in chiral tag rotational spectroscopy.

Next, the complexation energy of the two chiral tag complexes was studied using counterpoise correction of the theoretical structures. It was calculated that the complexation energies were all within ~0.4 Kcal/mol of each other for both the butynol and propylene oxide complexes. Moreover, the higher energy conformers had higher complexation energies than the lowest energy complexes. The complexation energies did not help increase the confidence in assignment, as the lack of observation of the higher energy complexes was not explained due to significantly lower complexation energies.

Finally, the last approach to increase confidence in the absolute configuration assignment was to remove systematic error from the quantum chemical calculations and test different combinations of choices for a set of structures. This Bayesian approach used an isotopically labeled ^{13}C-propylene oxide chiral tag to cause a shift in the principal moments-of-inertia, which can be calculated in both experimental and theoretical rotational constants. The difference in the shifts of rotational constants were then compared to increase confidence in the assigning the structure from the theoretical predictions. This method utilizes the sensitivity of rotational spectroscopy to differences in mass, allowing for verification of the change in mass at specific atomic coordinates when switching to the isotopically labeled tag. This allows for high confidence assignments

without the need for excessive sample consumption to observe ^{13}C rotational spectra in natural abundance for the atomic coordinate data.

This method of increasing confidence of theoretical structural calculations has been going on in the field of NMR spectroscopy for some time. A major difference between the NMR and chiral tag approaches is the use of an additional reagent. The isotopically labeled chiral tag also is more expensive, increasing overall cost. Also, an additional measurement is required to be able preform this analysis. In support of this method, this type of measurement only needs to be performed once, and once the assignment is made for the system it does not need to be made again. Another way to decrease measurement time is the possibility to create a gas tank that contains both the parent isotopologue propylene oxide and the isotopically labeled propylene oxide. This would allow for the observation of both species in the same spectrum, but the overall intensity for each species would decrease and spectral complexity would increase.

V. References

1. Ballatore, C.; Huryn, D. M.; Smith, A. B., 3rd, Carboxylic acid (bio)isosteres in drug design. *ChemMedChem* **2013,** *8* (3), 385-395.

2. Min, C.; Seidel, D., Asymmetric Brønsted acid catalysis with chiral carboxylic acids. *Chemical Society Reviews* **2017,** *46* (19), 5889-5902.

3. Guo, K.; Li, L., High-Performance Isotope Labeling for Profiling Carboxylic Acid-Containing Metabolites in Biofluids by Mass Spectrometry. *Analytical Chemistry* **2010,** *82* (21), 8789-8793.

4. Layden, B. T.; Angueira, A. R.; Brodsky, M.; Durai, V.; Lowe, W. L., Short chain fatty acids and their receptors: new metabolic targets. *Translational Research* **2013,** *161* (3), 131-140.

5. Jarboe, L.; Royce, L.; Liu, P., Understanding biocatalyst inhibition by carboxylic acids. *Frontiers in Microbiology* **2013,** *4* (272).

6. Blaskovich, M. A. T., Unusual Amino Acids in Medicinal Chemistry. *Journal of Medicinal Chemistry* **2016,** *59* (24), 10807-10836.

7. Hajduk, P. J.; Bures, M.; Praestgaard, J.; Fesik, S. W., Privileged Molecules for Protein Binding Identified from NMR-Based Screening. *Journal of Medicinal Chemistry* **2000,** *43* (18), 3443-3447.

8. Frisch, M. J.; Trucks, G. W.; Schlegel, H. B.; Scuseria, G. E.; Robb, M. A.; Cheeseman, J. R.; Scalmani, G.; Barone, V.; Petersson, G. A.; Nakatsuji, H.; Li, X.; Caricato, M.; Marenich, A. V.; Bloino, J.; Janesko, B. G.; Gomperts, R.; Mennucci, B.; Hratchian, H. P.; Ortiz, J. V.; Izmaylov, A. F.; Sonnenberg, J. L.; Williams; Ding, F.; Lipparini, F.; Egidi, F.; Goings, J.; Peng, B.; Petrone, A.; Henderson, T.; Ranasinghe, D.; Zakrzewski, V. G.;
Gao, J.; Rega, N.; Zheng, G.; Liang, W.; Hada, M.; Ehara, M.; Toyota, K.; Fukuda, R.; Hasegawa, J.; Ishida, M.; Nakajima, T.; Honda, Y.; Kitao, O.; Nakai, H.; Vreven, T.; Throssell, K.; Montgomery Jr., J. A.; Peralta, J. E.; Ogliaro, F.; Bearpark, M. J.; Heyd, J. J.; Brothers, E. N.; Kudin, K. N.; Staroverov, V. N.; Keith, T. A.; Kobayashi, R.; Normand, J.; Raghavachari, K.; Rendell, A. P.; Burant, J. C.; Iyengar, S. S.; Tomasi, J.; Cossi, M.; Millam, J. M.; Klene, M.; Adamo, C.; Cammi, R.; Ochterski, J. W.; Martin, R. L.; Morokuma, K.; Farkas, O.; Foresman, J. B.; Fox, D. J. *Gaussian 16 Rev. C.01*, Wallingford, CT, 2016.

9. Kisiel, Z. PROSPE, programs for rotational spectroscopy. http://info.ifpan.edu.pl/~kisiel/prospe.htm.

10. Pickett, H. M., The fitting and prediction of vibration-rotation spectra with spin interactions. *Journal of Molecular Spectroscopy* **1991,** *148* (2), 371-377.

11. Brauer, B.; Kesharwani, M. K.; Martin, J. M. L., Some Observations on Counterpoise Corrections for Explicitly Correlated Calculations on Noncovalent Interactions. *Journal of Chemical Theory and Computation* **2014,** *10* (9), 3791-3799.

12. Richard, R. M.; Bakr, B. W.; Sherrill, C. D., Understanding the Many-Body Basis Set Superposition Error: Beyond Boys and Bernardi. *Journal of Chemical Theory and Computation* **2018,** *14* (5), 2386-2400.

13. Sherrill, C. D., Counterpoise correction and basis set superposition error. *School of Chemistry and Biochemistry, Georgia Institute of Technology* **2010**.

14. Kruse, H.; Grimme, S., A geometrical correction for the inter-and intra-molecular basis set superposition error in Hartree-Fock and density functional theory calculations for large systems. *The Journal of chemical physics* **2012,** *136* (15), 04B613.

15. Salvador, P.; Paizs, B.; Duran, M.; Suhai, S., On the effect of the BSSE on intermolecular potential energy surfaces. Comparison of a priori and a posteriori BSSE correction schemes. *Journal of Computational Chemistry* **2001,** *22* (7), 765-786.

16. Boys, S. F.; Bernardi, F., The calculation of small molecular interactions by the differences of separate total energies. Some procedures with reduced errors. *Molecular Physics* **1970,** *19* (4), 553-566.

17. Burns, L. A.; Marshall, M. S.; Sherrill, C. D., Comparing Counterpoise-Corrected, Uncorrected, and Averaged Binding Energies for Benchmarking Noncovalent Interactions. *Journal of Chemical Theory and Computation* **2014,** *10* (1), 49-57.

18. Marcarino, M. O.; Zanardi, M. a. M.; Cicetti, S.; Sarotti, A. M., NMR Calculations with Quantum Methods: Development of New Tools for Structural Elucidation and Beyond. *Accounts of Chemical Research* **2020,** *53* (9), 1922-1932.

19. Smith, S. G.; Goodman, J. M., Assigning Stereochemistry to Single Diastereoisomers by GIAO NMR Calculation: The DP4 Probability. *Journal of the American Chemical Society* **2010,** *132* (37), 12946-12959.

20. Ermanis, K.; Parkes, K.; Agback, T.; Goodman, J., Doubling the power of DP4 for computational structure elucidation. *Organic & biomolecular chemistry* **2017,** *15* (42), 8998-9007.

21. Howarth, A.; Ermanis, K.; Goodman, J. M., DP4-AI automated NMR data analysis: straight from spectrometer to structure. *Chemical science* **2020,** *11* (17), 4351-4359.

22. Xin, D.; Jones, P.-J.; Gonnella, N. C., D i CE: Diastereomeric in Silico Chiral Elucidation, Expanded DP4 Probability Theory Method for Diastereomer and Structural Assignment. *The Journal of organic chemistry* **2018,** *83* (9), 5035-5043.

23. Smith, S. G.; Goodman, J. M., Assigning the Stereochemistry of Pairs of Diastereoisomers Using GIAO NMR Shift Calculation. *The Journal of Organic Chemistry* **2009,** *74* (12), 4597-4607.

VI. Appendix D

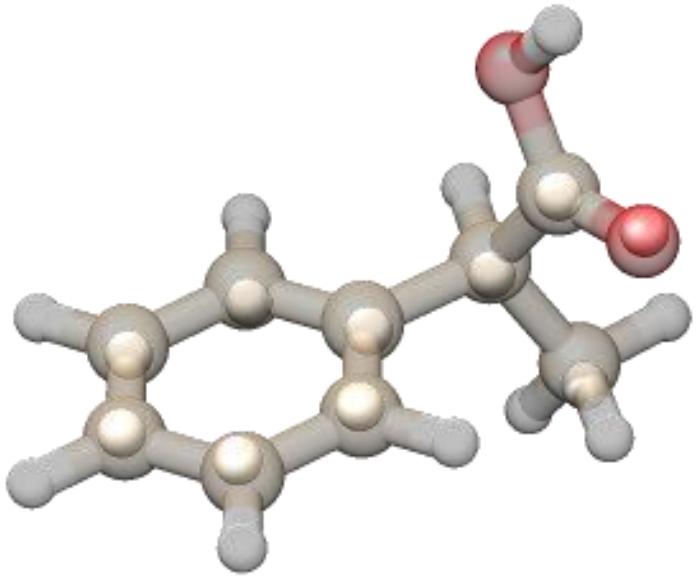

Figure D1: The Kraitchman structure, solid spheres, overlayed with the theoretically calculated structure, transparent ball and stick structure.

Table D1: Table of theoretical rotational parameters and energies of the two conformations of 2-phentlpropionic acid monomer and the experimentally fit rotational parameters.

	Conformer 1	Conformer 2	Experimental
A (MHz)	2060.1812	2072.6990	2060.2172(26)
B (MHz)	714.8942	719.4382	711.7240(42)
C (MHz)	707.2936	693.6552	709.4056(42)
μ_a (D)	0.811	-0.695	-
μ_b (D)	1.23	1.50	-
μ_c (D)	0.334	0.673	-
Δ_J (MHz)	-	-	0.0000913(29)
Δ_{Jk} (MHz)	-	-	0.000483(41)
Δ_k (MHz)	-	-	0.00019(10)
δ_J (MHz)	-	-	0.00000684(93)
δ_k (MHz)	-	-	0.0156(21)
E (Hartrees)	-499.6861	-499.6844	-
ΔE (cm^{-1})	0	372.88	-

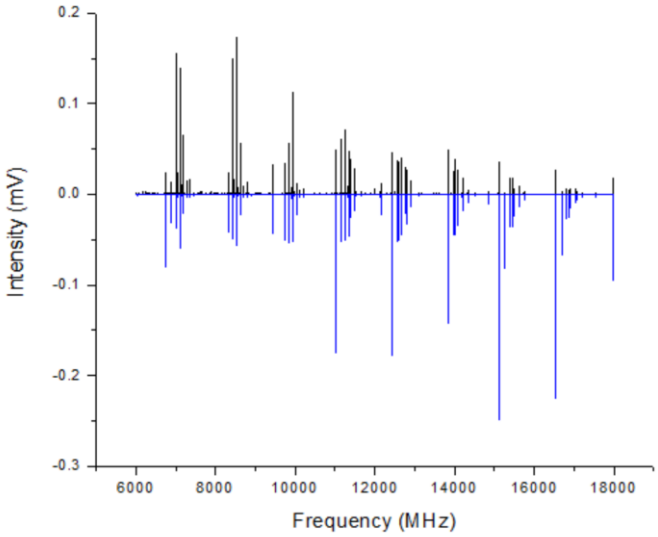

Figure D2: The experimental spectrum of 2-phenylpropionic acid, top, and the simulation of the experimentally fit spectrum, bottom. This shows that all observed transitions in the spectrum belong to one observed conformation of 2-phenylpropionic acid. The intensity falls off at the higher frequencies due to the performance of the traveling wave tube amplifier (twt) used in the instrument at these frequencies.

Table D2: Experimental determined dipole moment component mean scale factors for the hetero- and homochiral butynol complexes.

Complex	Hetero			Homo		
Dipole Component	A	B	C	A	B	C
Mean Scale factor	20.723	28.211	-	20.887	30.324	-
Standard Deviation	7.475	10.723	-	4.964	6.409	-
N	25	25	-	25	25	-
Relative	0.734572	1	0	0.688794	1	0

Table D3: Experimental determined dipole moment component mean scale factors for the hetero- and homochiral propylene oxide complexes.

Complex	Hetero			Homo		
Dipole Component	A	B	C	A	B	C
Mean Scale factor	18.171	5.036	7.155	18.239	11.268	8.162
Standard Deviation	3.972	0.386	1.969	4.229	4.86	2.638
N	25	4	13	25	25	16
Relative	1	0.277145	0.393759	1	0.617797	0.447503

Chapter 6

Potential of Covalent Modification for Chiral Analysis by Rotational Spectroscopy

I. Introduction

In the past chapters, the isomers for chiral tagging involved sampling using chemical intuition to guide where the tag will non-covalently bond to the analyte. This could lead to problems if the analyte does not contain an obvious hydrogen bond site. Covalent derivatization has a great appeal due to the many molecular mechanics programs that are available to sample the conformational space of an analyte as used in VCD. Monomers also will give a boost in sensitivity due to the signal reduction from complexation. In this chapter covalently modification of perfluorinated acids will be studied for chiral analysis with rotational spectroscopy.

The use of perfluorinated compounds have grown rapidly over the past century due to their wide applications. They have been used as refrigerants, surfactants, fire retardants, pesticides, and many more.[1-3] One reason they appeal to industrial and household products is the stability of a fluorine-carbon bond. A fluorine-carbon bond is one of the strongest in organic chemistry making fluorinated molecules highly stable and attractive for material and industrial products.[2-4] Naturally occurring fluorinated organic compounds tend to be rare despite fluorine being the 13th most abundant element in the earth's crust.[5, 6] Fluorinated organic compounds are found to be produced by very few plants and microorganisms and the molecules that are produced are all monofluorinated.[1, 5, 7] Synthetic fluorinated organic compounds, especially fluoropolymers, now have many fluorines bonded. Perfluorooctanoic acid, PFOA, is a commonly used

perfluorochemical chemical that is used to make fluoropolymers. Teflon is one of the most widely used and known of these polymers.

PFOA has been shown to cause liver, testicular, and pancreatic cancers in rats.[8, 9] Fluorinated organic compounds have been shown to exist in low levels in almost the entire US population.[10, 11] Perflourinated compounds are able to linger in the environment because of their stability and build up over time.[12] Emissions of fluorinated organic compounds from major chemical manufacturers into rivers often lead to contaminated drinking water for local citizens and wildlife.[13] Evidence of harmful diseases in humans have been limited and varied.[14, 15] A science panel in 2002-2012 was tasked by a court in West Virginia with finding out the health risk of PFOA, and a 'probable link' to human diseases was concluded.[16-18] In 2020, the authors of the panel revisited further evidence that had been collected since and found only few outcomes had been replicated, but the data was still limited.[19]

Longer chained fluorinated organic compounds were subjected to stricter regulations, and new shorter chain fluorinated organics were then pursued as replacements as they were deemed less toxic.[20] One of these replacements is hexafluoropropylene oxide dimer acid, FRD-903, whose ammonium salt is known by its tradename GenX. This compound is produced by Chemours, a spin-off of Dupont. Concentration levels of FRD-903 have been found to be around 4,500 ng/L in the Cape Fear River in North Carolina, and the same study found a concentration of 474 ng/L in drinking water that is derived from the Cape Fear River.[10, 21-23] The North Carolina Department of Health and Human Services issued a health goal of 140 ng/L in 2017 of FRD-903. The company has admitted to discharging wastewater since 1980 into the Cape Fear River, leaving many perfluorinated compounds in the water.[24] The health effects of these new fluorinated molecules

are currently being studied.[25, 26] Initial studies have shown that it can cause liver, testicular, and pancreatic cancers in rats, similar to that of PFOA. Another study has shown the half-life of GenX appears to be relatively short in humans.[27]

In collaboration with Dr. Willamson of the University of North Carolina, Wilmington, a method of chiral analysis for FRD-903 was needed. The goal of the project was to determine the absolute configuration of a sample of FRD-903 isolated from contaminated field samples collected from soil or water. When FRD is released either through aerial emission or through wastewater, microorganisms may impart an EE through biochemical degradation pathways even if the sample was initially racemic. The rate of the imparted EE could then be measured to establish a time frame of when a site was contaminated with FRD-903. As the initial project goal was to establish absolute configuration, chiral tagging was utilized on a racemic mixture of FRD-903. Additionally, an opportunity to further the chiral analysis methodology of chiral tag rotational spectroscopy with the study of analysis of large molecules. FRD-903 is large for rotational spectroscopy with a mass of 330 g/mol, and as molecules get larger the transition intensity is spread between many rotational energy levels. During the chiral tagging of analytes, usually the chiral tag complexes are only about 1-20% of the monomer signal heights, depending on number of isomers and the electric dipole moment. To avoid this drop in signal level, chiral derivatization via covalent modification would allow for chiral analysis of larger molecules by rotational spectroscopy. Instead of diastereomer complexes, diastereomer molecules could be analyzed by themselves in a CP-FTMW spectrometer to determine enantiomeric excess. This methodology is similar to the chiral derivatization methods used in NMR. A covalent chemical reaction was found to occur when analyzing FRD-903 via regular chiral tagging methodology. A reduction in the monomer spectrum of ~50% is expected

when the chiral tag is introduced, yet the monomer signals almost disappeared when propylene oxide was flowed over the FRD-903 sample. Upon further heating and disconnecting the propylene oxide gas tank, a new spectrum was observed with peak transition intensity at lower frequencies than the FRD-903 spectrum. This suggested a heavier molecule was present, possibly from a chemical reaction. Further investigation by an external reaction of FRD-903 and propylene oxide was performed to test this hypothesis and a reaction was found to have occurred. Further reactions were performed to elucidate the potential of chiral derivatization for the use of chiral analysis of larger molecules by rotational spectroscopy using trifluoroacetic acid to aid in this study.

II. Experimental

1) Materials

Racemic FRD-903 was purchased from ChemCruz as Perfluoro(2-methyl-3-oxahexanoic) acid. Enantiopure FRD-903 was not commercially available. An additional smaller fluorinated carboxylic acid, trifluoroacetic acid, was tested during this study, and was purchased from Synquest Laboratories. Propylene oxide was obtained from TCI. Both (*S*)-propylene oxide and racemic propylene oxide were used in the study and no enantiomeric excess was measured for propylene oxide. Trifluoroisopropyl alcohol was used as a chiral tag. It was obtained from Synquest Laboratories as 1,1,1-trifluoropropan-2-ol for the racemic and (*S*)-1,1,1-trifluoropropan-2-ol with a 99% enantiomeric excess reported in the certificate of analysis.

2) Methods

Each fluorinated carboxylic acid used two methods to probe the reaction product. The reactions were performed externally outside of the spectrometer. External reactions were performed by adding propylene oxide to each carboxylic acid in a 4:1 molar ratio. This higher propylene oxide ratio was used to ensure that as much of the carboxylic acid was reacted as possible. The reactions were highly exothermic and bumping of reactants in the reaction vial at ambient temperature could occur. As a result, the dropwise addition of reactants into the reaction vial that was submerged in an ice bath was utilized. The reaction mixtures were then loaded into the CP-FTMW spectrometer with no further purification or work up. The mixtures were initially pulsed until the monomer spectrum of the propylene oxide was no longer observed before heating the sample to 55°C and 60°C for the trifluoroacetic acid and FRD-903 reaction products, respectively. Reaction products were identified with computational quantum chemical calculations and fit rotational spectroscopic constants. Once the reaction products had been identified, electric dipole moment and enantiomeric excess analysis techniques presented in previous chapters were used to gain understanding of the covalent reactions' potential for chiral analysis of the fluorinated acids species. In the case of the trifluoroacetic acid, the only chiral center of the reaction product was that of the propylene oxide, so the reaction products were enantiomers and could not be identified via normal rotational spectroscopy. As a result, chiral tagging of the trifluoroacetic acid reaction product with a 0.1% trifluoroisopropyl alcohol in Ne gas mixture was performed.

3) Quantum Chemical Calculations

Both epoxide ring-opening reaction products where the ring-opens at the least- and most-substituted carbon with each diastereomer complex were created in Gaussian09.[28] These input files were then submitted to a GMMX conformational search on Biotool's ComputeVOA™ software (BioTools Inc., Jupiter, FL, USA). The software produces conformational outputs as Gaussian files that can then be ran as single-point energy calculations. About 2000 gaussian input files were created with GMMX that used B3LYP Pople's 6-311G++(d,p) method and basis set and including Grimme's D3BJ dispersion correction. Jobs were submitted as batch arrays to UVa's Rivanna supercomputing cluster as upwards of 100 or more output files could be run at once. [29] All the single-point energy calculation output files are processed by a simple Python script that orders the energy and name of the file starting by lowest energy. About 10-15 of the lowest energy structures are then submitted for electronic structure optimizations for determination of the rotational constants from the equilibrium structures using B3LYPD3BJ level of theory with def2TZVP basis set. Complexation calculations were also performed with Gaussian16 for the trifluoroacetic acid noncovalently bonded to trifluoroisopropyl alcohol.[30] All structures were fit using Pickett's SPFIT/SPCAT and Kisiel PROPOSE program packages.[31, 32]

III. Results and Discussion

1) FRD-903 Covalent Modification with Propylene Oxide

As discussed previously, the inspiration to extend chiral analysis by covalent modification of larger molecules was done based on a presumed chemical reaction between FRD-903 (Figure

6.1) and propylene oxide. The observed spectra of FRD-903 monomer, FRD-903 with a 0.1% propylene oxide in neon mixture gas flow, and when the heat was taken off are displayed in Figure 6.2. The largest monomer signals for FRD-903 were ~30 µV, while the new spectrum that appears is ~3µV with peak transition intensities at lower frequencies. In the external reaction mixture of the two monomers, the largest peaks reached about 20µV.

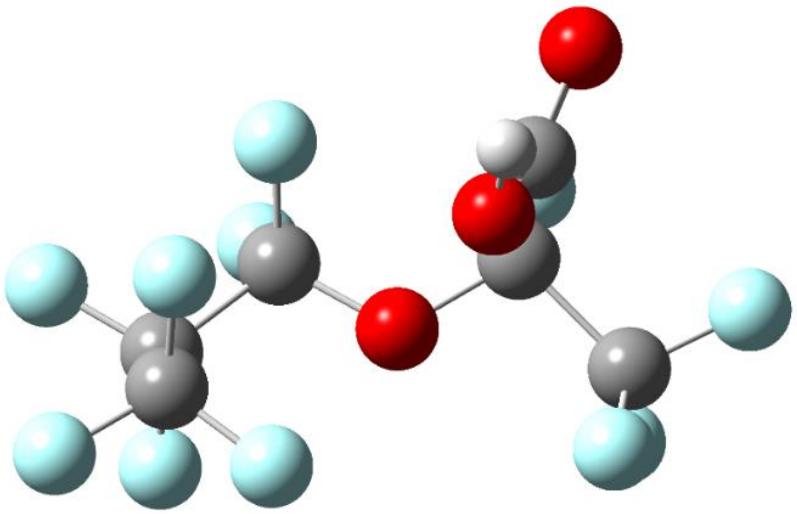

Figure 6.1: The computed optimized structure of FRD-903 using B3LYPD3BJ with def2TZVP basis set.

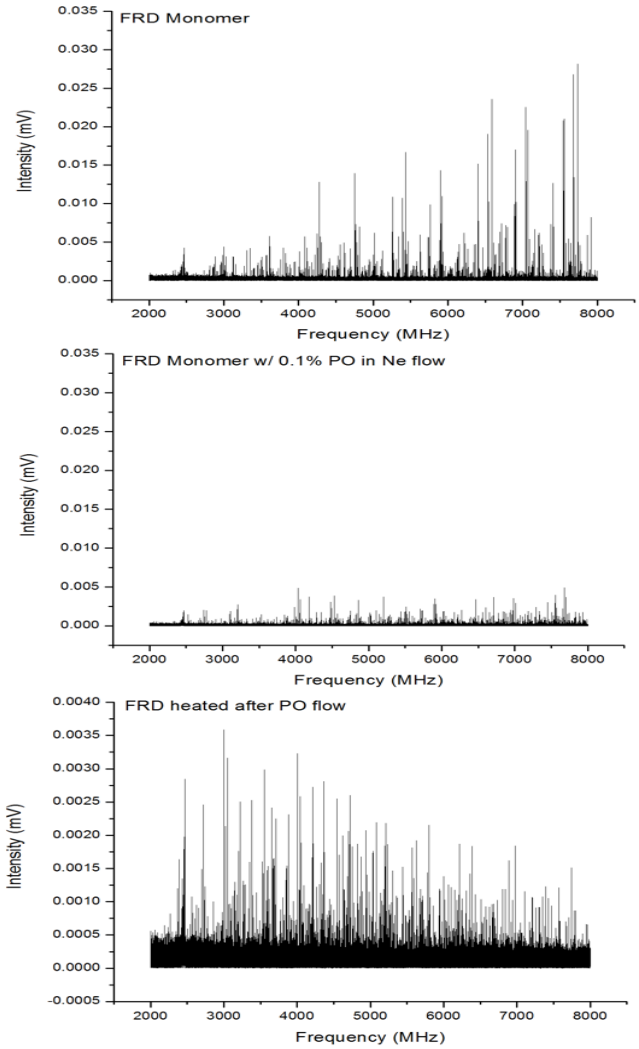

Figure 6.2: The spectra collected before, during and after flowing a 0.1% propylene oxide in neon gas mixture over FRD-903. The top is the spectra of FRD-903 before any propylene oxide was added, the middle was while the propylene oxide was flowing, and the bottom spectra was taken after the propylene oxide flow was cut, and the sample was heated to 60°C.

Ten different rotational spectra were fit from the new spectrum. The products of this reaction were most likely a result of the ring-opening of the epoxide from a carboxylic acid under acidic conditions. The conformational search for four unique products where the epoxide ring-opening that occurred at the least- and most-substituted carbons on the propylene oxide with each

having a diastereomer. Table 6.1 and 6.2 shows the theoretical rotational constants and the fit rotational constants for the FRD-903-propylene oxide reaction products. Two structures had no corresponding candidate theoretical structure (Table E1). The structures are provided in Figure 6.3. Nomenclature used to describe the reaction products are different in this case due to the chiral derivatization forming a new product. Homochiral describes combination of (*R*),(*R*) and (*S*),(*S*) chiral centers on the reaction product, and heterochiral describes the (*R*),(*S*) and (*S*),(*R*) chiral centers. As the rotational constants were within error of each other for the least-substituted hetero- and homochiral reaction product, an electric dipole analysis that has been presented in previous chapters was carried out (Figure 6.4 and 6.5). The a-type spectrum of the least-substituted homochiral reaction product allows for these two diastereomers to be distinguished from each other. The mean scale factors used to make the comparisons for the experimental relative squares of the electric dipole moment components are given in Table E2 and E3 in Appendix E. Dipole matches for some of the higher energy isomers could skewed by lower S/N-ratio making the experimental determination less accurate. To estimate the relative strengths of the electric dipole moment components, the second conformer of the least-substituted products were then scaled using observed quartets in JB95 and normalized to give the relative dipole strengths.

This illustrates the possibility to form diastereomers and measure them to perform the desired chiral analysis from rotational spectroscopy. However, the chiral center of the propylene oxide must be maintained for this strategy to work. Since the enantiopure forms of FRD-903 are not commercially available, the extent of chiral retention of the epoxide chiral center could not be determined from this reaction. So trifluroracetic acid was used to study the degree of chiral retention these epoxide ring-opening reactions achieve.

Table 6.1: Theoretical rotational constants and the experimental fit rotational constants for lowest calculated energy reaction products between FRD-903 and propylene oxide.

Complex	Least-Sub Heterochiral Theory	Least-Sub Heterochiral Experimental	Least-Sub Homochiral Theory	Least-Sub Homochiral Experimental
A /MHz	266.0889	267.27482(81)	265.9304	267.58469(72)
B /MHz	234.5606	236.4990(11)	235.5254	235.91199(48)
C /MHz	164.457	164.75412(55)	163.0225	163.08842(43)
Δ_J /MHz	-	0.0000051(19)	-	0.0000089(13)
Δ_{Jk} /MHz	-	0.0000076(41)	-	-0.0000104(68)
Δ_k /MHz	-	-	-	0.0000103(74)
δ_J /MHz	-	0.00000122(99)	-	0.00000269(67)
δ_k /MHz	-	-	-	-
μ_a /D	0.35	-	-1.30	-
μ_b /D	-2.31	-	1.72	-
μ_c /D	0.166	-	0.44	-
RMS /MHz	-	0.00658	-	0.0023
N	-	131	-	275
ΔE (cm^{-1})	181.5	-	218.6	-
Complex	Most-Sub Heterochiral Theory	Most-Sub Heterochiral Experimental	Most-Sub Homochiral Theory	Most-Sub Homochiral Experimental
A /MHz	294.3809	294.46316(55)	313.9338	316.97858(76)
B /MHz	225.3403	227.6550(10)	203.4636	203.31809(46)
C /MHz	177.9481	178.76268(57)	161.0880	161.38037(72)
Δ_J /MHz	-	0.0000076(16)	-	0.0000073(15)
Δ_{Jk} /MHz	-	-	-	-0.0000148(58)
Δ_k /MHz	-	-	-	0.0000290(68)
δ_J /MHz	-	0.00000167(76)	-	0.00000209(95)
δ_k /MHz	-	-	-	-
μa /D	1.12	-	-1.14	-
μb /D	-2.31	-	0.91	-
μc /D	0.186	-	2.26	-
RMS /MHz	-	0.0094	-	0.0034
N	-	102	-	233
ΔE (cm^{-1})	0	-	94.9	-

Table 6.2: Theoretical rotational constants and the experimental fit rotational constants for reaction products between FRD-903 and propylene oxide for the second lowest calculated structures.

Complex	Least-Sub Heterochiral 2 Theory	Least-Sub Heterochiral 2 Experimental	Least-Sub Homochiral 2 Theory	Least-Sub Homochiral 2 Experimental
A /MHz	282.2340	285.09692(76)	282.8423	284.25350(86)
B /MHz	213.6664	214.12447(46)	198.0806	198.19346(84)
C /MHz	153.1111	153.78277(47)	143.0595	143.05925(52)
Δ_J /MHz	-	0.0000060(10)	-	0.0000070(20)
Δ_{Jk} /MHz	-	-0.0000102(69)	-	0.0000215(95)
Δ_k /MHz	-	0.0000152(66)	-	-0.0000221(77)
δ_J /MHz	-	0.00000182(56)	-	0.0000025(10)
δ_k /MHz	-	-	-	0.0000168(70)
μ_a /D	1.02	-	0.95	-
μ_b /D	0.70	-	1.71	-
μ_c /D	-1.03	-	1.1	-
RMS /MHz	-	0.0032	-	0.0051
N	-	261	-	193
ΔE (cm^{-1})	261.7	-	413.3	-
Complex	Most-Sub Heterochiral 2 Theory	Most-Sub Heterochiral 2 Experimental	Most-Sub Homochiral 2 Theory	Most-Sub Homochiral 2 Experimental
A /MHz	288.5696	289.91641(66)	298.6686	301.08823(84)
B /MHz	232.9882	234.45122(97)	227.2372	227.55817(51)
C /MHz	177.5505	177.62363(86)	170.7490	171.23784(52)
Δ_J /MHz	-	0.0000061(18)	-	0.0000025(10)
Δ_{Jk} /MHz	-	-	-	0.0000201(66)
Δ_k /MHz	-	-	-	-0.0000150(71)
δ_J /MHz	-	0.0000030(25)	-	-
δ_k /MHz	-	-	-	-
μa /D	0.48	-	0.07	-
μb /D	2.14	-	-1.88	-
μc /D	-0.25	-	0.16	-
RMS /MHz	-	0.0000094	-	0.0037
N	-	102	-	163
ΔE (cm^{-1})	54.9	-	95.2	-

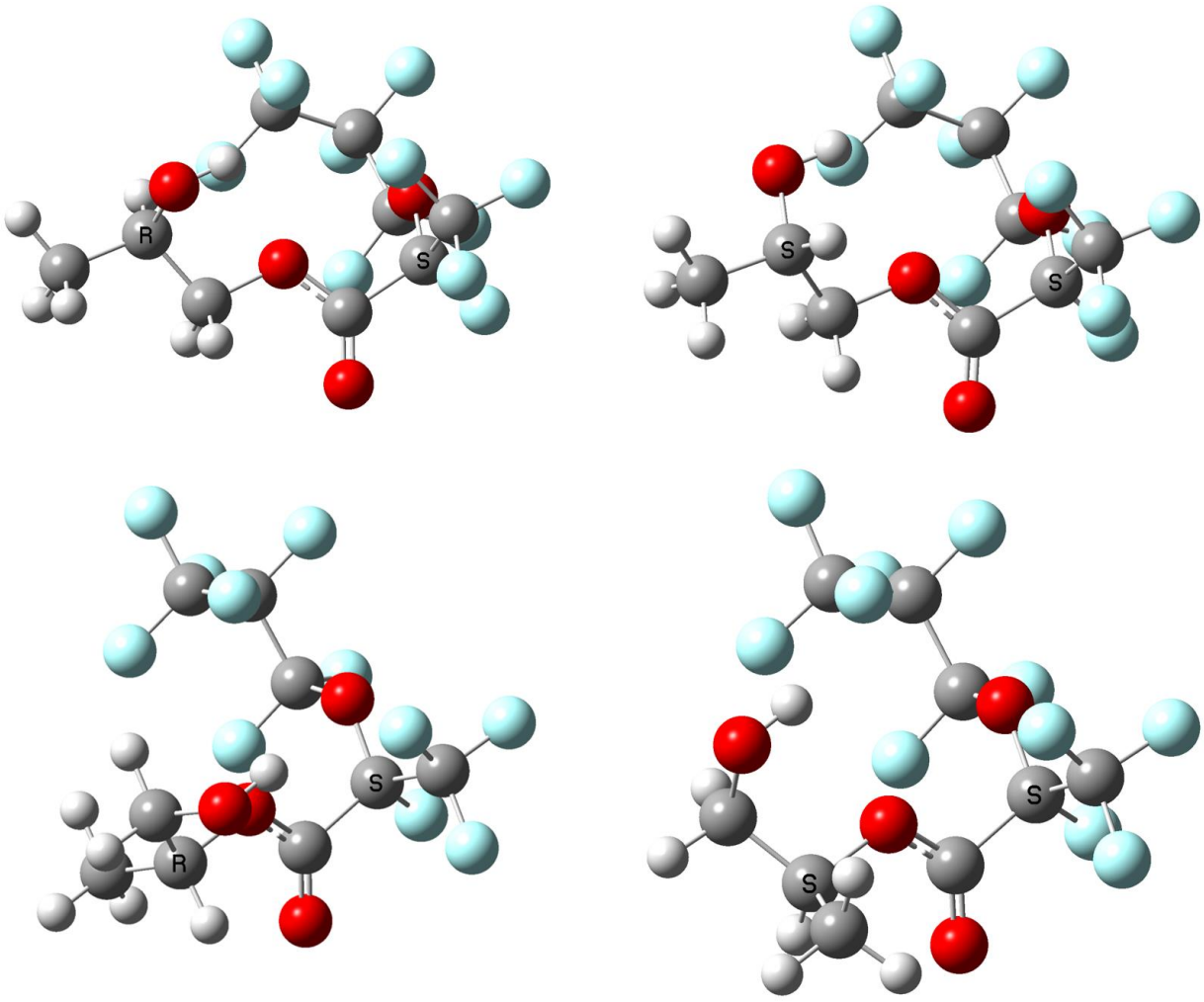

Figure 6.3: Computed geometry optimized structures for the reaction product diastereomers at the least-substituted carbon of the epoxide (Top) and the reaction product diastereomers at the most-substituted carbon on the epoxide (bottom). All geometry optimizations were done with B3LYPD3BJ method with def2TZVP basis set.

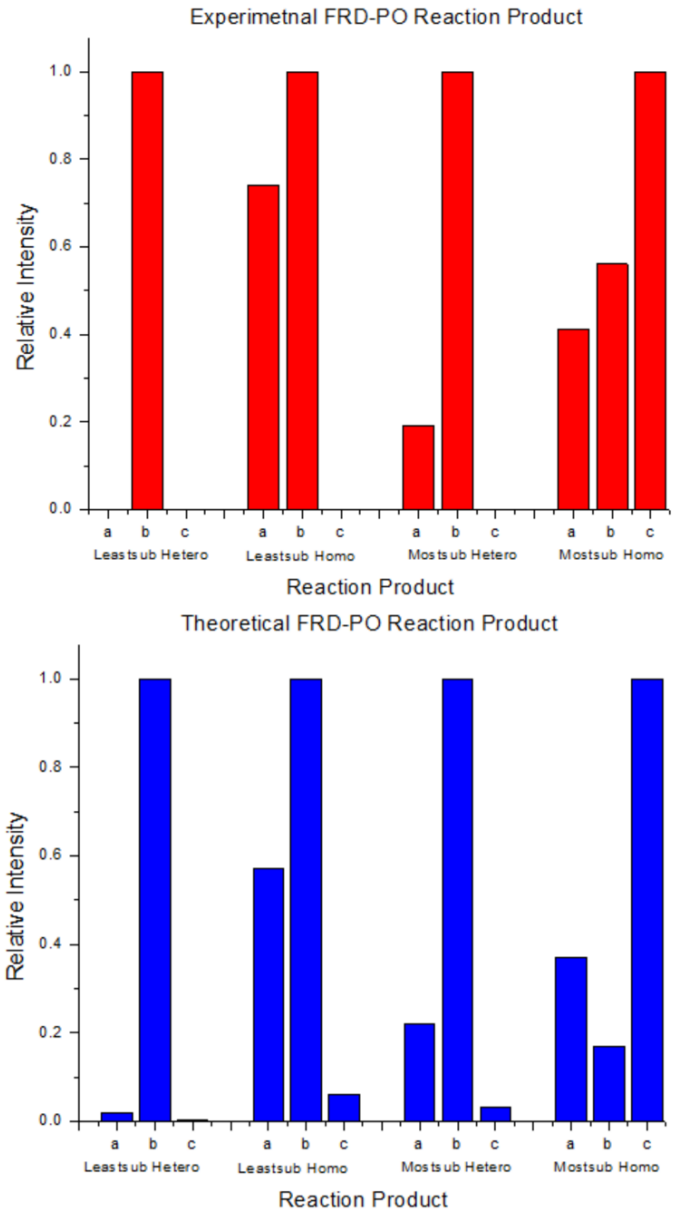

Figure 6.4: Experimental (top) and theoretical (bottom) comparisons of the squares of the electric dipole moment components for the calculated lowest energy structures.

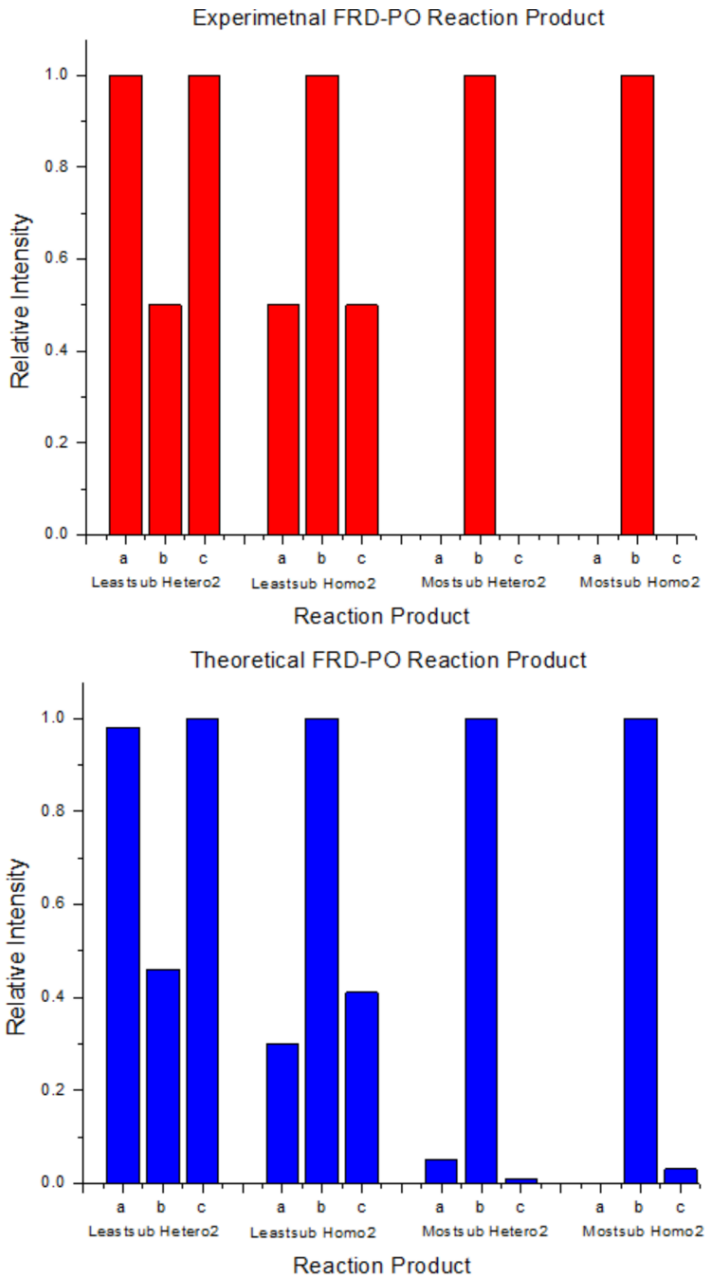

Figure 6.5: Experimental (top) and theoretical (bottom) comparisons of the squares of the electric dipole moment components for the calculated second lowest energy structures.

2) Trifluoroacetic Acid Chiral Retention

In order to test the retention of the propylene oxide's chiral center, a smaller fluorinated carboxylic acid was used as a probe. As stated above, signs of a reaction were observed when the two reagents were mixed. The reaction product of trifluoroacetic acid and propylene oxide are given in Figure 6.6. Two conformations of the reaction at the most- and least-substituted carbons of the propylene oxide were observed and fit (Table 6.3). Reaction products from the different enantiomers of propylene oxide bonded to the trifluoroacetic acid resulted in enantiomers rather than diastereomers due to the only chiral center in the product belonged to propylene oxide. In order to determine the retention of chirality of the epoxide during the ring-opening reaction, chiral tag rotational spectroscopy was used on the reaction product of racemic propylene oxide and enantiopure (*S*)-(-)-propylene oxide with trifluoroacetic acid. The (*S*)-(-)-propylene oxide used had a reported enantiopurity of 99.6% and measuring the enantiomeric excess would determine the degree of retention of the chiral center. To perform chiral tag rotational spectroscopy the reaction product was tagged with racemic and enantiopure (*S*)-trifluoroisopropyl alcohol. The noncovalent tag complexes are presented in Figure 6.7 with corresponding theoretical vs fit rotational constants given in Table 6.4. In this case, the measurement had the sensitivity to observe only one conformer of the trifluoracetic acid enantiomers tagged with the trifluoro-acetic acid. Since the optical rotation of the reaction product was not known and the reaction product only had one chiral center, the homochiral complexes will correspond to the (*R*)-(*R*) and (*S*)-(*S*) analyte-tag combinations while the heterochiral will correspond to the (*R*)-(*S*) and (*S*)-(*R*) analyte-tag complexes. The results from the chiral tag analysis of the trifluoroacetic acid are shown in Figure 6.8. As shown both the reaction products at the epoxide carbon site led to approximately racemic mixtures after reaction

with the enantiopure (*S*)-(-)-propylene oxide. Therefore, this reaction set-up is incapable of determining the enantiomeric excess of FRD-903 via chiral derivatization due to the lack of retention of the epoxide chiral center. However, if a new reaction scheme can be made to retain the chiral center of the epoxide, then chiral derivatization for chiral analysis by rotational spectroscopy for larger molecules may be achieved.

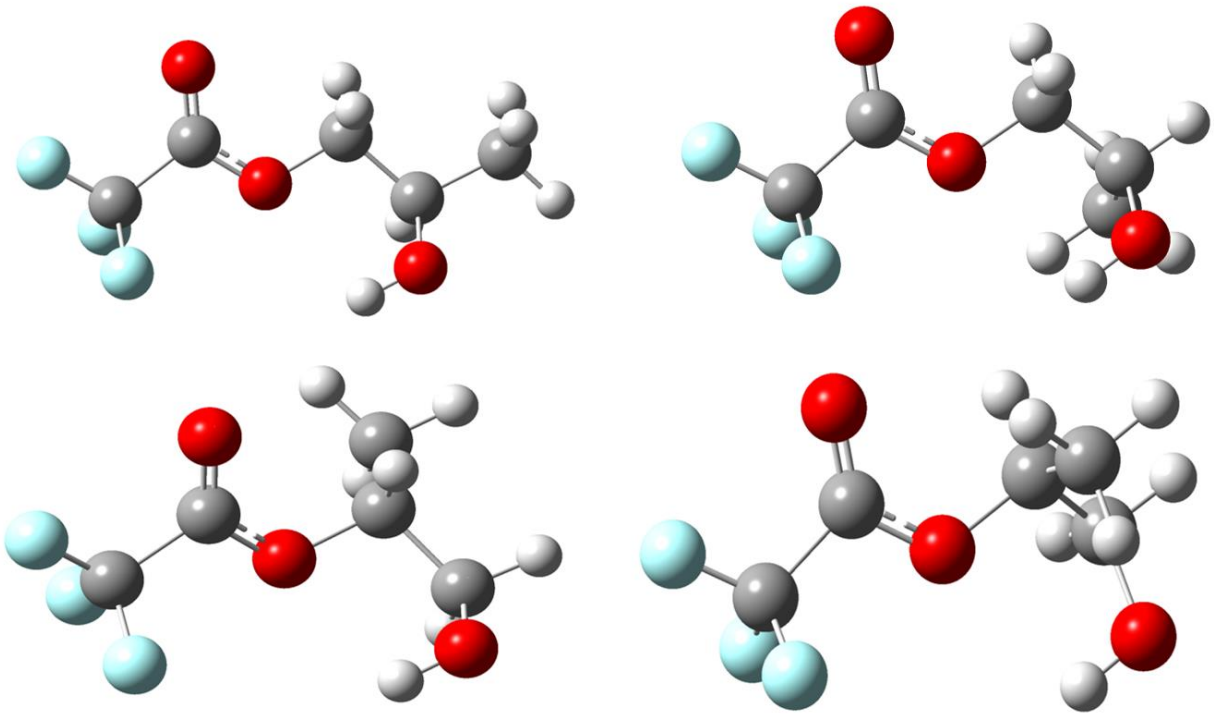

Figure 6.6: The theoretically computed structures of trifluoroacetic acid reacted with propylene oxide using B3LYPD3BJ with def2TZVP basis set. The top structures are the two conformers observed where the epoxide ring-opening occurred at the least-substituted carbon and the bottom are when the reaction occurs at the most-substituted carbon of the epoxide.

Table 6.3: Theoretical and experimental rotational parameters for the different conformations for the two reaction products of trifluoroacetic acid with propylene oxide.

Complex	Most-Sub Lowest Energy Theory	Most-Sub Lowest Energy Experimental	Most-Sub Higher Energy Theory	Most-Sub Higher Energy Experimental
A /MHz	1783.643	1796.5645(25)	1934.083	1950.4540(41)
B /MHz	658.5854	660.01986(84)	631.9874	634.9351(21)
C /MHz	577.787	578.20983(85)	561.6902	564.1604(23)
Δ_J /MHz	-	0.0000364(75)	-	0.000044(38)
Δ_{Jk} /MHz	-	0.000220(32)	-	0.00022(12)
Δ_k /MHz	-	0.000045(80)	-	-
δ_J /MHz	-	-	-	-
δ_k /MHz	-	-	-	-
μ_a /D	2.110249	-	-1.88569	-
μ_b /D	-0.72176	-	0.048063	-
μ_c /D	1.636799	-	0.493498	-
RMS /MHz	-	0.006422	-	0.002126
N	-	139	-	54
ΔE (cm^{-1})	0	-	96.7	-
Complex	Least-Sub Lowest Energy Theory	Least-Sub Lowest Energy Experimental	Least-Sub Higher Energy Theory	Least-Sub Higher Energy Experimental
A /MHz	2364.108	2379.9335(39)	2018.654	2033.2288(32)
B /MHz	521.3634	522.5220(11)	578.8286	581.0349(13)
C /MHz	477.1002	478.6365(11)	544.1091	546.6157(13)
Δ_J /MHz	-	0.000025(11)	-	0.000037(15)
Δ_{Jk} /MHz	-	0.000336(63)	-	0.000332(56)
Δ_k /MHz	-	-	-	-
δ_J /MHz	-	-	-	-
δ_k /MHz	-	-	-	-
μa /D	-2.06228	-	-2.04046	-
μb /D	0.068624	-	-0.24662	-
μc /D	1.21261	-	1.198022	-
RMS /MHz	-	0.002895	-	0.003968
N	-	81	-	78
ΔE (cm^{-1})	86.1	-	304.8	-

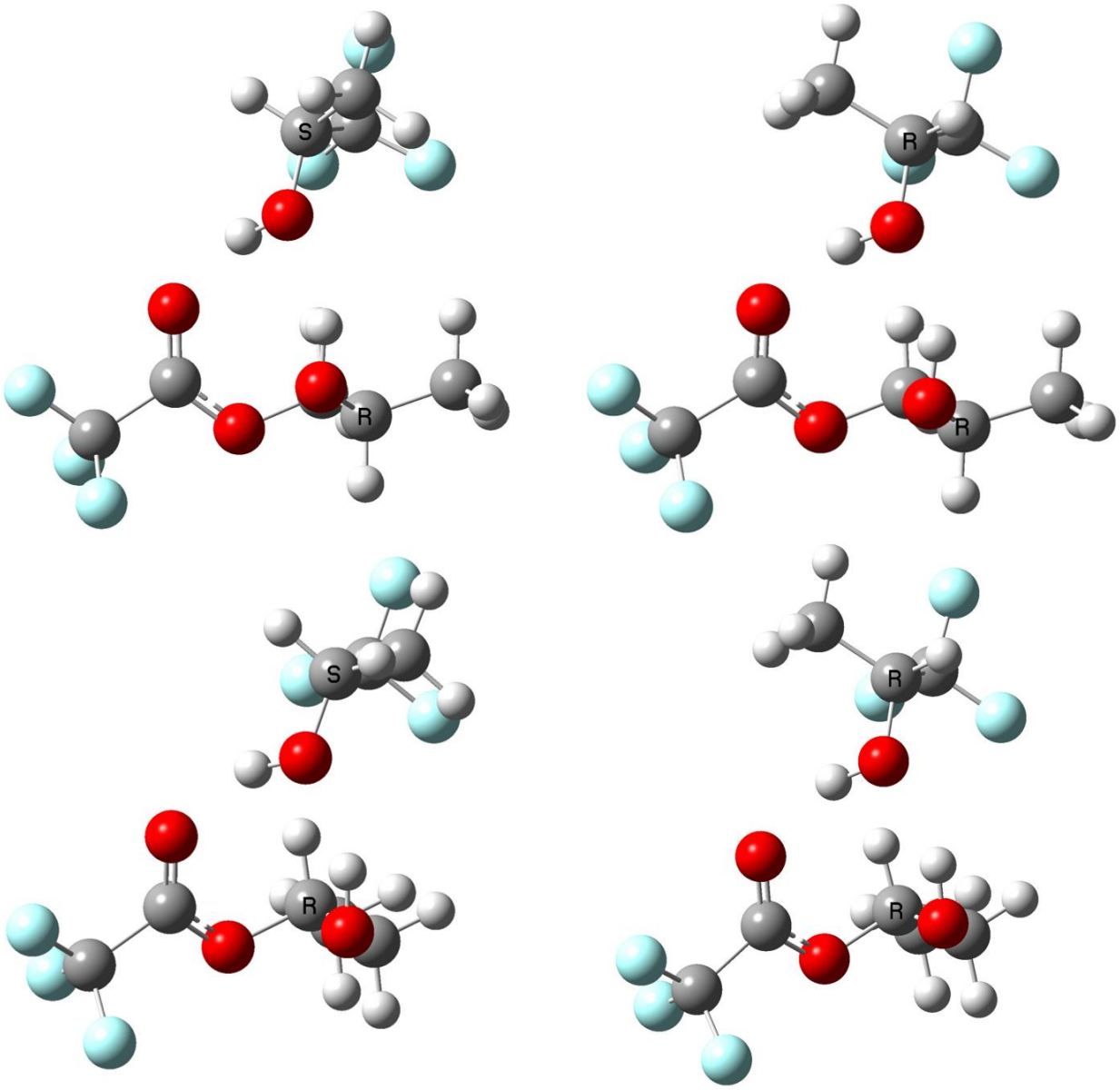

Figure 6.7: The geometry optimized structures calculated using B3LYP with def2TZVP basis set level of theory for trifluoroacetic acid-propylene oxide reaction product chiral tagged with trifluoroisopropyl alcohol. The top structure are reaction products at the least-substituted carbon, and the bottom are reaction products at the most-substituted carbon.

Table 6.4: The theoretical and fit rotational constants for trifluoroacetic acid noncovalently bonded to trifluoroisopropyl alcohol. The diastereomer complexes for the reaction at the least-substituted carbon are shown on the top, and the diastereomer complexes for the reaction at the most-substituted carbon are given on the bottom.

Complex	Least-Sub Homochiral Theory	Least-Sub Homochiral Experimental	Least-Sub Heterochiral Theory	Least-Sub Heterochiral Experimental
A /MHz	578.4645	577.487(21)	609.4078	609.531(35)
B /MHz	218.5401	216.6408(10)	205.3025	204.5344(10)
C /MHz	183.884	182.70390(85)	182.8825	181.57982(91)
Δ_J /MHz	-	0.00002016(90)	-	0.00001611(74)
Δ_{Jk} /MHz	-	-	-	-
Δ_k /MHz	-	-	-	-
δ_J /MHz	-	0.00000322(84)	-	0.00000249(83)
δ_k /MHz	-	-	-	-
μ_a /D	-1.79321	-	-2.18605	-
μ_b /D	-0.42455	-	-0.80697	-
μ_c /D	0.848325	-	0.750686	-
RMS /MHz	-	0.006307	-	0.00515
N	-	116	-	117
ΔE (cm^{-1})	235.1	-	193.8	-
Complex	Most-Sub Homochiral Theory	Most-Sub Homochiral Experimental	Most-Sub Heterochiral Theory	Most-Sub Heterochiral Experimental
A /MHz	625.6906	626.164(39)	650.2177	654.98(10)
B /MHz	217.0589	215.00508(61)	205.245	203.30273(63)
C /MHz	192.8052	191.28920(66)	192.6247	191.49564(63)
Δ_J /MHz	-	0.00001321(96)	-	0.00001149(78)
Δ_{Jk} /MHz	-	-	-	-
Δ_k /MHz	-	-	-	-
δ_J /MHz	-	-	-	-
δ_k /MHz	-	-	-	-
μa /D	-2.27012	-	-2.57543	-
μb /D	-0.46733	-	-1.02562	-
μc /D	1.434878	-	0.884514	-
RMS /MHz	-	0.006014	-	0.004494
N	-	104	-	109
ΔE (cm^{-1})	2.61	-	0	-

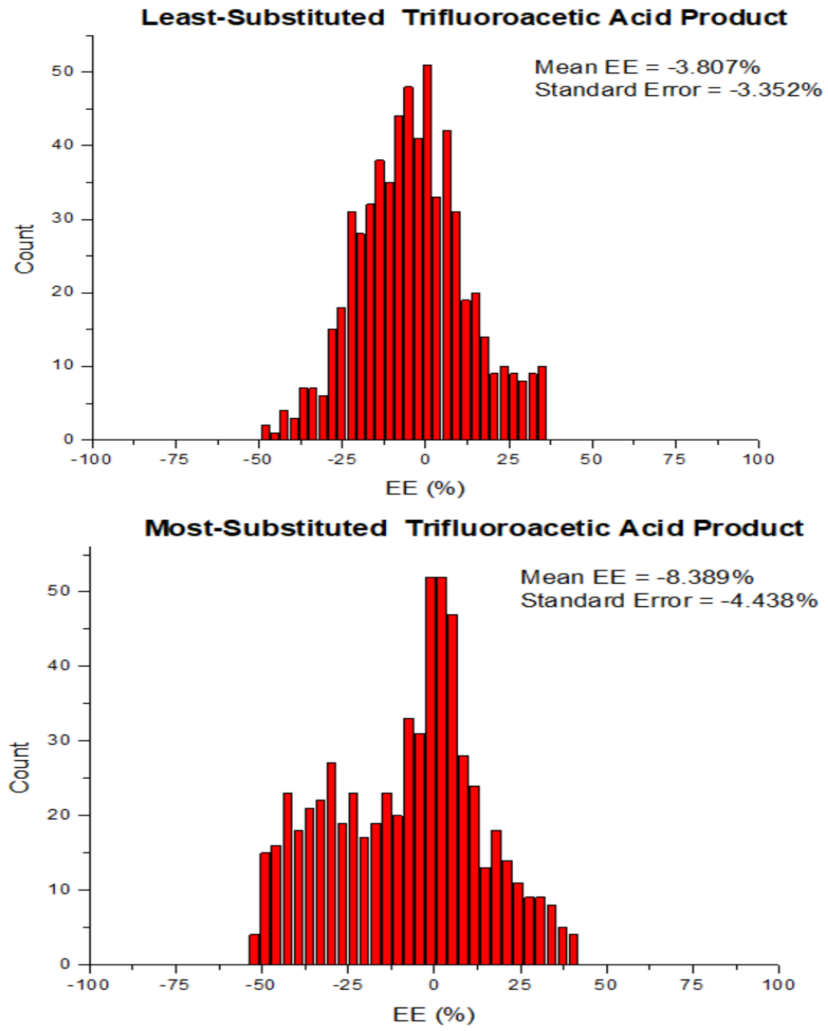

Figure 6.8: Results of the chiral tagging of the trifluoroacetic acid-propylene oxide products with trifluoroisopropyl alcohol. Both products show approximately racemic mixtures, meaning the chiral center is not retained on the epoxide.

3) Relative Amounts of Least- and Most-Substituted Carbon Product

In this section the relative amounts of the least- and most-substituted carbon product from the FRD-903 and trifluoroacetic acid reactions are quantified. The relative amounts of product were quantified by simulating the spectra for each species using SPCAT and scaling predicted

transition strengths to match the experimental peak value for the two strongest electric dipole moment components. The input variables into SPCAT comes from the ab initio electric dipole moment components from the quantum chemical structures. The a-component of the dipole moment was the strongest for all species in the trifluoracetic acid product while the c- dipole moment component was the second largest for each species The fractional abundance for the reaction products shows about a 55% to 45% mixture. The reaction favors occurring at the least-substituted carbon on the epoxide, Table 6.5. The percent abundance for the least- and most-substituted reaction products of the FRD-903 reaction product gave a 70% to 30% mixture with the reaction favoring the least-substituted reaction product, Table 6.6. However, this number maybe skewed as there are two experimental fits that have no structural assignments. An increase in sensitivity may be gained if the reaction products for both the TFA and FRD could be controlled to keep the reaction from occurring at one of the carbons of the epoxide. This will lessen the amount of quantum chemistry computation required by narrowing the conformational search to two products.

Table 6.5: Reaction product analysis for the least- and most-substituted TFA-PO reaction products. The table shows the calculated mean scale factor of the simulated spectrum for each observed structure to experimental peaks.

Reaction Product	Least-sub1	Least-sub2	Most-sub1	Most-sub2
Mean Scale Factor	221.949	27.05	134.856	63.126
Standard Deviation	98.637	10.994	51.879	28.302
N	16	16	16	16
Total Scale Factor	446.981			
Fraction Least-sub	0.557			
Fraction Most-sub	0.443			

Table 6.6: Reaction product analysis for the least- and most-substituted FRD-PO reaction products. The table shows the calculated mean scale factor of the simulated spectrum for each observed structure to experimental peaks.

Reaction Product	Least-sub hetero1	Least-sub Homo1	Most-sub Hetero1	Most-sub Homo1
Scale Factor	34.951	25.321	14.989	8.232
Standard Deviation	10.335	7.641	5.865	2.4
N	25	25	25	25
Reaction Product	Least-sub Hetero2	Least-sub Homo2	Most-sub Hetero2	Most-sub Homo2
Scale Factor	16.881	10.257	6.445	6.98
Standard Deviation	5.156	3.559	2.259	2.693
N	25	13	25	25
Total Scale Factor	134.315			
Fraction Least-sub	0.705			
Fraction Most-sub	0.295			

IV. Conclusion

Large molecules are one of the primary limitations of rotational spectroscopy as a technique, not to mention as an analytical chiral analysis technique. This project sought to examine the potential of covalent modification of large molecules to extend the molecular size range of chiral molecules to be analyzed by rotational spectroscopy. FRD-903 was found to cause an epoxide ring-opening reaction with propylene oxide and form a product that produced diastereomers from the enantiomers of both compounds. The reaction took place externally and the reaction mixture was able to be measured in the spectrometer with no further purification necessary. Eight sets of products were observed. This alone demonstrates that chiral derivatization is a feasible approach to analyzing larger molecules with rotational spectroscopy. As no enantiopure FRD-903 was commercially available, Trifluoroacetic acid was used as a test. TFA was reacted with racemic PO and enantiopure PO and chiral tagged to determine the retention of

the propylene oxide chiral center. Unfortunately, the chiral tagging of the TFA-PO reaction products showed that the chiral center of epoxide does not retain its known stereochemistry, but instead racemizes during the reaction. Future work should focus on a collaboration with organic chemists that can better control the reaction to retain the stereochemistry for this method to work. Furthermore, it was calculated to have about a 55:45 and 70:30 ratio of least-substituted to most-substituted carbon TFA-PO reaction product and FRD-PO reaction product, respectfully. If this chemistry could also be better controlled to produce more of one product, then the sensitivity of the measurements could increase as well.

V. References

1. Key, B. D.; Howell, R. D.; Criddle, C. S., Fluorinated Organics in the Biosphere. *Environmental Science & Technology* **1997,** *31* (9), 2445-2454.

2. Wilkinson, J. A., Recent advances in the selective formation of the carbon-fluorine bond. *Chemical reviews* **1992,** *92* (4), 505-519.

3. Murphy, C. D., Biodegradation and biotransformation of organofluorine compounds. *Biotechnology Letters* **2010,** *32* (3), 351-359.

4. O'Hagan, D., Understanding organofluorine chemistry. An introduction to the C–F bond. *Chemical Society Reviews* **2008,** *37* (2), 308-319.

5. Dinoiu, V., Fluorine chemistry: past, present and future. *Revue Roumaine de chimie* **2006,** *51* (12), 1141.

6. Kirk, K. L., Fluorination in Medicinal Chemistry: Methods, Strategies, and Recent Developments. *Organic Process Research & Development* **2008,** *12* (2), 305-321.

7. Murphy, C. D.; Schaffrath, C.; O'Hagan, D., Fluorinated natural products: the biosynthesis of fluoroacetate and 4-fluorothreonine in Streptomyces cattleya. *Chemosphere* **2003,** *52* (2), 455-461.

8. Biegel, L. B.; Hurtt, M. E.; Frame, S. R.; O'Connor, J. C.; Cook, J. C., Mechanisms of extrahepatic tumor induction by peroxisome proliferators in male CD rats. *Toxicological Sciences* **2001,** *60* (1), 44-55.

9. Kennedy, G. L.; Butenhoff, J. L.; Olsen, G. W.; O'Connor, J. C.; Seacat, A. M.; Perkins, R. G.; Biegel, L. B.; Murphy, S. R.; Farrar, D. G., The toxicology of perfluorooctanoate. *Critical reviews in toxicology* **2004,** *34* (4), 351-384.

10. Guillette, T. C.; McCord, J.; Guillette, M.; Polera, M. E.; Rachels, K. T.; Morgeson, C.; Kotlarz, N.; Knappe, D. R. U.; Reading, B. J.; Strynar, M.; Belcher, S. M., Elevated levels of per- and polyfluoroalkyl substances in Cape Fear River Striped Bass (Morone saxatilis) are associated with biomarkers of altered immune and liver function. *Environment International* **2020,** *136*, 105358.

11. Calafat, A. M.; Wong, L.-Y.; Kuklenyik, Z.; Reidy, J. A.; Needham, L. L., Polyfluoroalkyl chemicals in the US population: data from the National Health and Nutrition Examination Survey (NHANES) 2003–2004 and comparisons with NHANES 1999–2000. *Environmental health perspectives* **2007,** *115* (11), 1596-1602.

12. Beškoski, V. P.; Yamamoto, A.; Nakano, T.; Yamamoto, K.; Matsumura, C.; Motegi, M.; Beškoski, L. S.; Inui, H., Defluorination of perfluoroalkyl acids is followed by production of monofluorinated fatty acids. *Science of The Total Environment* **2018,** *636*, 355-359.

13. Lau, C.; Anitole, K.; Hodes, C.; Lai, D.; Pfahles-Hutchens, A.; Seed, J., Perfluoroalkyl acids: a review of monitoring and toxicological findings. *Toxicological sciences* **2007,** *99* (2), 366-394.

14. Eriksen, K. T.; Raaschou-Nielsen, O.; Sørensen, M.; Roursgaard, M.; Loft, S.; Møller, P., Genotoxic potential of the perfluorinated chemicals PFOA, PFOS, PFBS, PFNA and PFHxA in human HepG2 cells. *Mutation Research/Genetic Toxicology and Environmental Mutagenesis* **2010,** *700* (1), 39-43.

15. Barry, V.; Winquist, A.; Steenland, K., Perfluorooctanoic Acid (PFOA) Exposures and Incident Cancers among Adults Living Near a Chemical Plant. *Environmental Health Perspectives* **2013,** *121* (11-12), 1313-1318.

16. Nicole, W., PFOA and Cancer in a Highly Exposed Community: New Findings from the C8 Science Panel. *Environmental Health Perspectives* **2013,** *121* (11-12), A340-A340.

17. Steenland, K.; Fletcher, T.; Savitz, D. A., Epidemiologic Evidence on the Health Effects of Perfluorooctanoic Acid (PFOA). *Environmental Health Perspectives* **2010,** *118* (8), 1100-1108.

18. Steenland, K.; Jin, C.; MacNeil, J.; Lally, C.; Ducatman, A.; Vieira, V.; Fletcher, T., Predictors of PFOA Levels in a Community Surrounding a Chemical Plant. *Environmental Health Perspectives* **2009,** *117* (7), 1083-1088.

19. Steenland, K.; Fletcher, T.; Stein, C. R.; Bartell, S. M.; Darrow, L.; Lopez-Espinosa, M.-J.; Barry Ryan, P.; Savitz, D. A., Review: Evolution of evidence on PFOA and health following the assessments of the C8 Science Panel. *Environment International* **2020,** *145*, 106125.

20. McCord, J.; Strynar, M., Identification of Per- and Polyfluoroalkyl Substances in the Cape Fear River by High Resolution Mass Spectrometry and Nontargeted Screening. *Environmental Science & Technology* **2019,** *53* (9), 4717-4727.

21. Hopkins, Z. R.; Sun, M.; DeWitt, J. C.; Knappe, D. R. U., Recently Detected Drinking Water Contaminants: GenX and Other Per- and Polyfluoroalkyl Ether Acids. *Journal AWWA* **2018,** *110* (7), 13-28.

22. Cahoon, L. B., GenX in Cape Fear River Water Was Only One Part of the PFAS Story in North Carolina. In *Contaminants in Our Water: Identification and Remediation Methods*, American Chemical Society: 2020; Vol. 1352, pp 91-103.

23. Sun, M.; Arevalo, E.; Strynar, M.; Lindstrom, A.; Richardson, M.; Kearns, B.; Pickett, A.; Smith, C.; Knappe, D. R. U., Legacy and Emerging Perfluoroalkyl Substances Are Important Drinking Water Contaminants in the Cape Fear River Watershed of North Carolina. *Environmental Science & Technology Letters* **2016,** *3* (12), 415-419.

24. Kotlarz, N.; McCord, J.; Collier, D.; Lea, C. S.; Strynar, M.; Lindstrom, A. B.; Wilkie, A. A.; Islam, J. Y.; Matney, K.; Tarte, P.; Polera, M. E.; Burdette, K.; DeWitt, J.; May, K.; Smart, R. C.; Knappe, D. R. U.; Hoppin, J. A., Measurement of Novel, Drinking Water-Associated PFAS in Blood from Adults and Children in Wilmington, North Carolina. *Environmental Health Perspectives* **2020,** *128* (7), 077005.

25. Coperchini, F.; Croce, L.; Denegri, M.; Pignatti, P.; Agozzino, M.; Netti, G. S.; Imbriani, M.; Rotondi, M.; Chiovato, L., Adverse effects of in vitro GenX exposure on rat thyroid cell viability, DNA integrity and thyroid-related genes expression. *Environmental Pollution* **2020,** *264*, 114778.

26. Chappell, G. A.; Thompson, C. M.; Wolf, J. C.; Cullen, J. M.; Klaunig, J. E.; Haws, L. C., Assessment of the Mode of Action Underlying the Effects of GenX in Mouse Liver and Implications for Assessing Human Health Risks. *Toxicol Pathol* **2020,** *48* (3), 494-508.

27. Wen, Y.; Mirji, N.; Irudayaraj, J., Epigenetic toxicity of PFOA and GenX in HepG2 cells and their role in lipid metabolism. *Toxicology In Vitro* **2020,** *65*, 104797.

28. M. J. Frisch, G. W. T., H. B. Schlegel, G. E. Scuseria, M. A. Robb, J. R. Cheeseman, G. Scalmani, V. Barone, G. A. Petersson, H. Nakatsuji, X. Li, M. Caricato, A. Marenich, J. Bloino, B. G. Janesko, R. Gomperts, B. Mennucci, H. P. Hratchian, J. V. Ortiz, A. F. Izmaylov, J. L. Sonnenberg, D. Williams-Young, F. Ding, F. Lipparini, F. Egidi, J. Goings, B. Peng, A. Petrone, T. Henderson, D. Ranasinghe, V. G. Zakrzewski, J. Gao, N. Rega, G. Zheng, W. Liang, M. Hada, M. Ehara, K. Toyota, R. Fukuda, J. Hasegawa, M. Ishida, T. Nakajima, Y. Honda, O. Kitao, H. Nakai, T. Vreven, K. Throssell, J. A. Montgomery, Jr., J. E. Peralta, F. Ogliaro, M. Bearpark, J. J. Heyd, E. Brothers, K. N. Kudin, V. N. Staroverov, T. Keith, R. Kobayashi, J. Normand, K. Raghavachari, A. Rendell, J. C. Burant, S. S. Iyengar, J. Tomasi, M. Cossi, J. M. Millam, M. Klene, C. Adamo, R. Cammi, J. W. Ochterski, R. L. Martin, K. Morokuma, O. Farkas, J. B. Foresman, and D. J. Fox *Gaussian 09, Revision A.02*, Gaussian, Inc.: Wallingford, CT, 2016.

29. Grimme, S.; Ehrlich, S.; Goerigk, L., Effect of the damping function in dispersion corrected density functional theory. *Journal of computational chemistry* **2011,** *32* (7), 1456-1465.

30. Frisch, M. J.; Trucks, G. W.; Schlegel, H. B.; Scuseria, G. E.; Robb, M. A.; Cheeseman, J. R.; Scalmani, G.; Barone, V.; Petersson, G. A.; Nakatsuji, H.; Li, X.; Caricato, M.; Marenich, A. V.; Bloino, J.; Janesko, B. G.; Gomperts, R.; Mennucci, B.; Hratchian, H. P.; Ortiz, J. V.; Izmaylov, A. F.; Sonnenberg, J. L.; Williams; Ding, F.; Lipparini, F.; Egidi, F.; Goings, J.; Peng, B.; Petrone, A.; Henderson, T.; Ranasinghe, D.; Zakrzewski, V. G.; Gao, J.; Rega, N.; Zheng, G.; Liang, W.; Hada, M.; Ehara, M.; Toyota, K.; Fukuda, R.; Hasegawa, J.; Ishida, M.; Nakajima, T.; Honda, Y.; Kitao, O.; Nakai, H.; Vreven, T.; Throssell, K.; Montgomery Jr., J. A.; Peralta, J. E.; Ogliaro, F.; Bearpark, M. J.; Heyd, J. J.; Brothers, E. N.; Kudin, K. N.; Staroverov, V. N.; Keith, T. A.; Kobayashi, R.; Normand, J.; Raghavachari, K.; Rendell, A. P.; Burant, J. C.; Iyengar, S. S.; Tomasi, J.; Cossi, M.; Millam, J. M.; Klene, M.; Adamo, C.; Cammi, R.; Ochterski, J. W.; Martin, R. L.; Morokuma, K.; Farkas, O.; Foresman, J. B.; Fox, D. J. *Gaussian 16 Rev. C.01*, Wallingford, CT, 2016.

31. Pickett, H. M., The fitting and prediction of vibration-rotation spectra with spin interactions. *Journal of Molecular Spectroscopy* **1991,** *148* (2), 371-377.

32. Kisiel, Z. PROSPE, programs for rotational spectroscopy. http://info.ifpan.edu.pl/~kisiel/prospe.htm.

VI. Appendix E

Table E1: Fit spectra in the FRD-903-PO reaction product spectrum with no corresponding theoretical structure.

Complex	Unknown	Unknown2
A /MHz	309.31286(90)	280.31579(63)
B /MHz	198.14796(59)	206.39613(40)
C /MHz	170.02689(40)	155.02366(40)
Δ_J /MHz	0.0164(11)	0.00000915(84)
Δ_{Jk} /MHz	-0.0413(58)	-0.0000196(50)
Δ_k /MHz	0.0563(54)	0.0000234(51)
δ_J /MHz	0.00329(63)	0.00000243(46)
δ_k /MHz	-	-
N	206	131
RMS	0.0022	0.0037

Table E2: Results from the scaling of transitions strengths generated by SPCAT from corresponding dipole components to the experimental intensities of the lowest energy FRD-PO reaction products.

Reaction Product	Least-sub Hetero1			Least-sub Homo1		
Dipole	a	b	c	a	b	c
Mean Scale Factor	-	198.007	-	55.397	75.188	-
Standard Deviation	-	52.715	-	21.59	22.504	-
N	-	25	-	25	16	-
Relative	0	1	0	0.74	1	0
Reaction Product	Most-sub Hetero1			Most-sub Homo1		
Dipole	a	b	c	a	b	c
Mean Scale Factor	15.476	79.982	-	17.128	23.445	42.045
Standard Deviation	5.1	31.295	-	5.154	10.654	12.255
N	25	25	-	25	13	25
Relative	0.19	1	0	0.41	0.56	1

Table E3: Results from the scaling of transitions strengths generated by SPCAT from corresponding dipole components to the experimental intensities of the second lowest energy FRD-PO reaction products.

Reaction Product	Least-sub Hetero 2*			Least-sub Homo 2*		
Dipole	a	b	c	a	b	c
Mean Scale Factor	-	-	-	-	-	-
Standard Deviation	-	-	-	-	-	-
N	-	-	-			-
Relative	1	0.5	1	0.5	1	0.5
Reaction Product	Most-sub Hetero 2			Most-sub Homo 2		
Dipole	a	b	c	a	b	c
Mean Scale Factor	-	29.518	-	-	28.826	-
Standard Deviation	-	10.335	-	-	9.171	-
N	-	25	-	-	25	-
Relative	-	1	-	0	1	0

*****Scaling was done in JB95 using quartets because of signal-to-noise ratio of these transitions.

Chapter 7

Conclusion

I. Summary

In this thesis a new chiral analysis technique using rotational spectroscopy, chiral tag rotational spectroscopy, was presented. A new technique requires many studies to fully develop and understand how it compares to different methods, how it works for different systems, and possible extensions and improvements that can be made. First, the quantitative method for calculating error and enantiomeric excess was studied. This method works by forming noncovalently bound complexes of the analyte with a small chiral molecule of known stereochemistry designated as a "chiral tag". These complexes were studied using rotational spectroscopy on a CP-FTMW spectrometer in this thesis, formed in a seeded molecular beam within the spectrometer. The complexes produce convert the enantiomers into diastereomers that are then distinguishable by rotational spectroscopy. These diastereomeric complexes are comprised of homochiral combinations of (-)-(-) and (+)-(+) enantiomers of the analyte and tag, and heterochiral combinations of (+)-(-) and (-)-(+) enantiomers of the analyte and tag. The intensities of many transitions can then be measured and normalized by the intensities of the transitions using a racemic form of the tag. Two different calibration curves using propylene oxide, a hydrogen bond acceptor, and butynol, a hydrogen bond donor, were created using samples of known enantiomeric excess of isopulegol and 3-methylcyclohexanone, respectively. Results show that the ratios calculated by chiral tag rotational spectroscopy accurately measured the enantiomeric excess of a sample with only the enantiomeric excess of the tag needing to be corrected for. Furthermore, the study used modeling of a chiral tag measurement to analyze the

statistics of a chiral tag measurement. In a chiral tag measurement, the percent intensity fluctuations of spectra between back-to-back measurements result in a large uncertainty, observed by an increased histogram width, the closer to racemic the sample is. The uncertainty decrease and the histogram narrows, the more enantiopure the sample is. Different approaches to sample handling were tested to minimize uncertainty in the measurement. The large fluctuations can be attributed to the changes in the instrument response function that occur between measurements where vacuum was broken. Sampling by purging the volatile tag out, minimized changes in the instrument response. Signal averaging can also minimize uncertainty by averaging out the fluctuation in the number density of gas released by the nozzle in the spectrometer.

Next, quantum chemical calculations of a chiral tag system were benchmarked to determine accuracy for absolute configuration assignment and which methods and basis sets were practical for analytical applications in Chapter 3. Theoretical structure optimization is necessary for rotational spectroscopy to assign the rotational parameters to structures. Immediately, B3LYP was not advised for use as it was not able to optimize to the observed structures in the geometry optimizations. Overall, the B3LYP with dispersion correction, MP2 and B2PLYPD3 methods calculated rotational constants, relative electric dipole moment components, and atomic coordinates accurately. From an energetics perspective, the computationally intensive calculations of B2PLYPD3 were more accurate than the others, correctly predicting the lowest energy structure. However, dispersion corrected DFT was able to predict the isomers that were observed. Overall, the best method to use is the B3LYPD3BJ with either Pople's 6-311G++(d,p) or def2tzvp basis set, as they are quick and accurate, unless the study requires more accurate energy values.

The method was tested against another spectroscopy based chiral analysis technique, VCD,

in Chapter 4. Both techniques could determine the absolute configuration of the sample, however chiral tag rotational spectroscopy was able to calculate the enantiomeric excess without reference samples of the analyte. Low level diastereomer impurities, ~3%, were also quantified with rotational spectroscopy, whereas IR/VCD was not able to observe or quantify the low-level impurity. Chiral tag was also much faster than VCD for quantitative analysis. It took about 40 seconds to quantify the diastereomer impurity and about 6 minutes to get an enantiomeric excess calculation. The VCD spectrum took 18 hours to collect the spectrum and another 18 hours for a solvent background spectrum.

Finally, the molecular system of chiral tagging carboxylic acids was studied in Chapter 5 and 6. Carboxylic acids have a unique feature where the chiral tag complexes of the conformer formed by rotation of carboxylic acid 180° have similar rotational constants to one of the opposite diastereomer complexes. A way of increasing confidence in absolute configuration assignment was explored. In the study of the carboxylic acid, only one conformer of each was observed experimentally, while the other two higher energy conformations appeared to cool out in the supersonic expansion. Further confidence was achieved by gaining atomic coordinate information with the shifts of the principal moments-of-inertia using an isotopically labeled chiral tag. Isotopically labeled chiral tags allow for molecular coordinate information to be gained without the need for the sensitivity of ^{13}C spectra in natural abundance, which may not be achieved due to sample limits. Both sets of solutions to the different homo- and heterochiral complexes were assigned to the experimental fits and the errors are compared. One assignment of complexes matches the theoretical predicted shifts better than other, helping to improve confidence in the assignments.

Perfluorinated carboxylic acids were also studied but were found to react with propylene oxide forming a new covalently modified species. Two different reaction products were found where an epoxide ring-opening at the least and most substituted carbon occurred. This was then explored to test the applicability to measuring enantiomeric excess of large molecules by chiral tag rotational spectroscopy. Diastereomers were produced and measured, but it was found to racemize, precluding a measurement of the enantiomeric excess and absolute configuration.

II. Limitations of Chiral Tag Rotational Spectroscopy

While chiral tagging has been shown to enable accurate chiral analysis, it has many things that need to be addressed to become an adopted analytical technique. First, the range of molecules that can be analyzed by rotational spectroscopy is limited to smaller volatile compounds. A size range maximum of roughly 15-20 heavy atoms is the limit for chiral tag rotational spectroscopy. As a result, large biomolecules, which are very important for chiral analysis studies, are not able to be measured via rotational spectroscopy. Furthermore, molecules that are not thermally stable cannot be measured in the spectrometer, as they would decompose. The limited range of compounds that can be studied greatly reduces the utility of the method for biochemical applications and large natural product analysis. However, the technique may still be used in pharmaceutical applications, as the small molecular building blocks of drugs can be analyzed because larger chiral compounds often start with smaller chiral building blocks. These small chiral building blocks would be able to be characterized with chiral tag rotational spectroscopy.

Large molecules are often more conformationally flexible, leading to the spread of spectral intensities across many conformers. The ability of chiral tagging to complex with large

conformationally flexible molecules has not been fully explored and could pose additional issues. Likewise, multiple isomers of the chiral tag complexes also spread-out spectral intensity across the complexes spectra. Multiple isomers of chiral tag complexes have been observed for each analyte in this work. However, the analysis of this work has not been hindered by these isomers and may not affect the ability to analyze molecules but does decrease sensitivity. Chiral tagging of mixtures could lead to many issues as well, as the chiral tag can non-covalently bond with everything in the mixture leading to large spectral complexity, and decreased signals of the desired complexes. If the spectroscopy of the sample is known, then the desired molecule can be analyzed in a mixture, but the sensitivity again will be decreased and could require more sampling time to produce accurate results.

Another limitation to this technique is the computation requirement. As stated above, multiple isomers of the chiral tag complexes will likely form, requiring conformational searches of noncovalently bound complexes. There is no software that will search for the different isomers like there is for monomer conformational searches and requires an individual to place the tag in likely bounding sites. The individual chiefly uses chemical intuition to predict the likely structure. The need for high level computational theory is not required and dispersion corrected DFT methods have shown to sufficiently do the job of calculating and optimizing structures.

III. Future Directions

Chiral tag rotational spectroscopy is a recently discovered method that is still in its infancy. Many future studies are still needed to access its capabilities by improving instrumentation and theoretical approaches, as well as by assessing the limitations of the technique. The issue of

conformational flexible molecules has not yet been studied but is a logical suspected limitation. Research into the actual limits of conformational flexibility should be determined. The sampling for chiral tag measurements in this thesis was done on a lab instrument at the University of Virginia, and greater improvements for faster sampling for chiral tag should be tested. Cavity instruments have the potential to increase the sensitivity and decreases the required time of the measurement. BrightSpec, Inc. has started producing commercially available instruments that test these advantages in instrumentation, but still room remains for additional advances in instrumentations.[1] In extension to Chapter 3, a more thorough benchmarking of chiral tag measurements should be performed. Verbenone was a rigid molecule and only one chiral tag, butynol, was used in the study. The performance of computational methods for other chiral tags, such as propylene oxide and trifluoroisopropyl alcohol, should be analyzed. Chiral tag rotational spectroscopy is a developing technique that offers an alternative chiral analysis technique with unambiguous structural identification that will greatly benefit from continued research into optimizing its performance.

IV. References

1. Neill, J. L.; Yang, Y.; Muckle, M. T.; Reynolds, R. L.; Evangelisti, L.; Sonstrom, R. E.; Pate, B. H.; Gupton, B. F., Online Stereochemical Process Monitoring by Molecular Rotational Resonance Spectroscopy. *Organic Process Research & Development* **2019,** *23* (5), 1046-1051.